Engineering Journal

Second Quarter 2026 | Volume 63, No. 2

Smarter. Stronger. Steel.

Engineering Journal

American Institute of Steel Construction

Dedicated to the development and improvement of steel construction, through the interchange of ideas, experiences, and data.

 Engineering Journal (ISSN 0013-8029) is published quarterly. Published by the American Institute of Steel Construction at 130 E Randolph Street, Suite 2000, Chicago, IL 60601.

Parametric Demonstration of Load-Dependent Critical Temperatures for Flexural Fire Resistance of Composite W-Shape Floor Beams

MICHAEL M. DRURY and SPENCER E. QUIEL

ABSTRACT

Parametric numerical modeling was performed for three composite floor beam configurations (with different W-shape sections and one-way span lengths supported by shear connections) under exposure to one standard fire and three natural fire temperature-time histories. The parametric matrix included three levels of passive fire protection, four combinations of axial and rotational restraint at the beam ends, and three levels of applied flexural loading. A previously validated lumped mass heat transfer modeling approach was used to calculate steel temperatures for each flange and the web, and a one-dimensional finite element (FE) heat transfer modeling approach was used to calculate the temperature gradient through the structural thickness of the floor slab. A previously validated fiber-beam FE structural modeling approach was then used to model the flexural response of the one-way composite beam under fire. The results of parametric analysis showed that the loss of flexural resistance under any fire exposure can be conservatively predicted using a critical bottom flange temperature based on AISC 360-22, Table A-4.2.4, which is expressed as a function of the applied flexural utilization ratio, M/M_n. The bottom flange temperature at which flexural failure would occur was relatively consistent regardless of variations in beam end restraint as well as the level of applied fire protection. For composite beams that survived natural fire exposure through burnout, the bottom flange temperature always remained below the load-dependent critical value. In those cases, variations in beam end restraint significantly impacted the magnitude of residual tensile reaction forces that develop at the ends of the beam during cooling.

Keywords: composite W-shape floor beam, standard fire resistance, natural fire resilience, critical bottom flange temperature, passive fire protection, spray-applied fire resistive material (SFRM).

INTRODUCTION

Floor systems in steel-framed buildings commonly consist of W-shape filler beams that support a reinforced concrete slab, which is placed on light-gage corrugated metal decking (see Figure 1). The beam and slab are often constructed to be composite via the placement of shear studs at their interface, thereby enhancing their combined flexural stiffness and moment capacity (Vinnakota et al., 1988). The amount of passive fire protection applied to these beams must satisfy the hourly rating requirements of the *International Building Code* (IBC), Table 601 (ICC, 2023). To achieve these ratings in current practice, the W-shape beam is often contour-coated with spray-applied, fire-resistive material (SFRM), a lightweight cementitious product with low thermal diffusivity (UL, 2022a).

Michael M. Drury, Associate, Wiss, Janney, Elstner Associates, Inc., Princeton, N.J. Email: mdrury@wje.com

Spencer E. Quiel, Associate Professor, Department of Civil and Environmental Engineering, Lehigh University, Bethlehem, Pa. Email: seq213@lehigh.edu (corresponding)

Paper No. 2025–04

Hourly ratings represent the time at which a floor beam would be expected to "fail" (by reaching a specified thermal or structural response limit) when subjected to a standard fire exposure (see Figure 2). The initial 2 hr period of a standard fire curve such as ASTM E119 (ASTM, 2024) is intended to generally represent the ramp-up of temperature in a post-flashover building compartment. The fire temperature then increases gradually and indefinitely with no subsequent decay phase nor any consideration of the impact of active fire protection, such as sprinklers. This indefinite continuation of high temperature exposure ensures that the assembly will ultimately reach a targeted response limit when subjected to a standard fire test.

For composite floor beams, hourly ratings provide a standardized metric for flexural fire resistance that enables the selection and comparison of section configurations and passive fire protection materials based on testing. However, an hourly rating does not explicitly quantify the resilience of an assembly when exposed to a realistic or "natural" fire in a building. The temperature-time history for a natural fire exposure is characterized by a rapid initial increase to a fully developed state, followed by eventual "burnout" (i.e., a transition to a decay or cooling phase, as shown in Figure 2). The shape and duration of a natural fire curve depend on the characteristics of the building compartment, including geometry, fuel load, ventilation, and lining materials.

Performance-based structural fire design (PBSFD) evaluates structural response to natural fire, both at the peak response during the fire and (if failure does not occur) in its residual state following burnout and cooling (ASCE, 2020). PBSFD can be implemented per IBC Section 703.2.3 as an alternative method of design under approval of the building official or other authority having jurisdiction (AHJ) (ICC, 2023). Guidance for conducting PBSFD of steel building construction is available in design standards such as ASCE 7-22, Appendix E (ASCE, 2022) and AISC 360-22, Appendix 4 (2022), as well as other references such as the ASCE *Manual of Practice 138* (LaMalva, 2018).

When exposed to fire, flexurally loaded composite beams will thermally weaken and develop additional stress due to axial and rotational restraint of thermal expansion. If the steel beam reaches a "critical" temperature, then the floor

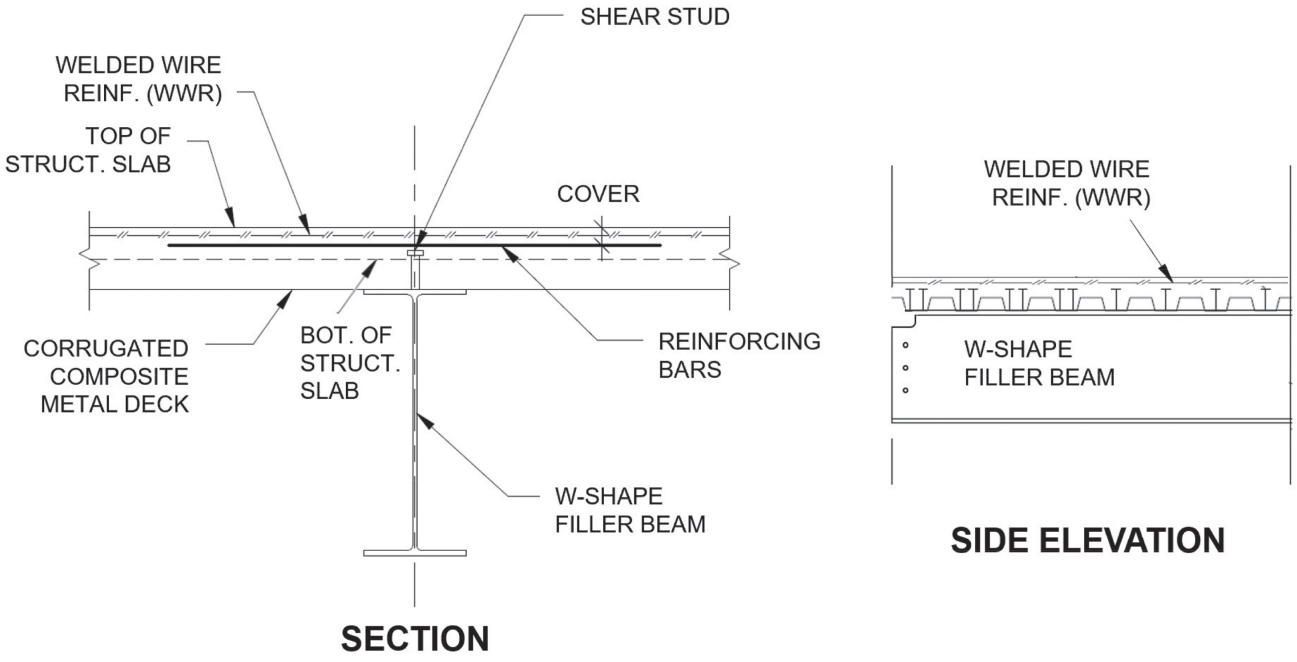

Fig. 1. Representative composite filler floor beam configuration. Side elevation is shown with bolt holes and top flange coping to accommodate a shear connection.

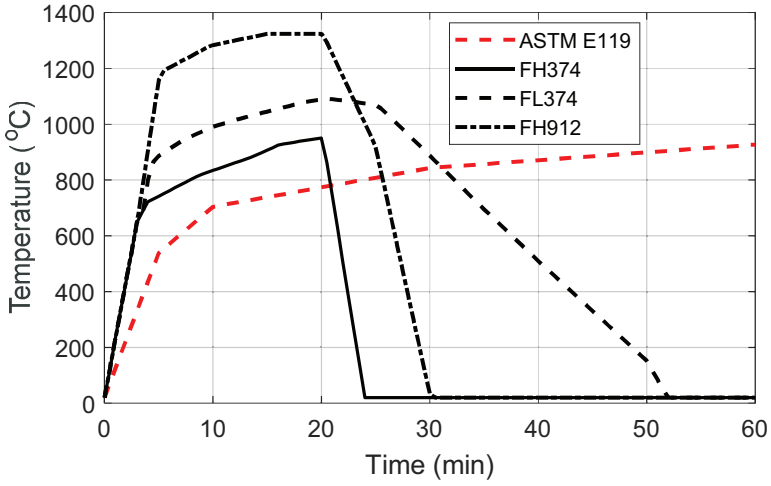

Fig. 2. Representative temperature-time histories of fire exposure: standard fire curve per ASTM E119 (2024) and three natural fire curves from an ASCE exemplar study (2020).

Table 1. Temperature-Dependent Moment Capacity Retention Factors for Composite Floor Beams (Reproduced from AISC 360-22, Table A-4.2.4)	
Moment Capacity Retention $k_{cb} = M_{n,T}/M_n$	**Bottom Flange Temperature $T_{s,BF}$, °F (°C)**
1.00	68 (20)
0.98	300 (150)
0.95	600 (320)
0.89	800 (430)
0.71	1000 (540)
0.49	1200 (650)
0.26	1400 (760)
0.12	1600 (870)
0.02	1800 (980)
0.00	2000 (1100)

system will experience a significant increase in deflection and be at risk of collapse due to the loss of flexural resistance. As would be expected, these critical temperatures are dependent on the level of applied loading, which can be expressed as a ratio of applied moment divided by the initial ambient moment capacity of the composite floor beam cross section. When the floor beam is heated by a fire below, the top flange temperature ($T_{s,TF}$) remains cooler than that of the web and bottom flange ($T_{s,web}$ and $T_{s,BF}$) because the upper surface of the top flange is in contact with the supported floor slab and is thus shielded from direct heating. The values of $T_{s,web}$ and $T_{s,BF}$ are often similar (AISC, 2022; CEN, 2008a), but the response of the bottom flange is more critical to the flexural fire resistance of the composite section (Drury, 2022; Selden, 2014). AISC 360-22, Table A-4.2.4 (2022) provides a moment capacity retention factor ($k_{cb} = M_{n,T}/M_n$) for composite beams as a function of $T_{s,BF}$. Those values (reproduced in Table 1) can be reframed as a function of critical bottom flange temperature, $T_{cr,BF}$, for varying levels of initially applied flexural utilization at ambient conditions, M/M_n (Drury and Quiel, 2025).

In this paper, parametric numerical analyses are used to demonstrate the robustness of the relationship between $T_{cr,BF}$ and M/M_n in Table 1 for one-way composite floor beams with realistic combinations of span length, beam section size, end restraint conditions, and applied SFRM thickness when subjected to either standard or natural fire exposure. By establishing $T_{cr,BF}$ as a consistent indicator of flexural failure under any fire, the hourly rating under standard fire exposure can be determined for a given composite beam and SFRM thickness by calculating the time history of $T_{s,BF}$ via the lumped mass methods presented in Drury and Quiel (2025). In the context of PBSFD, the relationship between $T_{cr,BF}$ and M/M_n in Table 1 can also serve as a threshold below which a composite beam assembly would be expected to survive natural fire exposure through burnout without experiencing flexural runaway. Using load-dependent $T_{cr,BF}$, a designer can thereby correlate an hourly rating for a given composite floor beam configuration to its survivability under a range of natural fire hazards and applied loading.

REVIEW OF PREVIOUS TESTING

Previous work by Drury and Quiel (2025) showed that reframing the relationship in Table 1 as a load-dependent $T_{cr,BF}$ can provide a conservatively accurate prediction of the loss of flexural resistance observed in numerous standard and quasi-standard fire tests (Alfawakhiri et al., 2016; Bletzacker, 1967; Choe et al., 2019, 2020; Drury and Quiel, 2025; Jiang et al., 2017; Kordosky et al., 2020; Wang et al., 2017a; Zhao and Kruppa, 1997) for a wide range of W-shape steel floor beam configurations:

- One-way spans varying from 3.35–12.2 m (11–40 ft).
- Varying section sizes with composite and noncomposite slabs.
- End conditions that are restrained, unrestrained, or partially restrained.
- Connections that range from idealized bearing supports to realistic shear connections.
- Applied loading that induces an initial value of M/M_n ranging from 25–80%.
- Varying levels of contour coated with spray-applied fire resistive material (SFRM), a lightweight cementitious

product with low thermal diffusivity that is commonly used as passive fire protection for W-shape floor beams in current practice).

For illustration, the setups for quasi-standard fire tests per Kordosky et al. (2020) and Choe et al. (2019) are summarized in Table 2. The temperature-time histories applied to each specimen from those programs are plotted in Figure 3. The tests on these W12×26 and W18×35 composite beams are referred to a quasi-standard because their temperature-time histories met or slightly exceeded that of the ASTM E119 standard, and the curves plotted in Figure 3 for these specimens are terminated when they experienced a rapid increase in deflection (i.e., when they approached flexural runaway) and the applied loading was removed. Plots of midspan deflection versus $T_{s,BF}$ in Figure 4 show that the values of $T_{cr,BF}$ for each corresponding M/M_n per Table 1 provide a very good indication of the onset of flexural runaway, regardless of the composite cross-section characteristics, span length, the presence of passive fire protection, and the restraint of the beam ends.

Setups for natural fire tests per Drury et al. (2021) and Drury and Quiel (2023a) are also summarized in Table 2. These tests on W8×10 and W8×28 composite beams were conducted such that the specimens were subjected to the corresponding natural temperature-time histories in Figure 3 and did not experience flexural runaway. Both beams developed significant midspan deflection and restraint reactions

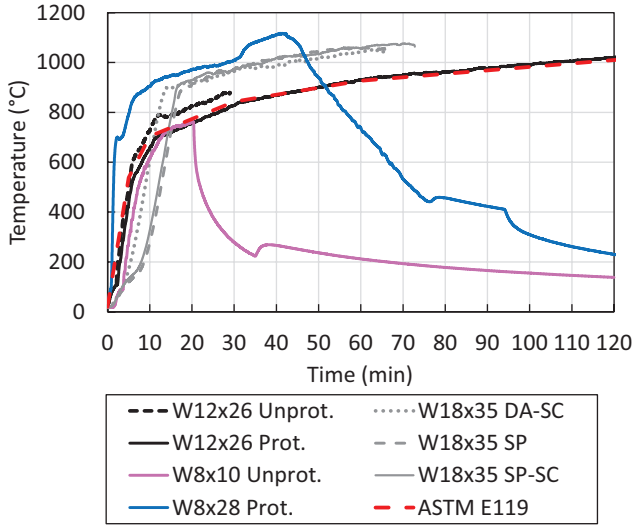

Fig. 3. Temperature-time histories of fire exposures for the tests listed in Table 2.

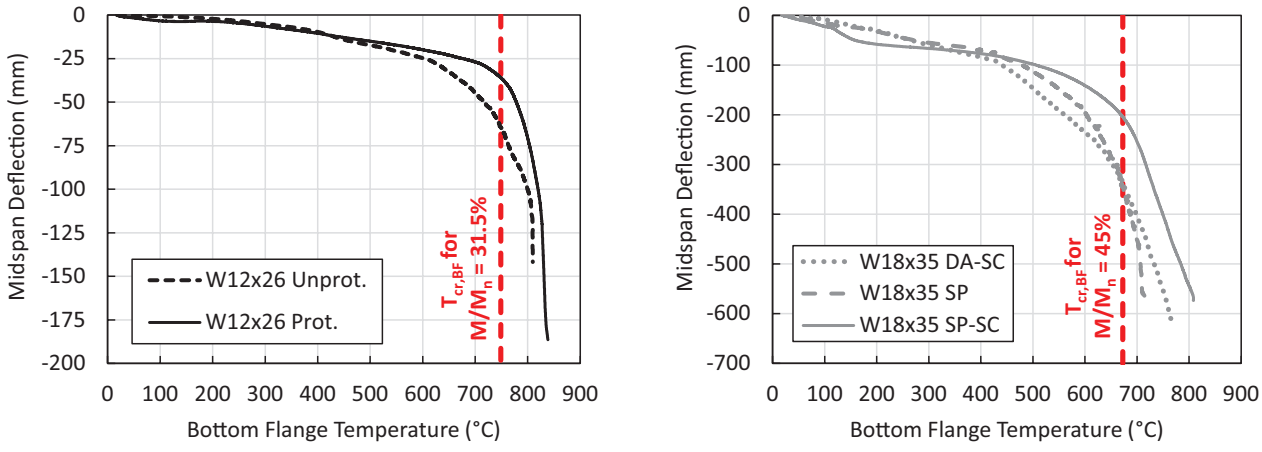

(a) Kordosky et al. (2020) *(b) Choe et al. (2019)*

Fig. 4. Midspan deflection versus $T_{s,BF}$ *from quasi-standard fire tests listed in Table 2 (conversion note: 25 mm = 0.984 in.).*

as the steel temperature increased during the heating phase. However, Figure 5 shows that the peak value of $T_{s,BF}$ for each specimen stopped short of their corresponding value of $T_{cr,BF}$ per Table 1, after which they began to cool during the fire's decay phase and developed significant residual midspan deflection. These test results indicate that $T_{cr,BF}$ as a function of M/M_n per Table 1 can represent a threshold below which a one-way composite beam would be able to maintain its flexural resistance through burnout. The bolted shear tab connections for both specimens exhibited some minor warping damage during post-test inspections but maintained their overall structural integrity (Drury et al., 2021; Drury and Quiel, 2023a). The slabs exhibited some minor post-test cracking but otherwise appeared to be structurally sound and continued to contribute to the residual flexural stiffness of the cooled specimen.

PARAMETRIC MODELING APPROACH

To demonstrate that the relationship for $T_{cr,BF}$ as a function of M/M_n per Table 1 is widely applicable, a modeling approach using fiber-beam elements is used to parametrically analyze the response of three generic composite floor beam assemblies to the fire curves plotted previously in Figure 2. Previous research has shown good agreement between experimental results and this thermo-structural modeling approach for standard [see Chapter 6 of the dissertation by Drury (2022)], quasi-standard (Drury et al., 2020; Drury and Quiel, 2023b), and natural (Drury et al., 2021; Drury and Quiel, 2023b) fire tests of restrained, unrestrained, and partially restrained one-way composite W-shape steel floor beam assemblies. Numerical analysis is conducted via two uncoupled steps: (1) thermal analysis of the fire-exposed structural element cross sections to obtain their temperature increase over the duration of fire exposure (with the fire's temperature-time history used as direct input) and (2) structural analysis of the heated structural assembly (in which the thermal analysis results are used as direct input).

Section and Span Properties

Table 3 summarizes three one-way composite W-shape floor beam configurations that are representative of North American construction practice for steel-frame office buildings (ASCE, 2020; Choe et al., 2019; Sadek et al., 2008). Specifically, the three composite sections were chosen to represent a range of realistic span lengths: 7.3 m (24 ft) for the W14×22, 9.1 m (30 ft) for the W16×26, and 12.2 m (40 ft) for the W18×35. All composite beams [ASTM A992 (2022a) steel with 345 MPa (50 ksi) yield strength] support a 82.6 mm (3.25 in.) lightweight concrete (LWC) slab [with density of 1762 kg/m^3 (110 pcf)] on 76.2 mm (3 in.) corrugated deck (oriented perpendicular to the beam's one-way span) with a compressive strength of 20.7 MPa (3000 psi). The 82.6 mm minimum thickness of LWC generally meets a 2 hr fire resistance rating for thermal transmission thru the slab per ASTM E119 (2024). The slab is reinforced at the mid-depth of its 82.6 mm structural thickness with W1.4×W1.4, 6×6 WWR with 450 MPa (65 ksi) yield strength per ASTM 1064 (2022b). The effective width of the composite slab for its section analysis is taken as $2(L/8)$ per AISC 360-22, Section I3.1a. The beam-slab interface has a single longitudinal line of 19 mm (0.75 in.) shear studs spaced at 304.8 mm (1 ft) above the beam centerline along the entire length of the top flange. This configuration develops 67% composite action based on the relative contributions of the beam, slab, and shear studs to flexural resistance (Vinnakota et al., 1988). It should be noted

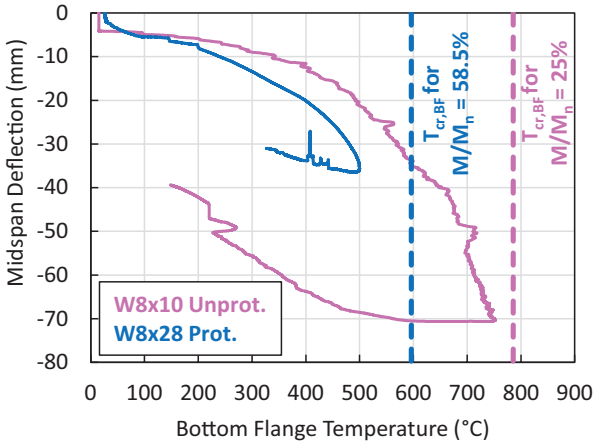

Fig. 5. Midspan deflection versus $T_{s,BF}$ *from natural fire tests listed in Table 2: unprotected W8×10 (Drury et al., 2021) and protected W8×28 (Drury and Quiel, 2023a) (conversion note: 10 mm = 0.394 in.).*

Table 2. Summary of Highlighted Fire Tests from 2019 to 2023 on One-Way Composite Steel Beam Assemblies							
Reference	**Span Length**	**Specimen Description**	**Beam End Conditions**	**Slab End Conditions**	**Protection**	**Fire Exposure**	M/M_n
Kordosky et al. (2020) (2 tests)	10.9 ft	*Beam:* W12×26 *Slab:* 3.25 in. thick on 2 in. profiled deck, 4 ft-8 in. width *Composite action:* 24%	Partial axial restraint with shear tab connection	Unrestrained	Unprotected beam (1 test); 2 hr rated SFRM on the beam (1 test); ceramic fiber blankets for all connections	ASTM E119	31.5%
Choe et al. (2019) (3 tests)	40.0 ft	*Beam:* W18×35 *Slab:* 3.25 in. thick on 3 in. profiled deck, 6 ft width *Composite action:* 82%	Axial restraint with shear tab (SP: 2 tests) or double angle (DA: 1 test) connection	Unrestrained (1 test); axial and rotational restraint to simulate slab continuity (SC: 2 tests)	2 hr rated SFRM on the beam; 3 hr rated SFRM on the connections	Parametric fire that emulated and exceeded ASTM E119	45%
Drury et al. (2021) (1 test)	11.0 ft	*Beam:* W8×10 *Slab:* 2 in. thick on 1.5 in. profiled deck, 4 ft-8 in. width *Composite action:* 52%	Partial axial restraint with shear tab connection	Unrestrained	Unprotected beam; ceramic fiber blankets for all connections	Natural fire with steep decay phase after furnace shutdown	25%
Drury and Quiel (2023a) (1 test)	10.4 ft	*Beam:* W8×28 *Slab:* 2.5 in. thick on 2 in. profiled deck, 4 ft-8 in. width *Composite action:* 97%	Partial axial restraint with shear tab connection	Rotational restraint	2 hr rated SFRM on the beam; ceramic fiber blankets for all connections	Natural fire with controlled decay phase	58.5%

that enhancements to the slab (in particular, an increase in reinforcement quantity or continuity) can enable a modest increase in fire resistance (ASCE, 2020; Gernay and Khorasani, 2020; Khorasani et al., 2019; McAllister, 2014); however, those parameters are outside the scope of this study.

When the underside of the assembly is exposed to fire, the temperature of the steel beam will increase faster than that of the slab, even if the beam is coated with SFRM (Drury et al., 2023a; Kordosky et al., 2020). The temperature of the shear studs will also increase due to conduction from the beam's top flange into the concrete slab; however, testing has shown that the stud temperature is only 75–80% of the top flange temperature (CEN, 2008a; Huang et al., 1999). Also, previous studies have also shown that the presence of slab edge continuity (representative of an actual building system) (Huang et al., 1999) as well as the use of profiled slabs on metal decking (such as that used in this study, rather than a flat slab) (Lim et al., 2020; Mirza and Uy, 2009) will enhance the robustness of the shear studs when the assembly is under fire.

The tensile strength of the steel beam is therefore reduced faster than the compressive strength of the slab or the shear strength of the studs. In recognition of this phenomenon, previous research has shown that composite floor assemblies with ambient composite percentages as low as 24% can rapidly transition to emulating fully composite behavior under fire, even before the fire develops its full intensity (Drury et al., 2020, 2021; Drury and Quiel, 2023a, 2023b; Jiang et al., 2014; Kodur et al., 2013; Kordosky et al., 2020; Wang et al., 2017a, 2017b; Wellman et al., 2011). Analyzing the beam-to-slab interface as fully composite for the purposes of capturing fire-exposed flexural response of the composite member is therefore justified and has been used for parametric numerical analysis on similar composite beam floor systems under fire (Gernay and Khorasani, 2020; Khorasani et al., 2019; Selden and Varma, 2016b, 2016c).

In this study, the composite beam assembly is modeled in SAFIR 2019.a6 (Franssen and Gernay, 2017, 2019) as shown in Figure 6, with separate fiber-beam elements used to represent the steel beam and the structural thickness of the concrete floor slab. Those fiber-beam elements are discretized 304.8 mm (1 ft) lengths based on previously published convergence studies (Drury and Quiel, 2023b;

Quiel and Garlock, 2010). The nodeline for each fiber-beam cross-section runs through its geometric centroid (see Figure 7). A rigid connector link element is used to develop full composite action between the beam and slab at each of their respective nodes.

The one-way span length L is analyzed as uniformly heated, which is commonly assumed for elements in a building compartment with post-flashover fire conditions (which are fully developed and well mixed, thus applying a single temperature-time history of heat exposure to all elements in the compartment). The temperature increases of the W-shape beam section and the composite slab when exposed to fire are calculated separately via uncoupled thermal analyses. The results of those analyses (which are described in the following subsections) are then mapped to the fibers in the cross sections shown in Figure 7.

Based on a previously published convergence study (Drury, 2022), each flange can be represented with a single fiber, and the web can be modeled with 30 equally spaced fibers over its height in order to capture the flexurally induced gradient of strain over the depth of the beam. Temperature-dependent structural properties for the hot-rolled steel beam are taken from Eurocode 3, Part 1-2 (CEN, 2005). The material model assigned to the bottom flange fiber permits the compression-induced onset of local buckling as a reduction of effective yield strength, which represents the reduction of the bottom flange effective width as per the provisions in Eurocode for buckling of unstiffened plates (Franssen et al., 2014). All of the aforementioned long-span fire tests conducted at the National Institute of Standards and Technology (NIST) (Choe et al., 2020) developed local buckling in the bottom flange at the partially restrained ends of the beam but remained stable with reduced end stiffness. Capturing bottom flange local buckling effects is essential for modeling restrained composite beams under fire, particularly for realistic span lengths. Temperature-dependent thermal properties for the steel are also taken from Eurocode 3, Part 1-2 (CEN, 2005) and are conservatively assumed to be reversible during cooling, based on the experimental validation conducted by Drury and Quiel (2023b) for composite floor beams under natural fire exposure.

The LWC slab was modeled with six concrete fibers over its structural thickness, with the WWR represented as a very thin layer at mid-thickness with equivalent area per unit width. Temperature-dependent structural properties for the slab were taken for calcareous concrete per Eurocode 2, Part 1-2 (CEN, 2008b) and include the consideration of explicit transient creep (Gernay and Franssen, 2012). Temperature-dependent structural properties for the WWR were taken for cold-drawn wire per Eurocode 2, Part 1-2 (CEN, 2008b) as well. The slab is assumed to have an in-situ moisture content of 3% and is modeled as having nonreversible thermal properties per Drury and Quiel (2023b), which closely resemble those for LWC in Part 1-2 of Eurocodes 2 and 4 (CEN, 2008a, 2008b).

Flexural Loads

The resulting nominal moment capacity, M_n, for each composite section in accordance with AISC 360-22, Section I3 is summarized in Table 3. Each floor beam is designed as simply supported in one-way bending to support a uniformly distributed line load w, which is assumed to remain constant throughout exposure to fire. For this study, each beam is analyzed for values of w that induce a maximum bending moment at midspan equal to three different percentages of $8M_n/L^2$ as shown in Table 4. These percentages are based on ϕM_n design targets of 30%, 45%, and 60%, with $\phi = 0.90$ per AISC 360-22, Section I3.2a.

In the model, self-weight is applied to each element as a uniformly distributed line load, and superimposed floor loading is applied as a uniformly distributed line load to the slab elements. To induce the initial flexural utilizations listed in Table 4, the value of w in Figure 6 represents the total contributions of self-weight and superimposed floor loads.

End Conditions

These parametric analyses focus on composite W-shape floor beams that are supported with bolted shear connections; girders with moment connections are therefore considered to be outside the scope of this study. These elements are conventionally designed as simply supported under ambient conditions; however, the ends of a heated composite W-shape floor beams in an actual building fire will experience partial (yet significant) restraint against thermally induced expansion and rotation (Moss et al., 2004). That restraint can be provided by the presence of slab continuity beyond the ends of the beam, the beam's connections to surrounding structural elements, as well as the relative stiffness of those supporting elements (Martinez and Jeffers, 2021; McAllister, 2014). Previous research has shown that even a shear connection will realistically exhibit at least some degree of rotational stiffness for floor beams at both ambient conditions (Kishi et al., 1997; Liu and Astaneh-Asl, 2004) and under fire exposure (Choe et al., 2019, 2020; Drury et al., 2021; Drury and Quiel, 2023a; Fischer et al., 2021; Fischer and Varma, 2017; Hantouche et al., 2020; Kordosky et al., 2020). Also, a modest increment of rotational stiffness at the beam ends can have a non-negligible impact on the anticipated structural behavior of the composite beam assembly under fire (Drury and Quiel, 2023b).

For this study, Figure 6 shows that nodal restraint at each end of the beam is approximated via an axial spring with

stiffness K_a and a rotational spring with stiffness K_r. As shown in Table 4, two levels of stiffness are considered for each spring as parameters in this study. The axial restraint low level (aL) is taken equal to $0.1EA_b/L$ for each beam per Dwaikat and Kodur (2011) as a lower-bound estimation of the stiffness provided by the surrounding structure against thermal expansion (where E is the elastic modulus of steel, A_b is the cross-sectional area of the beam, and L is the span length). The axial restraint high level (aH) is taken as a constant value of 190 kN/mm (1085 kip/in.), which was used by the aforementioned study on fire-exposed one-way composite beams at NIST (Choe et al., 2019, 2020; Ramesh et al., 2019) to represent a typical lateral restraining stiffness in a steel framed building. To represent a realistic upper bound of stiffness for a shear connection, the rotational stiffness high level (rH) for K_r is taken as $2EI_b/L$, which is the limiting value per AISC 360-22, Section C-B3.4, below which a connection can be considered simple (where I_b is taken as the steel beam's moment of inertia). The rotational stiffness low level (rL) is arbitrarily taken as 1/20th of that limiting value at $0.1EI_b/L$.

It should be noted that these stiffnesses are kept constant throughout each simulation, even though the connections and slab end conditions would realistically experience temperature-induced weakening and potential permanent deformation by restraining the beam's expansion and rotation (Block et al., 2013; Burgess et al., 2012; Garlock and Selamet, 2010; Hantouche et al., 2020). However, previous research has demonstrated that applying constant beam-end stiffness (similar to the models for this study) can enable close numerical predictions of flexural tests results for partially restrained one-way composite W-shape steel floor beam assemblies under quasi-standard (Drury et al., 2020; Drury and Quiel, 2023b), and natural (Drury et al., 2021; Drury and Quiel, 2023b) fire exposure. An explicit evaluation of the connections is beyond the scope of this study; however, the impact of natural fire exposure on connection reactions will be addressed later in this paper.

As shown in Figure 6, two additional slab elements are included beyond each end of the beam as an approximate representation of slab continuity. For simplification, the horizontal translation at the end node of this slab extension is constrained to that at the end of the beam (which is attached to the axial spring with stiffness, K_a). The vertical translation and rotation of the two slab nodes beyond the end of the beam are restrained, thus implying that the slab extension is compositely attached to the framing that supports the beam. When the assembly experiences a significant increase in fire-induced deflection, the slab extension elements will undergo tensile cracking via its strain compatibility with the rotating end of the composite beam. At this point, the WWR layer in the slab extension will become realistically engaged in a tensile hogging response.

Passive Fire Protection

Each floor beam is analyzed for three levels of passive fire protection (see Table 4): unprotected (i.e., bare steel) and two thicknesses of contour coated lightweight SFRM [with a density of 240 kg/m^3 (15 pcf), emulating the commonly used commercial product CAFCO 300 (Isolatek

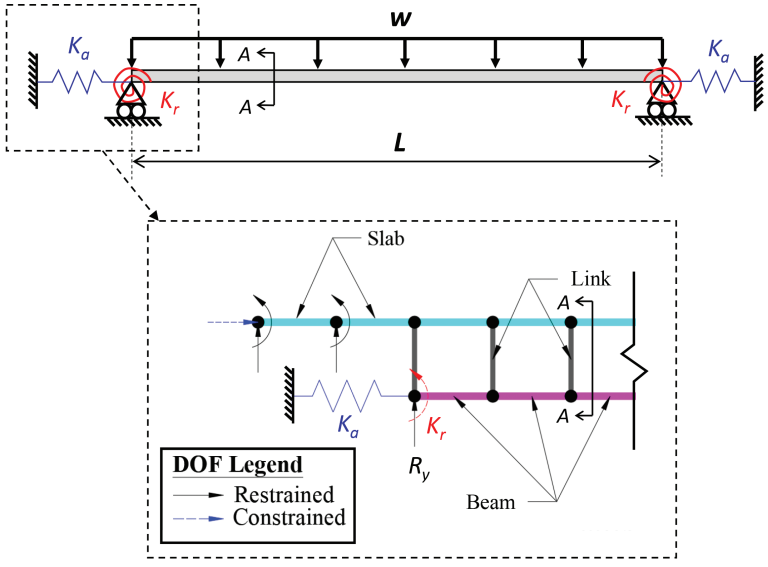

Fig. 6. Elevation schematic of the FE model used for parametric study of the one-way composite floor beam configurations in Tables 3 and 4.

Table 3. Summary of Generic Composite Floor Beam Configurations for Parametric Analysis						
Reference	Span Length (ft)	Beam Section	Slab Section	Composite Section M_n (kip-ft)	P1 SFRM Thickness (in.)	P2 SFRM Thickness (in.)
Sadek et al. (2008)	24	W14×22	3.25 in. LWC on 3 in. deck	277	7/16	7/8
ASCE (2020)	30	W16×26		361	7/16	7/8
Choe et al. (2019)	40	W18×35		535	3/8	13/16

Table 4. Matrix of Modeling Parameters				
Beam Section	Passive Fire Protection Level	Flexural Utilization (M/M_n)	Beam End Axial Stiffness (K_a)	Beam End Rotational Stiffness (K_r)
W14×22 W16×26 W18×35	Unprotected (U) 1 hr protected (P1) 2 hr protected (P2)	27.0% 41.5% 54.0%	aL: $0.1EA_b/L$ aH: 1085 k/in.	rL: $0.1EI_b/L$ rH: $2EI_b/L$

International, 2020)]. Composite floor members in Type I building construction are required to meet a 2 hr fire resistance rating per IBC Table 601 (ICC, 2023). This requirement is commonly met by selecting a 2-hr-rated SFRM thickness from UL Designs in the D900, N700, and N800 series (UL, 2022a), which are determined via ASTM E119 standard fire testing results for a particular composite section configuration. The published thickness for the tested beam in the selected UL design would then be adapted to the actual beam using the conversion equations in AISC 360-22, Section A-4.3.2c, which are a function of the relative section factors (i.e., the ratio of cross-sectional area divided by fire-exposed perimeter) between the two beams.

In this study, two thicknesses of lightweight SFRM are selected per UL D902 (UL, 2022b): P1 corresponds to a 1 hr unrestrained beam rating, and P2 corresponds to a 2 hr assembly rating (restrained and unrestrained). The resulting fire protection thicknesses, summarized in Table 3, are tailored to each W-shape section via the aforementioned conversion equations and rounded up to the nearest 1.58 mm (1/16 in.) increment, in accordance with typical practice. Note that the 1 hr unrestrained beam rating per UL D902 can also be used to represent a 2 hr restrained/unrestrained assembly rating per UL D982 (UL, 2022c), based on comparative fire testing completed in 2013 by AISC and AISI (Alfawakhiri et al., 2016; Carter and Alfawakhiri, 2013).

Temperature-dependent thermal properties for the SFRM are taken as the mean value of the stochastic functions proposed by Khorasani et al. (2015) (specifically, Equations 22 to 24 and Figure 9 from that paper). Those equations align well with the results of experimental testing for CAFCO 300 [see Chapter 7 of the dissertation by Drury (2022)] and other commercially available SFRMs of similar "lightweight" density (Carino et al., 2005; Harmathy, 1965; Jeanes, 1984; Kodur and Shakya, 2013). The temperature-dependent thermal properties for the SFRM are also conservatively assumed to be reversible during cooling, based on the experimental validation conducted by

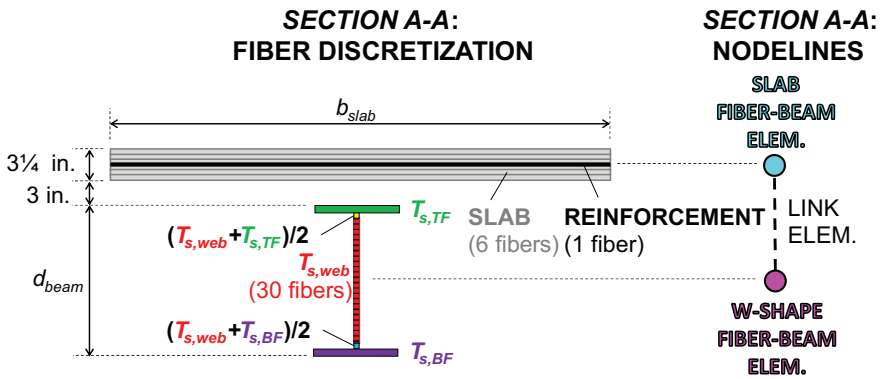

Fig. 7. Details of section A-A from Figure 6.

Drury and Quiel (2023b) for composite floor beams under natural fire exposure.

Fire Exposures

Standard fire temperature-time histories, such as those specified in ASTM E119 (2024) (see Figure 2), UL 263 (2020), or ISO 834 (2019), undergo a rapid rise past 800°C (1472°F) in the first 30 min, followed by a more gradual increase to ~1100°C (~2012°F) after 2 hr. The fire temperature then increases indefinitely with no subsequent decay phase until the assembly reaches a specified thermal or structural limit. Again, the application of standard fire curves constitutes the basis for hourly ratings per SFRD.

ASCE recently commissioned a series of PBSFD examples for generic steel framed buildings that were performed by several leading structural design firms in partnership with academic experts in structural fire engineering (ASCE, 2020). The temperature-time histories of the three natural fire curves in Figure 2 are reproduced from Chapter 7 of that report for a 1,277 m^2 (13,746 ft^2) compartment floor area with either high or low ventilation. The baseline fuel load of 374 MJ/m^2 (32.9 $kBtu/ft^2$) represents the 80% fractile fuel load per Eurocode 1, Part 1-2 (CEN, 2009), including a risk reduction factor for automatic sprinklers. An elevated fuel load of 912 MJ/m^2 (80.3 $kBtu/ft^2$) neglects the risk reduction factor for sprinklers and represents the 98% fractile fuel load (Khorasani et al., 2014). As shown in Figure 2, the curves FH374 (natural fire with high ventilation and 374 MJ/m^2 fuel load), FL374, and FH912 represent a range of intensities that exceed that of the ASTM E119 standard fire curve within the first ~20 min of the fire but then burn out with varying decay rates due to their differences in ventilation.

Parametric Model Configurations

The parametric matrix in Table 4 produces 108 total model configurations, which are named according to their parameters. For example, model name W14-U-27-rHaL denotes a W14×22 beam section with no SFRM (unprotected), initially loaded to 27% flexural utilization (M/M_n), with high rotational stiffness and low axial stiffness at the ends of the beam. Each model configuration is then subjected to each of the four temperature-time histories for fire exposure in Figure 2: the ASTM E119 standard fire, and natural fires FH374, FL374, and FH912.

THERMAL ANALYSIS: STEEL BEAM CROSS SECTION

The flanges and web are each represented as a lumped mass that absorbs heat from the fire and conducts heat between adjacent plates and to the composite slab. An experimentally validated three lumped mass (3LM) analysis, presented in Section 4.1 of the paper by Drury et al. (2020), is used to calculate the temperatures in each steel plate over the duration of fire exposure; for brevity, those equations are not recounted here. All surfaces of the bottom flange and web are assumed to be uniformly exposed to the fire's temperature-time history. The bottom and side surfaces of the top flange are also uniformly exposed to fire; its top surface, however, is in partial contact with the floor slab. Due to the corrugated deck, it is assumed that half of the top surface of the top flange is in contact with the slab. Conductive heat transfer from the top flange to the slab through that contact area is calculated using the closed-form relationship proposed by Ghojel and Wong (2005). For unprotected beams, the half of the top surface of the top flange that is not in contact with the slab is conservatively included in its fire-exposed perimeter (Drury et al., 2020, 2021). For protected beams, the gap between the top flange and the deck flutes is assumed to be filled with SFRM, which is common practice for this type of floor system (Drury and Quiel, 2023a; Kordosky et al., 2020). The half of the top surface of the top flange that is not in contact with the slab is considered to be heavily insulated by the SFRM infill and is therefore neglected when calculating the fire-exposed perimeter.

The fire-exposed perimeter of the SFRM for the protected beams is assumed to have the same temperature as the fire at any given time step, and heat transfer to the steel is calculated via conduction across the SFRM thickness. This assumption is common practice for fire-exposed surfaces of SFRM-protected steel sections (AISC, 2022; CEN, 2005). Heat transfer to the fire-exposed surfaces of unprotected beams is calculated using the following thermal boundary conditions:

- The convective heat transfer coefficient is taken as 25 W/m^2-K (4.4 $Btu/hr\text{-}ft^2\text{-}°F$) for surfaces heated by all fire exposures and 4 W/m^2-K (0.7 $Btu/hr\text{-}ft^2\text{-}°F$) for unheated surfaces or during cooling for natural fire exposure. It should be noted that Eurocode 3, Part 1-2 (CEN, 2005) recommends a convective coefficient of 35 W/m^2-K (6.2 $Btu/hr\text{-}ft^2\text{-}°F$) for surfaces heated by natural fire exposure; for this study, however, the same convective coefficient was used for all fire curves to maintain consistency in the thermal boundary conditions for direct comparison.

- Eurocode 3, Part 1-2 (CEN, 2005) recommends a resultant emissivity of 0.7 but with the potential inclusion of a shadow effect factor, which is dependent on the width of the bottom flange relative to the depth of the web. However, a reduced resultant emissivity of 0.5 is used as an implicit application of shadow effects for all sections based on previous experimental validations by Drury et al. (2020, 2021).

Preliminary 3LM thermal calculations indicated that a time step of 30 s was acceptably small to achieve a convergent thermal solution (Drury et al., 2020, 2021; Gamble, 1989).

The resulting time histories of $T_{s,BF}$, $T_{s,TF}$, and T_{web} from 3LM heat transfer analysis of the beam sections in Table 3 are plotted in Figure 8 for exposure to the ASTM E119 standard fire as well as the FH374 natural fire. The curves for $T_{s,BF}$ and T_{web} track closely together in all cases regardless of the presence or amount of passive fire protection. Also, the three beam section sizes exhibit similar thermal responses on a plate-by-plate basis for each passive fire protection case. The temperatures in all three plates of the unprotected beams are not only very similar, but closely follow the fire curve during heating. As the SFRM thickness is increased, the plates heat progressively slower, as would be expected. During the decay phase of the natural fire, the bottom flange and web cool at a faster rate than the top flange because they have a greater section factor (i.e., the ratio of exposed perimeter to cross-sectional steel area).

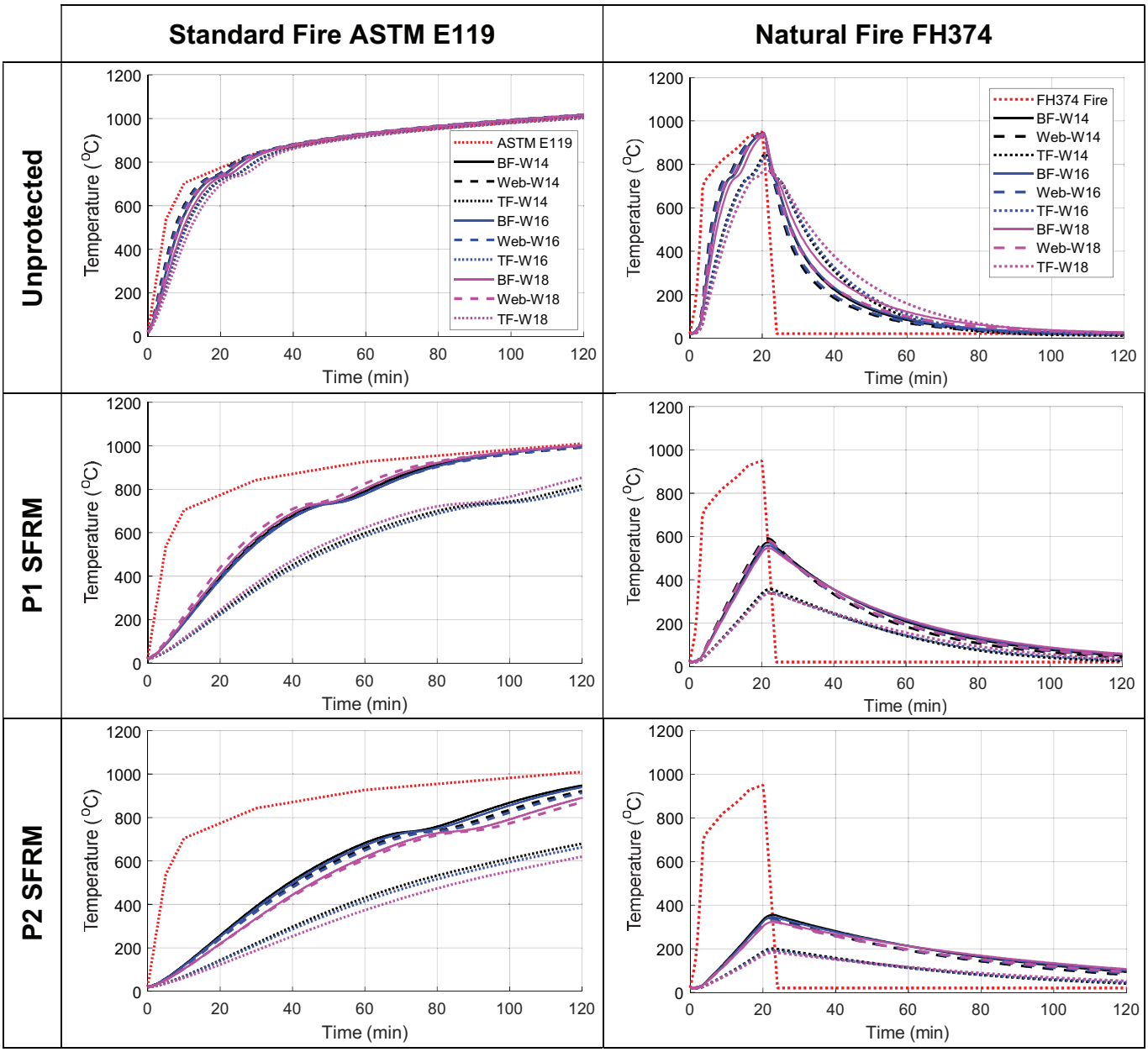

Fig. 8. Calculated temperature-time histories for the flange and web plates of the generic composite beam configurations under standard and natural fire exposure.

The steel temperatures for each lumped mass are then mapped to the 32 fibers in the beam cross section shown previously in Figure 7 as thermal input for structural FE analysis in SAFIR. $T_{s,BF}$ and $T_{s,TF}$ are assigned to their respective single fibers, and $T_{s,web}$ is assigned to the innermost 28 fibers in the web. The fibers at the top and bottom of the web are each used as transition elements and are taken as the average of the lumped mass temperatures from the web and adjacent flange plate. Preliminary modeling explored the application of a linear thermal gradient between mid-height of the web and the top flange [as suggested in AISC 360-22, Section A-4.2.4d(f)]; however, structural FE results were relatively unaffected, and the simpler approach outlined above was therefore used for all parametric analyses in this study.

THERMAL ANALYSIS: CONCRETE SLAB CROSS SECTION

Concrete has significantly less thermal diffusivity and thermal mass compared to steel, and the slab will therefore develop a thermal gradient through its thickness. For this reason, lumped mass methods are not appropriate for thermal analysis of the slab, which is instead examined via one-dimensional heat transfer analysis in SAFIR 2019.a6 (Franssen and Gernay, 2017, 2019). To account for the non-uniform thickness of the slab on the corrugated metal deck, two analyses are initially conducted for each fire exposure: the 82.8 mm (3.25 in.) "thin" section of the slab is vertically divided into 6 equal fibers, and the 158.8 mm (6.25- in.) "thick" section is likewise divided into 11 equal fibers as shown in Figure 9. The structural thickness of

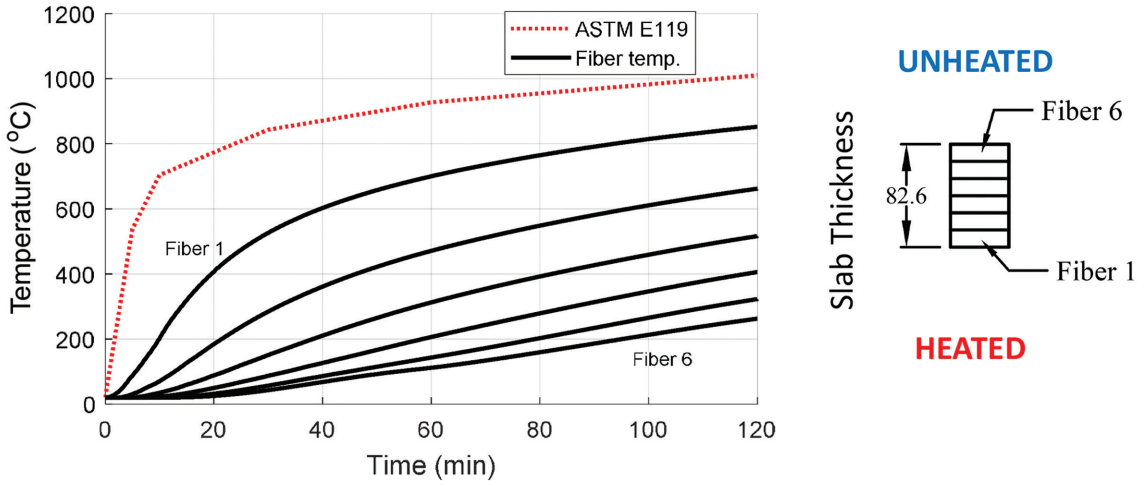

(a) 82.6 mm (3.25 in.) thin slab

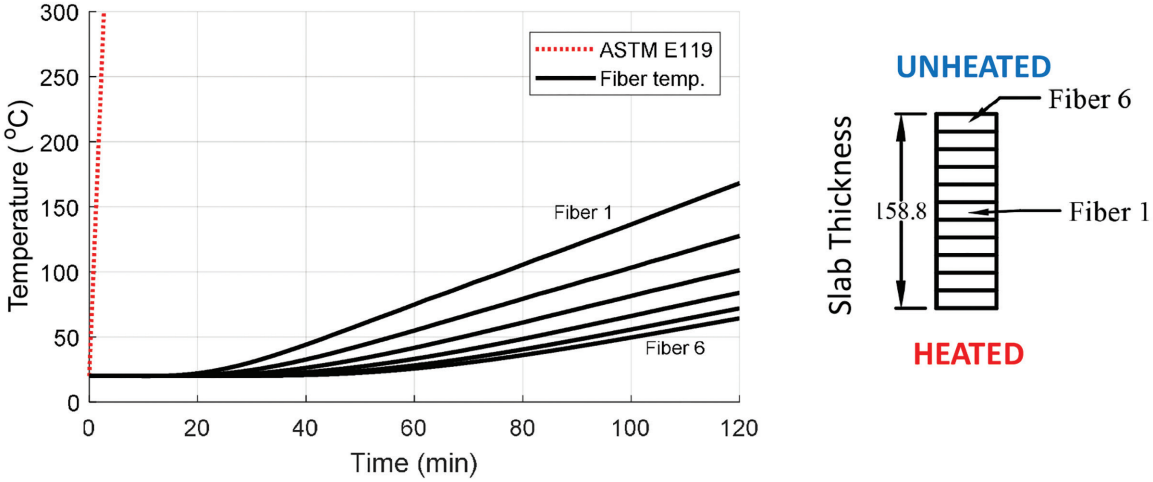

(b) 158.8 mm (6.25 in.) thick slab

Fig. 9. Fiber temperature-time histories for the thin and thick models of the concrete slab.

the slab is 82.8 mm (3.25 in.) thick and is taken as having the same 6-fiber discretization as the "thin" section. The temperature-time history in each fiber of the structural thickness under each fire exposure is calculated as a weighted average per Drury and Quiel (2023b) among all 6 fibers from the thin section and the upper 6 fibers from the thick section.

Convective heat transfer coefficients are taken as 25 W/m^2-K (4.4 Btu/hhr-ft^2-°F) for heated surfaces and 4 W/m^2-K (0.7 Btu/hr-ft^2-°F) for surfaces that are either not exposed to fire (such as the top surface of the slab) or cooling during the decay phase of a natural fire (CEN, 2008b; Drury and Quiel, 2023b). The resultant emissivity of the bottom surface of the slab is taken as 0.3 to account for shadow effect and reflectivity of the galvanized corrugated metal deck (Kodur et al., 2013). Note that the WWR at the mid-depth of the structural thickness is not explicitly included in the one-dimensional thermal models of the slab. Due to its low thermal mass and high conductivity relative to the LWC, the WWR would have a negligible impact on the thermal response of the LWC. Rather, the temperature of the WWR is simply taken as the average of neighboring fibers when using these thermal results as input for structural modeling.

The fiber temperature-time histories of the thick and thin slab sections are plotted in Figure 9 for exposure to the ASTM E119 standard fire. The resulting weighted average fiber temperatures for the slab's structural thickness are then shown in Figure 10. Fiber temperatures under natural fire exposure show a similar gradient through the slab thickness and are therefore not plotted here for brevity. Based on previously published research (Drury et al., 2020; Gernay and Khorasani, 2020; Wang, 2012), the fully composite assumption (and, in turn, the lack of consideration of stud temperatures) is justified since the temperature of the steel beam (in particular the bottom flange, which is critical in providing tensile resistance in flexure) will always outpace the temperature of not only the slab, but also the concrete-encased shear studs due to the inherent geometry of composite floor construction. Because full composite action is assumed in the structural model, the heating of shear studs is also not addressed. This simplification is further justified based on the experimental validation study previous conducted by Drury and Quiel (2023b) for similar composite beam specimens under standard and natural fire exposure.

FLEXURAL RESPONSE TO STANDARD FIRE EXPOSURE

The calculated midspan deflections for all composite beam configurations under ASTM E119 standard fire exposure are plotted in Figures 11, 12, and 13 (W14×22, W16×26, and W18×35, respectively) for all three levels of SFRM protection and for all levels of end restraint per Table 4. For brevity, each plot shows only the 27% and 54% flexural utilization levels because the results of these cases effectively bracket the results of the 40.5% utilization cases. Also included on each plot are several horizontal lines that correspond to the following deflection limits, which have conventionally been used to describe the loss of flexural resistance in one-way beam spans under fire:

- A deflection limit equal to $L/20$ or $L/30$ has been used as a practical stopping point for numerous standard fire tests on one-way composite steel floor beams (Jiang et al., 2017; Wang et al., 2017a; Choe et al., 2020). This level

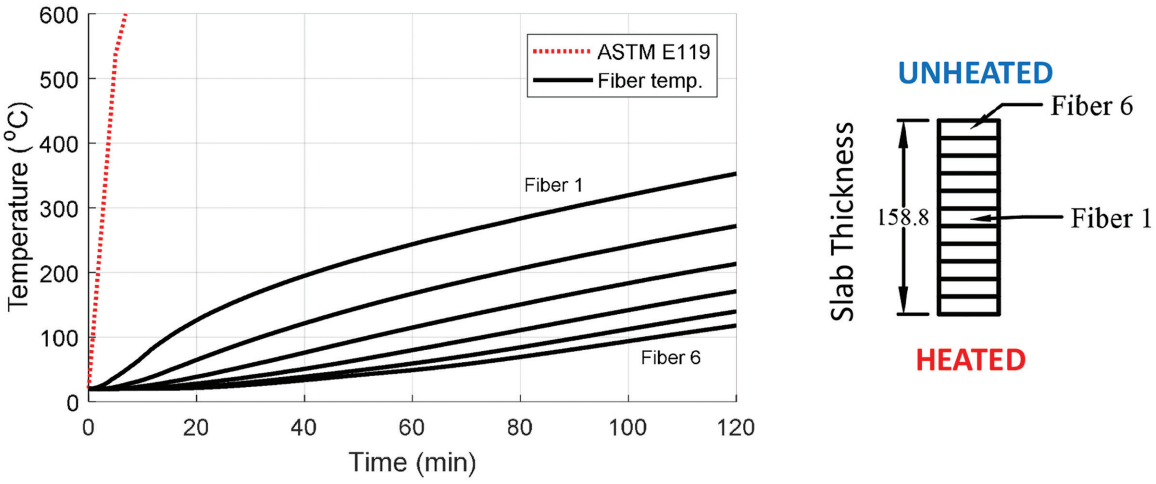

Fig. 10. Fiber temperature-time histories for the 82.6 mm (3.25 in.) structural thickness of the concrete slab, calculated as a weighted average of like fibers from the thick and thin section analyses.

of deflection is sufficiently large to imply the engagement of tensile membrane action in the beam (Martinez and Jeffers, 2021). The larger of these two limits, $L/20$, is marked on the plots of midspan deflection in Figures 11, 12, and 13.

- A deflection limit equal to $L^2/(400d)$ (where d is the distance between extreme fibers in the flexural cross-section) is used in combination with a limiting deflection rate for standard fire tests per ASTM E119 (ASTM, 2024) to approximate the loss of flexural resistance for loaded unrestrained beams. This deflection limit has been used in previous studies to also evaluate restrained beams, with d taken as either the steel beam depth, d_{beam}, (Rackauskaite et al., 2019; Selden, 2014) or the total depth of the steel beam plus the composite slab thickness, d_{comp} (Alfawakhiri et al., 2016; Kordosky et al., 2020). The values of $L^2/(400d_{beam})$ and $L^2/(400d_{comp})$ are both marked on Figures 11–13 for comparison.

All models exhibit a similar trend of midspan deflection when exposed to the ASTM E119 standard fire, regardless of the level of fire protection or beam end restraint. As the beam initially heats up, the deflection gradually increases until the onset of nonlinear stress-strain behavior in the heated beam, at which point the deflection rate increases.

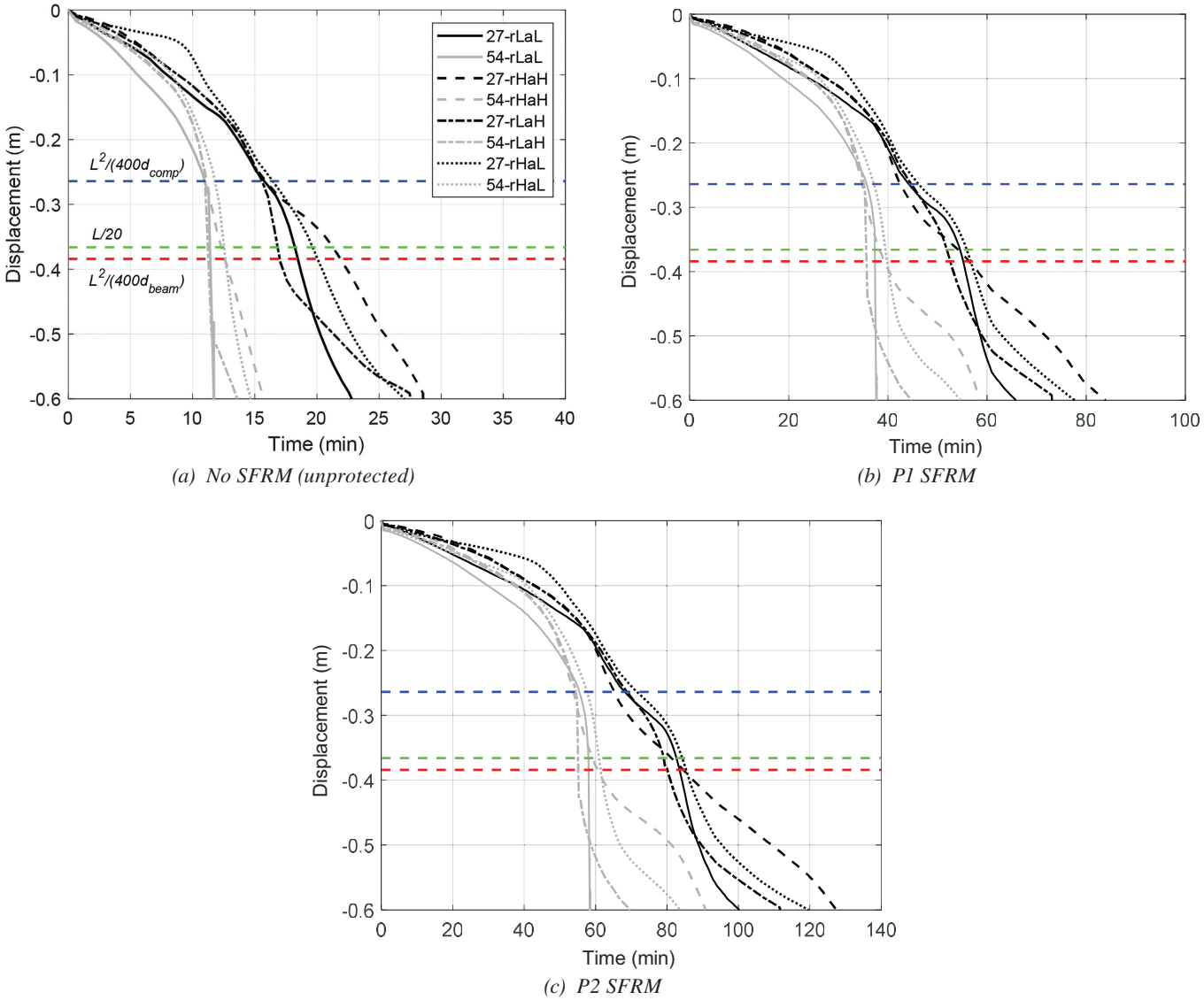

(a) No SFRM (unprotected)

(b) P1 SFRM

(c) P2 SFRM

Fig. 11. Midspan deflection for the one-way W14×22 composite beam configuration under ASTM E119 standard fire exposure with varying levels of SFRM per Table 4 (conversion note: 0.1 m = 3.94 in.).

Nonlinear behavior is generated by thermally induced losses of strength and stiffness as well as an increase in internal force due to the restraint of thermal expansion. As expected, higher flexural loading and lower rotational restraint on the beam ends (rL) enable an earlier increase in deflection rate. Once the deflection exceeds $L/20$, then the composite beam transitions from flexural response to a catenary response. Most models experience a slight stiffness recovery during the catenary phase due to the composite interaction of the beam and slab before eventually losing all resistance and reaching nonconvergence. A few models such as W14-U-57-rLaL plunge to runaway deflection almost immediately after losing flexural resistance due to the low axial and rotational stiffness at the ends of the composite beam.

The values of $T_{s,BF}$ at which each model reaches the three deflection milestones are plotted in Figure 14(a–c) as a function of initial flexural utilization. Figure 14(d) plots the $T_{s,BF}$ at the onset of an axial tension reaction at the ends of the beam, thus indicating a transition to catenary behavior. This milestone is structurally significant: If the connections and continuous slab can resist these tensile reactions, then the beam can develop additional fire resistance in the catenary state. If the connections fail under these reactions,

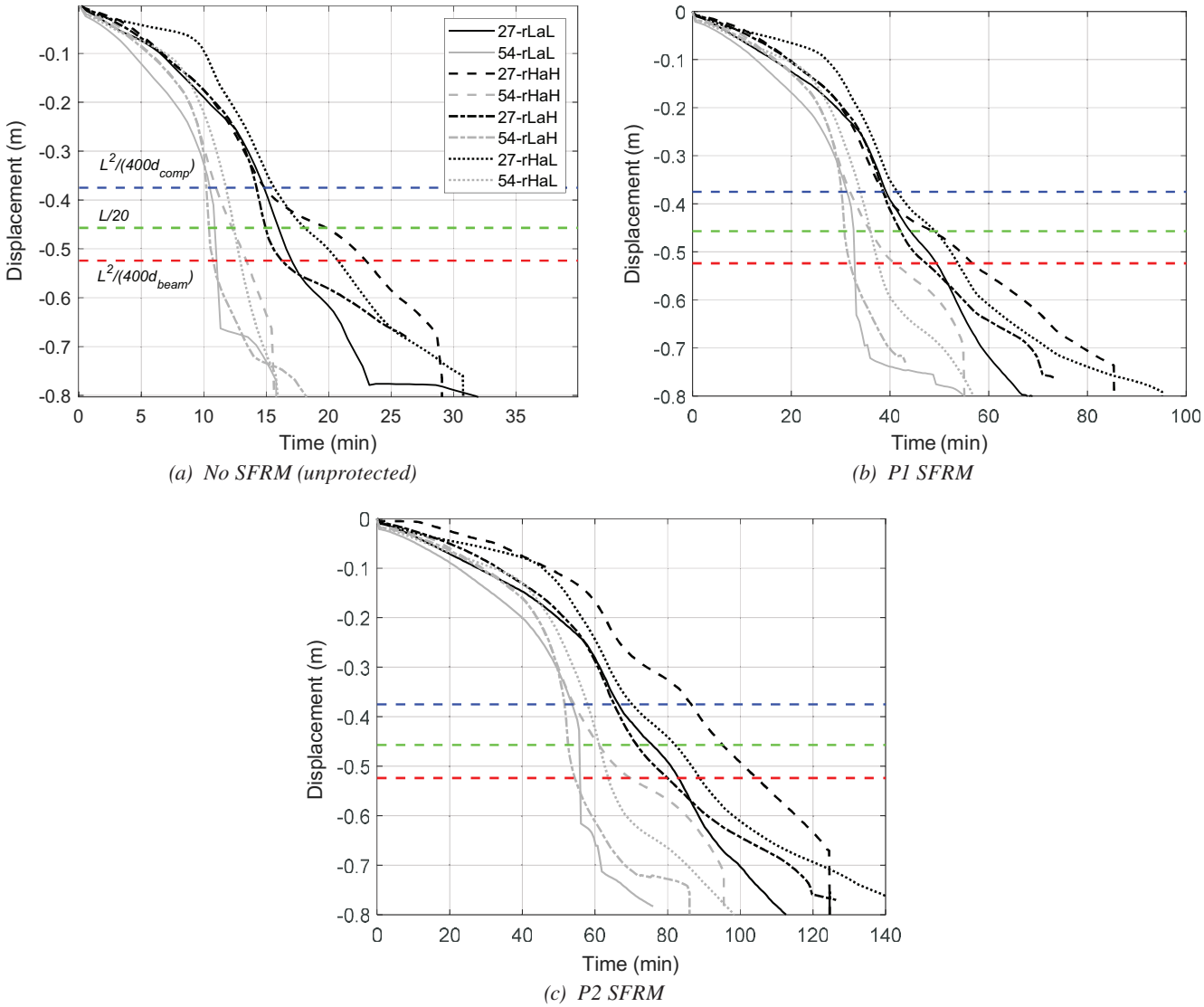

(a) No SFRM (unprotected)

(b) P1 SFRM

(c) P2 SFRM

Fig. 12. Midspan deflection for the one-way W16×26 composite beam configuration under ASTM E119 standard fire exposure with varying levels of SFRM per Table 4 (conversion note: 0.1 m = 3.94 in.).

then the assembly may collapse. The values of $T_{s,BF}$ in Figure 14(d) would therefore represent the true loss of flexural resistance; any subsequent catenary response can be regarded as a redundancy or hardening prior to ultimate failure.

It should be noted that standard fire tests per ASTM E119 (ASTM, 2024) and ISO 834 (ISO, 2019) are typically performed on specimens with bearing-plate end supports, rather than a realistic connection to the test fixture. If tested as restrained, the bearing ends of the beam will develop axial compression and rotational restraint in response to thermal expansion. However, a transition from flexural response to catenary action is not possible for those test specimens because the beam end can simply pull away from the horizontal bearing support (which cannot offer any axial tensile resistance) when flexural resistance is lost. The beam will therefore approach a runaway deflection rate soon after the loss of flexural resistance. The reader is referred to the previous paper by Drury and Quiel (2025) for more illustration of the end conditions for composite beam specimens in standard fire tests.

The values of $T_{s,BF}$ in Figures 14(a) and 14(b) for the $L/20$ and $L^2/(400d_{comp})$ deflection milestones are much lower (i.e., more conservative) compared to those in Figure 14(d) for the onset of catenary response. Those in Figure 14(c) for $L^2/(400d_{beam})$, however, show good overall agreement with

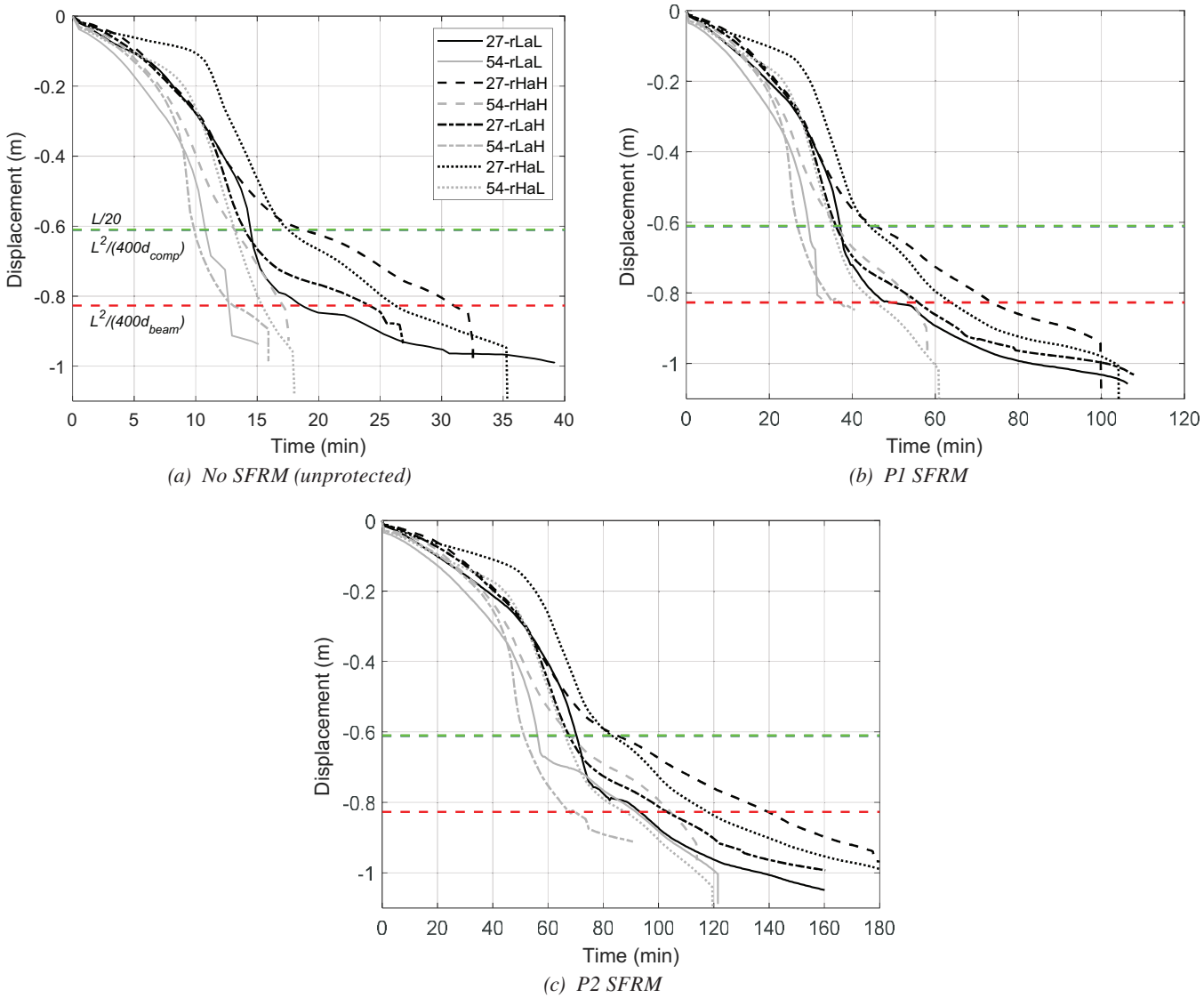

(a) No SFRM (unprotected)

(b) P1 SFRM

(c) P2 SFRM

Fig. 13. Midspan deflection for the one-way W18×35 composite beam configuration under ASTM E119 standard fire exposure with varying levels of SFRM per Table 4 (conversion note: 0.2 m = 7.87 in.).

those in Figure 14(d), though with a slightly greater vertical dispersion at each load level. These results indicate that the $L^2/(400d_{beam})$ can be used to appropriately denote the loss of flexural resistance under fire, which is consistent with previous work by Rackauskaite et al. (2019).

For comparison, the plots in Figure 14 also include two representations of critical bottom flange temperature, $T_{cr,BF}$: one per AISC 360-22, Table A-4.2.4 (reproduced previously in Table 1), and the other a constant value of $T_{cr,max} = 704°C$ (1300°F) per ASTM E119. The plotted $T_{s,BF}$ for all models in Figures 14(c) and 14(d) either fall above or very close to the load-dependent curve for $T_{cr,BF}$. This outcome is consistent with a recent review of standard fire tests on a wide range of one-way composite floor beam configurations (Drury and Quiel, 2025) and reinforces the notion that the moment retention factor per AISC 360-22, Table A-4.2.4, can serve as an appropriate load-dependent relationship for $T_{cr,BF}$ at the loss of flexural resistance under standard fire exposure. The constant $T_{cr,max}$ per ASTM E119, on the other hand, fails to capture the influence of initial flexural loading on the fire-induced response of these one-way composite beams.

In Figures 15 through 18, the midspan deflection for each model is normalized by its corresponding value of $L^2/(400d_{beam})$ and plotted against $T_{s,BF}$ for all four parametric combinations of beam end restraint in the following order: rLaL, rHaH, rLaH, and rHaL. The value of $T_{cr,BF}$ per AISC 360-22, Table A-4.2.4, for the corresponding level of applied loading is also marked on these plots as a vertical line—again, plots are provided only for initial flexural utilizations of 27% and 54% for brevity. Once the beams develop significant nonlinear stress-strain behavior at a deflection equaling 30–40% of $L^2/(400d_{beam})$, all models show a noticeable acceleration in deflection rate. These figures consistently show a loss of flexural resistance (following an acceleration of deflection) for all models under standard fire exposure when $T_{s,BF}$ reaches $T_{cr,BF}$ and the midspan deflection approaches $L^2/(400d_{beam})$. This outcome is robust across all parameters, including beam section size, one-way span length, the level of applied fire protection, the level of applied loading, and the level of beam end restraint.

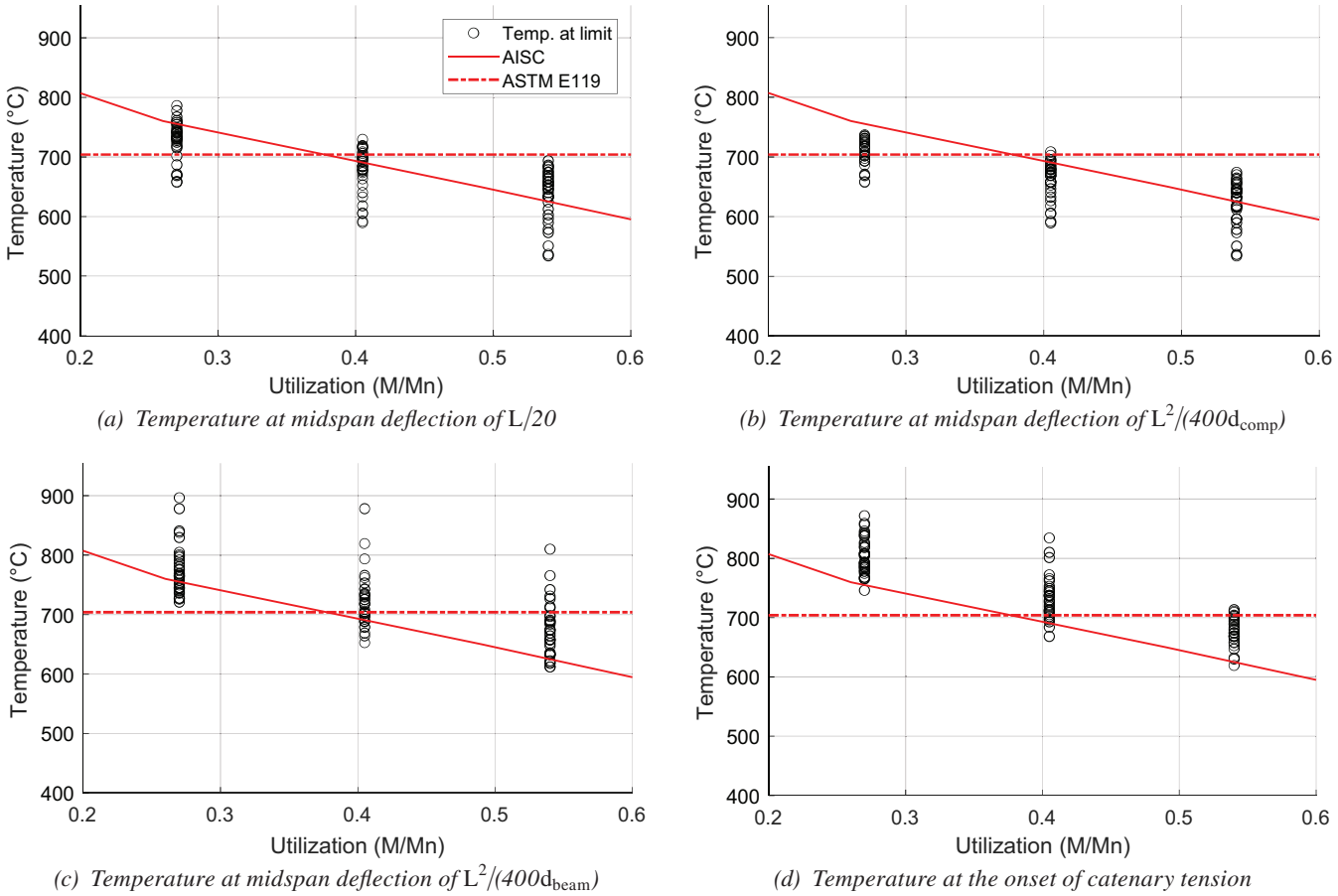

(a) Temperature at midspan deflection of $L/20$

(b) Temperature at midspan deflection of $L^2/(400d_{comp})$

(c) Temperature at midspan deflection of $L^2/(400d_{beam})$

(d) Temperature at the onset of catenary tension

Fig. 14. $T_{s,BF}$ *versus initial flexural utilization at several structural response milestones for all models under ASTM E119 fire exposure.*

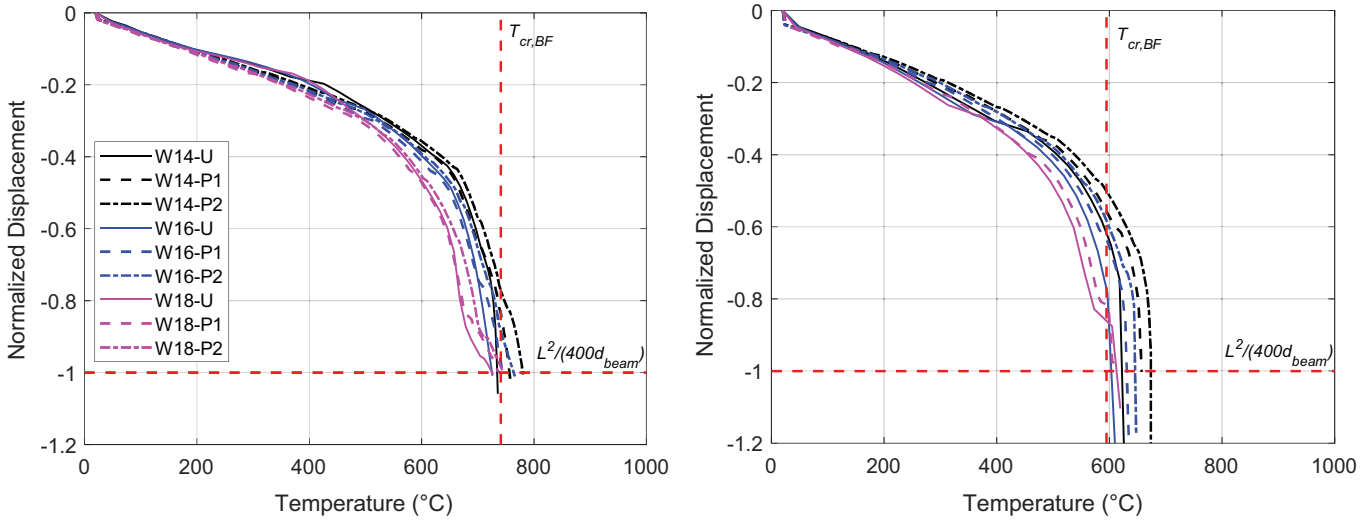

(a) 27% initial flexural utilization *(b) 54% initial flexural utilization*

Fig. 15. Midspan displacement [normalized by the corresponding value of $L^2/(400d_{beam})$] versus $T_{s,BF}$ under ASTM E119 fire exposure with rLaL restraint.

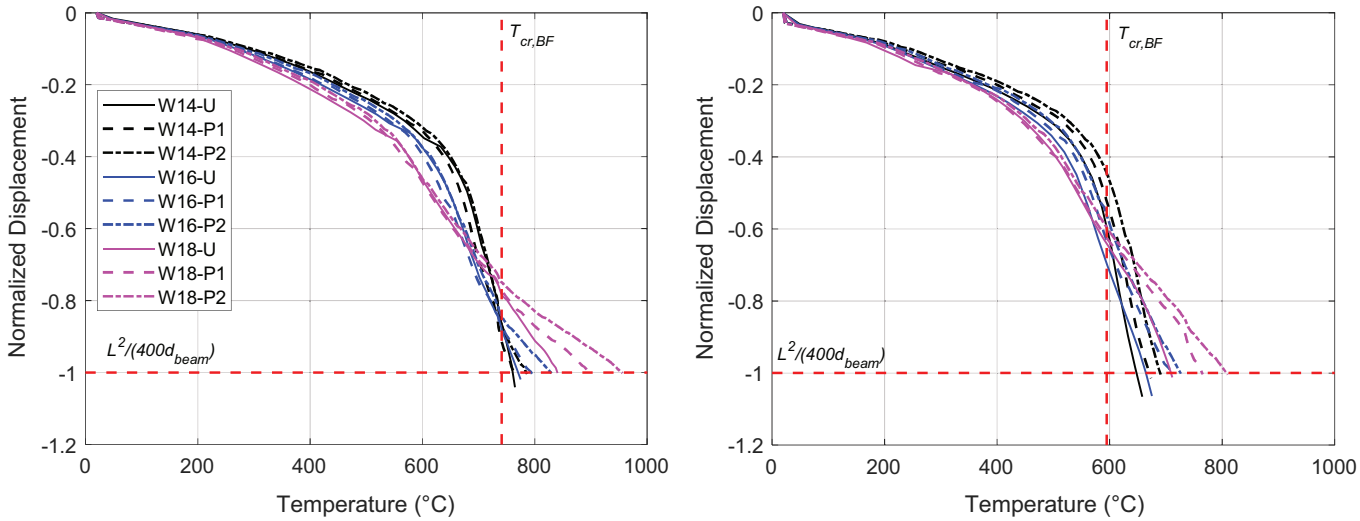

(a) 27% initial flexural utilization *(b) 54% initial flexural utilization*

Fig. 16. Midspan displacement [normalized by the corresponding value of $L^2/(400d_{beam})$] versus $T_{s,BF}$ under ASTM E119 fire exposure with rHaH restraint.

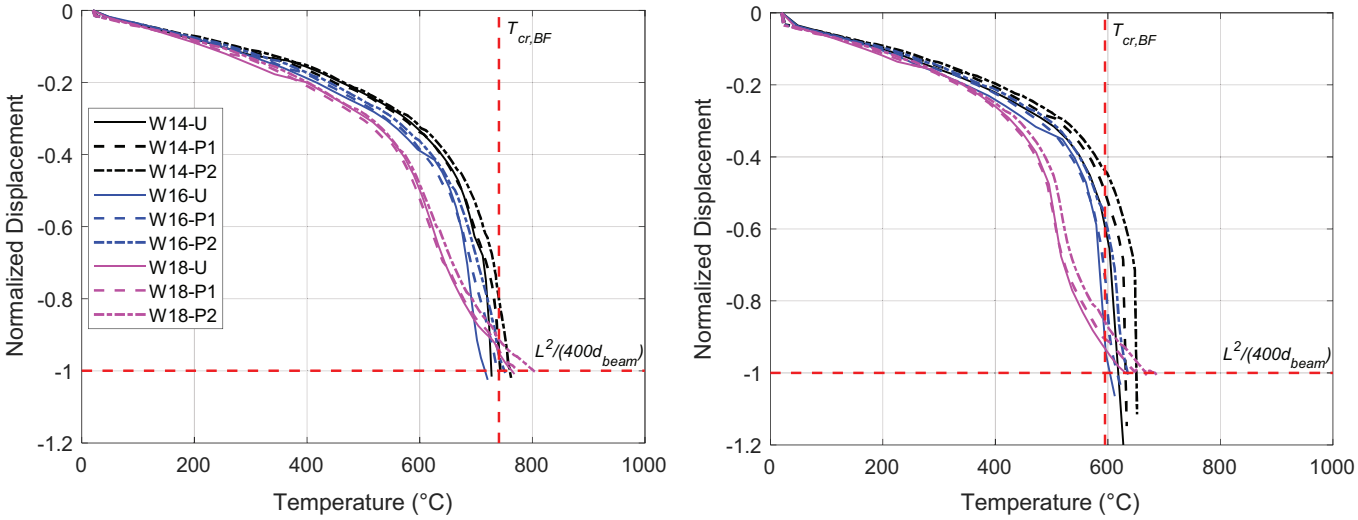

(a) 27% initial flexural utilization *(b) 54% initial flexural utilization*

Fig. 17. Midspan displacement [normalized by the corresponding value of $L^2/(400d_{beam})$*] versus* $T_{s,BF}$ *under ASTM E119 fire exposure with rLaH restraint.*

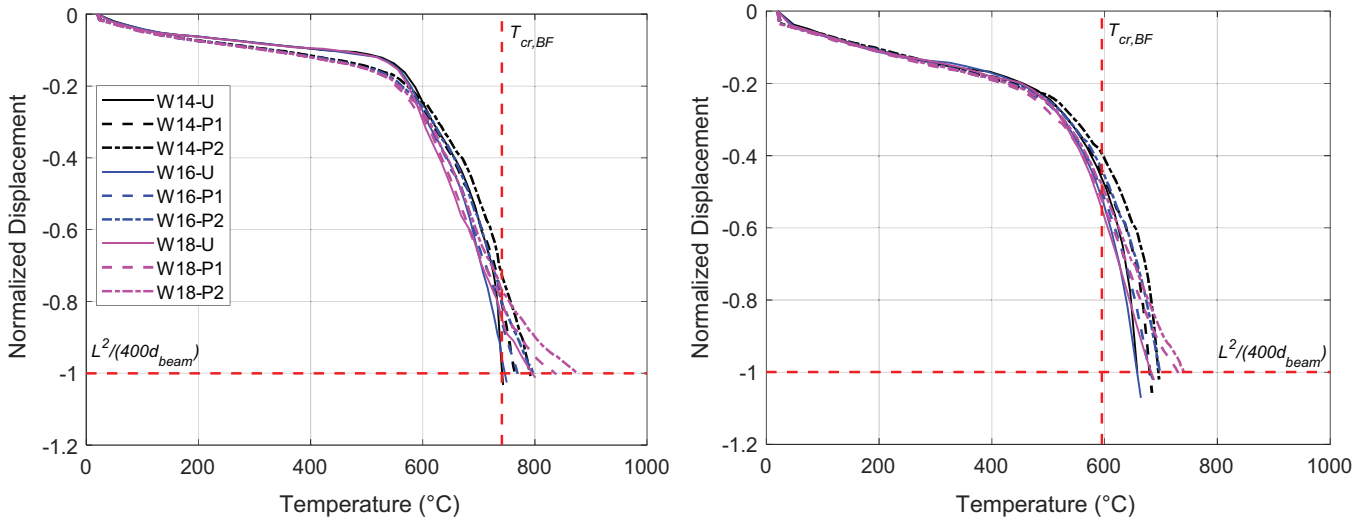

(a) 27% initial flexural utilization *(b) 54% initial flexural utilization*

Fig. 18. Midspan displacement [normalized by the corresponding value of $L^2/(400d_{beam})$*] versus* $T_{s,BF}$ *under ASTM E119 fire exposure with rHaL restraint.*

FLEXURAL RESPONSE TO NATURAL FIRE EXPOSURE

The calculated midspan deflections for all 108 composite beam configurations when exposed to the FH374 natural fire curve are plotted in Figures 19, 20, and 21 (W14×22, W16×26, and W18×35, respectively) for all three levels of SFRM protection and for all levels of end restraint per Table 4. As before, each plot shows only the 27% and 54% flexural utilization levels for brevity and includes a horizontal "limit" line corresponding a deflection of $L^2/(400d_{beam})$. Similar to the standard fire results in Figures 11–13, the results in Figures 19(a), 20(a), and 21(a) show that all unprotected beams experience a loss of flexural resistance during the heating phase of the FH374 fire and reach the $L^2/(400d_{beam})$ deflection milestone before proceeding to numerical nonconvergence.

When SFRM is applied, the (b) and (c) plots in Figures 19, 20, and 21 show that all composite beam configurations are able to survive the FH374 fire exposure through burnout. All protected beams experience a rapid increase in deflection during the active heating phase and then partially rebound to a stable magnitude of residual deflection when cooling during the decay phase. As expected, models with

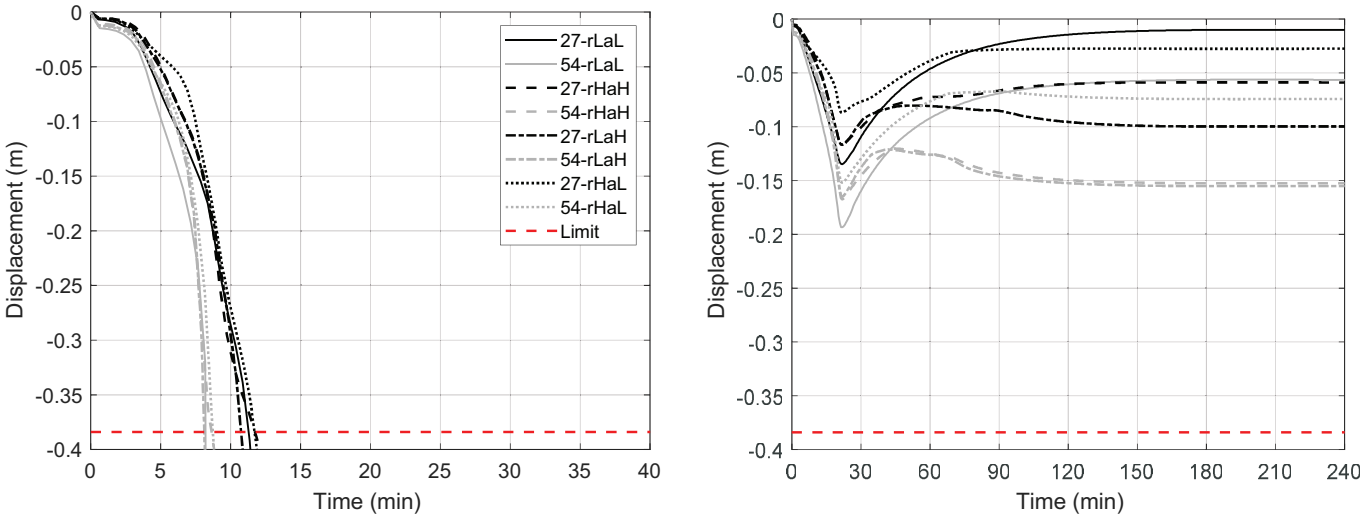

(a) No SFRM (unprotected)

(b) P1 SFRM

(c) P2 SFRM

Fig. 19. Midspan deflection for the one-way W14×22 composite beam configurations under FH374 natural fire exposure with varying levels of SFRM per Table 4 (conversion note: 0.05 m = 1.97 in.).

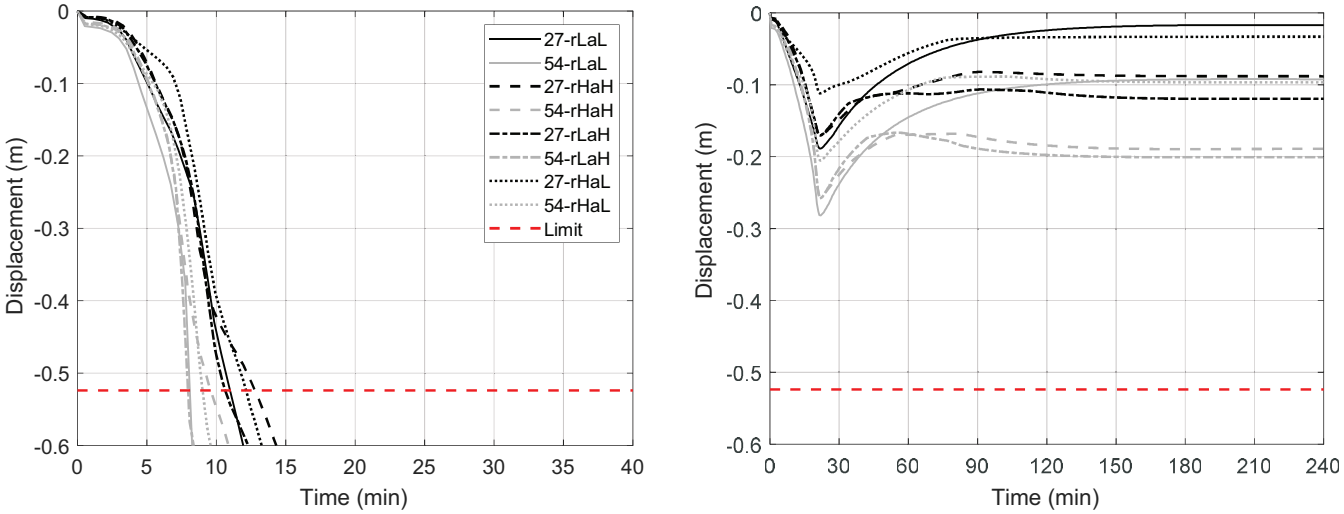

(a) No SFRM (unprotected)

(b) P1 SFRM

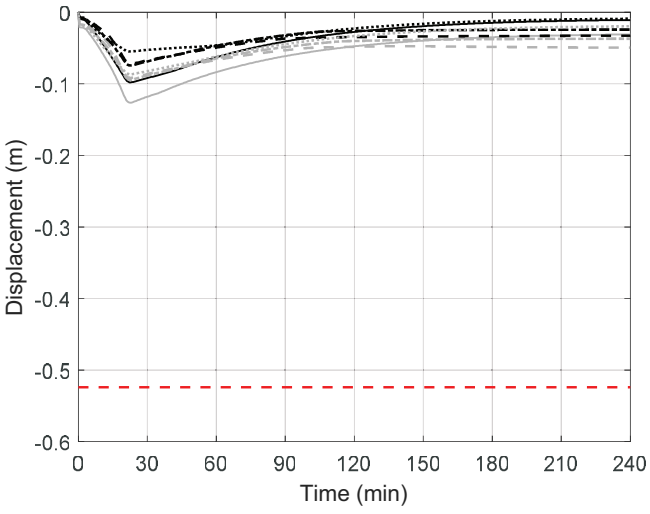

(c) P2 SFRM

Fig. 20. Midspan deflection for the one-way W16×26 composite beam configurations under FH374 natural fire exposure with varying levels of SFRM per Table 4 (conversion note: 0.1 m = 3.94 in.).

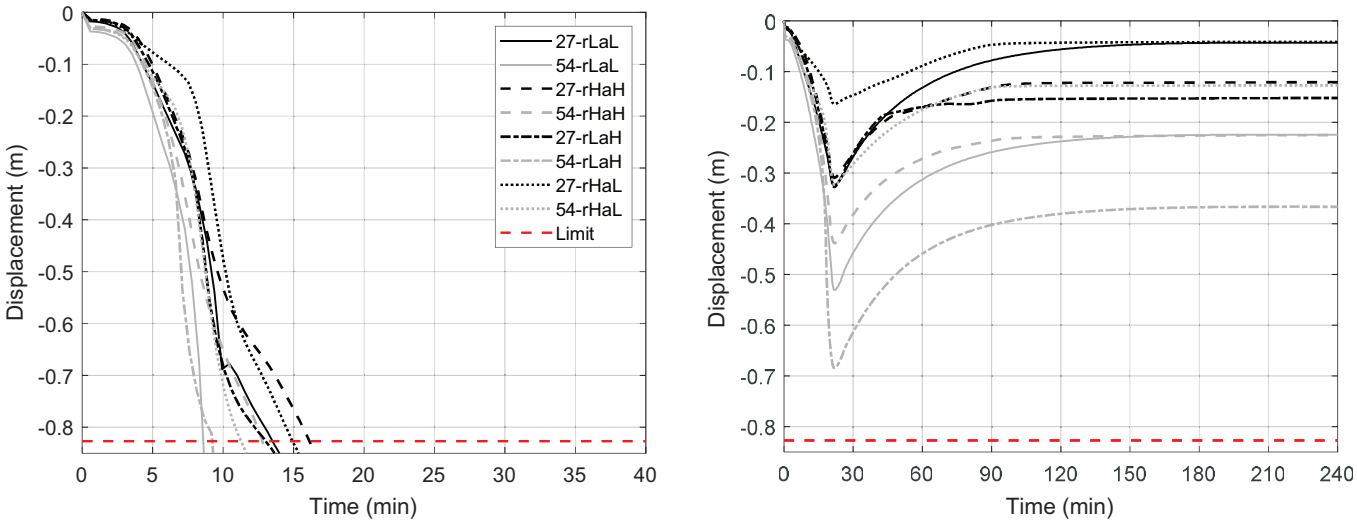

(a) No SFRM (unprotected)

(b) P1 SFRM

(c) P2 SFRM

Fig. 21. Midspan deflection for the one-way W18×35 composite beam configurations under FH374 natural fire exposure with varying levels of SFRM per Table 4 (conversion note: 0.1 m = 3.94 in.).

rL beam end restraint develop the largest peak deflections during heating by providing less direct resistance. Those with aH beam end restraint develop the largest magnitudes of residual deflection during cooling; these beams develop larger internal forces in response to higher axial restraint of thermal expansion, which thereby translates into larger permanent deflection once the assembly has cooled. Overall, models with higher levels of applied loading and the lower level of SFRM develop greater overall magnitudes and rates of deflection.

Calculated midspan deflections are plotted in Figures 22 and 23 for select composite beam configurations when exposed to the FL374 and FH912 natural fire curves, respectively. The responses of unprotected beam configurations to these fire curves are very similar to those shown in Figures 19(a), 20(a), and 21(a) for exposure to the FH374 natural fire and are therefore not plotted for brevity. Also, results are shown only for models with rL beam end restraint because they develop larger deflections and thus a more severe fire-induced response than those with rH beam

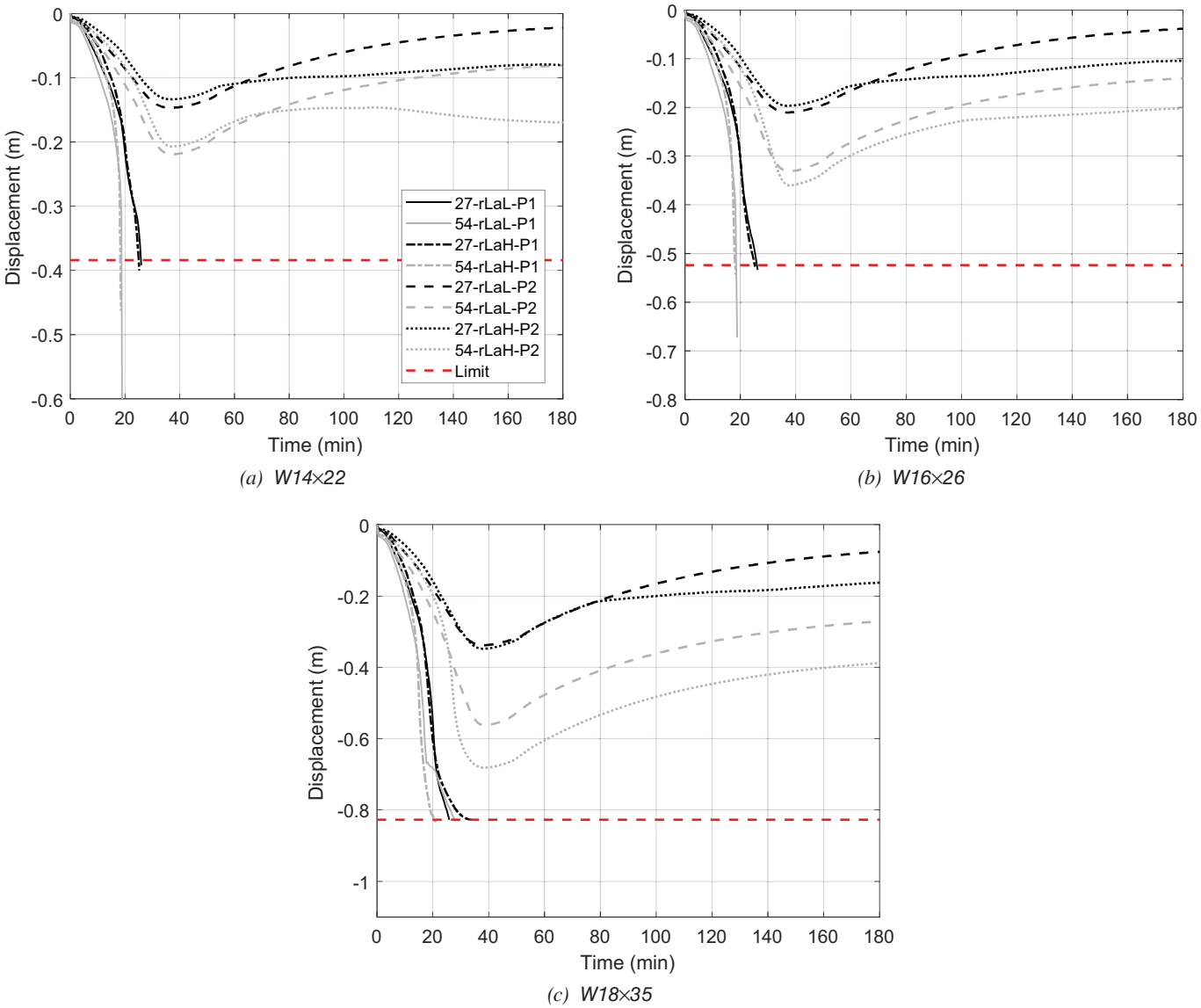

(a) W14×22

(b) W16×26

(c) W18×35

Fig. 22. Midspan deflection under FL374 natural fire exposure for composite beam configurations with rL restraint and P1 and P2 SFRM (conversion note: 0.1 m = 3.94 in.).

end restraint. As shown previously in Figure 2, the FL374 and FH912 fire curves are more severe (in terms of both maximum temperature and total duration) compared to that for FH374; as a result, the deflections for all P1 SFRM protected beam configurations in Figures 22 and 23 now also experience a loss of flexural resistance during the heating phase of these fires and reach the $L^2/(400d_{beam})$ deflection milestone before proceeding to numerical nonconvergence. Beams with the thicker P2 SFRM protection survive these fire exposures through burnout and develop stable residual deflection when cooling. As before, models with larger applied loading develop larger peak deflections, and models with aH beam end restraint develop larger residual deflections. Some of the models [particularly, W18–54-rLaH under the FH912 fire in Figure 23(c)] come very close to the $L^2/(400d_{beam})$ deflection limit before the heating phase ends, after which the beam is still able to develop a stable residual state with significant permanent deflection.

Similar to the standard fire results in Figure 14(c), Figure 24 shows that the values of $T_{s,BF}$ at a midspan deflection of $L^2/(400d_{beam})$ for the unprotected beams exposed to the FH374 natural fire curve are again above or very close to the load-dependent curve for $T_{cr,BF}$ per AISC 360-22, Table A-4.2.4. Similar to Figures 15–18, the midspan

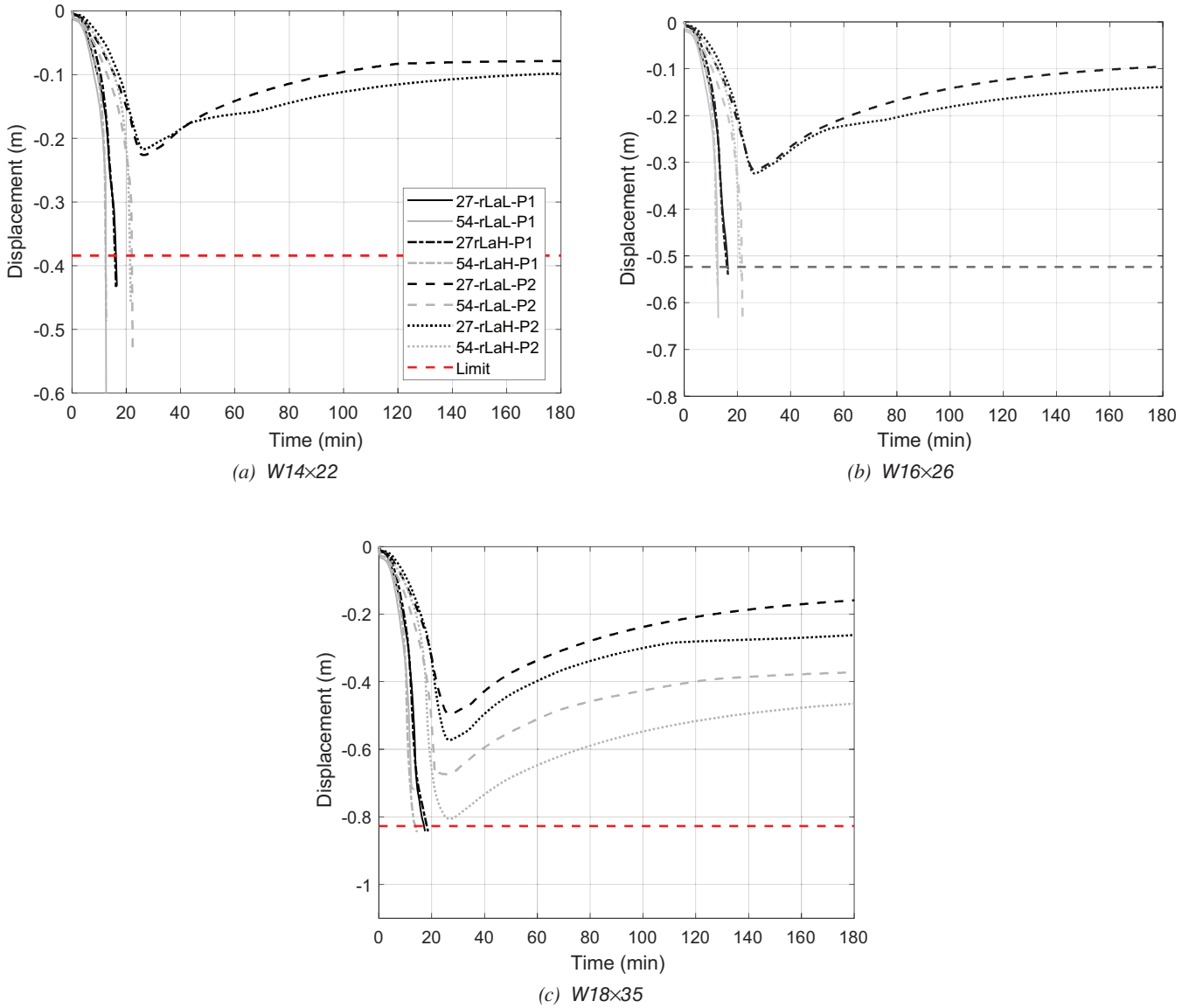

(a) W14×22

(b) W16×26

(c) W18×35

Fig. 23. Midspan deflection under FH912 natural fire exposure for composite beam configurations models with rL restraint and P1 and P2 SFRM (conversion note: 0.1 m = 3.94 in.).

deflection plotted previously for every SFRM-protected beam exposed to FH374 [Figures 19(b–c), 20(b–c), and 21(b–c)], FL374 (Figure 22), and FH912 (Figure 23) is normalized by its corresponding value of $L^2/(400d_{beam})$ and plotted against its $T_{s,BF}$ in Figures 25, 26, and 27. In these plots, all models that suffer a loss of flexural stiffness reached the intersection of the horizontal line for the $L^2/(400d_{beam})$ deflection limit with the vertical line for $T_{cr,BF}$ per AISC 360-22, Table A-4.2.4. Similar to the results for standard fire exposure, all models again show a noticeable acceleration in deflection rate once the deflections reach 30–40% of $L^2/(400d_{beam})$. All models that survive their respective natural fire curve experience a maximum $T_{s,BF}$ during the heating phase that clearly falls short of the vertical line for $T_{cr,BF}$ and partially rebounds to a residual deflection achieved during cooling. The magnitude of residual deflection is influenced by the maximum value of $T_{s,BF}$, the total duration of heating, the level of beam end restraint, and the level of applied loading, as well as the composite beam geometry. A full exploration of the influence of these parameters on residual deflections is outside the scope of this paper but are an important consideration for the selection of passive fire protection that can minimize damage and enable a speedier restoration of post-fire functionality

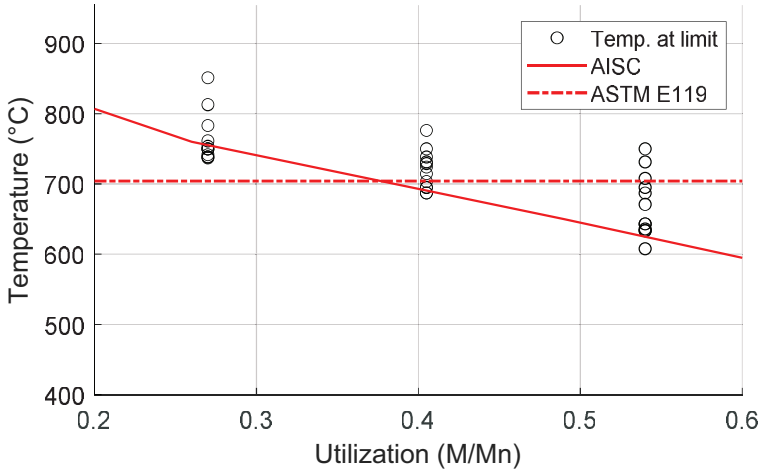

Fig. 24. $T_{s,BF}$ *at a midspan deflection of* $L^2/(400d_{beam})$ *versus initial flexural utilization for all unprotected composite beam configurations under FH374 natural fire exposure.*

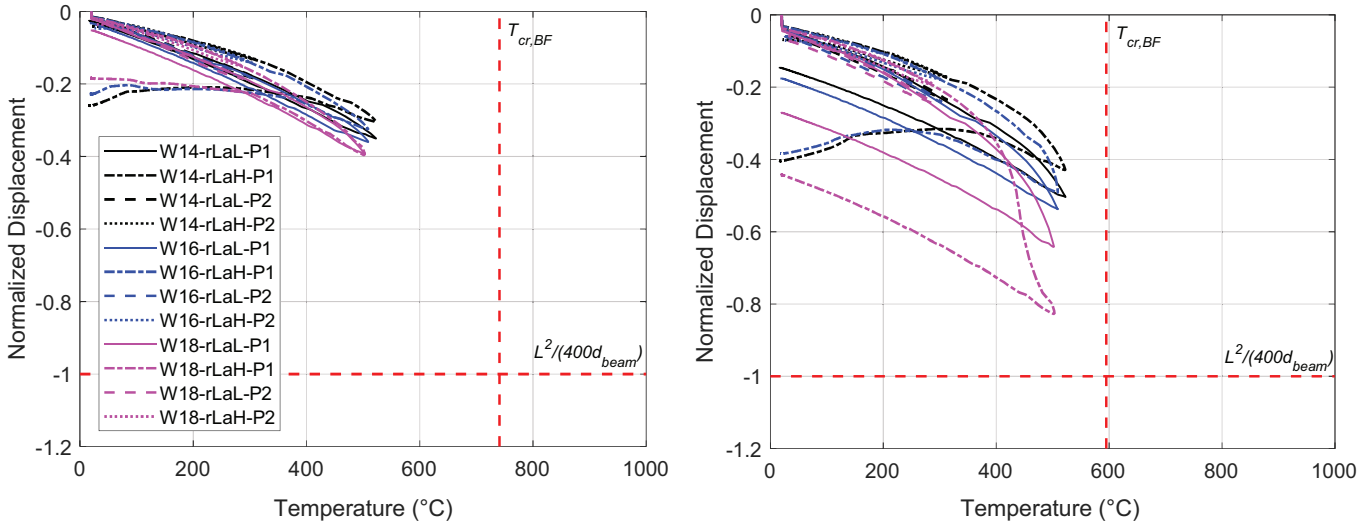

(a) 27% initial flexural utilization *(b) 54% initial flexural utilization*

Fig. 25. Midspan displacement [normalized by the corresponding value of $L^2/(400d_{beam})$*] versus* $T_{s,BF}$ *under FH374 natural fire exposure for models with rL restraint and P1 and P2 SFRM.*

(i.e., to enhance the resilience of these assemblies against natural fire exposure).

Commentary on Connection Reactions

The axial forces at the beam ends from the models subjected to the FH374 natural fire are plotted in Figures 28, 29, and 30 for the W14×22, W16×26, and W18×35 composite floor beam configurations, respectively. For rLaL models with the lowest level of beam end restraint, the residual tensile forces that develop during cooling are small compared to the compressive forces developed from the restraint of thermal expansion during heating. Specifically, these cases experience less permanent compressive strain due to lower restraint of thermal expansion during heating. Models with higher beam end restraint develop more permanent shortening when heated and therefore develop more residual tension in their connections when cooling. This outcome suggests that an optimal end restraint lies

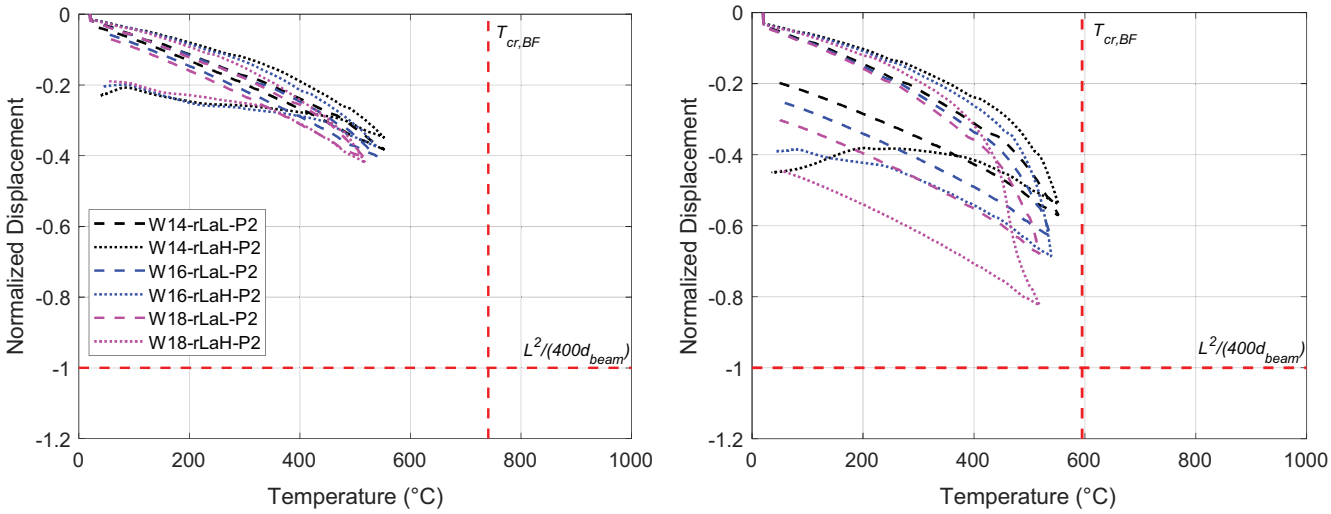

(a) 27% initial flexural utilization *(b) 54% initial flexural utilization*

Fig. 26. Midspan displacement [normalized by the corresponding value of $L^2/(400d_{beam})$*] versus* $T_{s,BF}$ *under FL374 natural fire exposure for models with rL restraint and P2 SFRM.*

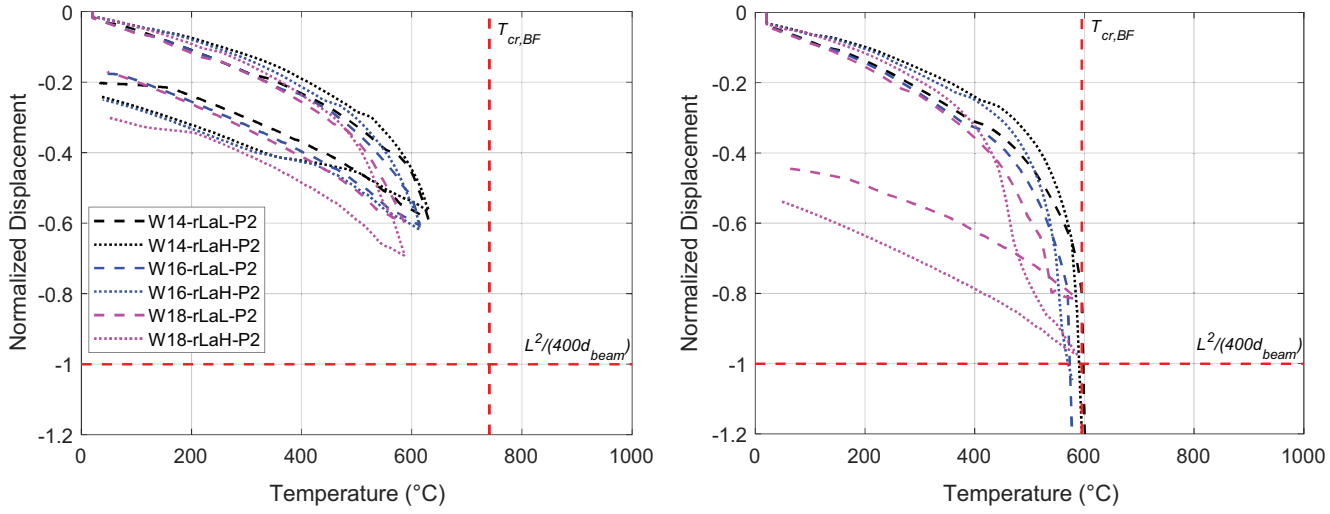

(a) 27% initial flexural utilization *(b) 54% initial flexural utilization*

Fig. 27. Midspan displacement [normalized by the corresponding value of $L^2/(400d_{beam})$*] versus* $T_{s,BF}$ *under FH912 natural fire exposure for models with rL restraint and P2 SFRM.*

somewhere between fully restrained and fully unrestrained (LaMalva et al., 2020; Moss et al., 2004). Conversely, Figures 28–30 show that the aH models develop the largest magnitudes of residual tension at their beam ends. Also, models with the lower P1 SFRM thickness develop higher beam temperature; the translation of the associated thermal expansion into larger restraining stresses therefore produces larger magnitudes of residual tension in these beams than their counterparts with the larger P2 SFRM thickness.

Due to the use of idealized beam end conditions, the values plotted in Figures 28–30 are not exact but instead represent an approximate range of reaction demands that the shear connections would experience due to natural fire exposure. To fully achieve a performance-based, fire-resistant design, the tensile capacity of the shear connections at the beam ends must be capable of withstanding these residual reactions. Large-scale tests on composite floor assemblies have shown that connection failures are possible both during heating as well as significantly after

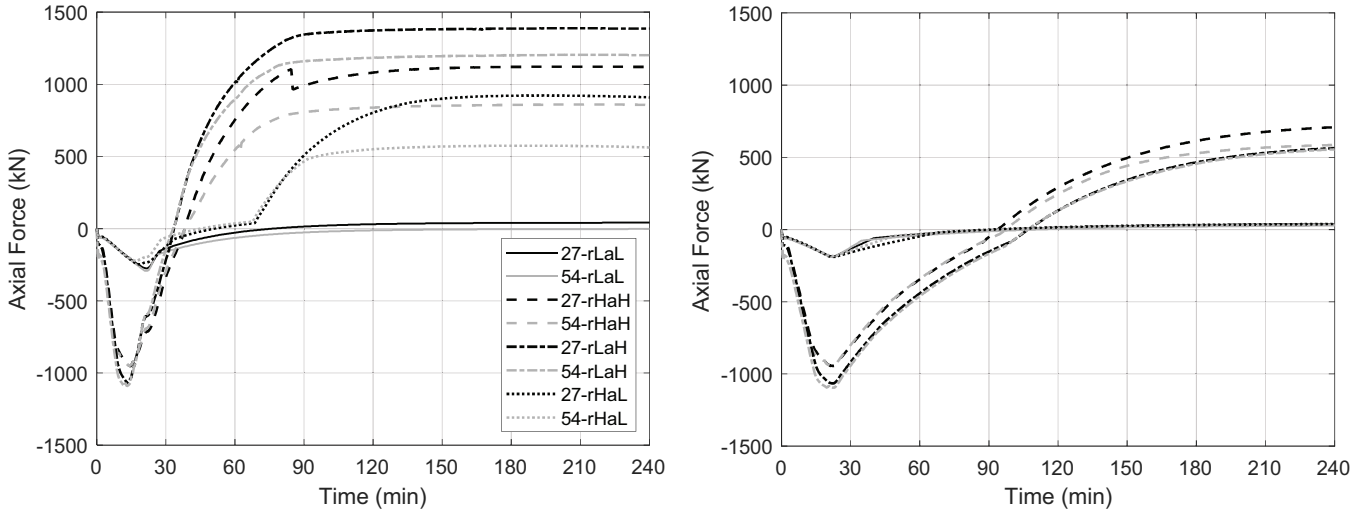

(a) P1 SFRM *(b) P2 SFRM*

Fig. 28. Beam end axial force for the W14×22 composite beam configurations under FH374 natural fire exposure with varying levels of SFRM (conversion note: 500 kN = 112.4 kips).

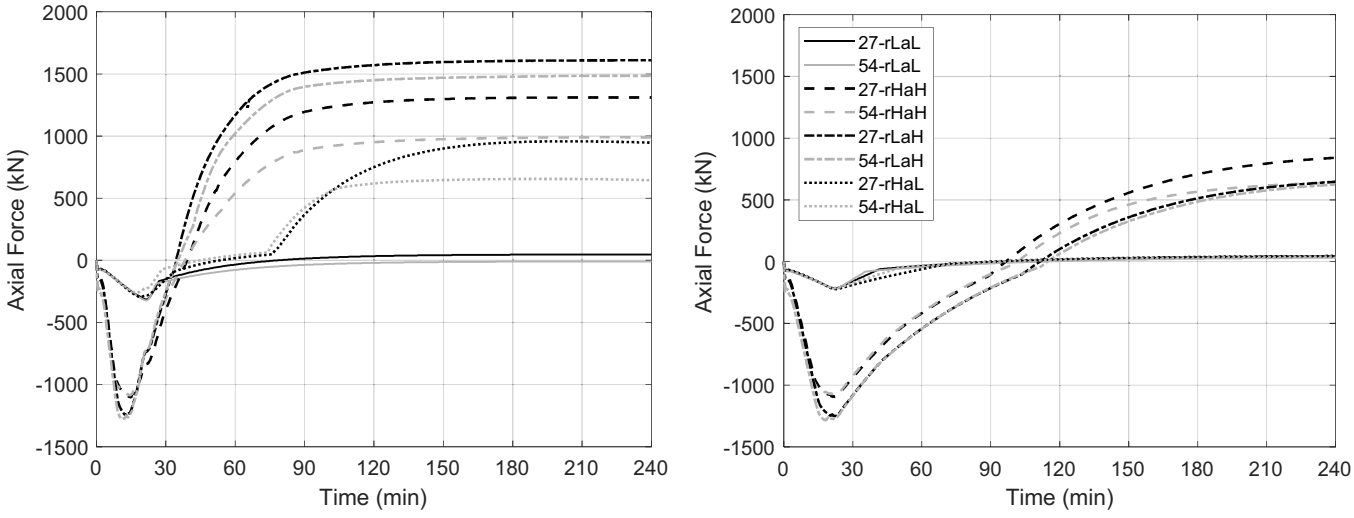

(a) P1 SFRM *(b) P2 SFRM*

Fig. 29. Beam end axial force for the W16×26 composite beam configurations under FH374 natural fire exposure with varying levels of SFRM (conversion note: 500 kN = 112.4 kips).

natural fire burnout while the deformed beam cools and contracts (Choe et al., 2019; Selden et al., 2016a). Rotational and tensile capacities of shear connections under fire have been investigated in several previous studies (Block et al., 2013; Liu and Astaneh-Asl, 2004; Seif et al., 2013; Selamet and Garlock, 2010; Yu and Frank, 2009); however, there is little consensus to date as to how these connections should be designed to survive natural fire exposure.

It should be noted that the simplified structural model used for this study applies the rotational and axial end restraint to the full cross-sectional area of the steel beam; however, shear connections for floor beams typically have a web attachment only. When the composite beam is heated, the bottom flange can come into contact with the supporting framing element via thermal expansion as well as end rotation from large deflection. Localized compression from this contact can induce local buckling in the bottom flange plate, thereby mitigating compression via damage absorption (Kordosky et al., 2020). Connection reactions during heating can also be reduced due to web local buckling or bolt slip within the connection (Hantouche et al., 2020; Liu and Astaneh-Asl, 2004). The top flange additionally transmits some of the restraint force into the slab through the shear studs at their composite interface, potentially mitigating some of the reaction to the shear connection. During the natural fire's decay phase, the onset of residual tension will be impacted by the various modes of thermal damage or permanent deformation that developed during heating. More research is needed on the actual development of the push-pull nature of shear connection response in composite floor beams during heating and cooling under natural fire. Also, more research is needed to explore potential modifications that can be made to a shear connection to enhance its resistance to these fire-induced actions (Safari and Broujerdian, 2020; Selamet and Garlock, 2010).

Commentary on Two-Way Slab Contributions

It should be emphasized that the results presented in this paper focus solely on the one-way flexural response of composite filler floor beams under fire. Large-scale experimental testing on common steel framed floor assemblies with composite W-shaped filler beams at Cardington in the UK (Bailey et al., 1999; Wald et al., 2006), NIST in the United States (Choe et al., 2021a, 2021b) and elsewhere (Li et al., 2017; Selamet and Yolaçan, 2017; Wellman et al., 2011) have shown that the natural fire survivability of composite steel floor beams can be enhanced by engaging the composite slab in two-way tensile membrane and catenary action. The aforementioned ASCE exemplar report (ASCE, 2020) and other studies (Gernay and Khorasani, 2020; Huang et al., 2003; Jiang et al., 2014; Khorasani et al., 2019; Lamont et al., 2006, 2007; McAllister, 2014; Sanad et al., 2000) have also used 3D finite element (FE) numerical models of steel framed buildings with W-shape composite floor beams to demonstrate the beneficial contributions of two-way tensile membrane action in the composite slab when the elevated reactions in the slab and connections are taken into account. To unlock these benefits via PBSFD, however, the slab thickness and reinforcement must often be enhanced beyond what is conventionally used in current North American practice to achieve adequate load redistribution when

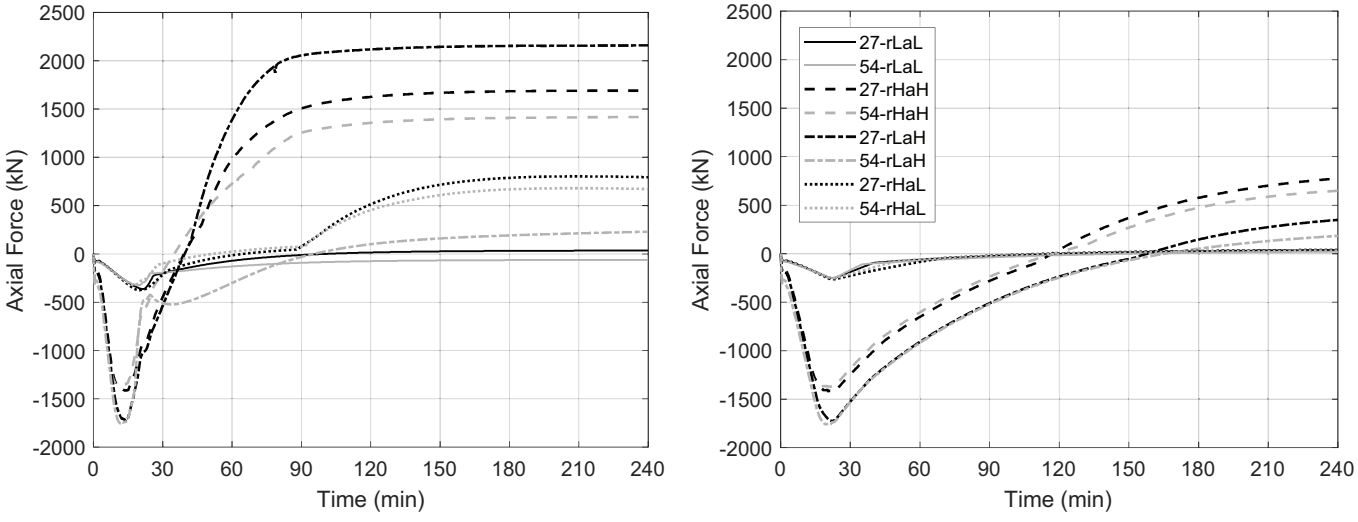

(a) P1 SFRM *(b) P2 SFRM*

Fig. 30. Beam end axial force for the W18×35 composite beam configurations under FH374 natural fire exposure with varying levels of SFRM (conversion note: 500 kN = 112.4 kips).

the filler beams develop large fire-induced deflections. Additionally, the aspect ratio of the floor system's bay dimensions and the relative fire resistance of beams and girders at the perimeter of each bay will play a role in the development of tensile slab contributions. Large deflections and catenary action will also increase the demand on the beam end connections. Tensile forces and increased rotation at high temperature would also need to be considered for connection design if the PBSFD performance objective relies on achieving large deflections.

The focus of this study on one-way flexural behavior for composite floor beams can still provide an efficient analytical alternative when the consideration of two-way slab action analysis may be cost prohibitive or impractical. The relationship for $T_{cr,BF}$ as a function of M/M_n per Table 1 would still provide a good prediction of the initial onset of rapid downward deflection for any fire-exposed W-shape floor beam assembly because tensile membrane and/or catenary effects would only be engaged once the beam achieves a significant amount of deflection. Any engagement of tensile slab effects would therefore provide a last resort for collapse prevention, though the structure would still be considered to be irreparably damaged if the relationship for $T_{cr,BF}$ as a function of M/M_n per Table 1 were exceeded.

CONCLUSIONS

Three realistically representative composite floor beam configurations (with different W-shape section sizes and one-way span lengths) were used for parametric numerical analysis, the matrix for which included the following: one standard fire curve and three natural fire curves, three levels of passive fire protection, realistic levels of axial and rotational restraint at the end of the beam to represent that provided by a shear connection, and varying levels of applied flexural loading. A previously validated heat transfer modeling approach was used for calculating steel temperatures for each flange and the web as individual lumped masses, and a one-dimensional FE heat transfer modeling approach was used to calculate the temperature gradient through the structural thickness of the floor slab. A previously validated fiber-beam FE structural modeling approach was used to model flexural response of the one-way composite beam assembly under fire. The following conclusions can be drawn based on the results of the parametric analyses:

- A deflection magnitude of $L^2/(400d_{beam})$ consistently indicated the loss of flexural resistance for exposure to any fire exposure in this study, regardless of parametric variation or composite beam configuration. This point also marks the onset of a catenary response in the beam end, which can only be supported if the beam end connections and the composite slab reinforcement have adequate capacity.
- The relationship in AISC 360-22, Table A-4.2.4, between moment retention factors and bottom flange temperature $T_{s,BF}$ can be reframed as a relationship between flexurally critical bottom flange temperature $T_{cr,BF}$ and the initially applied flexural utilization ratio M/M_n. This load-dependent representation of $T_{cr,BF}$ was also demonstrated as a reliably conservative indicator for the loss of flexural resistance for all composite beam model configurations under fire, again regardless of the level of applied fire protection, the level of beam end restraint, or the type of fire exposure.
- The relationship between midspan deflection and bottom flange temperature was relatively consistent across all beam configurations under all fire exposures in this study. These results suggest that $T_{s,BF}$ can be reliably used as an indicator of flexural response for one-way composite floor beams under fire. Specifically, the load-dependent values of $T_{cr,BF}$ based on AISC 360-22, Table A-4.2.4, can accurately signify the loss of flexural resistance under either standard or natural fire exposure. The application of various levels of axial and rotational restraint to the beam ends had a relatively marginal influence on the $T_{s,BF}$ at which the composite beam suffered a loss of flexural resistance at a given level of applied flexural loading.
- Variations in axial and rotational beam end restraint had more impact on the flexural response of these composite beam configurations when they were able to survive natural fire exposure thru burnout without flexural failure. Lower rotational stiffness at the beams ends produces increased deflection during the heating phase of a natural fire but less residual tensile force at the connections during cooling (due to less restraint of thermal expansion and therefore less permanent deformation during heating). Conversely, increased axial restraint initially provides a benefit to the composite floor assembly by reducing deflections during heating under natural fire but ultimately generates higher levels of residual tension in the connections during cooling (since the greater restraint of thermal expansion will have permanently shortened the beam during heating).
- Future work can extend the results of this study toward determining load-dependent values of $T_{s,BF}$ that correspond to varying levels of residual damage if the beam survives a natural fire through burnout. The residual reactions in the connections could also be quantified as a function of $T_{s,BF}$, initial M/M_n, and beam end restraint.

ACKNOWLEDGMENTS

Funding support for this project was provided by the American Institute of Steel Construction (AISC) via the Milek Faculty Fellowship (www.aisc.org/milek), of which Professor Quiel is the 2016 recipient. Additional funding to support Dr. Drury during his involvement in this research for his doctoral dissertation was provided by Lehigh University via a 2021 Faculty Innovation Grant. All opinions, findings, and conclusions expressed in this paper are the authors' and do not necessarily represent the policies and views of AISC or Lehigh University.

REFERENCES

AISC (2022), *Specification for Structural Steel Buildings*, ANSI/AISC 360-22, American Institute of Steel Construction, Chicago, Ill.

Alfawakhiri, F., Carter, C.J., Berhing, R.M., Zeeveld, P., Hervey, F.E., and Woods, L.C. (2016), "The Effects of Load Intensity and Restraint on the Fire Resistance of Steel and Composite Beams," *Proceedings of the 9th International Conference on Structures in Fire (SiF'16)*, Princeton University, Princeton, N.J.

ASCE (2020), *Performance-Based Structural Fire Design: Exemplar Designs of Four Regionally Diverse Buildings Using ASCE 7-16, Appendix E*, American Society of Civil Engineers, Reston, Va., https://doi.org/10.1061/9780784482698.

ASCE (2022), *Minimum Design Loads for Buildings and Other Structures*, ASCE/SEI 7-22, American Society of Civil Engineers, Reston, Va., https://doi.org/10.1061/9780784415788.

ASTM (2022a), *Standard Specification for Structural Steel Shapes*, ASTM A992/992M-22, ASTM International, West Conshohocken, Pa., https://doi.org/10.1520/A0992_A0992M-22.

ASTM (2022b), *Standard Specification for Steel Wire and Welded Wire Reinforcement, Plain and Deformed, for Concrete*, ASTM A1064-22, ASTM International, West Conshohocken, Pa., https://doi.org/10.1520/A1064_A1064M-22.

ASTM (2024), *Test Methods for Fire Tests of Building Construction and Materials*, ASTM E119-24, ASTM International, West Conshohocken, Pa., https://doi.org/10.1520/E0119-24.

Bailey, C.G., Lennon, T., and Moore, D.B. (1999), "The Behaviour of Full-Scale Steel-Framed Buildings Subjected to Compartment Fires," *The Structural Engineer*, Vol. 77, No. 8, pp. 15–21.

Bletzacker, R. (1967), "Fire Resistance of Protected Steel Beam Floor and Roof Assemblies as Affected by Structural Restraint," *Symposium on Fire Test Methods—Restraint & Smoke 1966*, ASTM International, West Conshohocken, Pa., https://doi.org/10.1520/STP41306S.

Block, F.M., Davison, J.B., Burgess, I.W., and Plank, R.J. (2013), "Principles of a Component-Based Connection Element for the Analysis of Steel Frames in Fire," *Engineering Structures*, Vol. 49, pp. 1,059–1,067, https://doi.org/10.1016/j.engstruct.2012.07.025.

Burgess, I.W., Davison, J.B., Dong, G., and Huang S.-S. (2012), "The Role of Connections in the Response of Steel Frames to Fire," *Structural Engineering International*, Vol. 22, No. 4, pp. 449–461, https://doi.org/10.2749/101686612X13363929517811.

Carino, N.J., Starnes, M.A., Gross, J.L., Yang, J.C., Kukuck, S.R., Prasad, K.R., and Bukowski, R.W. (2005), *Passive Fire Protection. Federal Building and Fire Safety Investigation of the World Trade Center Disaster*, NIST NCSTAR 1-6A, National Institute of Standards and Technology, Gaithersburg, Md., https://tsapps.nist.gov/publication/get_pdf.cfm?pub_id=101041.

Carter, C.J. and Alfawakhiri, F. (2013), "Restrained or Unrestrained?" *Modern Steel Construction*, September, https://www.aisc.org/globalassets/modern-steel/archives/2013/09/uld982.

CEN (2005), *Eurocode 3: Design of Steel Structures—Part 1-2: General Rules—Structural Fire Design*, EN 1993-1-2:2005, European Commission for Standardization, Brussels, Belgium.

CEN (2008a), *Eurocode 4: Design of Composite Steel and Concrete Structures—Part 1-2: General Rules—Structural Fire Design*, EN 1994-1-2:2005, European Commission for Standardization, Brussels, Belgium.

CEN (2008b), *Eurocode 2: Design of Concrete Structures—Part 1-2: General Rules—Structural Fire Design*, EN 1992-1-2:2004, European Commission for Standardization, Brussels, Belgium.

CEN (2009), *Eurocode 1: Actions on Structures—Part 1-2: General Actions—Actions on Structures Exposed to Fire*, EN 1991-1-2:2002, European Commission for Standardization, Brussels, Belgium.

Choe, L., Ramesh, S., Dai, X., Hoehler, M., and Bundy, M. (2021a), "Experimental Study on Fire Resistance of a Full-Scale Composite Floor Assembly in a Two-Story Steel Framed Building," *Journal of Structural Fire Engineering*, Vol. 13, No. 2, pp. 145–161, https://doi.org/10.1108/JSFE-05-2021-0030.

Choe, L., Ramesh, S., Grosshandler, W., Hoehler, M., Seif, M., Gross, J., and Bundy, M. (2020), "Behavior and Limit States of Long-Span Composite Floor Beams with Simple Shear Connections Subject to Compartment Fires: Experimental Evaluation," *Journal of Structural Engineering*, Vol. 146, No. 6, p. 04020088, https://doi.org/10.1061/(ASCE)ST.1943-541X.0002627.

Choe, L., Ramesh, S., Hoehler, M., Seif, M., Bundy, M., Reilly, J., and Glisic, B. (2019), *Compartment Fire Experiments on Long-Span Composite-Beams with Simple Shear Connections, Part 2: Test Results*, NIST TN 2055, National Institute of Standards and Technology, Gaithersburg, Md., https://doi.org/10.6028/NIST.TN.2055.

Choe, L., Ramesh, S., Zhang, C., and Clifton, C. (2021b), "Behavior of Composite Floor Assemblies Subject to Fire: Influence of Slab Reinforcement," *Ce/Papers*, Vol. 4, No. 2-4, pp. 1,353–1,360, https://doi.org/10.1002/cepa.1431.

Drury, M.M. (2022), *Critical Temperature Relationships for the Performance-Based Design of Realistically-Restrained Steel Composite Floor Assemblies*, Ph.D. Thesis, Lehigh University, Bethlehem, Pa.

Drury, M.M., Kordosky, A.N., and Quiel, S.E. (2020), "Structural Fire Resistance of Partially Restrained, Partially Composite Floor Beams, II: Modeling," *Journal of Constructional Steel Research*, Vol. 167, p. 105946, https://doi.org/10.1016/j.jcsr.2020.105946.

Drury, M.M., Kordosky, A.N., and Quiel, S.E. (2021), "Robustness of a Partially Restrained, Partially Composite Steel Floor Beam to Natural Fire Exposure: Novel Validation and Parametric Analysis," *Journal of Building Engineering*, Vol. 44, p. 102533, https://doi.org/10.1016/j.jobe.2021.102533.

Drury, M.M. and Quiel, S.E. (2023a), "Standard versus Natural Fire Resistance for Partially Restrained Composite Floor Beams: 1—Testing," *Journal of Constructional Steel Research*, Vol. 202, p. 107768, https://doi.org/10.1016/j.jcsr.2022.107768.

Drury, M.M. and Quiel, S.E. (2023b), "Standard versus Natural Fire Resistance for Partially Restrained Composite Floor Beams: 2—Analysis," *Journal of Constructional Steel Research*, Vol. 202, p. 107767, https://doi.org/10.1016/j.jcsr.2022.107767.

Drury, M.M. and Quiel, S.E. (2025), "Load-Dependent Critical Temperatures for Standard Fire Resistance of W-Shape Floor Beam Assemblies: Experimental Validation and Simplified Analysis," *Engineering Journal*, AISC, Vol. 62, No. 1, pp. 3–26, https://doi.org/10.62913/engj.v62i1.1335.

Dwaikat, M.M.S. and Kodur, V.K.R. (2011), "A Performance Based Methodology for Fire Design of Restrained Steel Beams," *Journal of Constructional Steel Research*, Vol. 67, No. 3, pp. 510–524, https://doi.org/10.1016/j.jcsr.2010.09.004.

Fischer, E.C., Chicchi, R., and Choe, L. (2021), "Review of Research on the Fire Behavior of Simple Shear Connections," *Fire Technology*, Vol. 57, No. 4, pp. 1,519–1,540, https://doi.org/10.1007/s10694-021-01105-1.

Fischer, E.C. and Varma, A.H. (2017), "Fire Resilience of Composite Beams with Simple Connections: Parametric Studies and Design," *Journal of Constructional Steel Research*, Vol. 128, pp. 119–135, https://doi.org/10.1016/j.jcsr.2016.08.004.

Franssen, J.-M., Cowez, B., and Gernay, T. (2014), "Effective Stress Method to Be Used in Beam Finite Elements to Take Local Instabilities into Account," *Fire Safety Science*, Vol. 11, pp. 544–557, https://doi.org/10.3801/IAFSS.FSS.11-544.

Franssen, J.-M. and Gernay, T. (2017), "Modeling Structures in Fire with SAFIR®: Theoretical Background and Capabilities," *Journal of Structural Fire Engineering*, Vol. 8, No. 3, pp. 300–323, https://doi.org/10.1108/JSFE-07-2016-0010.

Franssen, J.-M. and Gernay, T. (2019), *User's Manual for SAFIR 2019: A Computer Program for Analysis of Structures Subjected to Fire*, University of Liege, Liege, Belgium.

Gamble, W.L. (1989), "Predicting Protected Steel Member Fire Endurance Using Spread-Sheet Programs," *Fire Technology*, Vol. 25, No. 3, pp. 256–273, https://doi.org/10.1007/BF01039782.

Garlock, M.E. and Selamet, S. (2010), "Modeling and Behavior of Steel Plate Connections Subject to Various Fire Scenarios," *Journal of Structural Engineering*, Vol. 136, No. 7, pp. 897–906, https://doi.org/10.1061/(ASCE)ST.1943-541X.0000179.

Gernay, T. and Franssen, J.-M. (2012), "A Formulation of the Eurocode 2 Concrete Model at Elevated Temperature That Includes an Explicit Term for Transient Creep," *Fire Safety Journal*, Vol. 51, pp. 1–9, https://doi.org/10.1016/j.firesaf.2012.02.001.

Gernay, T. and Khorasani, N.E. (2020), "Recommendations for Performance-Based Fire Design of Composite Steel Buildings Using Computational Analysis," *Journal of Constructional Steel Research*, Vol. 166, p. 105906, https://doi.org/10.1016/j.jcsr.2019.105906.

Ghojel, J.I. and Wong, M.B. (2005), "Three-Sided Heating of I-Beams in Composite Construction Exposed to Fire," *Journal of Constructional Steel Research*, Vol. 61, No. 6, pp. 834–844, https://doi.org/10.1016/j.jcsr.2004.11.006.

Hantouche, E.G., Khatib, K.K.A., and Jabotian, H.V. (2020), "Design of Simple Steel Connections under Fire Temperatures," *Engineering Journal,* AISC, Vol. 57, No. 3, pp. 145–178, https://doi.org/10.62913/engj.v57i3.1168.

Harmathy, T.Z. (1965), "Effect of Moisture on the Fire Endurance of Building Elements," in A.F. Robertson, ed., *Moisture in Materials in Relation to Fire Tests*, ASTM International, West Conshohocken, Pa., https://doi.org/10.1520/STP48429S.

Huang, Z., Burgess, I.W., and Plank, R.J. (1999), "The Influence of Shear Connectors on the Behaviour of Composite Steel-Framed Buildings in Fire," *Journal of Constructional Steel Research*, Vol. 51, No. 3, pp. 219–237, https://doi.org/10.1016/S0143-974X(99)00028-0.

Huang, Z., Burgess, I.W., and Plank, R.J. (2003), "Modeling Membrane Action of Concrete Slabs in Composite Buildings in Fire. II: Validations," *Journal of Structural Engineering*, Vol. 129, No. 8, pp. 1103–1112, https://doi.org/10.1061/(ASCE)0733-9445(2003)129:8(1103).

ICC (2023), *2024 International Building Code*, International Code Council, Country Club Hills, Ill., ISBN: 978-1-959851-62-2.

ISO (2019), *ISO 834-11:2014 Fire Resistance Tests—Elements of Building Construction—Part 11: Specific Requirements for the Assessment of Fire Protection to Structural Steel Elements*, International Organization for Standardization, Geneva, Switzerland.

Isolatek International (2020), "CAFCO 300 Spray-Applied Fireproofing Technical Data Sheet C-TDS-05-20," available at: https://www.isolatek.com/wp-content/uploads/2020/05/CAFCO-300_C-TDS_05-20.pdf.

Jeanes, D.C. (1984), *Predicting Temperature Rise in Fire Protected Structural Steel Beams*, SFPE TR84-1, Society of Fire Protection Engineers, Boston, Mass.

Jiang, J., Usmani, A., and Li, G.-Q. (2014), "Modelling of Steel-Concrete Composite Structures in Fire Using OpenSees," *Advances in Structural Engineering*, Vol. 17, No. 2, pp. 249–264, https://doi.org/10.1260/1369-4332.17.2.249.

Jiang, S.-C., Ranzi, G., Chen, L.-Z., and Li, G.-Q. (2017), "Behaviour and Design of Composite Beams with Composite Slabs at Elevated Temperatures," *Advances in Structural Engineering*, Vol. 20, No. 10, pp. 1451–1465, https://doi.org/10.1177/1369433216682507.

Khorasani, N.E., Gardoni, P., and Garlock, M. (2015), "Probabilistic Fire Analysis: Material Models and Evaluation of Steel Structural Members," *Journal of Structural Engineering*, Vol. 141, No. 12, p. 04015050, https://doi.org/10.1061/(ASCE)ST.1943-541X.0001285.

Khorasani, N.E., Garlock, M., and Gardoni, P. (2014), "Fire Load: Survey Data, Recent Standards, and Probabilistic Models for Office Buildings," *Engineering Structures*, Vol. 58, pp. 152–165, https://doi.org/10.1016/j.engstruct.2013.07.042.

Khorasani, N.E., Gernay, T., and Fang, C. (2019), "Parametric Study for Performance-Based Fire Design of U.S. Prototype Composite Floor Systems," *Journal of Structural Engineering*, Vol. 145, No. 5, p. 04019030, https://doi.org/10.1061/(ASCE)ST.1943-541X.0002315.

Kishi, N., Hasan, R., Chen, W.F., and Goto, Y. (1997), "Study of Eurocode 3 Steel Connection Classification," *Engineering Structures*, Vol. 19, No. 9, pp. 772–779, https://doi.org/https://doi.org/10.1016/S0141-0296(96)00151-4.

Kodur, V., Aziz, E., and Dwaikat, M. (2013), "Evaluating Fire Resistance of Steel Girders in Bridges," *Journal of Bridge Engineering*, Vol. 18, No. 7, pp. 633–643, https://doi.org/10.1061/(ASCE)BE.1943-5592.0000412.

Kodur, V.K.R., Naser, M., Pakala, P., and Varma, A. (2013), "Modeling the Response of Composite Beam–Slab Assemblies Exposed to Fire," *Journal of Constructional Steel Research*, Vol. 80, pp. 163–173, https://doi.org/10.1016/j.jcsr.2012.09.005.

Kodur, V.K.R. and Shakya, A.M. (2013), "Effect of Temperature on Thermal Properties of Spray Applied Fire Resistive Materials," *Fire Safety Journal*, Vol. 61, pp. 314–323, https://doi.org/10.1016/j.firesaf.2013.09.011.

Kordosky, A.N., Drury, M.M., and Quiel, S.E. (2020), "Structural Fire Resistance of Partially Restrained, Partially Composite Floor Beams, I: Experiments," *Journal of Constructional Steel Research*, Vol. 167, p. 105945, https://doi.org/10.1016/j.jcsr.2020.105945.

LaMalva, K.J. (ed.). (2018), *Manual of Practice 138: Structural Fire Engineering*, American Society of Civil Engineers, Reston, Va., https://doi.org/10.1061/9780784415047.

LaMalva, K., Bisby, L., Gales, J., Gernay, T., Hantouche, E., Jones, C., Morovat, A., Solomon, R., and Torero, J. (2020), "Rectification of 'Restrained vs. Unrestrained,'" *Fire and Materials*, Vol. 44, No. 3, pp. 341–351, https://doi.org/10.1002/fam.2771.

Lamont, S., Gillie, M., and Usmani, A.S. (2007), "Composite Steel-Framed Structures in Fire with Protected and Unprotected Edge Beams," *Journal of Constructional Steel Research*, Vol. 63, No. 8, pp. 1,138–1,150, https://doi.org/10.1016/j.jcsr.2006.10.001.

Lamont, S., Lane, B., Flint, G., and Usmani, A. (2006), "Behavior of Structures in Fire and Real Design—A Case Study," *Journal of Fire Protection Engineering*, Vol. 16, No. 1, pp. 5–35, https://doi.org/10.1177/1042391506054038.

Li, G.-Q., Zhang, N., and Jiang, J. (2017), "Experimental Investigation on Thermal and Mechanical Behaviour of Composite Floors Exposed to Standard Fire," *Fire Safety Journal*, Vol. 89, pp. 63–76, https://doi.org/10.1016/j.firesaf.2017.02.009.

Lim, O.K., Choi, S., Kang, S., Kwon, M., and Choi, J.Y. (2020), "Fire Performance of Headed Shear Studs in Profiled Steel Sheeting," *Journal of Constructional Steel Research*, Vol. 164, p. 105791, https://doi.org/10.1016/j.jcsr.2019.105791.

Liu, J. and Astaneh-Asl, A. (2004), "Moment–Rotation Parameters for Composite Shear Tab Connections," *Journal of Structural Engineering*, Vol. 130, No. 9, pp. 1,371–1,380, https://doi.org/10.1061/(ASCE)0733-9445(2004)130:9(1371).

Martinez, J. and Jeffers, A.E. (2021), "Analysis of Restrained Composite Beams Exposed to Fire," *Engineering Structures*, Vol. 234, p. 111740, https://doi.org/10.1016/j.engstruct.2020.111740.

McAllister, T.P. (2014), "Sensitivity of Composite Floor System Response at Elevated Temperatures to Structural Features," *Engineering Structures*, Vol. 58, pp. 115–128, https://doi.org/10.1016/j.engstruct.2013.09.026.

Mirza, O. and Uy, B. (2009), "Behaviour of Headed Stud Shear Connectors for Composite Steel–Concrete Beams at Elevated Temperatures," *Journal of Constructional Steel Research*, Vol. 65, No. 3, pp. 662–674, https://doi.org/10.1016/j.jcsr.2008.03.008.

Moss, P.J., Buchanan, A.H., Seputro, J., Wastney, C., and Welsh, R. (2004), "Effect of Support Conditions on the Fire Behaviour of Steel and Composite Beams," *Fire and Materials*, Vol. 28, No. 2-4, pp. 159–175, https://doi.org/10.1002/fam.855.

Quiel, S. and Garlock, M. (2010), "Parameters for Modeling a High-Rise Steel Building Frame Subject to Fire," *Journal of Structural Fire Engineering*, Vol. 1, No. 2, pp. 115–134, https://doi.org/10.1260/2040-2317.1.2.115.

Rackauskaite, E., Kotsovinos, P., Jeffers, A., and Rein, G. (2019), "Computational Analysis of Thermal and Structural Failure Criteria of a Multi-Storey Steel Frame Exposed to Fire," *Engineering Structures*, Vol. 180, pp. 524–543, https://doi.org/10.1016/j.engstruct.2018.11.026.

Ramesh, S., Choe, L., Seif, M., Hoehler, M., Grosshandler, W., Sauca, A., Bundy, M., Luecke, W., Bao, Y., Klegseth, M., Chen, G., Reilly, J., and Glisic, B. (2019), *Compartment Fire Experiments on Long-Span Composite-Beams with Simple Shear Connections Part 1: Experimental Design and Beam Behavior at Ambient Temperature*, NIST TN 2054, National Institute of Standards and Technology, Gaithersburg, Md., https://doi.org/10.6028/NIST.TN.2054.

Sadek, F., El-Tawil, S., and Lew, H.S. (2008), "Robustness of Composite Floor Systems with Shear Connections: Modeling, Simulation, and Evaluation," *Journal of Structural Engineering*, Vol. 134, No. 11, pp. 1,717–1,725, https://doi.org/10.1061/(ASCE)0733-9445(2008)134:11(1717).

Safari, P. and Broujerdian, V. (2020), "Strategies to Increase the Survivability of Steel Connections in Fire," *Structures*, Vol. 28, pp. 2335–2354, https://doi.org/10.1016/j.istruc.2020.10.033.

Sanad, A.M., Rotter, J.M., Usmani, A.S., and O'Connor, M.A. (2000), "Composite Beams in Large Buildings under Fire—Numerical Modelling and Structural Behaviour," *Fire Safety Journal*, Vol. 35, No. 3, pp. 165–188, https://doi.org/10.1016/S0379-7112(00)00034-5.

Seif, M.S., Main, J.A., and McAllister, T.P. (2013), "Performance of Steel Shear Tab Connections at Elevated Temperatures," *Proceedings of the Annual Stability Conference*, April, St. Louis, Mo., https://www.aisc.org/globalassets/continuing-education/ssrc-proceedings/2013/performance-of-steel-shear-tab-connections-at-elevated-temperatures.pdf.

Selamet, S. and Garlock, M.E. (2010), "Robust Fire Design of Single Plate Shear Connections," *Engineering Structures*, Vol. 32, No. 8, pp. 2,367–2,378, https://doi.org/10.1016/j.engstruct.2010.04.011.

Selamet, S. and Yolaçan, T.F. (2017), "Steel Frame—Concrete Slab Composite Floor Fire Resistance Experiment," *Teknik Dergi*, Vol. 28, No. 3, pp. 8,007–8,022, https://eskisakarya.imo.org.tr/resimler/ekutuphane/pdf/17888_23_42.pdf.

Selden, K.L. (2014), *Structural Behavior and Design of Composite Beams Subjected to Fire*, Ph.D. Thesis, Purdue University, West Lafayette, Ind.

Selden, K.L., Fischer, E.C., and Varma, A.H. (2016a), "Experimental Investigation of Composite Beams with Shear Connections Subjected to Fire Loading," *Journal of Structural Engineering*, Vol. 142, No. 2, p. 04015118, https://doi.org/10.1061/(ASCE)ST.1943-541X.0001381.

Selden, K.L. and Varma, A.H. (2016b), "Composite Beams under Fire Loading: Numerical Modeling of Behavior," *Journal of Structural Fire Engineering*, Vol. 7, No. 2, pp. 142–157, https://doi.org/10.1108/JSFE-06-2016-011.

Selden, K.L. and Varma, A.H. (2016c), "Flexural Capacity of Composite Beams Subjected to Fire: Fiber-Based Models and Benchmarking," *Fire Technology*, Vol. 52, No. 4, pp. 995–1014, https://doi.org/10.1007/s10694-016-0565-7.

UL (2020), *UL 263: Standard for Fire Tests of Building Construction and Materials*, Underwriters Laboratories, Inc., Northbrook, Ill.

UL (2022a), *Fire Resistance Directory*, Underwriters Laboratories, Inc., Northbrook, Ill., http://productspec.ul.com/index.php.

UL (2022b), "BXUV.D902—Fire-Resistance Ratings—ANSI/UL 263: Design D902," Underwriters Laboratories, Inc., Northbrook, Ill., https://iq.ulprospector.com/en/profile?e=13878.

UL (2022c), "BXUV.D982—Fire-Resistance Ratings—ANSI/UL 263: Design D982," Underwriters Laboratories, Inc., Northbrook, Ill., https://iq.ulprospector.com/en/profile?e=13952.

Vinnakota, M.R., Foley, C.M., and Vinnakota, S. (1988), "Design of Partially or Fully Composite Beams with Ribbed Metal Deck Using LRFD Specifications," *Engineering Journal*, AISC, Vol. 25, No. 2, pp. 60–78, https://doi.org/10.62913/engj.v25i2.498.

Wald, F., Simões da Silva, L., Moore, D.B., Lennon, T., Chladná, M., Santiago, A., Beneš, M., and Borges, L. (2006), "Experimental Behaviour of a Steel Structure under Natural Fire," *Fire Safety Journal*, Vol. 41, No. 7, pp. 509–522, https://doi.org/10.1016/j.firesaf.2006.05.006.

Wang, A.J. (2012), "Numerical Investigation into Headed Shear Connectors under Fire," *Journal of Structural Engineering*, Vol. 138, No. 1, pp. 118–122, https://doi.org/10.1061/(ASCE)ST.1943-541X.0000428.

Wang, W., Engelhardt, M.D., Li, G., and Huang, G. (2017a), "Behavior of Steel–Concrete Partially Composite Beams Subjected to Fire—Part 1: Experimental Study," *Fire Technology*, Vol. 53, No. 3, pp. 1,039–1,058, https://doi.org/10.1007/s10694-016-0618-y.

Wang, W., Wang, K., Engelhardt, M.D., and Li, G. (2017b), "Behavior of Steel–Concrete Partially Composite Beams Subjected to Fire—Part 2: Analytical Study," *Fire Technology*, Vol. 53, No. 3, pp. 1,147–1,170, https://doi.org/10.1007/s10694-016-0624-0.

Wellman, E.I., Varma, A.H., Fike, R., and Kodur, V. (2011), "Experimental Evaluation of Thin Composite Floor Assemblies under Fire Loading," *Journal of Structural Engineering*, Vol. 137, No. 9, pp. 1,002–1,016, https://doi.org/10.1061/(ASCE)ST.1943-541X.0000451.

Yu, L. and Frank, K.H. (2009), "Shear Behavior of A325 and A490 High-Strength Bolts in Fire and Post-Fire," *Engineering Journal,* AISC, Vol. 46, No. 2, pp. 99–106, https://doi.org/10.62913/engj.v46i2.1226.

Zhao, B. and Kruppa, J. (1997), *Fire Resistance of Composite Slabs with Profiled Steel Sheet and of Composite Steel Concrete Beams, Part 2: Composite Beams Final Report*, Publications Office of the European Commission: Directorate-General for Research and Innovation, Luxembourg.

New Equations and Table for Design of Eccentrically Loaded WT Compression Members

ABBAS AMINMANSOUR

ABSTRACT:

Equations and a design table are developed to determine the available axial compressive strength of eccentrically loaded WT shapes with $F_y = 50$ ksi using both the LRFD and ASD methods. WTs considered are made from W-shapes ordinarily used as columns. Tabulated values account for the bending moment created in the member due to the load eccentricity, including second-order effects, and follow the provisions of Section H1.1 of the AISC *Specification for Structural Steel Buildings* (2022) for design of members subject to combined forces. Applicable limit states and cross-section classifications are considered in the development of the equations and the design table. Numerical example problems are presented.

Keywords: WT shapes, compression, combined forces, eccentric loading, design aid.

INTRODUCTION

WT shapes are commonly used as compression members, particularly in bracing systems. Typically, the member is connected at the ends using gusset plates attached to the outer surface of the flange (Figure 1) using bolted or welded joints. This arrangement causes the applied load to be eccentric, resulting in both flexural and compressive stresses. The member should therefore be designed for combined forces in accordance with Section H1.1 of the AISC *Specification for Structural Steel Buildings* (2022), hereafter referred to as the AISC *Specification*, including AISC *Specification* Equations H1-1a and H1-1b.

$$\frac{P_r}{P_c}+\frac{8}{9}\left(\frac{M_{rx}}{M_{cx}}+\frac{M_{ry}}{M_{cy}}\right)\le 1.0 \quad \text{(AISC } \textit{Spec.} \text{ Eq. H1-1a)}$$

$$\frac{P_r}{2P_c}+\left(\frac{M_{rx}}{M_{cx}}+\frac{M_{ry}}{M_{cy}}\right)\le 1.0 \quad \text{(AISC } \textit{Spec.} \text{ Eq. H1-1b)}$$

The LRFD and ASD versions of these equations are presented and used later. A list of symbols, their definitions, and units are provided later in this article. The term *force* in this article refers to both axial load as well as bending moment.

Abbas Aminmansour, Associate Professor, Structures Concentration, School of Architecture, University of Illinois at Urbana-Champaign. Email: aamin@illinois.edu

Paper No. 2025–05

A table of reduction factors (P_r/P_c) for WT sections subjected to compressive loads with connection eccentricity was previously developed by Mark E. Gordon (2010), based on the provisions of the 2005 AISC *Specification* (AISC, 2005a) and the 13th Edition of the AISC *Steel Construction Manual* (AISC, 2005b), hereafter referred to as the AISC *Manual*. The table was developed based on ½ in. gusset plates in all cases.

This article introduces newly developed equations and a design table that directly provide the compressive strength of eccentrically loaded WT members, in accordance with the latest editions of the AISC *Specification* (2022) and *Manual* (2023a). Gusset plate thicknesses based on member flange thickness are used. Other member properties useful in the design are listed at the bottom of the table.

RATIONALE FOR THE DEVELOPMENT OF THE COMPRESSIVE STRENGTH EQUATIONS AND DESIGN TABLE

It is common to connect WT compression members using a gusset plate connected to the flange of the WT at each end as discussed. This configuration results in load eccentricity in the member, considerably reducing its available compressive strength.

AISC *Manual* Table 4-7, titled "Available Strength in Axial Compression, Concentrically Loaded WT-Shapes," assumes that the applied load does not have any eccentricity and gives very unconservative results for members subject to eccentric loading. For example, a 14-ft-long WT7×66 connected with a ¾ in. gusset plate at each end will have an available eccentric compressive strength of 184 kips using the LRFD method. The same member has an available concentric compressive strength of 438 kips given in

Table 4-7. Use of Table 4-7 in this case results in significant under-design.

Shortly, two example problems will be presented that will include manual solutions based on AISC *Specification* provisions and equations. As will be observed, the proposed design table reduces the work necessary for calculating the available strength of eccentrically loaded WT compression members from a few pages of calculations to simply looking up the value from the design table resulting in significant savings of time and effort.

CLARIFICATION OF LATERALLY UNBRACED LENGTHS FOR WT COMPRESSION MEMBERS

Laterally bracing a WT compression member against flexural buckling about the y-axis braces the member at the same location against lateral torsional buckling as well, namely, $L_b = L_y$.

Ordinarily, there is no restriction on the relative magnitude of unbraced lengths L_x, L_y, L_z, and L_b for a member subject to combined forces. One can use manual calculations to determine the strength of an eccentrically loaded WT compression member for different unbraced lengths using AISC *Specification* provisions and equations. As explained later, this study requires all the unbraced lengths to be equal, as shown in Figure 2, namely, $L_x = L_y = L_z = L_b = L$.

Plate connections at the ends of a member as described earlier create pin connections for both column and beam actions. Further, unbraced lengths for flexural buckling and flexural torsional buckling are also pin-ended. For this study, the values of K_x, K_y, and K_z are all taken as 1.0. Consequently, $L_{cx} = K_x L_x = (1)L_x = L_x$. Similarly, L_{cy} equals L_y, and L_{cz} equals L_z.

Given that the members in question are subject to combined compression and bending, the available eccentric compressive strength for any L_{cx} depends on the nominal

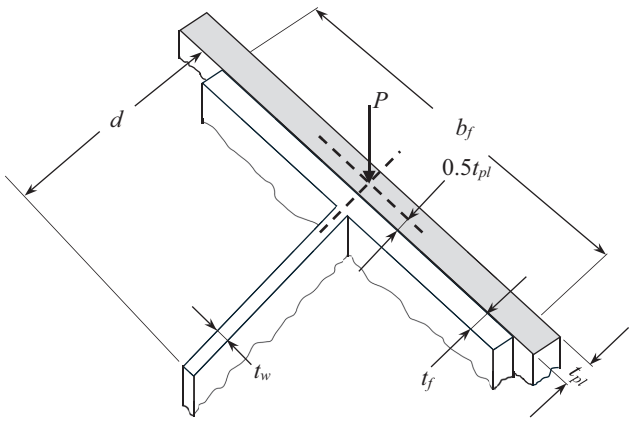

Fig. 1. WT member subject to eccentric axial compression (joint details not shown).

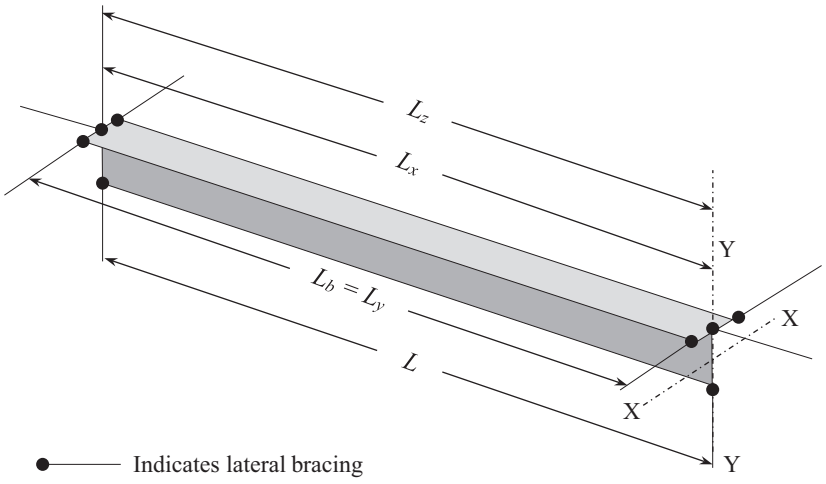

Fig. 2. Identification of lateral bracing and unbraced lengths.

flexural strength, M_n, which, in turn, depends on L_b and thus L_{cy}. Therefore, the member's flexural and compressive strengths are interlinked as are their unbraced lengths. This concept is important to recognize in the development and use of the equations and design table that follow.

ANALYSIS OF THE MEMBER, INCLUDING SECOND-ORDER EFFECT

In the following discussion, it is assumed that the compression load is applied at the mid-width of the WT flange and at mid-thickness of the plate as shown in Figure 3. Further, it is assumed that end connections are identical, no transverse loads are applied along the member length, and there is no bending about the *y*-axis. Member weight is not included as is the case in AISC *Manual* tables.

In the proposed design table, it is assumed that $L_{cx} = L_{cy} = L_{cz} = L_b = L$. Also assumed are connection plate widths and thicknesses. These same assumptions were made in the two design example manual solutions so that the computed results could be compared with the tabulated results. The manual solutions can be modified for other unbraced lengths and connection plate dimensions.

As shown in Figure 4, the eccentricity of the load, measured from the centroid of the WT, is as follows.

$$e = 0.5t_{pl} + \overline{y} \tag{1}$$

This eccentricity results in a constant bending moment of force times the eccentricity, *Pe*, in the member.

The approximate second-order analysis presented in AISC *Specification* Appendix 8, Section 8.1, is used to calculate the required flexural strength of the member as follows.

$$M_r = B_1 M_{nt} + B_2 M_{lt}$$
(AISC *Spec.* Eq. A-8-1)

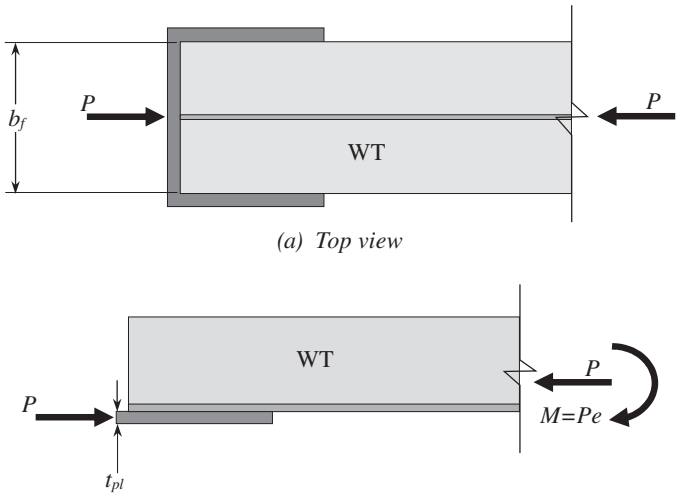

Fig. 3. Typical end connection of WT compression members (joint details not shown).

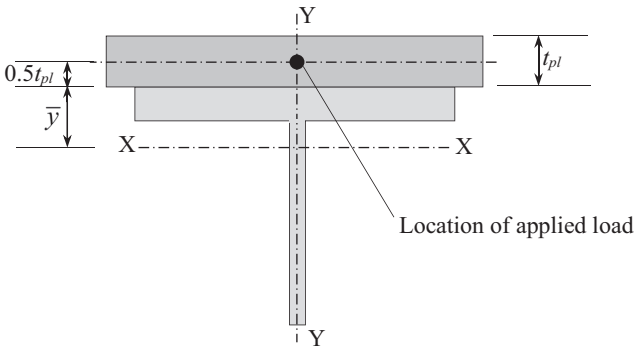

Fig. 4. Anatomy of the WT section and connected plate.

$$P_r = P_{nt} + B_2 P_{lt}$$

(AISC *Spec.* Eq. A-8-2)

Because there is no relative lateral translation of the member ends, there is no P-Δ effect, thus B_2, M_{lt}, and P_{lt} do not apply. Further, recall that the member is not subject to transverse loads.

LRFD Method

There is no bending about the y-axis ($M_{uy} = 0$). Therefore, member forces including P-δ effect are as follows.

$$M_{ux} = B_{1x} M_{ntx} \tag{2}$$

$$P_u = P_{nt} \tag{3}$$

with

$$M_{ntx} = P_u e \tag{4}$$

Therefore,

$$M_{ux} = B_{1x} P_u e \tag{5}$$

where

$$B_{1x} = \frac{C_{mx}}{1 - \frac{\alpha P_r}{P_{e1x}}} \geq 1.0$$

(AISC *Spec.* Eq. A-8-3)

and

$$C_{mx} = 0.6 - 0.4\left(M_{1x}/M_{2x}\right)$$

(AISC *Spec.* Eq. A-8-4)

M_{1x} and M_{2x} are the member end moments. In this case, $M_{1x} = M_{2x}$ and the member bends in single curvature. Therefore, $\left(M_{1x}/M_{2x}\right) = -1.0$ with the negative sign for single curvature bending.

$$\begin{aligned} C_{mx} &= 0.6 - 0.4\left(M_{1x}/M_{2x}\right) \\ &= 0.6 - 0.4(-1) \\ &= 1.0 \end{aligned}$$

AISC *Specification* Equation A-8-3, modified with $C_{mx} = 1.0$ and utilizing the LRFD design method ($\alpha = 1.0$ and $P_r = P_u$) results in the following.

$$B_{1x} = \frac{C_{mx}}{1 - \frac{\alpha P_r}{P_{e1x}}} = \frac{1}{1 - \frac{(1.0) P_u}{P_{e1x}}} \geq 1.0 \tag{6}$$

or

$$B_{1x} = \frac{P_{e1x}}{P_{e1x} - P_u} \geq 1.0 \tag{7}$$

where

$$P_{e1x} = \frac{\pi^2 E I_x}{(L_{c1x})^2}$$

(AISC *Spec.* Eq. A-8-5)

ASD Method

The following are pertinent equations, without discussion, for the ASD method developed similar to those presented for the LRFD method. Note that $C_{mx} = 1.0$ and for ASD, $\alpha = 1.6$ and $P_r = P_a$. These equations will be used and referenced in Design Example 2.

$$M_{ax} = B_{1x} M_{ntx} \tag{8}$$

$$P_a = P_{nt} \tag{9}$$

$$M_{ntx} = P_a e \tag{10}$$

$$M_{ax} = B_{1x} P_a e \tag{11}$$

$$B_{1x} = \frac{1}{1 - \frac{1.6 P_a}{P_{e1x}}} \geq 1.0$$

(AISC *Spec.* Eq. A-8-3)

or

$$B_{1x} = \frac{P_{e1x}}{P_{e1x} - 1.6 P_a} \geq 1.0 \tag{12}$$

EXAMPLE PROBLEMS WITH MANUAL SOLUTIONS

The following example problems are provided to offer detailed manual solutions for calculation of the available strengths of eccentrically loaded WT compression members using ASD and LRFD methods.

The use of the proposed design table is based on a number of assumptions such as certain plate width thickness and that $L_{cx} = L_{cy} = L_{cz} = L_b$. However, the solutions to the following problems are not limited to any of those restrictions. In the examples that follow, the condition $L_{cx} = L_{cy} = L_{cz} = L_b$ was used so that the results may be compared with the values in the proposed design table. However, the manual solutions can be modified appropriately for any unbraced lengths.

Design Example 1

Given:

The WT7×45 compression member shown in Figure 5 with ASTM A992/A992M (2020) steel is braced at the ends and connected at each end with a 14½ in. × ½ in. gusset plate of ASTM A572/A572M (2021) Grade 50 steel. $L_{cx} = L_{cy} = L_{cz} = L_b = L =$ 12 ft. Assume an adequate bolted or welded joint exists between each gusset plate and the member. Determine the available eccentric axial compressive strength of the member using AISC *Specification* provisions for the LRFD method.

Solution:

From AISC *Manual* Table 1-8, the geometric properties for a WT7×45 are as follows:

$A = 13.2$ in.^{2} $b_f = 14.5$ in. $t_f = 0.710$ in. $b_f/2t_f = 10.2$ $d/t_w = 15.9$ $I_x = 36.5$ in.^{4} $S_x = 6.16$ in.^{3}
$r_x = 1.66$ in. $\bar{y} = 1.09$ in. $Z_x = 11.5$ in.^{3} $r_y = 3.70$ in. $J = 2.03$ in.^{4} $C_w = 8.31$ in.^{6}

Beam Action

Check the section element width-to-thickness ratios using the limits given in AISC *Specification* Table B4.1b.

For Case 10(3), the flange element compact limit is:

$$\lambda_{pf} = 0.38\sqrt{\frac{E}{F_y}}$$
$$= 0.38\sqrt{\frac{29{,}000 \text{ ksi}}{50 \text{ ksi}}}$$
$$= 9.15$$

For Case 10(3), the flange element noncompact limit is:

$$\lambda_{rf} = 1.0\sqrt{\frac{E}{F_y}}$$
$$= 1.0\sqrt{\frac{29{,}000 \text{ ksi}}{50 \text{ ksi}}}$$
$$= 24.1$$

Fig. 5. Design Example 1 detail.

Because $\lambda_{pf} = 9.15 < \lambda_f = b_f / 2t_f = 10.2 < \lambda_{rf} = 24.1$, the flange element is noncompact.

The stem is in tension for flexure, and therefore, there is no need to check the width-to-thickness ratio of the stem for flexure.

$$L_p = 1.76 r_y \sqrt{\frac{E}{F_y}} \quad \text{(AISC } \textit{Spec.} \text{ Eq. F9-8)}$$

$$= (1.76)(3.70 \text{ in.}) \sqrt{\frac{29{,}000 \text{ ksi}}{50 \text{ ksi}}}$$

$$= 157 \text{ in.} \left(\frac{1 \text{ ft}}{12 \text{ in.}} \right)$$

$$= 13.1 \text{ ft}$$

Because $L_b = 12 \text{ ft} < L_p = 13.1 \text{ ft}$, lateral torsional buckling does not apply per AISC *Specification* Section F9.2(a)(1).

Because the section is noncompact, AISC *Specification* Equation F9-14 applies for calculation of M_n.

$$M_{nx} = M_{px} - (M_{px} - 0.7 F_y S_{xc}) \left(\frac{\lambda - \lambda_{pf}}{\lambda_{rf} - \lambda_{pf}} \right) \leq 1.6 M_y \quad \text{(AISC } \textit{Spec.} \text{ Eq. F9-14)}$$

where

$$M_{px} = F_y Z_x \leq 1.6 M_y \quad \text{(AISC } \textit{Spec.} \text{ Eq. F9-2)}$$

$$M_y = F_y S_x \quad \text{(AISC } \textit{Spec.} \text{ Eq. F9-3)}$$

$$= (50 \text{ ksi})(6.16 \text{ in.}^3)$$

$$= 308 \text{ kip-in.} \left(\frac{1 \text{ ft}}{12 \text{ in.}} \right)$$

$$= 25.7 \text{ kip-ft}$$

$$M_{px} = F_y Z_x \leq 1.6 M_y$$

$$= (50 \text{ ksi})(11.5 \text{ in.}^3)$$

$$= 575 \text{ kip-in.} \left(\frac{1 \text{ ft}}{12 \text{ in.}} \right)$$

$$= 47.9 \text{ kip-ft, but must be} \leq 1.6 M_y = (1.6)(25.7 \text{ kip-ft}) = 41.1 \text{ kip-ft}$$

Therefore, use $M_{px} = 41.1$ kip-ft.

$$S_{xc} = \frac{I_x}{\bar{y}}$$

$$= \frac{36.5 \text{ in.}^4}{1.09 \text{ in.}}$$

$$= 33.5 \text{ in.}^3$$

$$0.7 F_y S_{xc} = (0.70)(50 \text{ ksi})(33.5 \text{ in.}^3)$$

$$= 1{,}172 \text{ kip-in.} \left(\frac{1 \text{ ft}}{12 \text{ in.}} \right)$$

$$= 97.7 \text{ kip-ft}$$

Apply AISC *Specification* Equation F9-14.

$$M_{nx} = 41.1 \text{ kip-ft} - \left\{ \left[(41.1 \text{ kip-ft}) - (97.5 \text{ kip-ft}) \right] \left(\frac{10.2 - 9.15}{24.1 - 9.15} \right) \right\}$$
$$= 45.1 \text{ kip-ft, but must be} \le 1.6M_y = (1.60)(25.7 \text{ kip-ft}) = 41.1 \text{ kip-ft}$$

Therefore, use $M_{nx} = 41.1$ kip-ft.

$$\phi_b M_{nx} = (0.90)(41.1 \text{ kip-ft})$$
$$= 37.0 \text{ kip-ft}$$

Column Action

Check the section element width-to-thickness ratios using the limits given in AISC *Specification* Table B4.1a.

Case 1(5), flange element nonslender limit

$$\lambda_{rf} = 0.56\sqrt{\frac{E}{F_y}}$$
$$= 0.56\sqrt{\frac{29{,}000 \text{ ksi}}{50 \text{ ksi}}}$$
$$= 13.5$$

Because $\lambda_f = \frac{b_f}{2t_f} = 10.2 < \lambda_{rf} = 13.5$, the flange element is nonslender.

Case 4, web element nonslender limit

$$\lambda_{rw} = 0.75\sqrt{\frac{E}{F_y}}$$
$$= 0.75\sqrt{\frac{29{,}000 \text{ ksi}}{50 \text{ ksi}}}$$
$$= 18.1$$

Because $\lambda_w = \frac{d}{t_w} = 15.9 < \lambda_{rw} = 18.1$, the web element is nonslender.

Flexural Buckling Strength

AISC *Specification* Section E3 applies.

$$\frac{L_{cx}}{r_x} = \frac{(12 \text{ ft})(12 \text{ in./ft})}{1.66 \text{ in.}}$$
$$= 86.7 < 200 \qquad \textbf{o.k.}$$

$$\frac{L_{cy}}{r_y} = \frac{(12 \text{ ft})(12 \text{ in./ft})}{3.70 \text{ in.}}$$
$$= 38.9 < 200 \qquad \textbf{o.k.}$$

Use $\frac{L_c}{r} = 86.7$.

In the following equations, subscripts *FB* and *FTB* are used to distinguish between values calculated for flexural buckling and flexural-torsional buckling, respectively.

$$(F_e)_{FB} = \frac{\pi^2 E}{\left(\frac{L_c}{r}\right)^2} \quad \text{(AISC } \textit{Spec.} \text{ Eq. E3-4)}$$
$$= \frac{\pi^2 (29{,}000 \text{ ksi})}{(86.7)^2}$$
$$= 38.0 \text{ ksi}$$

Because $\frac{F_y}{(F_e)_{FB}} = \frac{50.0 \text{ ksi}}{38.0 \text{ ksi}} = 1.32 < 2.25$, use AISC *Specification* Equation E3-2.

$$(F_n)_{FB} = \left[0.658^{\frac{F_y}{F_e}}\right](F_y) \quad \text{(AISC } \textit{Spec.} \text{ Eq. E3-2)}$$
$$= \left[0.658^{(1.32)}\right](50 \text{ ksi})$$
$$= 28.8 \text{ ksi}$$

Flexural-Torsional Buckling Strength (AISC *Specification* Section E4 applies)

$$F_{ey} = \frac{\pi^2 E}{\left(\frac{L_{cy}}{r_y}\right)^2} \quad \text{(AISC } \textit{Spec.} \text{ Eq. E4-6)}$$
$$= \frac{\pi^2 (29{,}000 \text{ ksi})}{(38.9)^2}$$
$$= 189 \text{ ksi}$$

From the AISC *Shapes Database* (2023b), $H = 0.968$ and $\bar{r}_o = 4.12$ in. Alternatively, AISC *Specification* Equations E4-8 and E4-9 can be used to calculate H and $\bar{r}_o^2$.

Calculate F_{ez} as follows.

$$F_{ez} = \left(\frac{\pi^2 E C_w}{L_{cz}^2} + GJ\right)\frac{1}{A_g \bar{r}_o^2} \quad \text{(AISC } \textit{Spec.} \text{ Eq. E4-7)}$$
$$= \left\{\frac{\pi^2 (29{,}000 \text{ ksi})(8.31 \text{ in.}^6)}{\left[(12 \text{ ft})(12 \text{ in./ft})\right]^2} + (11{,}200 \text{ ksi})(2.03 \text{ in.}^4)\right\}\left[\frac{1}{(13.2 \text{ in.}^2)(4.12 \text{ in.})^2}\right]$$
$$= 102 \text{ ksi}$$

The first component of the preceding equation that includes C_w is about 0.5% of the calculated F_{ez}. This is consistent with a User Note in AISC *Specification* Section E4 that states, "For tees and double angles, the term with C_w may be omitted when computing F_{ez}."

Calculate $(F_e)_{FTB}$ as follows.

$$(F_e)_{FTB} = \left(\frac{F_{ey}+F_{ez}}{2H}\right)\left[1-\sqrt{1-\frac{4F_{ey}F_{ez}H}{(F_{ey}+F_{ez})^2}}\right] \quad \text{(AISC } \textit{Spec.} \text{ Eq. E4-3)}$$

$$= \left[\frac{189 \text{ ksi}+102 \text{ ksi}}{2(0.968)}\right]\left[1-\sqrt{1-\frac{4(189 \text{ ksi})(102 \text{ ksi})(0.968)}{(189 \text{ ksi}+102 \text{ ksi})^2}}\right]$$

$$= 98.6 \text{ ksi}$$

Because $\frac{F_y}{(F_e)_{FTB}} = \frac{50.0 \text{ ksi}}{98.6 \text{ ksi}} = 0.507 < 2.25$, use AISC *Specification* Equation E3-2.

$$(F_n)_{FTB} = \left[0.658^{\frac{F_y}{F_e}}\right](F_y) \quad \text{(AISC } \textit{Spec.} \text{ Eq. E3-2)}$$

$$= \left[0.658^{(0.507)}\right](50 \text{ ksi})$$

$$= 40.4 \text{ ksi}$$

$(F_n)_{FTB} = 40.4 \text{ ksi} > (F_n)_{FB} = 28.8 \text{ ksi}$; therefore, use $F_n = (F_n)_{FB} = 28.8$ ksi.

$$P_n = F_n A_g$$

$$= (28.8 \text{ ksi})(13.2 \text{ in.}^2)$$

$$= 380 \text{ kips}$$

$$\phi_c P_n = (0.90)(380 \text{ kips})$$

$$= 342 \text{ kips}$$

Required Flexural Strength, Including Second-Order Effect

In the following calculations, the available strength in compression of the eccentrically loaded member is referred to as $\phi_c P_{n\,ecc}$. Note that this replaces P_u used in Equation 7 as well as in the interaction equations later.

The required moment in the member, including a second-order effect, is calculated as follows.

$$P_{e1x} = \frac{\pi^2 E I_x}{(L_{c1x})^2} \quad \text{(AISC } \textit{Spec.} \text{ Eq. A-8-5)}$$

$$= \frac{\pi^2 (29{,}000 \text{ ksi})(36.5 \text{ in.}^4)}{\left[(12 \text{ ft})(12 \text{ in./ft})\right]^2}$$

$$= 503 \text{ kips}$$

Use Equation 7 to calculate B_{1x} as follows.

$$B_{1x} = \frac{P_{e1x}}{P_{e1x} - \phi_c P_{n\,ecc}} \geq 1.0$$

$$= \frac{503 \text{ kips}}{503 \text{ kips} - \phi_c P_{n\,ecc}} \geq 1.0$$

Use Equation 1 to calculate the total load eccentricity.

$$e = 0.5t_{pl} + \overline{y} \tag{1}$$
$$= (0.50)(0.50 \text{ in.}) + 1.09 \text{ in.}$$
$$= 1.34 \text{ in.}\left(\frac{1 \text{ ft}}{12 \text{ in.}}\right)$$
$$= 0.112 \text{ ft}$$

Recall that, $P_u = \phi_c P_{n\,ecc}$ as described before. Therefore,

$$M_{ux} = B_{1x} P_u e \tag{5}$$
$$= (B_{1x})(\phi_c P_{n\,ecc})(e)$$
$$= \left(\frac{503 \text{ kips}}{503 \text{ kips} - \phi\, P_{n\,ecc}}\right)(\phi_c P_{n\,ecc})(0.112 \text{ ft})$$
$$= \frac{56.3(\phi_c P_{n\,ecc})}{503 - \phi_c P_{n\,ecc}} \text{ kip-ft}$$

Check the Appropriate Interaction Equation for Combined Forces

Assume $\frac{P_u}{\phi_c P_n} = \frac{\phi_c P_{n\,ecc}}{\phi_c P_n} \geq 0.20$, and apply the LRFD version of AISC *Specification* Equation H1-1a as follows. Set the interaction equation equal to unity (1.0) to find the member available eccentric axial compressive strength. Note that $\phi_c = \phi_b = 0.90$ and $M_{uy} = 0$. Also, recall that, $\phi_c P_n = 342$ kips, $\phi_b M_{nx} = 37.0$ kip-ft, and P_u is replaced by $\phi_c P_{n\,ecc}$.

$$\frac{\phi_c P_{n\,ecc}}{\phi_c P_n} + \frac{8}{9}\left(\frac{M_{ux}}{\phi_b M_{nx}} + \frac{M_{uy}}{\phi_b M_{ny}}\right) = \frac{\phi_c P_{n\,ecc}}{\phi_c P_n} + \frac{8M_{ux}}{9\phi_b M_{nx}} = 1.0$$

Insert values of available strengths and replace M_{ux} with its equivalent found earlier.

$$\frac{\phi_c P_{n\,ecc}}{342 \text{ kips}} + \frac{8\left[\frac{56.3(\phi_c P_{n\,ecc})}{503 - \phi_c P_{n\,ecc}}\right]}{9(37.0 \text{ kip-ft})} = \frac{\phi_c P_{n\,ecc}}{342 \text{ kips}} + \frac{1.35(\phi_c P_{n\,ecc})}{503 - \phi_c P_{n\,ecc}}$$
$$= 1.0$$

This is a quadratic equation with a root $\phi_c P_{n\,ecc} = 149$ kips (solution details not shown).

Check the value of B_{1x} using Equation 7.

$$B_{1x} = \frac{503 \text{ kips}}{503 \text{ kips} - \phi_c P_{n\,ecc}}$$
$$= \frac{503 \text{ kips}}{503 \text{ kips} - 149 \text{ kips}}$$
$$= 1.42 > 1.0 \quad \textbf{o.k.}$$

Check the assumption that $\frac{P_u}{\phi_c P_n} = \frac{\phi_c P_{n\,ecc}}{\phi_c P_n} \geq 0.20$.

$$\frac{P_u}{\phi_c P_n} = \frac{P_{n\,ecc}}{\phi_c P_n}$$
$$= \frac{149 \text{ kips}}{342 \text{ kips}}$$
$$= 0.436 > 0.20 \quad \textbf{o.k.}$$

Had this assumption turned out to be incorrect, the solution would be repeated using AISC *Specification* Eq. H1-1b instead of AISC *Specification* Eq. H1-1a. All assumptions made earlier were proven correct. Therefore, the available eccentric compressive strength of the WT7×45 compression member is $\phi_c P_{n\,ecc} = 149$ kips.

As a check, calculate the compressive strength of the gusset plate assuming that flexural buckling does not apply. See AISC *Specification* Section J4.4(a) and Equation J4–6.

The gross area of the plate is

$$(A_g)_{pl} = (b)(t)$$
$$= (14.5 \text{ in.})(0.50 \text{ in.})$$
$$= 7.25 \text{ in.}^2$$

$$(P_n)_{pl} = (F_y A_g)_{pl} \qquad \text{(AISC Spec. Eq. J4-6)}$$
$$= (50 \text{ ksi})(7.25 \text{ in.}^2)$$
$$= 362 \text{ kips}$$

$$(\phi_c P_n)_{pl} = (0.90)(P_n)_{pl}$$
$$= (0.90)(362 \text{ kips})$$
$$= 326 \text{ kips} > 149 \text{ kips} \quad \textbf{o.k.}$$

Design Example 2

Given:

The WT7×30.5 compression member shown in Figure 6 is ASTM A992/A992M steel, braced at the ends and connected at each end with a 10 in. × ½ in. gusset plate of ASTM A572/A572M Grade 50 steel. $L_{cx} = L_{cy} = L_{cz} = L_b = L = 10$ ft. Assume an adequate bolted or welded joint exists between each gusset plate and the member. Determine the available eccentric axial compressive strength of the member using AISC *Specification* provisions for the ASD method.

Fig. 6. Design Example 2 detail.

Solution:

From AISC *Manual* Table 1-8, the geometric properties for a WT7×30.5 are:

$A = 8.96$ in.^{2} $d = 6.95$ in. $b_f = 10.0$ in. $t_f = 0.645$ in. $b_f/2t_f = 7.75$ $d/t_w = 18.5$ $I_x = 28.9$ in.^{4} $S_x = 5.07$ in.^{3}
$r_x = 1.80$ in. $\bar{y} = 1.25$ in. $Z_x = 9.15$ in.^{3} $I_y = 53.7$ in.^{4} $r_y = 2.45$ in. $J = 1.09$ in.^{4} $C_w = 2.29$ in.^{6}

Beam Action

Check the section element width-to-thickness ratios using the limits given in AISC *Specification* Table B4.1b.

For Case 10(3), the flange element compact limit is:

$$\lambda_{pf} = 0.38\sqrt{\frac{E}{F_y}}$$
$$= 0.38\sqrt{\frac{29{,}000 \text{ ksi}}{50 \text{ ksi}}}$$
$$= 9.15$$

Because $\lambda_f = b_f/2t_f = 7.75 < \lambda_{pf} = 9.15$, the flange element is compact.

Because the web is in tension for flexure, there is no need to check width-to-thickness ratio for flexure.

$$L_p = 1.76 r_y\sqrt{\frac{E}{F_y}} \quad \text{(AISC } \textit{Spec.} \text{ Eq. F9-8)}$$
$$= (1.76)(2.45 \text{ in.})\sqrt{\frac{29{,}000 \text{ ksi}}{50 \text{ ksi}}}$$
$$= 104 \text{ in.}\left(\frac{1 \text{ ft}}{12 \text{ in.}}\right)$$
$$= 8.67 \text{ ft}$$

$$L_r = 1.95\left(\frac{E}{F_y}\right)\frac{\sqrt{I_y J}}{S_x}\sqrt{2.36\left(\frac{F_y}{E}\right)\frac{dS_x}{J}+1} \quad \text{(AISC } \textit{Spec.} \text{ Eq. F9-9)}$$
$$= 1.95\left(\frac{29{,}000 \text{ ksi}}{50 \text{ ksi}}\right)\frac{\sqrt{(53.7 \text{ in.}^4)(1.09 \text{ in.}^4)}}{(5.07 \text{ in.}^3)}\sqrt{2.36\left(\frac{50 \text{ ksi}}{29{,}000 \text{ ksi}}\right)\frac{(6.95 \text{ in.})(5.07 \text{ in.}^3)}{(1.09 \text{ in.}^4)}+1}$$
$$= 1{,}816 \text{ in.}\left(\frac{1 \text{ ft}}{12 \text{ in.}}\right)$$
$$= 151 \text{ ft}$$

Note that AISC *Specification Commentary* Section F9, Tees and Double Angles Loaded in the Plane of Symmetry, states, "For most shapes, the length, L_r, is impractically long."

$L_p = 8.67 \text{ ft} < L_b = 10 \text{ ft} < L_r = 151 \text{ ft}$

Inelastic lateral torsional buckling governs. Provisions of AISC *Specification* Section F9.2(a)(2) and Equation F9-6 apply to calculating M_n. But first calculate M_{px} as follows.

$$M_{px} = F_y Z_x < 1.6M_y \quad \text{(AISC } \textit{Spec}\text{. Eq. F9-2)}$$

$$M_y = F_y S_x \quad \text{(AISC } \textit{Spec}\text{. Eq. F9-3)}$$

$$= (50 \text{ ksi})(5.07 \text{ in.}^3)$$

$$= 254 \text{ kip-in.}\left(\frac{1 \text{ ft}}{12 \text{ in.}}\right)$$

$$= 21.1 \text{ kip-ft}$$

$$M_{px} = F_y Z_x$$

$$= (50 \text{ ksi})(9.15 \text{ in.}^3)$$

$$= 458 \text{ kip-in.}\left(\frac{1 \text{ ft}}{12 \text{ in.}}\right)$$

$$= 38.1 \text{ kip-ft, but must be} \le 1.6M_y = (1.6)(21.1 \text{ kip-ft}) = 33.8 \text{ kip-ft}$$

Therefore, use $M_{px} = 33.8$ kip-ft.

$$M_{nx} = M_{px} - (M_{px} - M_y)\left(\frac{L_b - L_p}{L_r - L_p}\right) \le 1.6M_y \quad \text{(AISC } \textit{Spec}\text{. Eq. F9-6)}$$

$$= (33.8 \text{ kip-ft}) - \left[(33.8 \text{ kip-ft}) - (21.1 \text{ kip-ft})\right]\left(\frac{10.0 \text{ ft} - 8.67 \text{ ft}}{151 \text{ ft} - 8.67 \text{ ft}}\right)$$

$$= 33.7 \text{ kip-ft} < 1.6M_y = 33.8 \text{ kip-ft}$$

Therefore, $M_{nx} = 33.7$ kip-ft and $M_n/\Omega_b = (33.7 \text{ kip-ft})/(1.67) = 20.2$ kip-ft.

Column Action

Check the section element width-to-thickness ratios using the limits given in AISC *Specification* Table B4.1a.

For Case 1(5), the flange element nonslender limit is:

$$\lambda_{rf} = 0.56\sqrt{\frac{E}{F_y}}$$

$$= 0.56\sqrt{\frac{29{,}000 \text{ ksi}}{50 \text{ ksi}}}$$

$$= 13.5$$

Because $\lambda_f = \dfrac{b_f}{2t_f} = 7.75 < \lambda_{rf} = 13.5$, the flange element is nonslender.

For Case 4, the web element nonslender limit is:

$$\lambda_{rw} = 0.75\sqrt{\frac{E}{F_y}}$$

$$= 0.75\sqrt{\frac{29{,}000 \text{ ksi}}{50 \text{ ksi}}}$$

$$= 18.1$$

Because $\lambda_w = \dfrac{d}{t_w} = 18.5 > \lambda_{rw} = 18.1$, the web element is slender.

Flexural Buckling Strength

AISC *Specification* Section E3 applies.

$$\frac{L_{cx}}{r_x} = \frac{(10 \text{ ft})(12 \text{ in./ft})}{1.80 \text{ in.}}$$
$$= 66.7 < 200 \quad \textbf{o.k.}$$

$$\frac{L_{cy}}{r_y} = \frac{(10 \text{ ft})(12 \text{ in./ft})}{2.45 \text{ in.}}$$
$$= 49.0 < 200 \quad \textbf{o.k.}$$

Use $\frac{L_c}{r} = 66.7$.

In the following equations, subscripts *FB* and *FTB* are used to distinguish between values calculated for flexural buckling and flexural-torsional buckling, respectively.

$$(F_e)_{FB} = \frac{\pi^2 E}{\left(\frac{L_c}{r}\right)^2} \quad \text{(AISC } \textit{Spec.} \text{ Eq. E3-4)}$$
$$= \frac{\pi^2 (29{,}000 \text{ ksi})}{(66.7)^2}$$
$$= 64.3 \text{ ksi}$$

Because $\frac{F_y}{(F_e)_{FB}} = \frac{50.0 \text{ ksi}}{64.3 \text{ ksi}} = 0.778 < 2.25$, use AISC *Specification* Equation E3-2.

$$(F_n)_{FB} = \left[0.658^{\frac{F_y}{F_e}}\right](F_y) \quad \text{(AISC } \textit{Spec.} \text{ Eq. E3-2)}$$
$$= \left[0.658^{(0.778)}\right](50 \text{ ksi})$$
$$= 36.1 \text{ ksi}$$

Flexural-Torsional Buckling Strength (AISC *Specification* Section E4 applies)

$$F_{ey} = \frac{\pi^2 E}{\left(\frac{L_{cy}}{r_y}\right)^2} \quad \text{(AISC } \textit{Spec.} \text{ Eq. E4-6)}$$
$$= \frac{\pi^2 (29{,}000 \text{ ksi})}{(49.0)^2}$$
$$= 119 \text{ ksi}$$

From the AISC *Shapes Database* V16.0 (2023b), $H = 0.915$ and $\bar{r}_o = 3.17$ in. Alternatively, AISC *Specification* Equations E4-8 and E4-9 can be used to calculate H and $\bar{r}_o^2$.

Calculate F_{ez} as follows.

$$F_{ez} = \left(\frac{\pi^2 EC_w}{L_{cz}^2} + GJ\right)\frac{1}{A_g \bar{r}_o^2} \quad \text{(AISC } \textit{Spec.} \text{ Eq. E4-7)}$$

$$= \left\{\frac{\pi^2 (29{,}000 \text{ ksi})(2.29 \text{ in.}^6)}{[(10 \text{ ft})(12 \text{ in./ft})]^2} + (11{,}200 \text{ ksi})(1.09 \text{ in.}^4)\right\}\left[\frac{1}{(8.96 \text{ in.}^2)(3.17 \text{ in.})^2}\right]$$

$$= 136 \text{ ksi}$$

Calculate $(F_e)_{FTB}$ as follows.

$$(F_e)_{FTB} = \left(\frac{F_{ey} + F_{ez}}{2H}\right)\left[1 - \sqrt{1 - \frac{4F_{ey}F_{ez}H}{(F_{ey} + F_{ez})^2}}\right] \quad \text{(AISC } \textit{Spec.} \text{ Eq. E4-3)}$$

$$= \left[\frac{119 \text{ ksi} + 136 \text{ ksi}}{2(0.915)}\right]\left[1 - \sqrt{1 - \frac{4(119 \text{ ksi})(136 \text{ ksi})(0.915)}{(119 \text{ ksi} + 136 \text{ ksi})^2}}\right]$$

$$= 97.8 \text{ ksi}$$

$$\frac{F_y}{(F_e)_{FTB}} = \frac{50.0 \text{ ksi}}{97.8 \text{ ksi}}$$

$$= 0.511 < 2.25$$

AISC *Specification* Equation E3-2 applies.

$$(F_n)_{FTB} = \left[0.658^{\frac{F_y}{F_e}}\right](F_y) \quad \text{(AISC } \textit{Spec.} \text{ Eq. E3-2)}$$

$$= \left[0.658^{(0.511)}\right](50 \text{ ksi})$$

$$= 40.4 \text{ ksi}$$

$$(F_n)_{FTB} = 40.4 \text{ ksi} > (F_n)_{FB} = 36.1 \text{ ksi}$$

Therefore, $F_n = (F_n)_{FB} = 36.1$ ksi.

Effective Area

Recall that $\lambda_w = \frac{d}{t_w} = 18.5 > (\lambda_r)_w = 18.1$. Therefore, the web element is slender.

$$\lambda_r\sqrt{\frac{F_y}{F_n}} = (18.1)\sqrt{\frac{50 \text{ ksi}}{36.1 \text{ ksi}}} \quad \text{(AISC } \textit{Spec.} \text{ Eq. E7-2)}$$

$$= 21.3$$

$$\lambda = 18.5 < \lambda_r\sqrt{\frac{F_y}{F_n}} = 21.3$$

AISC *Specification* Equation E7-2 applies. The stem is fully effective; $d_e = d = 6.95$ in. and $A_e = A = 8.96$ in.^{2}

$$P_n = F_n A_g$$

$$= (36.1 \text{ ksi})(8.96 \text{ in.}^2)$$

$$= 323 \text{ kips}$$

$$P_n/\Omega = 323 \text{ kips}/1.67$$

$$= 193 \text{ kips}$$

Required Flexural Strength, Including Second-Order Effects

In the following calculations, the available strength in compression of the eccentrically loaded member is referred to as $(P_{n\,ecc})/\Omega_c$. Note that this replaces P_a used in Equation 12 as well as in the interaction equations later.

The required moment in the member, including second-order effects, is calculated as follows.

First, calculate B_{1x}.

$$P_{e1x} = \frac{\pi^2 EI_x}{(L_{c1x})^2} \qquad \text{(AISC } \textit{Spec.} \text{ Eq. A-8-5)}$$

$$= \frac{\pi^2 (29{,}000 \text{ ksi})(28.9 \text{ in.}^4)}{\left[(10 \text{ ft})(12 \text{ in./ft})\right]^2}$$

$$= 574 \text{ kips}$$

and

$$B_{1x} = \frac{P_{e1x}}{P_{e1x} - 1.6P_a} \qquad (12)$$

$$= \frac{574 \text{ kips}}{574 \text{ kips} - 1.6\left(\frac{P_{n\,ecc}}{\Omega_b}\right)}$$

$$= \frac{359 \text{ kips}}{359 \text{ kips} - \left(\frac{P_{n\,ecc}}{\Omega_b}\right)}$$

Use Equation 1 to calculate the total load eccentricity as follows.

$$e = 0.5t_{pl} + \bar{y} \qquad (1)$$

$$= (0.50)(0.50 \text{ in.}) + 1.25 \text{ in.}$$

$$= 1.50 \text{ in.}\left(\frac{1 \text{ ft}}{12 \text{ in.}}\right)$$

$$= 0.125 \text{ ft}$$

Recall from Equation 11 that

$$M_{ax} = B_{1x}P_a e$$

$$= \left[\frac{359 \text{ kips}}{359 \text{ kips} - \left(\frac{P_{n\,ecc}}{\Omega_b}\right)}\right]\left(\frac{P_{n\,ecc}}{\Omega_b}\right)(0.125 \text{ ft})$$

$$= \frac{44.9\left(\frac{P_{n\,ecc}}{\Omega_b}\right)}{359 - \left(\frac{P_{n\,ecc}}{\Omega_b}\right)} \text{ kip-ft}$$

Check the Appropriate Interaction Equation for Combined Forces

Assume $\frac{\Omega_c P_a}{P_n} = \frac{\Omega_c}{P_n}\left(\frac{P_{n\,ecc}}{\Omega_c}\right) \geq 0.20$, and apply the ASD version of AISC *Specification* Equation H1-1a as follows. Set the interaction equation equal to unity (1.0) to find the member available eccentric axial compressive strength. Note that $\Omega_c = \Omega_b = 1.67$ and $M_{ay} = 0$. Also, recall that, $P_n/\Omega_c = 193$ kips, $M_{nx}/\Omega_b = 20.2$ kip-ft, and P_a is replaced by $\left(\frac{P_{n\,ecc}}{\Omega_b}\right)$.

$$\frac{P_a}{\left(\frac{P_n}{\Omega_c}\right)} + \frac{8}{9}\left[\frac{M_{ax}}{\left(\frac{M_{nx}}{\Omega_b}\right)} + \frac{M_{ay}}{\left(\frac{M_{ny}}{\Omega_b}\right)}\right] = \frac{\Omega_c P_a}{P_n} + \frac{8}{9}\left(\frac{\Omega_b M_{ax}}{M_{nx}} + 0\right) = 1.0$$

or

$$\frac{\Omega_c}{P_n}\left(\frac{P_{n\,ecc}}{\Omega_b}\right) + \frac{8}{9}\left(\frac{\Omega_b M_{ax}}{M_{nx}}\right) = 1.0$$

Insert values of available strengths and replace M_{ax} with its equivalent found earlier.

$$\frac{\left(\frac{P_{n\,ecc}}{\Omega_b}\right)}{193 \text{ kips}} + \frac{8\left[\frac{44.9\left(\frac{P_{n\,ecc}}{\Omega_b}\right)}{359 - \left(\frac{P_{n\,ecc}}{\Omega_b}\right)} \text{ kip-ft}\right]}{9(20.2 \text{ kip-ft})} = \frac{\left(\frac{P_{n\,ecc}}{\Omega_b}\right)}{193} + \left[\frac{1.98\left(\frac{P_{n\,ecc}}{\Omega_b}\right)}{359 - \left(\frac{P_{n\,ecc}}{\Omega_b}\right)} \text{ kip-ft}\right]$$

$$= 1.0$$

This is a quadratic equation with a root $\frac{P_{n\,ecc}}{\Omega_b} = 81.5$ kips (solution details not shown).

Check the value of B_{1x} using the equation developed previously.

$$B_{1x} = \frac{359 \text{ kips}}{359 \text{ kips} - \left(\frac{P_{n\,ecc}}{\Omega_b}\right)}$$

$$= \frac{359 \text{ kips}}{359 \text{ kips} - 81.5 \text{ kips}}$$

$$= 1.29 > 1.0 \quad \textbf{o.k.}$$

Check the assumption that $\frac{\Omega_c P_a}{P_n} = \frac{\Omega_c}{P_n}\left(\frac{P_{n\,ecc}}{\Omega_c}\right) \geq 0.20$.

$$\frac{\Omega_c P_a}{P_n} = \frac{\left(\frac{P_{n\,ecc}}{\Omega_b}\right)}{193 \text{ kips}}$$

$$= \frac{81.5 \text{ kips}}{193 \text{ kips}}$$

$$= 0.422 > 0.20 \quad \textbf{o.k.}$$

Had this assumption turned out to be incorrect, the solution would be repeated using AISC *Specification* Eq. H1-1b instead of AISC *Specification* Eq. H1-1a.

All assumptions made earlier were proven correct. Therefore, the available eccentric compressive strength of the WT7×30.5 compression member is $P_a = 81.5$ kips.

As a check, calculate the compressive strength of the gusset plate assuming that flexural buckling does not apply. See AISC *Specification* Section J4.4(a) and Equation J4-6.

$$\begin{aligned}(A_g)_{pl} &= (b)(t)\\ &= (10.0\text{ in.})(0.50\text{ in.})\\ &= 5.00\text{ in.}^2\end{aligned}$$

$$\begin{aligned}(P_n)_{pl} &= (F_y A_g)_{pl}\\ &= (50\text{ ksi})(5.00\text{ in.}^2)\\ &= 250\text{ kips}\end{aligned}$$

$$\begin{aligned}\left(\frac{P_n}{\Omega_c}\right)_{pl} &= \left(\frac{P_n}{1.67}\right)_{pl}\\ &= \frac{250\text{ kips}}{1.67}\\ &= 150\text{ kips} > 81.5\text{ kips}\end{aligned}$$

DEVELOPMENT OF EQUATIONS FOR THE DESIGN TABLE VALUES

Development of the equations for the available compressive strength of eccentrically loaded WT compression members, $\phi c P_{n\ ecc}$ (LRFD) or $(P_{n\ ecc})/\Omega c$ (ASD), including a second-order effect, based on the AISC *Specification* Section H1.1 provisions follows.

LRFD Method

Given the dominance of the axial force and that the bending moment present in the member is due to the load eccentricity, it is expected that in a majority of cases, the ratio $P_u/\phi_c P_n \geq 0.20$.

When $\dfrac{P_u}{\phi_c P_n} \geq 0.20$, the LRFD version of AISC *Specification* Equation H1-1a applies as follows.

$$\frac{P_u}{\phi_c P_n} + \frac{8}{9}\left(\frac{M_{ux}}{\phi_b M_{nx}} + \frac{M_{uy}}{\phi_b M_{ny}}\right) \leq 1.0 \qquad \text{(AISC } \textit{Spec.}\text{ Eq. H1-1a)}$$

To obtain the available compressive strength of the eccentrically loaded member, set the preceding interaction equation equal to 1.0. At the same time, note that there is no bending about the *y*-axis of the member; therefore, $M_{uy} = 0$. AISC *Specification* Equation H1-1a then simplifies to the following.

$$\frac{P_u}{\phi_c P_n} + \frac{8}{9}\left(\frac{M_{ux}}{\phi_b M_{nx}}\right) = 1.0 \qquad (13)$$

Recall from Equation 5 that,

$$M_{ux} = B_{1x} P_u e \qquad (5)$$

Replace P_u with $\phi_c P_{n\ ecc}$ in Equation 5.

$$M_{ux} = B_{1x}\left(\phi_c P_{n\,ecc}\right)e \qquad (14)$$

Substituting M_{ux} from Equation 14 and replacing P_u with $\phi_c P_{n\ ecc}$ into Equation 13, we obtain the following.

$$\begin{aligned}\frac{\phi_c P_{n\ ecc}}{\phi_c P_n} + \frac{8}{9}\left[\frac{B_{1x}(\phi_c P_{n\ ecc})e}{\phi_b M_{nx}}\right] &= (\phi_c P_{n\ ecc})\left(\frac{1}{\phi_c P_n} + \frac{8B_{1x}e}{9\phi_b M_{nx}}\right)\\ &= 1.0\end{aligned} \qquad (15)$$

Equation 15 is simplified to the following.

$$(\phi_c P_{n\ ecc})\left(\frac{9\phi_b M_{nx} + 8B_{1x}e\phi_c P_n}{9\phi_c P_n \phi_b M_{nx}}\right) = 1.0 \qquad (16)$$

or

$$\phi_c P_{n\ ecc} = \left(\frac{9\phi_c P_n \phi_b M_{nx}}{9\phi_b M_{nx} + 8B_{1x}e\phi_c P_n}\right) \qquad (17)$$

Simplify Equation 17 using $\phi_b = \phi_c = 0.90$ to obtain the following equation, which is in terms of nominal strengths only. Note that this is still an LRFD equation.

$$\phi_c P_{n\ ecc} = \frac{8.1 P_n M_{nx}}{9M_{nx} + 8B_{1x}P_n e} \qquad (18)$$

When $\frac{P_u}{\phi_c P_n} = \frac{\phi_c P_{n\ ecc}}{\phi_c P_n} < 0.20$, the LRFD version of AISC *Specification* Equation H1-1b applies, and the following equation is developed.

$$\phi_c P_{n\ ecc} = \frac{1.8 P_n M_{nx}}{M_{nx} + 2B_{1x} P_n e} \tag{19}$$

ASD Method

A process similar to the one used for the LRFD method leads to the following equations for the eccentric available compressive strength of the member (details not shown).

When $\frac{\Omega_c P_a}{P_n} = \frac{\Omega_c \left(\frac{P_{n\ ecc}}{\Omega_c} \right)}{P_n} \geq 0.20$,

$$\left(\frac{P_{n\ ecc}}{\Omega_c} \right) = \frac{P_n M_{nx}}{1.67 M_{nx} + 1.48 B_{1x} P_n e} \tag{20}$$

When $\frac{\Omega_c \left(\frac{P_{n\ ecc}}{\Omega_c} \right)}{P_n} < 0.20$,

$$\left(\frac{P_{n\ ecc}}{\Omega_c} \right) = \frac{P_n M_{nx}}{0.835 M_{nx} + 1.67 B_{1x} P_n e} \tag{21}$$

Values of P_n and M_{nx} are calculated based on the appropriate provisions of the AISC *Specification* as listed in Table 1.

DEVELOPMENT OF THE DESIGN TABLE

Equations developed earlier are summarized in Table 2. These equations were used in the development of the proposed design table (Table 4).

Note that e, P_n, P_{e1x}, and M_{nx} are all known values. The only unknown in the equations of Table 2 is the desired available compressive strength, $\phi_c P_{n\ ecc}$ (LRFD) or $(P_{n\ ecc})/\Omega_c$ (ASD).

Equations for $\phi_c P_{n\ ecc}$ or $(P_{n\ ecc})/\Omega_c$ are all a function of B_{1x}, which itself is a function of the available eccentric axial load $\phi_c P_{n\ ecc}$ or $(P_{n\ ecc})/\Omega_c$. Therefore, equations of Table 2 are all quadratic equations in terms of available strengths $\phi_c P_{n\ ecc}$ or $(P_{n\ ecc})/\Omega_c$. For example, the quadratic equation for case 1 of Table 2 is as follows.

$$9M_{nx}(\phi_c P_{n\ ecc})^2 - (\phi_c P_{n\ ecc})(9M_{nx}P_{e1x} + 8eP_nP_{e1x} + 8.1P_nM_{nx}) + 8.1P_nM_{nx}P_{e1x} = 0 \tag{22}$$

with

$$\phi_c P_{n\ ecc} = \frac{(9M_{nx}P_{e1x} + 8eP_nP_{e1x} + 8.1P_nM_{nx}) \pm \sqrt{(9M_{nx}P_{e1x} + 8eP_nP_{e1x} + 8.1P_nM_{nx})^2 - 4(9M_{nx})(8.1P_nM_{nx}P_{e1x})}}{18M_{nx}} \tag{23}$$

Given the complexity of the quadratic equations for $\phi_c P_{n\ ecc}$ or $(P_{n\ ecc})/\Omega_c$ such as Equation 22 and its solution, Equation 23, it was decided to use an iterative process to find the available strengths $\phi_c P_{n\ ecc}$ or $(P_{n\ ecc})/\Omega_c$ using a spreadsheet. The procedure used is as follows.

1. Calculate $\phi_c P_{n\ ecc}$ or $(P_{n\ ecc})/\Omega_c$ using the equation for case 1 (LRFD) or 3 (ASD) from Table 2; initially, use $B_{1x} = 1.0$.
2. Use the value of $\phi_c P_{n\ ecc}$ or $(P_{n\ ecc})/\Omega_c$ found in step 1 to calculate a new B_{1x} using Equation 7 (LRFD) or 12 (ASD).
3. Use this new value of B_{1x} in the equation for case 1 (LRFD) or 3 (ASD) from Table 2 to calculate a new value for $\phi_c P_{n\ ecc}$ or $(P_{n\ ecc})/\Omega_c$.
4. Use the value of $\phi_c P_{n\ ecc}$ or $(P_{n\ ecc})/\Omega_c$ found in step 3 to calculate a new B_{1x} using Equation 7 (LRFD) or 12 (ASD).
5. Repeat this process until the values of $\phi_c P_{n\ ecc}$ or $(P_{n\ ecc})/\Omega_c$ and B_{1x} stabilize.

If calculations resulted in $\frac{\phi_c P_{n\ ecc}}{\phi_c P_n} < 0.20$ (LRFD) or $\frac{\Omega_c \left(\frac{P_{n\ ecc}}{\Omega_c} \right)}{P_c} < 0.20$ (ASD), equations in case 2 (LRFD) or case 4 (ASD) of Table 2 were used as appropriate. In the worst-case scenario, seven iterations were used in the spreadsheet to calculate the tabulated $\phi_c P_{n\ ecc}$ or $(P_{n\ ecc})/\Omega_c$ values with the largest difference between $\phi_c P_{n\ ecc}$ or $(P_{n\ ecc})/\Omega_c$ of the last two iterations being 0.68%.

Tabulated member strengths were calculated in the spreadsheet for effective lengths of 0 to 40 ft at 1 ft increments. However, the design table skips some unbraced lengths due to limited space per page as is the case in AISC *Manual* tables.

Table 4 values follow the practice of using three significant figures. For more information on this topic as well as on the use of interpolation between tabulated values see the section titled Using the Manual Tables in Part 2 of the AISC *Manual*.

Table 1. Applicable Limit States and Appropriate Provisions/Equations of the AISC *Specification*[1]		
Limit State[2]	**AISC *Specification* Provisions**	**AISC *Specification* Equation**
Flexure[3]		
Yielding	F9.1	F9-1 to F9-3
Flange local buckling[4]	F9.3(a)(2)	F9-14
Lateral torsional buckling	F9.2(a)(1) to F9.2(a)(3)	F9-6 to F9-11
Compression		
Flexural buckling	E3	E3-1 to E3-4
Stem local buckling[5]	E7.1	E7-1 to E7-5
Flexural-torsional buckling	E4(b)	E4-1, E4-3, and E4-5 to E4-9[6]

[1] For WT shapes made from column section listed in AISC *Manual* Table 4-1a.
[2] For $F_y = 50$ ksi.
[3] Stem in tension for flexure.
[4] Only WT7×49.5, WT7×45, WT6×32.5, and WT4×15.5 have noncompact flange elements under flexural compression. There are no WT shapes among those under consideration with slender flange elements under flexural compression.
[5] Only WT7×30.5, WT7×26.5, WT7×24, WT7×21.5, and WT6×20 have slender stems under axial compression. There are no WT shapes among those under consideration with slender flange element under axial compression.
[6] Values of r_o and H are listed in the AISC *Shapes Database*, but not in AISC *Manual* Table 1-8.

Table 2. Equations for Calculating the Available Eccentric Axial Compressive Strength of WTs			
Case	**Axial Load Ratio, $\frac{P_r}{P_c}$**	**Equation**	
LRFD Method[a]			
1	$\frac{\phi_c P_{n\,ecc}}{\phi_c P_n} \geq 0.20$	$\phi_c P_{n\,ecc} = \frac{8.1 P_n M_{nx}}{9M_{nx} + 8B_{1x}P_n e}$	(Eq. 18)
2	$\frac{\phi_c P_{n\,ecc}}{\phi_c P_n} < 0.20$	$\phi_c P_{n\,ecc} = \frac{1.8 P_n M_{nx}}{M_{nx} + 2B_{1x}P_n e}$	(Eq. 19)
ASD Method[b]			
3	$\frac{\Omega_c\left(\frac{P_{n\,ecc}}{\Omega_c}\right)}{P_n} \geq 0.20$	$\left(\frac{P_{n\,ecc}}{\Omega_c}\right) = \frac{P_n M_{nx}}{1.67M_{nx} + 1.48B_{1x}P_n e}$	(Eq. 20)
4	$\frac{\Omega_c\left(\frac{P_{n\,ecc}}{\Omega_c}\right)}{P_n} < 0.20$	$\left(\frac{P_{n\,ecc}}{\Omega_c}\right) = \frac{P_n M_{nx}}{0.835M_{nx} + 1.67B_{1x}P_n e}$	(Eq. 21)

[a] $B_{1x} = \frac{P_{e1x}}{P_{e1x} - \phi_c P_{n\,ecc}}$ LRFD (Eq. 7: P_u replaced with $\phi_c P_{n\,ecc}$)

[b] $B_{1x} = \frac{P_{e1x}}{P_{e1x} - 1.6\left(\frac{P_{n\,ecc}}{\Omega_c}\right)}$ ASD (Eq. 12: P_a replaced with $P_{n\,ecc}/\Omega_c$)

ESTABLISHING THE GUSSET PLATE DIMENSIONS FOR DEVELOPMENT OF THE DESIGN TABLE

For the purposes of connection design, it was decided that the gusset plate width will be the same as b_f, the flange width of the connected WT. Larger plate widths may be selected with no adverse effects.

It is convenient to use a standard such as a multiple of the WT's flange thickness, t_f, for the plate thickness in developing Table 4.

In the first round of calculating the available strengths, a gusset plate thickness of $t_{pl} = 1.5t_f$ was used, where t_f is the thickness of the WT flange. This is a similar approach to the development of AISC *Manual* Table 4–12, Available Strength in Axial Compression, Eccentrically Loaded Single Angles, where $t_{pl} = 1.5t$ was used with t being the thickness of the angle.

Using $t_{pl} = 1.5t_f$ resulted in plate thicknesses that were unreasonably large. The fact is that load eccentricity significantly reduces the available strength of WT compression members. Therefore, the $t_{pl} = 1.5t_f$ assumption resulted in considerably overdesigned plates. Further, a larger plate thickness results in a larger eccentricity (see Equation 1) and leads to a lower available compressive strength of the member.

Several plate thicknesses were tried in the spreadsheet to calculate the available compressive strength while ensuring that the plate had sufficient compressive strength to resist the applied load. This process involved taking the largest available strength of each member and calculating the required plate thickness to resist this load using F_y = 50 ksi and assuming that the gusset plate is as wide as b_f of the WT. In the end, it was determined that a standard plate thickness $t_{pl} = 0.6t_f$ works for all shapes. The calculated values of plate thicknesses were then rounded up to practical plate thicknesses considering availability.

The thickest plate needed based on the preceding approach is 3¾ in. (for WT7×436.5), which still meets the thickness limitations of plates available in the preferred material specification (A572/A572M Grade 50 steel) per AISC *Manual* Table 2–5.

LIMITATIONS OF UNBRACED LENGTHS

As discussed earlier under the section titled "Clarification of Laterally Unbraced Lengths for WT Compression Members," the laterally unbraced length for flexural buckling about the y-axis, L_y, and the laterally unbraced length for lateral torsional buckling, L_b, are equal ($L_y = L_b$).

Further, all equations of Table 2 include P_n, the nominal concentric compressive strength of the member. P_n itself depends on both L_{cx} and L_{cy}. Therefore, it was assumed in the development of the table that $L_{cx} = L_{cy}$. Otherwise, the table would be three-dimensional. In summary, the values of Table 4 assume that $L_{cx} = L_{cy} = L_{cz} = L_b$. Note that based on the member end connections, $K_x = K_y = K_z = 1.0$. Therefore, laterally unbraced lengths and the corresponding effective lengths are equal, namely, $L_{cx} = L_x$, $L_{cy} = L_y$, and $L_{cz} = L_z$.

There is no interaction between the member strength for flexural torsional buckling about x-axis versus the y-axis and z-axis buckling. The values of Table 4 are all based on L_{cx} which governs member strength in all cases.

ASSUMPTIONS MADE IN THE DEVELOPMENT OF THE DESIGN TABLE VALUES

The following is a list of assumptions made in the development of the design table.

1. WTs considered are those made from W-shapes ordinarily used as columns per AISC *Manual* Table 4–1a (some very large shapes excluded).
2. ASTM A992/A992M (F_y = 50 ksi) steel is used for WT shapes.
3. The width of the gusset plate was taken as the flange width, b_f, of the connected WT shape. Wider plates may be used without adverse effect.
4. Plates are of A572/A572M Grade 50 steel.
5. The gusset plates have a thickness of about $t_{pl} = 0.6t_f$, where t_f is the thickness of the flange of the WT member. Plate thicknesses used and identified at the top of each column in Table 4 were rounded up to the next practical available plate thickness.
6. The compression load is applied at the mid-width of the flange of the WT and at mid-thickness of the gusset plate.
7. No transverse loads are applied between the member ends.
8. The member is braced against lateral displacement at the ends only.
9. There is no relative lateral translation of the member ends ($P_{lt} = M_{lt} = 0$) and thus no P-D effect.
10. There is no bending about the y-axis of the member.
11. Based on the end connections described earlier, the member will act as pinned at the ends for flexural and flexural-torsional buckling limit states ($K_x = K_y = K_z$ = 1.0).
12. Unbraced lengths are identified as follows.
    a. For flexural buckling, L_{cx} and L_{cy}, ft (mm).
    b. For flexural-torsional buckling, L_{cz}, ft (mm).

c. For lateral-torsional buckling, L_b, ft (mm).

d. $L_{cx} = L_{cy} = L_{cz} = L_b$, ft (mm).

13. Design of the member end connections, including bolted or welded joints between the gusset plates and the flange of the WT compression member, is not addressed in this article. It is assumed that the designer will establish appropriate designs for those components.

14. Member weight is not accounted for in the development of the design table as is the case with AISC *Manual* tables.

OBSERVATIONS FROM THE DATA

Variation of Nominal Flexural Strength (M_n) and Nominal Compressive Strengths (P_n)

The nominal flexural strengths, M_n, of the WT members considered over the unbraced lengths 0 ft ≤ L_b ≤ 40 ft do not change significantly (Figure 7). But their nominal concentric compressive strengths, P_n, follow the typical pattern of singly symmetric compression members with considerable change of strength over the range of the unbraced lengths with flexural-torsional buckling governing over very short unbraced lengths.

Generally, the values of L_r for WT flexural members are unusually large. Among the WT members considered in this study, the smallest value of L_r is 89.5 ft, which is far larger than any practical unbraced length. This is consistent with AISC *Specification* Commentary Section F9, Tees and Double Angles Loaded in the Plane of Symmetry, which states, "For most shapes, the length, L_r, is impractically long." Therefore, it can be concluded that elastic lateral torsional buckling limit state does not govern the design of any of the WT shapes and for the range of unbraced lengths (0 ft ≤ L_b ≤ 40 ft) considered in this study.

Per AISC *Specification* Equation F9-6, the slope of the chart for the nominal flexural strength, M_n, over the range $L_p < L_b \le L_r$ of the WTs considered is very shallow. In all but a few cases (WT7×213 to WT7×436.5), the slope of this portion of the chart is less than 0.10 kip-ft/ft. In other words, while the nominal flexural strength, M_n, remains

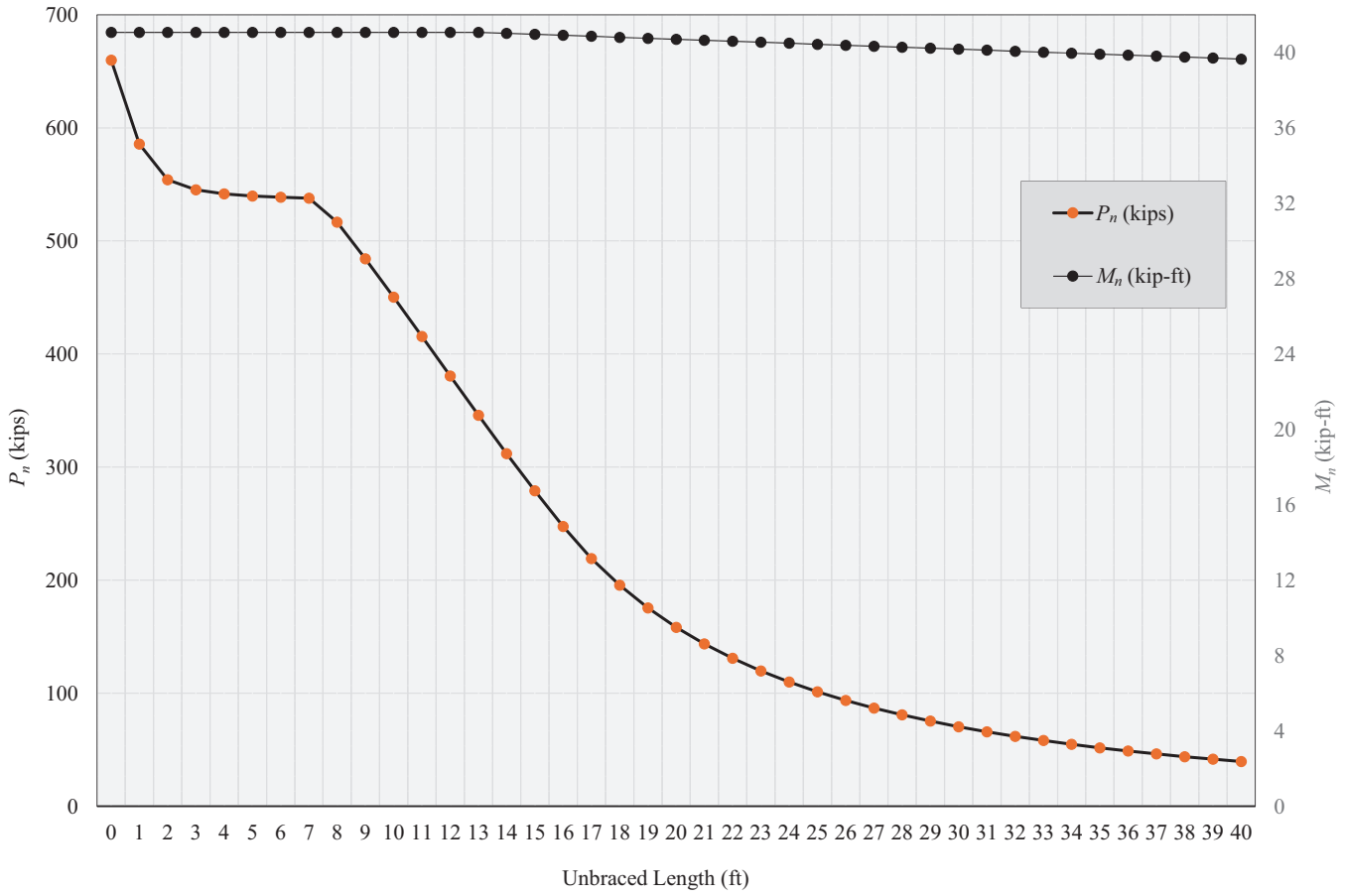

Fig. 7. Variations of P_n *and* M_n *versus unbraced length for a* WT7×45.

Table 3. Sample Variation of M_n Over the Range $0 \le L_b \le 40$ ft			
	(kip-ft)		
Shape	$L_b = 0$ ft	$L_b = 40$ ft	Change (%)
WT7×436.5	873	868	0.576
WT7×199	251	248	1.21
WT7×96.5	96.0	94.4	1.69
WT5×24.5	15.9	15.1	5.29
WT4×15.5	8.53	7.89	8.11

constant over the range $L_b \le L_p$, it does not change considerably over the range $L_b > L_P$ either. Table 3 provides five examples over the range of heavy to light WT sections.

The largest change in M_n among all members over 0 ft $\le L_b \le 40$ ft is WT7×21.5 with $M_n = 26.5$ kip-ft at $L_b = 0$ ft and $M_n = 22.5$ kip-ft at $L_b = 40$ ft with a change in M_n of 17.8% (Figure 8). Based on the preceding discussion, it can be stated that for the WT shapes considered and for unbraced lengths used ($0 \le L_b \le 40$ ft), the values of the nominal flexural strength, M_n, are significantly less dependent on the unbraced length L_b than values of P_n are dependent on L_c.

The available strengths of WTs listed in Table 4 are functions of nominal flexural strength, M_n, and nominal (concentric) axial compressive strength, P_n, with the assumptions that $L_{cx} = L_{cy} = L_{cz} = L_b$. Under these circumstances, the available strength in compression based on L_{cx} governs for all shapes and values of unbraced length considered.

Variation of Available Eccentric Axial Compressive Strength versus Effective Length

The general shape of the charts for the available eccentric axial compressive strengths of WTs is similar to those

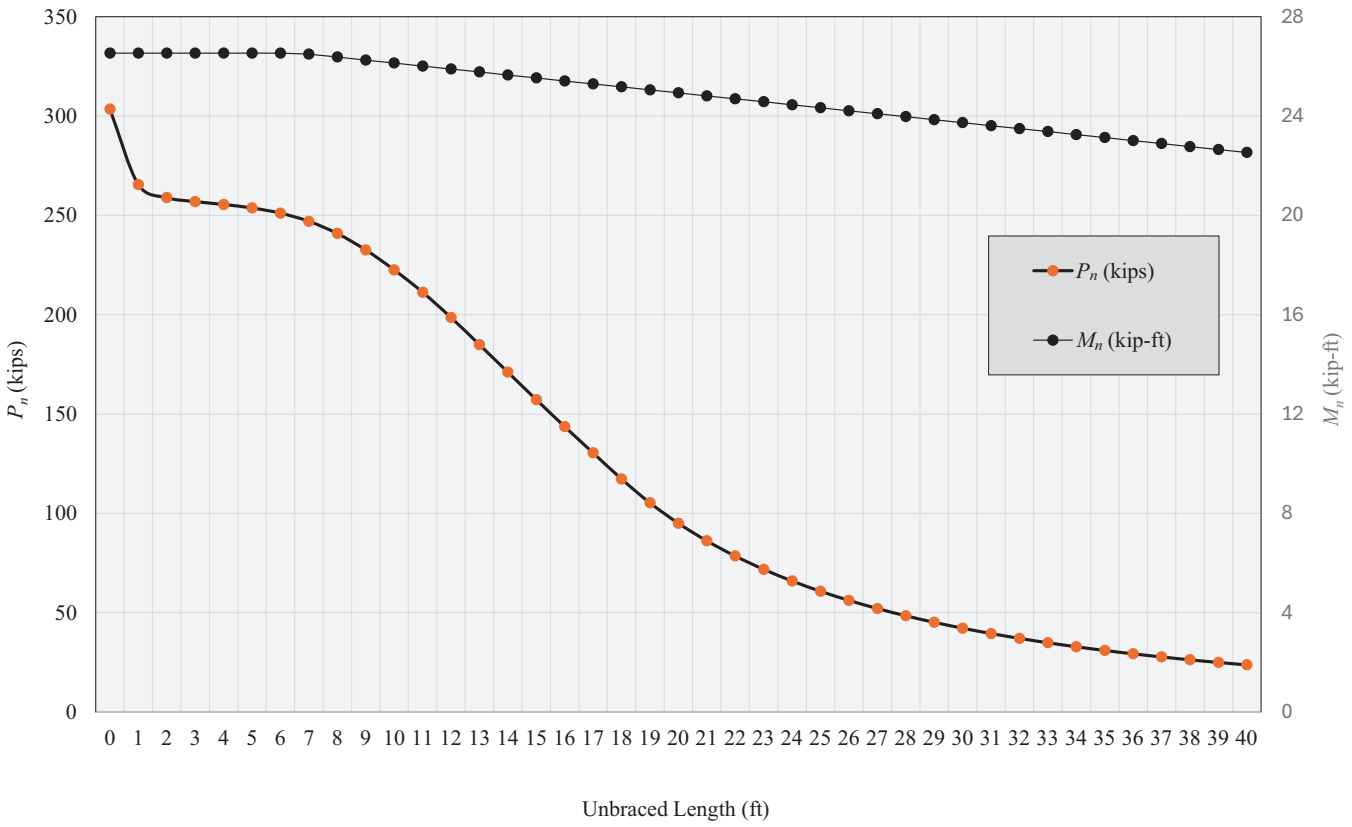

Fig. 8. Variations of P_n *and* M_n *versus unbraced length for a WT7×21.5 (worst-case scenario.)*

of members subject to concentric axial load. The available strength is reduced as the effective unbraced length increases. Further, the strength charts have similar curvature to concentrically loaded members—concave down over shorter unbraced lengths and concave up for larger lengths indicating inelastic and elastic flexural buckling. Figure 9 shows charts of the available eccentric axial compressive strengths of a number of WT members with relatively light to relatively heavy weights over the slenderness ratio range $L_c/r \leq 200$.

Cost of Eccentricity

As expected, there is a cost for applying the axial compressive load eccentrically to WT members. The load eccentricity causes bending moment in the member, reducing its remaining available strength in axial compression. For example, an 8-ft-long WT7×185 has an available concentric compressive strength $\phi_c P_n$ = 2,080 kips. However, for the same conditions, the available eccentric axial compressive strength is 589 kips, resulting in a ratio of available eccentric to concentric axial compressive strength of 0.283, reflecting a severe penalty due to the eccentricity.

Figure 10 shows the charts for available axial compressive strengths for concentric and eccentric loads applied to a WT7×185 compression member. Figure 11 shows the variation of the ratio of the available eccentric to concentric axial compressive strength of a WT7×185 over unbraced lengths between zero and 40 ft.

The cost of eccentricity is related to the member size and its unbraced length with it being considerably higher for heavy shapes with short unbraced lengths. In such cases, the high axial compressive strength causes large bending moments due to load eccentricity, leaving less available compressive strength for an eccentric load.

As observed from Figure 9, the ratios of eccentric to concentric available compressive strengths ranges from a minimum of 26.9% to 60.1% for a WT7×185, with the lowest values belonging to smaller unbraced lengths. For all members considered, the ratios of the available eccentric to concentric axial compressive strength ranged from a minimum of 0.184 to a maximum of 0.876. As the slenderness ratio increases, the effect of eccentricity is reduced, and flexural buckling strength becomes more dominant.

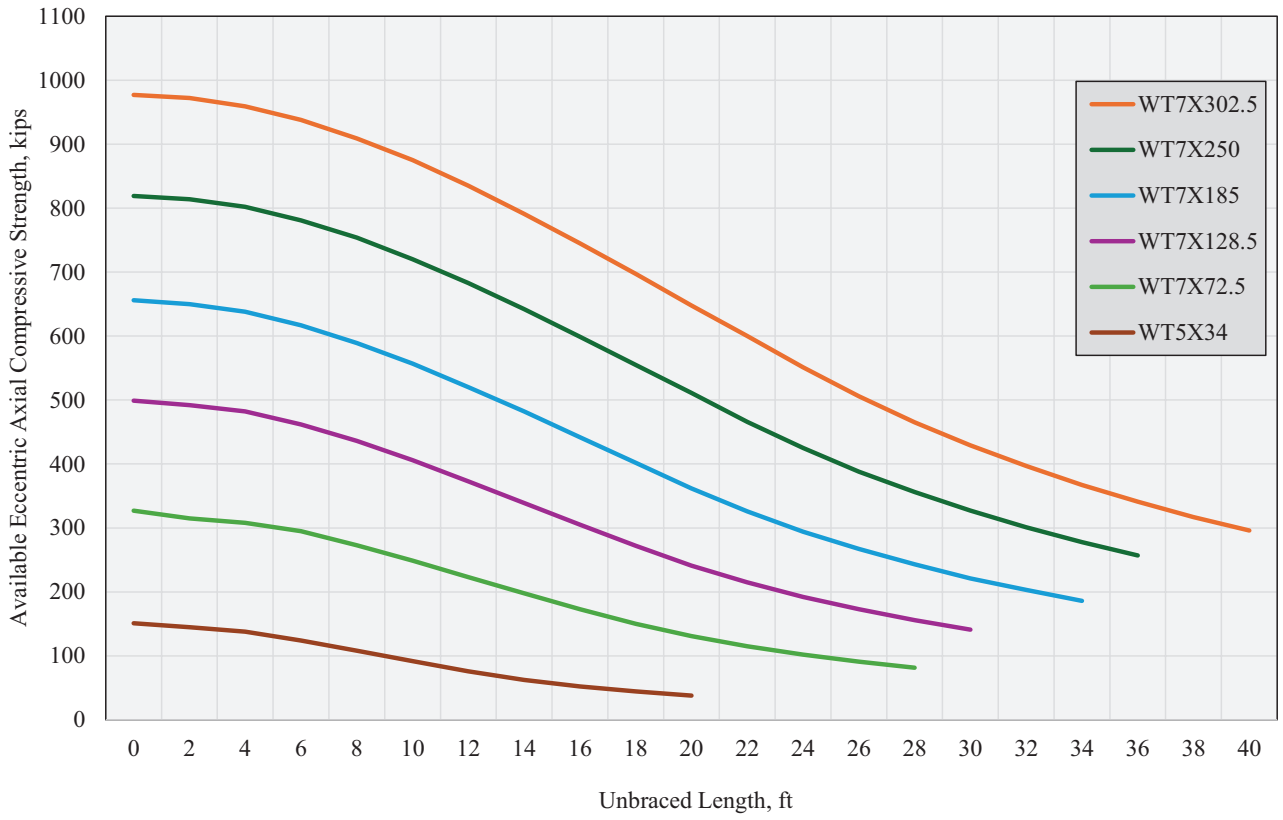

Fig. 9. Sample available strengths of eccentrically loaded WT compression members for $L_c/r \leq 200$.

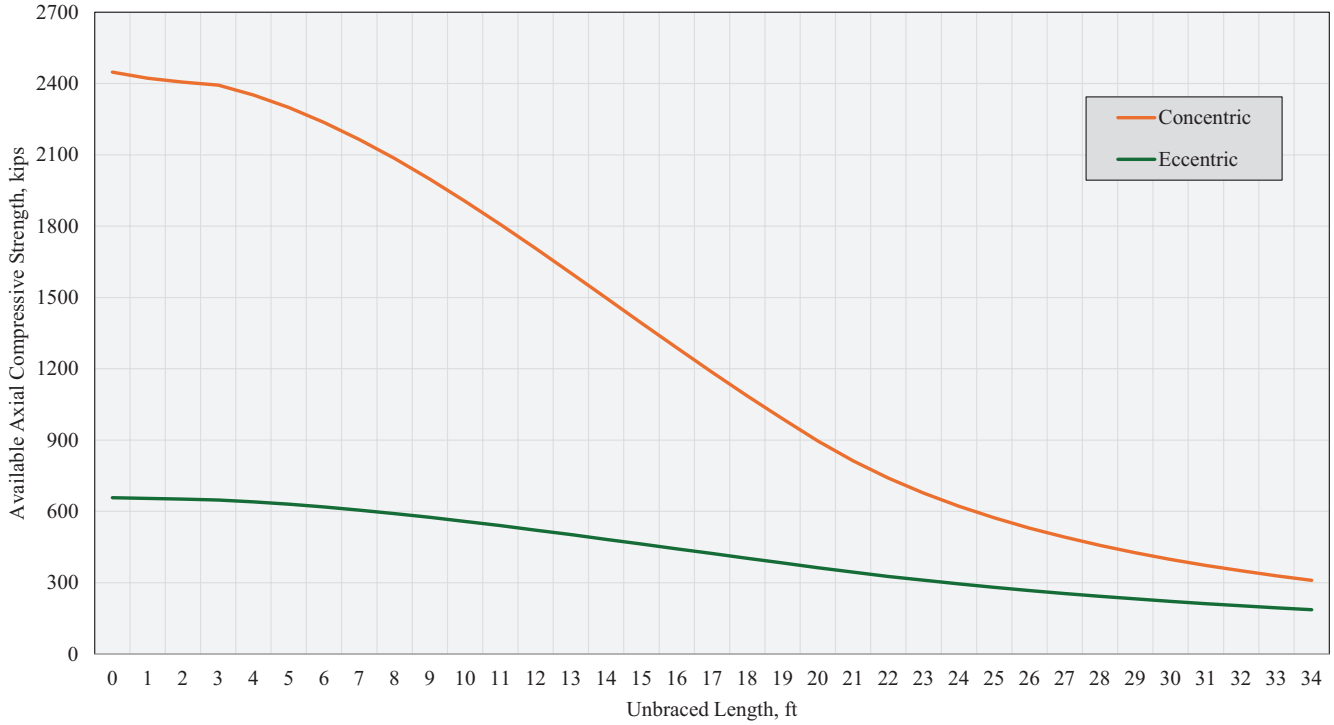

Fig. 10. Available concentric and eccentric axial compressive strengths of WT7×185.

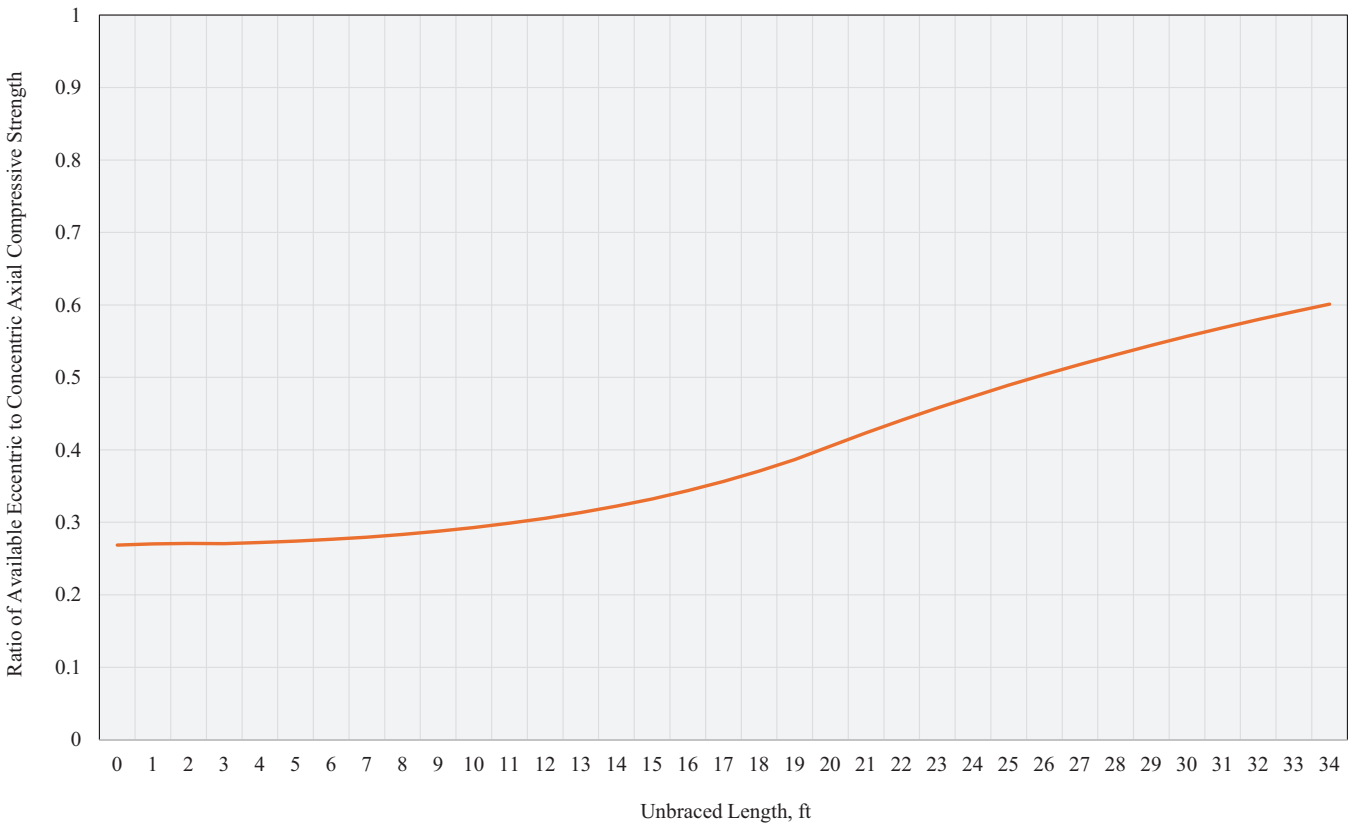

Fig. 11. Ratios of available eccentric to concentric axial compressive strengths of WT7×185.

Table 4

Available Strength
Axial Compression, kips
Eccentrically Loaded WT-Shapes

$F_y = 50$ ksi

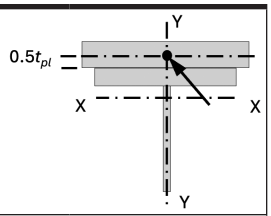

Shape		WT7×											
lb/ft		436.5[h]		404[h]		365[h]		332.5[h]		302.5[h]		275[h]	
t_{pl} (in.)		3¾		3½		3¼		3		2¾		2½	
Design		P_n/Ω_c	$\phi_c P_n$	P_n/Ω_c	$\phi_c P_n$	P_n/Ω_c	$\phi_c P_n$	P_n/Ω_c	$\phi_c P_n$	P_n/Ω_c	$\phi_c P_n$	P_n/Ω_c	$\phi_c P_n$
		ASD	LRFD	ASD	LRFD	ASD	LRFD	ASD	LRFD	ASD	LRFD	ASD	LRFD
$L_{cx} = L_{cy} = L_{cz} = L_b$, ft	0	933	1400	871	1310	769	1150	708	1060	652	977	603	904
	1	932	1400	870	1300	768	1150	707	1060	650	975	602	902
	2	930	1390	868	1300	766	1150	705	1060	648	972	600	899
	3	926	1390	864	1300	762	1140	701	1050	645	967	596	894
	4	920	1380	858	1290	757	1140	696	1040	639	959	591	886
	5	913	1370	851	1280	750	1130	689	1030	633	950	584	877
	6	905	1360	842	1270	742	1110	681	1020	625	938	576	865
	8	884	1330	821	1230	722	1090	661	994	605	909	556	836
	10	858	1290	796	1200	698	1050	637	959	581	875	532	801
	12	828	1250	766	1150	670	1010	609	919	553	835	505	762
	14	794	1200	733	1110	639	964	579	874	524	791	476	719
	16	758	1150	697	1050	606	915	547	827	492	745	445	674
	18	721	1090	660	999	571	864	513	777	460	697	413	627
	20	681	1030	622	943	535	812	479	726	427	648	382	580
	22	641	973	583	885	500	759	444	675	394	600	350	533
	24	601	913	544	827	464	706	410	624	362	551	320	487
	26	561	854	506	770	429	652	377	575	332	506	292	445
	28	522	794	468	713	396	603	348	530	305	465	268	409
	30	485	738	434	662	367	559	321	490	281	429	246	376
	32	451	687	403	615	340	518	297	454	260	397	227	347
	34	420	641	375	572	316	482	276	421	241	367	210	321
	36	392	599	350	534	294	449	256	391	223	341	194	297
	38	367	560	327	499	274	419	239	365	208	317	181	276
	40	344	525	306	467	256	392	223	341	193	296		
Properties													
A_g, in.^{2}		129		119		107		97.8		89.0		80.9	
r_x, in.		2.84		2.75		2.62		2.52		2.43		2.34	
r_y, in.		4.89		4.82		4.69		4.62		4.55		4.49	
r_x/r_y		0.581		0.571		0.559		0.545		0.534		0.521	

ASD	LRFD
$\Omega_b = 1.67$	$\phi_b = 0.90$
$\Omega_c = 1.67$	$\phi_c = 0.90$

[h] Flange thickness is greater than 2 in. Special requirements may apply per AISC *Specification* Section A3.1d.

Note: Heavy line indicates L_c/r_y equal to or greater than 200.

Table 4 (continued)

Available Strength
Axial Compression, kips
Eccentrically Loaded WT-Shapes

$F_y = 50$ ksi

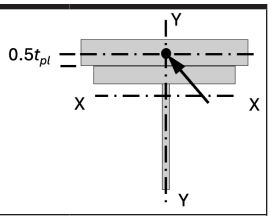

Shape		WT7×											
lb/ft		250[h]		227.5[h]		213[h]		199[h]		185[h]		171[h]	
t_{pl} (in.)		2½		2¼		2		2		1¾		1¾	
Design		P_n/Ω_c	$\phi_c P_n$	P_n/Ω_c	$\phi_c P_n$	P_n/Ω_c	$\phi_c P_n$	P_n/Ω_c	$\phi_c P_n$	P_n/Ω_c	$\phi_c P_n$	P_n/Ω_c	$\phi_c P_n$
		ASD	LRFD	ASD	LRFD	ASD	LRFD	ASD	LRFD	ASD	LRFD	ASD	LRFD
$L_{cx} = L_{cy} = L_{cz} = L_b$, ft	0	546	819	509	763	487	731	455	683	437	656	405	608
	1	545	817	508	761	486	729	454	681	436	653	403	605
	2	543	814	506	758	484	725	452	678	433	650	401	602
	3	540	809	502	754	480	721	449	673	430	646	398	598
	4	534	802	497	746	475	713	443	666	425	638	393	590
	5	528	793	490	737	468	703	437	656	418	629	387	581
	6	520	781	483	725	460	692	429	645	410	617	379	570
	8	501	754	463	698	441	664	411	618	391	589	361	544
	10	478	720	441	664	418	630	388	586	369	557	339	512
	12	452	683	415	627	392	593	364	550	344	520	316	477
	14	424	642	388	587	365	553	338	511	318	482	291	441
	16	395	599	359	545	337	511	311	471	291	442	265	403
	18	366	555	331	502	309	469	284	431	264	402	240	365
	20	336	511	302	459	281	427	257	391	238	362	215	328
	22	306	466	274	417	254	386	232	353	214	326	193	295
	24	279	425	249	379	230	350	209	319	193	294	174	266
	26	255	388	226	345	209	318	190	290	175	267	158	241
	28	233	356	207	316	190	290	173	264	159	243	143	219
	30	214	327	189	289	174	266	158	242	145	221	130	199
	32	197	301	174	266	160	244	145	222	132	203	119	182
	34	182	278	160	245	147	225	133	204	122	186		
	36	168	257	148	227								
	38												
	40												

Properties						
A_g, in.^{2}	73.5	66.9	62.7	58.4	54.4	50.3
r_x, in.	2.26	2.19	2.14	2.10	2.05	2.01
r_y, in.	4.43	4.38	4.34	4.31	4.27	4.24
r_x/r_y	0.510	0.500	0.493	0.487	0.480	0.474

ASD	LRFD
$\Omega_b = 1.67$	$\phi_b = 0.90$
$\Omega_c = 1.67$	$\phi_c = 0.90$

[h] Flange thickness is greater than 2 in. Special requirements may apply per AISC *Specification* Section A3.1d.

Note: Heavy line indicates L_c/r_y equal to or greater than 200.

Table 4 (continued)

Available Strength
Axial Compression, kips
Eccentrically Loaded WT-Shapes

$F_y = 50$ ksi

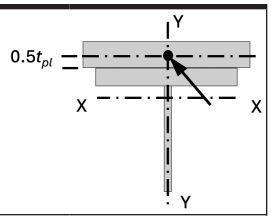

Shape		WT7×											
lb/ft		155.5[h]		141.5[h]		128.5		116.5		105.5		96.5	
t_{pl} (in.)		1½		1½		1¼		1¼		1¼		1	
Design		P_n/Ω_c	$\phi_c P_n$	P_n/Ω_c	$\phi_c P_n$	P_n/Ω_c	$\phi_c P_n$	P_n/Ω_c	$\phi_c P_n$	P_n/Ω_c	$\phi_c P_n$	P_n/Ω_c	$\phi_c P_n$
		ASD	LRFD	ASD	LRFD	ASD	LRFD	ASD	LRFD	ASD	LRFD	ASD	LRFD
$L_{cx} = L_{cy} = L_{cz} = L_b$, ft	0	382	573	350	525	333	499	304	456	279	418	268	402
	1	380	570	348	522	330	495	301	452	276	414	265	397
	2	378	567	346	518	328	492	299	449	274	411	262	393
	3	375	563	343	515	325	488	296	445	271	407	259	389
	4	370	556	338	508	321	482	293	440	268	403	256	385
	5	364	547	332	499	314	473	287	431	262	394	251	377
	6	356	535	325	488	307	462	279	420	256	385	244	367
	8	338	509	307	463	289	436	262	396	239	361	227	343
	10	316	477	287	433	268	406	243	367	221	334	209	316
	12	292	442	264	400	246	373	222	337	201	305	189	287
	14	268	406	241	366	223	339	201	305	181	276	169	258
	16	243	369	218	332	201	305	180	273	162	246	150	228
	18	219	333	195	297	178	272	159	242	142	217	131	200
	20	195	297	174	265	158	241	140	214	126	192	115	176
	22	174	266	155	237	141	215	125	190	111	170	102	156
	24	157	239	139	212	126	192	111	170	99	152	90.7	139
	26	141	216	125	191	113	173	100	153	89.0	136	81.1	124
	28	128	196	113	173	102	156	90.0	138	80.2	123	72.9	112
	30	116	178	103	158	92.4	141	81.5	125	72.5	111		
	32	106	162	93.9	144								
	34												
	36												
	38												
	40												

Properties						
A_g, in.^{2}	45.7	41.6	37.8	34.2	31.0	28.4
r_x, in.	1.96	1.92	1.88	1.84	1.81	1.78
r_y, in.	4.20	4.17	4.13	4.10	4.07	4.05
r_x/r_y	0.467	0.460	0.455	0.449	0.445	0.440

ASD	LRFD
$\Omega_b = 1.67$	$\phi_b = 0.90$
$\Omega_c = 1.67$	$\phi_c = 0.90$

[h] Flange thickness is greater than 2 in. Special requirements may apply per AISC *Specification* Section A3.1d.

Note: Heavy line indicates L_c/r_y equal to or greater than 200.

Table 4 (continued)

Available Strength
Axial Compression, kips
Eccentrically Loaded WT-Shapes

$F_y = 50$ ksi

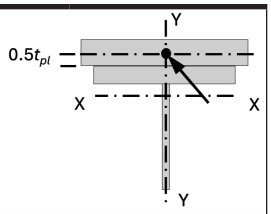

Shape		WT7×											
lb/ft		88		79.5		72.5		66		60		54.5	
t_{pl} (in.)		1		1		¾		¾		⅝		⅝	
Design		P_n/Ω_c	$\phi_c P_n$	P_n/Ω_c	$\phi_c P_n$	P_n/Ω_c	$\phi_c P_n$	P_n/Ω_c	$\phi_c P_n$	P_n/Ω_c	$\phi_c P_n$	P_n/Ω_c	$\phi_c P_n$
		ASD	LRFD	ASD	LRFD	ASD	LRFD	ASD	LRFD	ASD	LRFD	ASD	LRFD
$L_{cx} = L_{cy} = L_{cz} = L_b$, ft	0	248	372	226	339	218	327	202	304	191	287	175	262
	1	244	366	222	333	213	320	198	297	186	279	169	254
	2	241	362	219	329	210	315	195	292	183	274	166	249
	3	239	359	217	325	208	312	192	289	181	271	164	246
	4	236	355	214	321	205	308	190	285	178	268	161	242
	5	232	348	210	316	202	303	187	281	175	263	158	238
	6	225	339	204	307	196	295	182	274	171	258	155	234
	8	209	316	190	286	181	273	168	254	158	238	143	216
	10	192	290	173	262	164	249	153	231	143	216	129	196
	12	173	263	156	236	147	223	137	208	127	194	115	174
	14	155	235	139	211	130	198	121	184	112	171	101	153
	16	137	208	122	186	114	173	106	161	97.6	149	87.1	133
	18	119	182	106	162	98.5	150	91.8	140	84.3	129	75.0	115
	20	105	160	92.9	142	85.9	131	80.0	122	73.3	112	65.1	100
	22	92.4	141	81.9	125	75.5	115	70.3	108	64.3	98.3	57.0	87.2
	24	82.1	126	72.7	111	66.8	102	62.2	95.2	56.7	86.8	50.3	76.9
	26	73.3	112	64.8	99.2	59.5	91.0	55.4	84.8	50.4	77.2	44.6	68.3
	28	65.9	101	58.2	89.1	53.3	81.5	49.6	75.9	45.1	69.1	39.9	61.1
	30												
	32												
	34												
	36												
	38												
	40												

Properties						
A_g, in.^{2}	25.9	23.4	21.3	19.4	17.7	16.0
r_x, in.	1.76	1.73	1.71	1.73	1.71	1.68
r_y, in.	4.02	4.00	3.98	3.76	3.74	3.73
r_x/r_y	0.438	0.433	0.430	0.460	0.457	0.450

ASD	LRFD
$\Omega_b = 1.67$	$\phi_b = 0.90$
$\Omega_c = 1.67$	$\phi_c = 0.90$

[h] Flange thickness is greater than 2 in. Special requirements may apply per AISC *Specification* Section A3.1d.

Note: Heavy line indicates L_c/r_y equal to or greater than 200.

Table 4 (continued)

Available Strength
Axial Compression, kips
Eccentrically Loaded WT-Shapes

$F_y = 50$ ksi

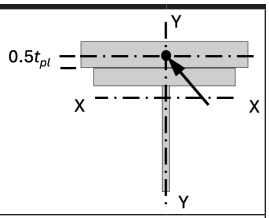

Shape		WT7×											
lb/ft		49.5[f]		45[f]		41		37		34		30.5[c]	
t_{pl} (in.)		⅝		½		⅝		⅝		½		½	
Design		P_n/Ω_c	$\phi_c P_n$	P_n/Ω_c	$\phi_c P_n$	P_n/Ω_c	$\phi_c P_n$	P_n/Ω_c	$\phi_c P_n$	P_n/Ω_c	$\phi_c P_n$	P_n/Ω_c	$\phi_c P_n$
		ASD	LRFD	ASD	LRFD	ASD	LRFD	ASD	LRFD	ASD	LRFD	ASD	LRFD
$L_{cx} = L_{cy} = L_{cz} = L_b$, ft	0	161	242	153	229	139	209	127	190	120	180	109	163
	1	155	233	145	218	135	203	123	184	115	173	104	155
	2	151	227	141	212	134	200	121	181	113	170	102	153
	3	149	224	139	209	132	199	120	180	112	168	101	151
	4	147	221	137	206	131	196	118	178	111	166	99.3	149
	5	145	217	134	202	129	193	116	175	109	164	97.7	147
	6	142	213	132	198	126	189	114	172	107	161	95.8	144
	8	132	199	123	186	117	176	106	160	100	150	90.0	136
	10	119	180	111	168	107	161	96.3	146	90.3	137	81.5	123
	12	105	160	97.7	149	95.9	146	86.3	131	80.7	123	72.7	110
	14	92.0	140	85.1	130	85.3	130	76.5	116	71.3	108	64.1	97.5
	16	79.4	121	73.2	112	75.1	114	67.0	102	62.3	95.0	55.9	85.3
	18	68.3	104	62.7	95.9	65.4	100	58.2	88.9	53.9	82.4	48.3	73.8
	20	59.3	90.6	54.3	83.0	57.0	87.1	50.6	77.4	46.8	71.6	41.9	64.0
	22	51.9	79.3	47.4	72.5	50.0	76.5	44.4	67.9	41.0	62.7	36.6	56.0
	24	45.7	69.9	41.7	63.8	44.2	67.6	39.2	60.0	36.1	55.3	32.2	49.4
	26	40.5	62.1	36.9	56.6	39.3	60.2	34.8	53.3	32.1	49.1	28.6	43.8
	28					35.2	53.9	31.1	47.7	28.6	43.9	25.5	39.1
	30					31.6	48.5	28.0	42.9	25.7	39.4	22.9	35.1
	32												
	34												
	36												
	38												
	40												
Properties													
A_g, in.^{2}		14.6		13.2		12.0		10.9		10.0		8.96	
r_x, in.		1.67		1.66		1.85		1.82		1.81		1.80	
r_y, in.		3.71		3.70		2.48		2.48		2.46		2.45	
r_x/r_y		0.450		0.449		0.746		0.734		0.736		0.735	

ASD	LRFD
$\Omega_b = 1.67$	$\phi_b = 0.90$
$\Omega_c = 1.67$	$\phi_c = 0.90$

[c] Shape is slender for compression with $F_y = 50$ ksi; tabulated values have been adjusted accordingly.
[f] Shape exceeds compact limit for flexure with $F_y = 50$ ksi; tabulated values have been adjusted accordingly.
Note: Heavy line indicates L_c/r_y equal to or greater than 200.

Table 4 (continued)

Available Strength
Axial Compression, kips
Eccentrically Loaded WT-Shapes

$F_y = 50$ ksi

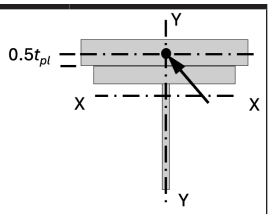

Shape		WT7×						WT6×					
lb/ft		26.5[c]		24[c]		21.5[c]		168[h]		152.5[h]		139.5[h]	
t_{pl} (in.)		½		½		⅜		2		2		1¾	
Design		P_n/Ω_c	$\phi_c P_n$	P_n/Ω_c	$\phi_c P_n$	P_n/Ω_c	$\phi_c P_n$	P_n/Ω_c	$\phi_c P_n$	P_n/Ω_c	$\phi_c P_n$	P_n/Ω_c	$\phi_c P_n$
		ASD	LRFD	ASD	LRFD	ASD	LRFD	ASD	LRFD	ASD	LRFD	ASD	LRFD
$L_{cx} = L_{cy} = L_{cz} = L_b$, ft	0	96.0	144	87.6	131	80.2	120	379	569	343	515	327	490
	1	92.2	138	83.4	125	75.4	113	378	567	342	513	325	488
	2	90.9	137	82.3	124	74.1	111	376	564	341	511	324	486
	3	90.0	135	81.4	122	73.3	110	373	559	337	506	320	481
	4	88.8	133	80.4	121	72.4	109	368	552	333	499	316	474
	5	87.3	131	79.1	119	71.3	107	362	544	327	491	310	465
	6	85.4	129	77.4	117	69.8	105	355	533	320	481	303	455
	8	79.9	120	72.7	110	65.7	99.2	337	508	303	457	286	431
	10	73.0	110	66.5	101	60.3	91.2	317	478	284	429	266	402
	12	65.7	100	59.8	90.8	54.3	82.4	295	446	263	398	245	371
	14	58.4	88.9	53.2	80.9	48.1	73.2	271	411	241	365	223	339
	16	51.4	78.3	46.8	71.4	42.2	64.3	247	375	218	331	201	306
	18	44.7	68.3	40.7	62.2	36.6	55.9	223	339	196	298	180	273
	20	38.8	59.4	35.3	54.0	31.7	48.4	200	304	175	266	160	243
	22	34.0	52.0	30.9	47.3	27.7	42.3	180	274	157	239	143	218
	24	30.0	45.9	27.2	41.7	24.3	37.3	162	247	141	215	128	195
	26	26.6	40.8	24.2	37.0	21.6	33.0	146	224	127	195	115	176
	28	23.8	36.4	21.6	33.1	19.2	29.5	133	203	116	177	104	159
	30	21.4	32.7	19.4	29.7	17.2	26.4	121	185	105	161	94.8	145
	32							111	170				
	34												
	36												
	38												
	40												
Properties													
A_g, in.^{2}		7.80		7.07		6.31		49.5		44.7		41.0	
r_x, in.		1.88		1.88		1.86		1.96		1.90		1.86	
r_y, in.		1.92		1.91		1.89		3.47		3.42		3.38	
r_x/r_y		0.979		0.984		0.984		0.565		0.556		0.550	

ASD	LRFD
$\Omega_b = 1.67$	$\phi_b = 0.90$
$\Omega_c = 1.67$	$\phi_c = 0.90$

[c] Shape is slender for compression with $F_y = 50$ ksi; tabulated values have been adjusted accordingly.
[h] Flange thickness is greater than 2 in. Special requirements may apply per AISC *Specification* Section A3.1d.
Note: Heavy line indicates L_c/r_y equal to or greater than 200.

Table 4 (continued)

Available Strength
Axial Compression, kips
Eccentrically Loaded WT-Shapes

$F_y = 50$ ksi

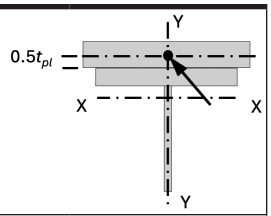

Shape		WT6×											
lb/ft		126[h]		115[h]		105		95		85		76	
t_{pl} (in.)		1½		1½		1¼		1¼		1¼		1	
Design		P_n/Ω_c	$\phi_c P_n$	P_n/Ω_c	$\phi_c P_n$	P_n/Ω_c	$\phi_c P_n$	P_n/Ω_c	$\phi_c P_n$	P_n/Ω_c	$\phi_c P_n$	P_n/Ω_c	$\phi_c P_n$
		ASD	LRFD	ASD	LRFD	ASD	LRFD	ASD	LRFD	ASD	LRFD	ASD	LRFD
$L_{cx} = L_{cy} = L_{cz} = L_b$, ft	0	306	460	281	421	268	403	243	364	219	329	208	313
	1	305	457	280	419	267	400	241	362	217	326	206	309
	2	303	455	278	417	265	397	239	359	216	323	204	307
	3	300	450	275	413	262	393	237	355	213	320	202	304
	4	295	443	270	406	257	386	232	349	209	314	198	298
	5	289	435	264	398	251	378	227	341	204	307	193	290
	6	282	424	258	388	244	368	220	331	198	298	186	281
	8	265	400	242	364	228	344	204	309	183	276	172	259
	10	246	371	223	337	209	317	187	283	167	253	155	235
	12	225	341	204	308	190	288	169	256	150	227	138	210
	14	203	309	183	279	170	258	150	228	133	202	122	185
	16	182	277	163	249	150	228	132	201	116	177	106	161
	18	161	246	144	220	131	200	115	176	101	154	91.5	140
	20	143	218	127	194	116	177	101	154	88.7	135	79.9	122
	22	127	194	113	173	103	157	89.4	137	78.3	120	70.3	107
	24	114	174	101	154	91.3	140	79.5	122	69.5	106	62.2	95.2
	26	102	156	90.8	139	81.8	125	71.1	109	62.1	95.0	55.4	84.9
	28	92.3	141	81.9	125	73.6	113	63.9	97.9				
	30	83.7	128										
	32												
	34												
	36												
	38												
	40												

Properties						
A_g, in.^{2}	37.1	33.8	30.9	28.0	25.0	22.4
r_x, in.	1.81	1.77	1.73	1.68	1.65	1.62
r_y, in.	3.34	3.31	3.28	3.25	3.22	3.19
r_x/r_y	0.542	0.535	0.527	0.517	0.512	0.508

ASD	LRFD
$\Omega_b = 1.67$	$\phi_b = 0.90$
$\Omega_c = 1.67$	$\phi_c = 0.90$

[h] Flange thickness is greater than 2 in. Special requirements may apply per AISC *Specification* Section A3.1d.

Note: Heavy line indicates L_c/r_y equal to or greater than 200.

Table 4 (continued)

Available Strength
Axial Compression, kips
Eccentrically Loaded WT-Shapes

$F_y = 50$ ksi

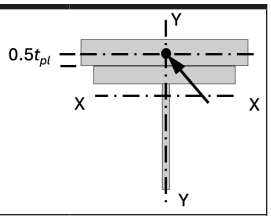

Shape		WT6×											
lb/ft		68		60		53		48		43.5		39.5	
t_{pl} (in.)		1		¾		¾		⅝		⅝		½	
Design		P_n/Ω_c	$\phi_c P_n$	P_n/Ω_c	$\phi_c P_n$	P_n/Ω_c	$\phi_c P_n$	P_n/Ω_c	$\phi_c P_n$	P_n/Ω_c	$\phi_c P_n$	P_n/Ω_c	$\phi_c P_n$
		ASD	LRFD	ASD	LRFD	ASD	LRFD	ASD	LRFD	ASD	LRFD	ASD	LRFD
$L_{cx} = L_{cy} = L_{cz} = L_b$, ft	0	189	284	178	267	158	237	149	223	137	206	130	195
	1	187	280	175	262	155	232	145	218	133	200	125	188
	2	185	277	173	260	153	230	143	214	131	197	123	184
	3	183	274	171	257	151	227	141	212	129	194	121	182
	4	179	270	168	253	149	223	139	208	127	191	119	179
	5	174	262	163	245	144	217	135	203	124	187	116	175
	6	174	262	158	238	138	209	129	195	119	180	112	169
	7	167	252	151	228	132	200	123	186	114	171	106	161
	8	159	241	144	217	126	190	117	177	108	163	101	152
	9	151	229	136	206	119	180	110	167	101	154	94.7	143
	10	143	217	129	195	112	170	104	157	95.1	144	88.6	134
	11	135	205	121	184	105	159	96.8	147	88.8	135	82.5	125
	12	127	193	113	172	98.0	149	90.1	137	82.5	126	76.5	116
	13	119	180	106	161	91.2	139	83.6	127	76.4	116	70.7	108
	14	111	168	98.4	150	84.5	129	77.2	118	70.5	108	65.0	99.2
	15	103	157	91.1	139	78.0	119	71.1	108	64.8	98.9	59.7	91.1
	16	95.2	145	84.2	129	72.1	110	65.5	100	59.7	91.2	54.9	83.8
	18	82.1	125	72.5	111	61.9	94.6	56.1	85.7	51.0	78.0	46.8	71.5
	20	71.5	109	62.9	96.2	53.6	82.0	48.5	74.2	44.1	67.4	40.3	61.6
	22	62.7	95.9	55.1	84.2	46.9	71.7	42.3	64.7	38.4	58.7	35.0	53.6
	24	55.4	84.7	48.5	74.3	41.3	63.2	37.1	56.9	33.7	51.6	30.7	47.0
	26	49.2	75.3	43.1	66.0								
	28												
	30												
Properties													
A_g, in.^{2}		20.0		17.6		15.6		14.1		12.8		11.6	
r_x, in.		1.59		1.57		1.53		1.51		1.50		1.49	
r_y, in.		3.16		3.13		3.11		3.09		3.07		3.05	
r_x/r_y		0.503		0.502		0.492		0.489		0.489		0.489	

ASD	LRFD
$\Omega_b = 1.67$	$\phi_b = 0.90$
$\Omega_c = 1.67$	$\phi_c = 0.90$

Note: Heavy line indicates L_c/r_y equal to or greater than 200.

Table 4 (continued)

Available Strength
Axial Compression, kips
Eccentrically Loaded WT-Shapes

$F_y = 50$ ksi

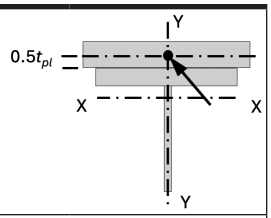

Shape		WT6×											
lb/ft		36		32.5[f]		29		26.5		25		22.5	
t_{pl} (in.)		½		½		½		⅜		½		⅜	
Design		P_n/Ω_c	$\phi_c P_n$	P_n/Ω_c	$\phi_c P_n$	P_n/Ω_c	$\phi_c P_n$	P_n/Ω_c	$\phi_c P_n$	P_n/Ω_c	$\phi_c P_n$	P_n/Ω_c	$\phi_c P_n$
		ASD	LRFD	ASD	LRFD	ASD	LRFD	ASD	LRFD	ASD	LRFD	ASD	LRFD
$L_{cx} = L_{cy} = L_{cz} = L_b$, ft	0	120	180	110	164	97.9	147	94.3	141	86.9	130	81.4	122
	1	115	172	104	156	93.8	141	89.3	134	83.6	125	77.5	116
	2	112	169	101	152	92.2	138	87.6	131	82.4	124	76.3	115
	3	111	166	100	150	90.9	137	86.3	130	81.4	122	75.3	113
	4	109	164	97.9	147	89.4	134	84.8	128	80.1	120	74.1	111
	5	106	160	95.8	144	87.4	132	83.0	125	78.4	118	72.5	109
	6	103	156	93.3	141	84.3	127	80.9	122	76.0	114	70.5	106
	7	98.0	148	89.0	134	80.1	121	76.9	116	72.5	109	67.5	102
	8	92.6	140	84.0	127	75.7	115	72.6	110	68.8	104	63.9	96.6
	9	86.9	132	78.8	119	71.2	108	68.1	103	64.9	98.3	60.2	91.1
	10	81.2	123	73.5	112	66.5	101	63.6	96.5	61.0	92.5	56.4	85.5
	11	75.6	115	68.3	104	61.9	94.1	59.1	89.9	57.1	86.7	52.7	80.0
	12	70.0	107	63.2	96.2	57.4	87.3	54.7	83.3	53.2	80.9	49.0	74.5
	13	64.6	98.4	58.2	88.7	53.0	80.7	50.5	76.9	49.4	75.3	45.4	69.2
	14	59.3	90.5	53.4	81.5	48.7	74.4	46.4	70.8	45.8	69.8	42.0	64.0
	15	54.4	83.0	48.9	74.6	44.7	68.2	42.4	64.8	42.3	64.5	38.7	59.0
	16	49.9	76.3	44.9	68.6	41.1	62.7	38.9	59.5	38.9	59.4	35.5	54.2
	18	42.5	65.1	38.2	58.4	35.0	53.5	33.1	50.6	33.2	50.8	30.2	46.2
	20	36.6	56.0	32.8	50.2	30.1	46.0	28.4	43.5	28.6	43.8	26.0	39.8
	22	31.8	48.7	28.5	43.6	26.1	40.0	24.6	37.7	24.9	38.1	22.6	34.5
	24	27.8	42.7	24.9	38.2	22.9	35.1	21.5	33.0	21.8	33.5	19.8	30.3
	26									19.3	29.6	17.4	26.7
	28												
	30												

Properties						
A_g, in.^{2}	10.6	9.54	8.52	7.78	7.30	6.56
r_x, in.	1.48	1.47	1.50	1.51	1.60	1.59
r_y, in.	3.04	3.02	2.51	2.48	1.96	1.95
r_x/r_y	0.487	0.487	0.598	0.609	0.816	0.815

ASD	LRFD
$\Omega_b = 1.67$	$\phi_b = 0.90$
$\Omega_c = 1.67$	$\phi_c = 0.90$

[f] Shape exceeds compact limit for flexure with $F_y = 50$ ksi; tabulated values have been adjusted accordingly.

Note: Heavy line indicates L_c/r_y equal to or greater than 200.

Table 4 (continued)

Available Strength
Axial Compression, kips
Eccentrically Loaded WT-Shapes

$F_y = 50$ ksi

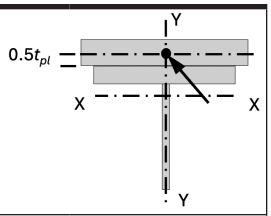

Shape		WT6×		WT5×									
lb/ft		20[c]		56		50		44		38.5		34	
t_{pl} (in.)		3/8		1		3/4		3/4		5/8		5/8	
Design		P_n/Ω_c	$\phi_c P_n$	P_n/Ω_c	$\phi_c P_n$	P_n/Ω_c	$\phi_c P_n$	P_n/Ω_c	$\phi_c P_n$	P_n/Ω_c	$\phi_c P_n$	P_n/Ω_c	$\phi_c P_n$
		ASD	LRFD	ASD	LRFD	ASD	LRFD	ASD	LRFD	ASD	LRFD	ASD	LRFD
$L_{cx} = L_{cy} = L_{cz} = L_b$, ft	0	72.3	108	144	215	137	206	123	184	112	168	101	151
	1	68.4	103	142	213	136	203	121	181	110	165	98.1	147
	2	67.3	101	140	211	134	201	119	179	108	163	96.5	145
	3	66.4	100	138	207	131	197	117	176	106	160	94.7	142
	4	65.3	98.2	134	201	127	191	113	170	103	155	91.7	138
	5	63.9	96.2	128	193	122	183	108	163	97.9	148	87.2	131
	6	62.3	93.9	123	185	116	174	103	155	92.4	140	82.2	124
	7	60.1	90.7	116	175	109	165	96.6	146	86.6	131	76.9	116
	8	56.8	85.8	109	166	102	155	90.3	137	80.6	122	71.3	108
	9	53.4	80.8	102	155	95.2	144	83.9	127	74.6	113	65.8	100
	10	49.9	75.8	95.5	145	88.2	134	77.5	118	68.5	104	60.3	91.7
	11	46.6	70.7	88.5	135	81.2	124	71.2	108	62.6	95.4	54.9	83.7
	12	43.2	65.8	81.6	124	74.5	113	65.1	99.2	56.9	86.7	49.7	75.8
	13	40.0	61.0	74.9	114	67.9	104	59.2	90.3	51.6	78.7	45.0	68.7
	14	36.9	56.3	68.7	105	62.1	94.8	54.1	82.5	46.9	71.7	40.9	62.5
	15	33.9	51.8	63.2	96.4	56.9	86.9	49.5	75.6	42.9	65.5	37.4	57.1
	16	31.1	47.6	58.3	89.0	52.5	80.2	46.0	70.4	39.6	60.5	34.7	53.1
	18	26.5	40.5	49.9	76.3	44.7	68.4	39.1	59.9	33.5	51.3	29.3	44.9
	20	22.7	34.8	43.2	66.1	38.5	58.9	33.6	51.5	28.7	44.0	25.1	38.4
	22	19.7	30.2	37.7	57.7								
	24	17.3	26.4										
	26	15.2	23.3										
	28												
	30												
Properties													
A_g, in.^{2}		5.84		16.5		14.7		13.0		11.3		10.0	
r_x, in.		1.57		1.32		1.29		1.27		1.24		1.22	
r_y, in.		1.94		2.67		2.65		2.63		2.60		2.58	
r_x/r_y		0.809		0.494		0.487		0.483		0.477		0.473	

ASD	LRFD
$\Omega_b = 1.67$	$\phi_b = 0.90$
$\Omega_c = 1.67$	$\phi_c = 0.90$

[c] Shape is slender for compression with $F_y = 50$ ksi; tabulated values have been adjusted accordingly.

Note: Heavy line indicates L_c/r_y equal to or greater than 200.

Table 4 (continued)

$F_y = 50$ ksi

Available Strength
Axial Compression, kips
Eccentrically Loaded WT-Shapes

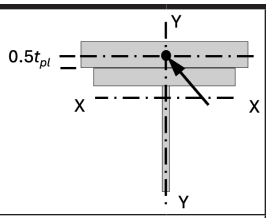

Shape		WT5×											
lb/ft		30		27		24.5		22.5		19.5		16.5	
t_{pl} (in.)		½		½		⅜		½		⅜		⅜	
Design		P_n/Ω_c	$\phi_c P_n$	P_n/Ω_c	$\phi_c P_n$	P_n/Ω_c	$\phi_c P_n$	P_n/Ω_c	$\phi_c P_n$	P_n/Ω_c	$\phi_c P_n$	P_n/Ω_c	$\phi_c P_n$
		ASD	LRFD	ASD	LRFD	ASD	LRFD	ASD	LRFD	ASD	LRFD	ASD	LRFD
$L_{cx} = L_{cy} = L_{cz} = L_b$, ft	0	93.6	140	84.5	127	81.1	122	73.0	109	66.9	100	58.8	88.2
	1	90.5	136	81.1	122	77.2	116	70.6	106	63.9	96.0	55.0	82.6
	2	88.9	134	79.5	119	75.5	113	69.5	104	62.8	94.4	54.0	81.0
	3	87.2	131	77.9	117	73.9	111	68.2	103	61.7	92.7	53.0	79.6
	4	84.9	128	75.9	114	72.0	108	66.3	100	60.1	90.5	51.7	77.8
	5	80.5	121	72.2	109	68.8	104	63.0	95.0	57.5	86.7	50.1	75.6
	6	75.7	114	67.7	102	64.3	97.2	59.3	89.5	54.0	81.5	47.5	71.7
	7	70.5	107	62.9	95.3	59.6	90.3	55.3	83.7	50.2	76.1	44.2	66.9
	8	65.2	99.0	58.0	88.1	54.8	83.2	51.2	77.7	46.4	70.4	40.8	61.9
	9	60.0	91.1	53.2	80.8	50.0	76.1	47.1	71.5	42.5	64.6	37.4	56.9
	10	54.7	83.3	48.4	73.7	45.3	69.1	43.0	65.5	38.8	59.0	34.1	52.0
	11	49.7	75.7	43.8	66.8	40.9	62.4	39.1	59.7	35.2	53.6	31.0	47.2
	12	44.8	68.4	39.4	60.1	36.6	56.0	35.4	54.0	31.7	48.4	27.9	42.7
	13	40.5	61.8	35.5	54.3	33.0	50.4	32.0	48.8	28.6	43.6	25.1	38.4
	14	36.7	56.1	32.2	49.2	29.8	45.6	29.0	44.3	25.8	39.5	22.7	34.8
	15	33.4	51.1	29.3	44.8	27.1	41.4	26.4	40.3	23.5	35.9	20.6	31.6
	16	30.5	46.7	26.7	40.9	24.7	37.8	24.1	36.9	21.4	32.8	18.8	28.8
	17	28.0	42.9	24.5	37.5	22.6	34.6	22.1	33.8	19.6	30.0	17.2	26.4
	18	25.8	39.5	22.5	34.5	20.7	31.8	20.3	31.1	18.0	27.6	15.8	24.2
	19	23.8	36.4	20.8	31.8	19.1	29.3	18.7	28.7	16.6	25.4	14.6	22.3
	20	22.0	33.7					17.3	26.6	15.3	23.5	13.4	20.6
	21											12.5	19.1
	22												
	23												

Properties						
A_g, in.^{2}	8.84	7.90	7.21	6.63	5.73	4.85
r_x, in.	1.21	1.19	1.18	1.24	1.24	1.26
r_y, in.	2.57	2.56	2.54	2.01	1.98	1.94
r_x/r_y	0.471	0.465	0.465	0.617	0.626	0.649

ASD	LRFD
$\Omega_b = 1.67$	$\phi_b = 0.90$
$\Omega_c = 1.67$	$\phi_c = 0.90$

Note: Heavy line indicates L_c/r_y equal to or greater than 200.

Table 4 (continued)

$F_y = 50$ ksi

Available Strength
Axial Compression, kips
Eccentrically Loaded WT-Shapes

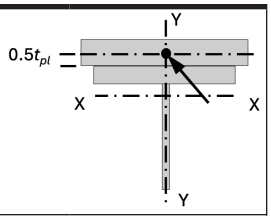

Shape		WT4×											
lb/ft		33.5		29		24		20		17.5		15.5[f]	
t_{pl} (in.)		5/8		5/8		1/2		3/8		3/8		3/8	
Design		P_n/Ω_c	$\phi_c P_n$	P_n/Ω_c	$\phi_c P_n$	P_n/Ω_c	$\phi_c P_n$	P_n/Ω_c	$\phi_c P_n$	P_n/Ω_c	$\phi_c P_n$	P_n/Ω_c	$\phi_c P_n$
		ASD	LRFD	ASD	LRFD	ASD	LRFD	ASD	LRFD	ASD	LRFD	ASD	LRFD
$L_{cx} = L_{cy} = L_{cz} = L_b$, ft	0	91.2	137	81.2	122	69.5	104	63.3	95.0	56.1	84.2	50.8	76.2
	1	89.8	135	79.6	119	67.8	102	61.0	91.6	53.6	80.4	47.9	71.9
	2	88.4	133	78.3	118	66.5	100	59.7	89.7	52.3	78.6	46.7	70.2
	3	85.3	128	75.6	114	64.2	96.6	58.1	87.4	50.8	76.5	45.4	68.3
	4	81.1	122	71.7	108	60.5	91.2	54.7	82.5	48.1	72.6	43.5	65.6
	5	76.2	115	67.2	101	56.3	85.0	50.7	76.6	44.4	67.1	40.1	60.6
	6	70.8	107	62.2	94.1	51.7	78.3	46.3	70.2	40.5	61.3	36.5	55.3
	7	65.2	98.8	57.0	86.5	47.0	71.3	41.9	63.6	36.5	55.4	32.8	49.9
	8	59.5	90.4	51.8	78.7	42.3	64.3	37.5	57.1	32.5	49.5	29.3	44.5
	9	53.8	81.9	46.7	71.1	37.7	57.5	33.3	50.8	28.7	43.8	25.8	39.4
	10	48.3	73.7	41.7	63.6	33.4	50.9	29.3	44.8	25.2	38.5	22.6	34.6
	11	43.2	65.9	37.2	56.7	29.6	45.2	25.9	39.6	22.2	34.0	19.9	30.5
	12	38.8	59.3	33.3	50.9	26.4	40.4	23.1	35.3	19.7	30.2	17.7	27.1
	13	35.0	53.5	30.0	45.8	23.7	36.2	20.6	31.5	17.6	27.0	15.8	24.2
	14	31.7	48.5	27.1	41.5	21.4	32.7	18.5	28.4	15.8	24.2	14.2	21.7
	15	28.8	44.1	24.6	37.7	19.3	29.6	16.7	25.6	14.3	21.9	12.8	19.6
	16	26.3	40.2	22.4	34.3	17.6	26.9	15.2	23.3	12.9	19.8	11.6	17.7
	17	24.1	36.9	20.5	31.4								
	18												
	19												
	20												
	21												
	22												
	23												
Properties													
A_g, in.^{2}		9.84		8.54		7.05		5.87		5.14		4.56	
r_x, in.		1.05		1.03		0.986		0.988		0.968		0.969	
r_y, in.		2.12		2.10		2.08		2.04		2.03		2.02	
r_x/r_y		0.495		0.490		0.474		0.484		0.477		0.480	

ASD	LRFD
$\Omega_b = 1.67$	$\phi_b = 0.90$
$\Omega_c = 1.67$	$\phi_c = 0.90$

[f] Shape exceeds compact limit for flexure with $F_y = 50$ ksi; tabulated values have been adjusted accordingly.

Note: Heavy line indicates L_c/r_y equal to or greater than 200.

Design Example 3 Using Table 4

Given:

Member of Design Example 1; WT7×45, pin-connected and braced at the ends using 14½ in. × ½ in. gusset plates, LRFD method, $L_{cx} = L_{cy} = L_{cz} = L_b = L = 12$ ft. Determine the available eccentric axial compressive strength using Table 4.

Solution:

From Table 4; for a WT7×45, at $L_{cx} = 12$ ft, $\phi_c P_{n\,ecc} = 149$ kips. This is the same value calculated in Example 1 earlier.

Design Example 4 Using Table 4

Given:

Member of Design Example 2; WT7×30.5, pin-connected and braced at the ends using 10 in. × ½ in. gusset plates, ASD method, $L_{cx} = L_{cy} = L_{cz} = L_b = L = 10$ ft. Determine the available eccentric axial compressive strength using Table 4.

Solution:

From Table 4; for a WT7×30.5, at $L_{cx} = 10$ ft, $(P_{n\,ecc})/\Omega_c = 78.5$ kips. This is the same value calculated in Example 2 earlier.

USING THICKER GUSSET PLATES THAN RECOMMENDED

The gusset plate thickness recommended in this paper for eccentrically loaded WT compression members are about $t_{pl} = 0.6t_f$, rounded up to the next practical and readily available plate thickness. Recommended plate thicknesses are listed at the top of each column in Table 4.

Plate thicknesses recommended in Table 4 may seem low. For instance, a recommended plate thickness of 2.50 in. for connecting to a WT7×250 with a flange thickness of $t_f =$ 3.50 in. may appear inadequate. The designer may feel it is conservative to use a thicker gusset plate for the connection than recommended. While this may be true for the gusset plate strength, a thicker plate increases load eccentricity (see Eq. 1), resulting in a decrease in the WT compression member's available strength.

It is noted that plate thicknesses recommended are based on plate compressive strength assuming that plate flexural buckling does not apply and $F_n = F_y$. See AISC *Specification* Section J4.4(a) and Equation J4-6.

IMPACT OF α ON THE AVAILABLE STRENGTH BASED ON THE LRFD AND ASD METHODS

Ordinarily, the ratio of the available strength of a member in LRFD and ASD is 1.50, namely,

$$\phi R_n = (1.50)\left(\frac{R_n}{\Omega}\right) \tag{24}$$

This ratio was checked for all values of Table 4. The 1.50 ratio holds for most, but not all cases in Table 4. The values of this ratio for shapes and unbraced length considered in this study ranged from 1.49 to 1.54. This variation is due to the role of α in the B_{1x} equation for LRFD and ASD. Further discussion of this subject is beyond the scope of this paper.

SYMBOLS

B_1	Multiplier to account for P-δ effects, determined for each member, and each direction of bending of the member (B_{1x} and B_{1y}) in accordance with AISC *Specification* Appendix 8, Section 8.1.2
B_2	Multiplier to account for P-Δ effects, determined for each story of the structure and each direction of lateral translation of the story (B_{2x} and B_{2y}) in accordance with AISC *Specification* Appendix 8, Section 8.1.3
C_m	Equivalent uniform moment factor, assuming no relative translation of the member ends, for bending in each direction (C_{mx} and C_{my})
L_{c1}	Effective length in the plane of bending (L_{c1x} and L_{c1y}), calculated based on the assumption of no lateral translation at the member ends, set equal to the laterally unbraced length of the member unless analysis justifies a smaller value, in. (mm)
M_{ax}	Required moment including P-δ effect using ASD load combinations, kip-in. (N-mm)
M_{lt}	First-order moment using LRFD or ASD load combinations, due to lateral translation of the structure only, kip-in. (N-mm)

M_{ntx} First-order moment about x-axis using LRFD or ASD load combinations, with the structure restrained against lateral translation, kip-in. (N-mm)

M_{nx} Nominal strength in flexure based on the limit states of yielding, flange local buckling, and lateral torsional buckling, kip-in. (N-mm)

M_r Required second-order flexural strength, kip-in. (N-mm)
$= M_u$ (LRFD)
$= M_a$ (ASD)

M_{ux} Required moment including P-δ effect using LRFD load combinations, kip-in. (N-mm)

P Axial compressive load, kips (N)
$= P_u$ (LRFD)
$= P_a$ (ASD)

P_a Axial compressive force using ASD load combinations, kips (N)

P_{e1} Elastic critical buckling strength of the member in the plane of bending (P_{e1x} and P_{e1y}), calculated based on the assumption of no lateral translation at the member ends, kips (N)

$$= \frac{\pi^2 EI}{(L_{c1})^2} \qquad \text{(AISC } \textit{Spec.} \text{ Eq. A-85)}$$

P_{lt} First-order axial force due to lateral translation of the structure only using LRFD or ASD load combinations, kips (N)

P_n Nominal concentric compressive strength based on the limit states of flexural and flexural-torsional buckling in interaction with local buckling, kips (N)

$P_{n\,ecc}$ Nominal eccentric compressive strength based on the limit states of flexural and flexural-torsional buckling in interaction with local buckling, kips (N)

P_{nt} First-order axial force with the structure restrained against lateral translation using LRFD or ASD load combinations, kips (N)

P_r Required second-order axial strength using LRFD or ASD load combinations, kips (N)
$= P_u$ (LRFD)
$= P_a$ (ASD)

P_u Axial compressive force using LRFD load combinations, kips (N)

e Load eccentricity along the y-axis of the applied load measured from the centroid of the WT section, in. (mm)
$= 0.5t_f + \overline{y}$

t_f Thickness of the flange of the WT-section, in. (mm)

t_{pl} Thickness of the gusset plate, in. (mm)

$\overline{y}$ Distance along the y-axis from the centroid of the WT-section to the outside of the flange, in. (mm)

Ω_b Safety factor for flexure (ASD)
$= 1.67$

Ω_c Safety factor for compression (ASD)
$= 1.67$

α $= 1.0$ (LRFD)
$= 1.6$ (ASD)

$\phi_c P_{n\,ecc}$ Available strength in axial compression for an eccentrically loaded WT member using LRFD load combinations, kips (N)

$\frac{P_{n\,ecc}}{\Omega_c}$ Available strength in axial compression for an eccentrically loaded WT member using ASD load combinations, kips (N)

ϕ_b Resistance factor for flexure (LRFD)
$= 0.90$

ϕ_c Resistance factor for compression (LRFD)
$= 0.90$

REFERENCES

AISC (2005a), *Specification for Structural Steel Buildings*, ANSI/AISC 360-05, American Institute of Steel Construction, Chicago, Ill.

AISC (2005b), *Steel Construction Manual*, 13th Ed., American Institute of Steel Construction, Chicago, Ill.

AISC (2022), *Specification for Structural Steel Buildings*, ANSI/AISC 360-22, American Institute of Steel Construction, Chicago, Ill.

AISC (2023a), *Steel Construction Manual*, 16th Ed., American Institute of Steel Construction, Chicago, Ill.

AISC (2023b), *AISC Shapes Database*, Version 16.0, American Institute of Steel Construction, Chicago, Ill., https://bit.ly/3AS6RqW.

ASTM (2020), *Standard Specification for High-Strength Low-Alloy Columbuam-Vanadium Structural Steel*, ASTM A992/992M, ASTM International, West Conshohocken, Pa.

ASTM (2021), *Standard Specification for Structural Steel Shapes*, ASTM A572/572M, ASTM International, West Conshohocken, Pa.

Gordon, M.E. (2010), "Tables for Eccentrically Loaded WT Shapes in Compression," *Engineering Journal*, AISC, Vol. 47, No. 2, pp. 91–100, https://doi.org/10.62913/engj.v47i2.979.

Flexural Buckling Curves of High-Strength, Wide-Flange Steel Columns

SHAHRIAR QUAYYUM

ABSTRACT

Rolled shapes using structural steel with a specified yield strength, F_y, of 65 ksi or higher are considered an alternative solution to built-up shapes using conventional steel grades. However, major evidence exists that current design rules (e.g., AISC 360, Eurocode 3) are likely overly conservative for these higher-strength steels with $F_y \geq 65$ ksi—particularly at yield strengths of 80 ksi and above when employed as structural steel columns—due in part to assumptions regarding residual stresses. In order to understand the extent of these conservative predictions and explore if alternative design provisions could be provided to engineers utilizing specific shapes and high-strength materials grade, this study presents comprehensive nonlinear finite element analyses of rolled W-shape columns made from ASTM A992 ($F_y = 50$ ksi) and A913 Grade 80 ($F_y = 80$ ksi) steels. The models incorporate validated multiaxial residual stress distributions, geometric imperfections, and nonlinear material behavior, and are benchmarked against experimental data.

Column flexural buckling curves are developed for a range of cross-sectional geometries and slenderness ratios and compared to predictions from AISC 360 and Eurocode 3 for both major and minor axis buckling. For A992 ($F_y = 50$ ksi), the AISC column curve overestimates the buckling strength for heavier sections and underestimates it for more slender or lightly built shapes, reflecting shape-dependent divergence. For A913 Grade 80 ($F_y = 80$ ksi), simulation results are generally close to AISC predictions, with a 5–14% increase in buckling strength observed, depending on the section geometry and slenderness. The findings generally support the use of AISC 360-22 but suggest refinement might be needed for heavier or high-strength rolled shapes in the inelastic buckling range. The results also highlight the potential need for shape- or grade-specific column curves. Future experimental validation will be essential to confirm these trends and guide potential updates to design standards.

Keywords: high-strength steel, finite element analysis, flexural buckling, initial imperfection, residual stresses, rolled shape, W section.

INTRODUCTION

Rolled shapes using high-strength structural steel (HS3) with a specified yield strength, F_y, of 65 ksi (450 MPa) or higher can provide improvements in cost, speed, simplicity, footprint, performance, and embodied carbon content when applied in lower stories of high-rise buildings and other non-stiffness-controlled structural members such as long span trusses. These hot-rolled shapes are desirable when considering alternative solutions such as built-up shapes using conventional steel grades. Several examples exist in the United States today, where high-strength rolled shapes were selected for columns. A notable example of high-strength, rolled-shape application is the 320 S. Canal project (Union Station Tower) in Chicago, which utilized ASTM A913 (2019b) Grade 80 wide-flange columns in the tower's upper perimeter framing. This marked the first documented use of Grade 80 rolled shapes in a U.S. building project, enabling more compact section sizes and a 20% steel tonnage reduction in upper-story framing. Such applications underscore the growing demand for optimized column design provisions for rolled HS3 products. The readers are also referred to HS3 Ad Hoc Task Group Report on High Strength Steel (AISC, 2019) for other examples. High-strength rolled shape columns have also been used in several major structures worldwide, particularly in high-rise buildings and large infrastructure projects, that showcase how rolled-shape columns (mainly wide-flange beams, H-sections, and hollow structural sections) are incorporated into modern high-strength steel structures to enhance load-bearing capacity, seismic performance, and overall efficiency. Reports have shown that for larger load applications, rolled high-strength steel shapes can save up to 46% of the fabrication cost compared to Gr. 50 built-up members (ArcelorMittal, 2019).

Currently, select producers are capable of rolling plates with a specified yield stress up to 130 ksi using quenching and tempering processes. Hot-rolled wide flange shapes with a specified yield stress up to 80 ksi made by the quenched and self-tempering (QST) process are also available, while other hot-rolled shapes with a specified yield stress of 65 ksi or greater are also available. Although several U.S.-based steel producers are capable of producing these HS3 products, a lack of guidance and standards has seemingly kept designers from implementing HS3 into their

Shahriar Quayyum, Assistant Professor, Department of Civil & Environmental Engineering, Manhattan University, Riverdale, N.Y. Email: shahriar.quayyum@manhattan.edu

Paper No. 2025–06

Table 1. Materials Listed in AISC 360-22, Table A3.1, with $F_y \geq 65$ ksi		
Specified Yield Stress (F_y)	**Standard Designation of Listed Material in AISC 360-22**	**Steel Type and Production Process**
65 ksi (450 MPa)	ASTM A572/A572M Gr. 65 [450], Type 1, 2, or 3	High-strength low-alloy (HSLA) steel
	A709/A709M QST 65 [QST 450]	HSLA steel produced by quenching and self-tempering process (QST)
	A913/A913M Gr. 65 [450]	HSLA steel produced by quenching and self-tempering process (QST)
70 ksi (485 MPa)	A709/A709M QST 70 [QST 485]	HSLA steel produced by quenching and self-tempering process (QST)
	A913/A913M Gr. 70 [485]	HSLA steel produced by quenching and self-tempering process (QST)
80 ksi (550 MPa)	A913/A913M Gr. 80 [550]	HSLA steel produced by quenching and self-tempering process (QST)

building designs, which has, in turn, limited the production of the material (Stall et al., 2024). While high-strength steel is still more expensive on a per-ton basis, the cost premium for rolled shapes with $F_y = 65$ ksi is generally modest (5–10%), whereas for $F_y = 80$ ksi, the premium may range from 10–20%, depending on section availability, production methods, and regional market conditions (AISC, 2019; ArcelorMittal, 2020). Although high-strength steel may have a higher unit cost, its use can reduce total material tonnage and fabrication effort, leading to potential cost savings at the system level, particularly in long-span or high-rise applications.

High-strength rolled shape steel columns, particularly those specified under ASTM A572 (2021b) Grade 65 and A913 Grades 65, 70, and 80, have become increasingly viable for structural applications due to advances in QST manufacturing. These grades offer enhanced strength and comparable ductility to conventional steels, enabling potential reductions in member size, weight, and embodied carbon. However, design provisions such as those in AISC 360, *Specification for Structural Steel Buildings* (2022b), hereafter referred to as AISC 360, have not yet been recalibrated to fully reflect the unique residual stress patterns and imperfection behavior of these modern high-strength materials. While previous studies on welded and cold-formed high-strength steel (e.g., S690 plates, rectangular HSS, box sections) have contributed to understanding flexural buckling behavior in high-strength applications, those findings may not directly translate to rolled W-shape columns, where residual stress magnitudes, distributions, and geometry differ substantially. A more targeted evaluation of design curve applicability is therefore needed for high-strength rolled shapes, particularly those produced to ASTM A913 specifications.

The hot-rolled wide flange shapes that have been used in U.S. building construction to date are high-strength low-alloy (HSLA), including the use of the QST process with specified yield strengths up to 80 ksi (550 MPa). These products are readily available for supply to projects in the United States and across the world, although domestic production of rolled shapes exceeding $F_y = 65$ ksi is currently limited to a small number of producers. These products are permitted for use in steel buildings per AISC 360 (2022b), Section A3.1a (Listed Materials), and shown in Table A3.1. Hot-rolled wide-flange shapes listed in Table A3.1 with F_y values of 65 ksi (450 MPa) or greater are duplicated here in Table 1. As shown in Table 1, ASTM A913 is a quenching-and-self-tempering (QST) processed specification developed specifically for rolled structural shapes in Grades 65, 70, and 80. ASTM A572 is a general-purpose, high-strength low-alloy steel specification applicable to plates, bars, and shapes, but it does not require QST processing. ASTM A709 (2018b) is a bridge steel specification that integrates requirements from A913 or A572, depending on the grade and intended application. For instance, A709 Grade 70W (QST) corresponds to A913 Grade 70 with additional requirements for notch toughness and weldability. This study focuses exclusively on wide-flange shapes produced to ASTM A913 Grade 80.

AISC 360-22 allows the usage of the materials shown in Table 1 with a specified F_y of 65 ksi to be used without any special limits or considerations, including designing by inelastic analysis (AISC 360-22, Appendix 1). The allowable use of inelastic analysis infers these steels possess adequate static ductility when designing within the prescribed limits of AISC 360, including utilizing limits on cross-sectional geometrical limits and component slenderness.

For materials listed in AISC 360-22 with a specified yield stress greater than 65 ksi (in Table 1, this would include A913/A913M Gr. 70 and Gr. 80 material), there are both explicit prescribed limitations when using these materials (such as prohibition to use them if plastic hinging is

expected based on inelastic analysis per Appendix 1, Section 1.3.2a) and design rules that likely do not apply to these materials in the same way as lower strength materials. However, major evidence exists that current design rules (e.g., AISC 360-22, Eurocode 3, Part 1-1) are likely overly conservative for these high-strength steels when employed as structural steel columns, due in part to assumptions regarding residual stresses (Ban et al., 2013; Shi et al., 2012; Li et al., 2016; Stroetmann and Penner, 2024).

The column design curve adopted in Eurocode 3, Part 1-1 (CEN, 2005a), are based on the Perry-Robertson formulation, with calibration performed using an extensive experimental database assembled by the European Convention for Constructional Steelwork (ECCS). The curve families (designated by imperfection factors α) reflect the effect of geometric imperfections and residual stresses across different cross-section types. These include cold-formed, hot-rolled, and built-up shapes, with the choice of α determined by member type and fabrication method. Based on these conditions, Eurocode 3 (EC3) provides a family of five column buckling curves (a_0, a, b, c, d), with each curve tailored to different residual stress distributions, imperfection sensitivities, and section types. Curve a_0, for example, reflects high-quality hot-rolled sections with low imperfection amplitudes, while curves c and d are reserved for fabricated or cold-formed members more prone to geometric variability. This multiplicity of curves allows Eurocode 3 to better reflect the diverse behaviors of different steel column types.

In contrast, AISC 360, Chapter E, adopted a single unified column design curve for simplicity and conservatism, which was developed based on calibration studies primarily using mild steel grades such as ASTM A36 (2019a) and A572 Grade 50. These calibrations—originally developed through the Structural Stability Research Council (SSRC) and summarized in its *Guide to Stability Design Criteria for Metal Structures* (Galambos, 1998)—assumed idealized residual stress patterns (e.g., $\pm 0.3F_y$ for flanges and webs) and geometric imperfections representative of conventional rolling and fabrication processes from the 1960s to 1980s. The development of this column curve is based on assumptions regarding initial out-of-straightness and residual stress distributions, as outlined in Appendix 1 of AISC 360. However, modern high-strength rolled shapes (e.g., A913 Grade 80) produced by QST processes tend to exhibit reduced residual stress magnitudes (relative to F_y) and more uniform geometric tolerances due to tighter production controls. As a result, application of the existing AISC curve—originally intended as a single conservative envelope—may be overly restrictive for such shapes, especially in the inelastic slenderness range where residual stresses and geometric imperfections play a dominant role. In this study, the validity of these assumptions is assessed for high-strength rolled W-shape columns by explicitly modeling residual stress distributions and initial imperfections in finite element (FE) simulations. The resulting buckling strengths are then compared to those predicted by Chapter E to evaluate whether the current design curve remains appropriate for A913 Gr. 80 shapes, or if modification may be warranted.

The primary objective of this study is to investigate the flexural buckling behavior of wide-flange rolled steel columns fabricated from both conventional mild steel [ASTM A992 (2020), $F_y = 50$ ksi] and high-strength structural steel (ASTM A913 Grade 80, $F_y = 80$ ksi). Finite element models are developed to incorporate validated residual stress distributions, initial geometric imperfections, and nonlinear material behavior. The simulated minor and major axis buckling responses are used to evaluate the accuracy and applicability of the current AISC 360-22 column design provisions across a range of cross-sectional geometries and slenderness ratios. The inclusion of A992 serves as a reference baseline to benchmark current design performance, while the comparison to A913 Gr. 80 highlights potential deviations that may warrant refinement of existing design curves for high-strength rolled W-shape columns. As mentioned before, AISC 360 and Eurocode 3 design column curves are rooted in decades of experimental and analytical research and are the result of rigorous reliability-based calibration procedures (e.g., the SSRC Column Curves for AISC and Perry-Robertson-based methods for EC3). These were based on extensive databases covering a wide range of geometries, materials, and imperfections, providing statistically defensible strength predictions across broad design applications. The current study does not attempt to replicate this statistical calibration effort but, instead, uses validated finite element simulations to assess how the EC3 and AISC 360 curves compare when applied to A913 Gr. 80 (F_y = 80 ksi) wide-flange sections.

PRIOR RESEARCH ON HIGH-STRENGTH STEEL

Numerous experimental and numerical studies have examined the flexural buckling behavior of high-strength steel members. Much of the prior work has focused on built-up or welded sections fabricated from plate products such as S690 ($F_y = 690$ MPa or 100 ksi) steel, which can exhibit different residual stress profiles and imperfection sensitivities compared to rolled shapes. Studies have also investigated cold-formed hollow structural sections (HSS), including square and rectangular tubes formed from high-strength strip steel. These sections often behave differently due to the cold-forming process and are governed by different design provisions.

Rasmussen and Hancock (1995) investigated the flexural buckling capacity of 12 welded H-sections and 13 box sections with yield strengths of 100 ksi and higher. They found that the Australian, American, and British standards

were conservative, and they suggested using buckling curve *a* instead of curve *c* in European standards for minor axis buckling when using HS3. Li et al. (2012) conducted 12 tests on welded box and H-sections and confirmed that buckling curve *a* is more accurate than curve *c* in European standards, and certain European buckling curves may be overly conservative for high-strength steel columns. Ban et al. (2013) tested six welded box and H-sections made from 140 ksi steel, evaluating their buckling behavior and suggesting modifications to existing design curves. They recommended buckling curve *a* in European standards for these columns. In addition, their study suggested a revised imperfection factor for European standards with further validation. Khan et al. (2013) investigated 15 welded box sections, focusing on composite columns, and recommended using buckling curve *a* in European standards for composite high-strength steel and high-strength concrete (HSC) sections. Wang and Gardner (2013) tested eight hot-finished rectangular HSS columns with yield strength of 100 ksi and recommended using AISC 360 as-is or Eurocode 3, Part 1-1, with some modifications. Ma et al. (2015) investigated welded H-sections made from S690 steel, assessing the applicability of existing design standards to slender columns. Their study concluded that Eurocode 3, Part 1-1, underestimates buckling resistance and AISC 360 better matches actual failure loads. Somodi and Kövesdi (2016, 2017) studied the flexural buckling behavior of 12 cold-formed rectangular HSS columns made of 100 and 140 ksi steels. Their study suggested that curve *b* in European standards should be used for columns made of 70–100 ksi steel and curve *a* should be used for 140 ksi steel columns. Additional tests on six welded box-sections indicated that curve *c* is conservative, recommending curve *a* for 70–140 ksi steel columns.

More recently, Sun et al. (2020), presented experimental and numerical studies on the flexural buckling of S690 high-strength steel welded I-section columns. Comparisons with European (Eurocode 3, Part 1-2), American [ANSI/AISC 360 (2016)], and Australian [AS 4100 (2020)] standards showed that Eurocode 3, Part 1-2 (CEN, 2005b) and AS 4100 were overly conservative in predicting buckling resistance, whereas AISC 360-16 provided reasonable predictions, but with some overestimated resistances for intermediate and long columns. The authors proposed an improved design approach that modifies the EC3 buckling curve, leading to safer and more accurate resistance predictions. Ferreira Filho et al. (2022) studied the flexural buckling resistance of S690 high-strength steel welded I-section columns and beam-columns. The research includes experimental testing, numerical modeling, and an evaluation of current design standards (Eurocode 3, AISC 360, AS 4100). The results of the study indicated that EC3 was overly conservative, underestimating buckling resistance, whereas AISC 360 was more accurate but slightly overestimated resistance in some cases. AS 4100 results were also conservative, similar to Eurocode 3. Hence, the authors proposed a revision of buckling curves in EC3 to better reflect welded I-section column behavior.

Yun et al. (2023) investigated the flexural buckling behavior of homogeneous and hybrid welded I-section columns across a range of steel grades (S235 to S960). The research includes residual stress analysis, experimental testing, finite element modeling (FEM), and evaluation of current design standards. Eurocode 3, Part 1-1 (CEN, 2005a), and AISC 360 were assessed. The results from the study demonstrated that EC3 was too conservative for high-strength steels, underestimating buckling resistance, whereas AISC 360 performed better but was inconsistent for lower steel grades. Based on the responses, the study suggested revising EC3 buckling curves to reflect the effect of steel grade on buckling resistances, which improved accuracy and consistency. Stroetmann and Penner (2024) investigated the buckling resistance and residual stress distributions in welded box columns made from high-strength steel (S460 to S960). The research aims to reassess EC3 (CEN, 2005a, 2005b) buckling curves for HSS columns. It was observed that current EC3 underestimates buckling resistance for high-strength steel columns, and hence, the study suggested revision of buckling curves for welded box sections in EC3. These findings indicate that current design standards (AISC 360, EC3) for HS3 flexural buckling may be overly conservative as indicated in Figure 1 and may need revision to prevent overly conservative and uneconomical designs.

In Figure 1, the critical buckling strength is normalized by the yield stress, F_{cr}/F_y and plotted in the vertical axis, and the nondimensional slenderness ratio λ is plotted in the horizontal axis, which is given by Equation 1 as follows:

$$\lambda = \frac{1}{\pi}\frac{L_c}{r}\sqrt{\frac{F_y}{E}} \tag{1}$$

In this plot, comparisons are made among the experimental responses, AISC 360, and EC3 high-strength column buckling curves. This figure clearly demonstrates that the column buckling strengths predicted from the design standards are overly conservative. The EC3 column buckling curve *a* is comparable with the AISC 360 column curve, and EC3 column buckling curve a_0 is showing the most reasonable prediction of the experimental buckling strengths. Note that the addition of curve a_0 in EC3 was done because it was noted that relatively higher-strength steels are generally used in tubular profiles, resulting in higher resistances (Beer and Schulz, 1975). As a result, it is anticipated that the a_0 curve will represent the experimental responses better than the other EC3 curves. Also note that most of the experimental data plotted in Figure 1 are based on tests on

welded H, I, and box sections that may not behave similar to rolled shapes. While valuable in understanding the broader behavior of high-strength steel columns, the findings from these prior studies may not be directly transferable to hot-rolled W-shape columns produced via QST. Therefore, while it is important to acknowledge the broader literature on high-strength steel members, the present study focuses specifically on rolled W-shape sections produced to ASTM A913 standards (Grade 80), where residual stress distributions, material hardening, and geometric imperfections differ substantially from built-up or cold-formed sections.

FINITE ELEMENT MODELING

Three-dimensional (3D) nonlinear finite element models are developed for wide-flange rolled-shape columns using the finite element analysis (FEA) software ANSYS (ANSYS, 2023). The finite element models include geometric and material nonlinearities. The simply supported columns are modeled and discretized by 20-noded solid brick elements (SOLID 186). It is defined by 20 nodes having three degrees of freedom at each node: translations in the nodal x, y, and z directions. This type of element has plasticity, hyperelasticity, stress stiffening, creep, large deflection, and large strain capabilities. A typical finite element mesh of a column along with the boundary conditions for simulating major and minor axis buckling is shown in Figure 2. The fillet present in the rolled shapes is not modeled and the cross-sectional area, moment of inertia, and radius of gyration are calculated without consideration of the fillets. The x-axis corresponds to the longitudinal column axis, and the y- and z-axes are in the plane of the cross section. The y-axis is parallel to the web, and the z-axis is parallel to the flanges. All the column configurations for

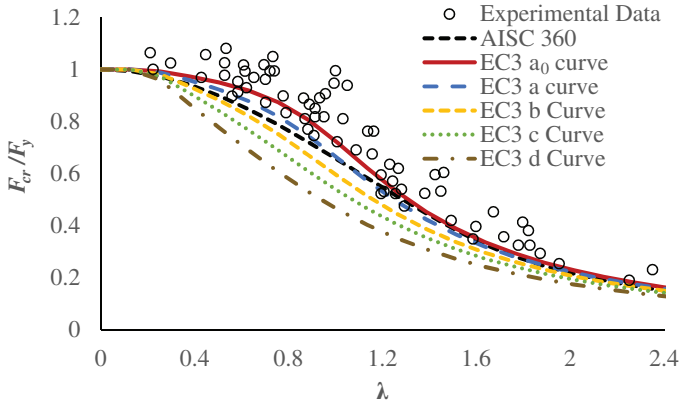

Fig. 1. Comparison of the experimental results (Rasmussen and Hancock, 1995; Li et al., 2012; Ban et al., 2013; Khan et al., 2013; Wang and Gardner, 2013; Ma et al., 2015; and Somodi and Kövesdi, 2016, 2017) on HS3 columns and the normalized flexural buckling curves.

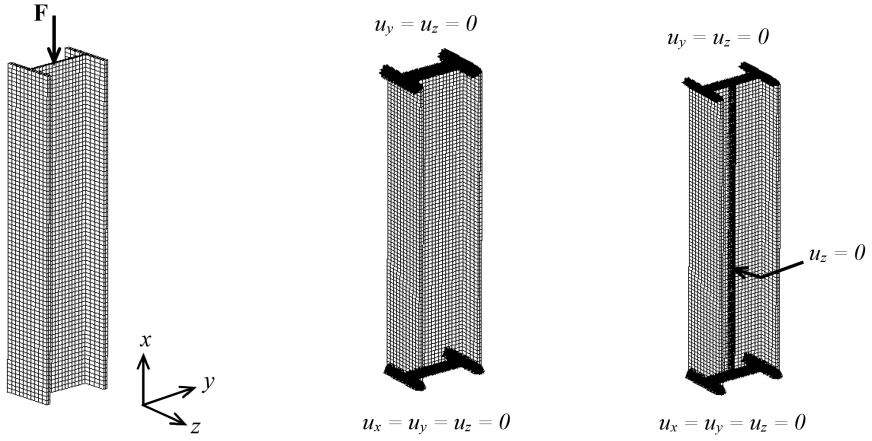

(a) FE mesh *(b) Minor axis buckling* *(c) Major axis buckling*

Fig. 2. A typical finite element mesh of a wide flange column with boundary conditions for minor and major axis buckling.

the present investigation are simply supported. The column is pin-supported at the bottom, and the same boundary condition is applied at the top with the exception that vertical translation is permitted [Figures 2(b) and 2(c)]. For major axis buckling, the column is restrained against minor axis deflections by translational supports along the length as shown in Figure 2(c).

Material Model

In the finite element modeling of columns, it is important to use the characteristic yield stress related to the grade of steel and the shape of the material stress-strain curve. It has been demonstrated that the yield plateau and strain hardening have an influence on short columns with low slenderness (Snijder et al., 2014; Jönsson and Stan, 2017); however, for slender columns, no significant difference is seen, with respect to differences in strain hardening or having a yield plateau (Moghadam, 2015; Jönsson and Stan, 2017). Most of the studies in the literature demonstrated that an elastic-perfectly plastic material model can reasonably provide the code-specified column buckling responses (Snijderet al., 2014).). In this study, column buckling responses are investigated for ASTM A992 steel and A913/A913M Gr. 80 high-strength steel to understand the applicability of AISC 360-22 column curves in predicting the column buckling strength. The nonlinear material properties of ASTM A992 steel and A913/A913M Gr. 80 structural steel in ANSYS are incorporated using the multilinear kinematic hardening model with the initial elastic modulus, Poisson's ratio, and stress-strain data obtained from the uniaxial tension tests.

The multilinear kinematic hardening model is a rate-independent plasticity model that accounts for the effect of plastic deformation on the Bauschinger effect (Bauschinger, 1886). The constitutive equations are based on a von Mises yield function, associated flow rule, and a kinematic hardening rule. An overview of the multilinear kinematic hardening model is given below to show different features of the model. The yielding is determined by von Mises criterion:

$$f(\underline{\sigma}-\underline{\alpha})=\left[\frac{3}{2}(\underline{s}-\underline{a})(\underline{s}-\underline{a})\right]^{1/2}=\sigma_0 \tag{2}$$

where $\underline{\sigma}$ is the stress tensor, $\underline{\alpha}$ is the current center of the yield surface in the total stress space, $\underline{s}$ is the deviatoric stress tensor, $\underline{a}$ is the current yield surface center in the deviatoric space, and σ_0 is the initial size of the yield surface. The associated flow rule is used to calculate the rate-independent plastic strain increments:

$$d\underline{\varepsilon}^p=d\lambda\frac{\partial f}{\partial\underline{\sigma}}=\frac{3}{2}dp\frac{\underline{s}-\underline{a}}{\sigma_0} \tag{3}$$

The kinematic hardening rule is based on backstress evolution, which defines the translation of the yield surface. The general form is as follows:

$$d\underline{a}=\frac{2}{3}Cd\underline{\varepsilon}^p-\gamma\underline{a}dp \tag{4}$$

where C is the initial kinematic hardening modulus, γ is hardening parameter that controls how backstress saturates, and dp is the plastic strain rate. The multilinear approach approximates nonlinear hardening behavior using piecewise linear segments, instead of using a smooth curve. The total backstress is computed as:

$$d\underline{a}=\sum_{i=1}^{n}d\underline{a}_i \tag{5}$$

where each $\underline{a}_i$ follows a linear hardening rule with its own modulus.

The uniaxial tension test data for ASTM A992 was obtained from the tests performed by Morrison (2015) as shown in Figure 3(a) along with the fitted multilinear model in engineering stress-strain format for consistency with the original test data. However, for numerical implementation in ANSYS, the experimental data were converted to true stress-true plastic strain, which is the required input format for the multilinear kinematic hardening model. Similar to other conventional mild steel, A992 steel exhibited a yield plateau with a longer strain-hardening region and higher ductility. Additionally, it is important to note that the multilinear plasticity models in ANSYS Mechanical APDL do not accept negative slopes in the stress-strain input data. That is, the input curve must be nondecreasing in stress with respect to strain. For this reason, material softening cannot be captured directly in this model. As a result, the plasticity curves were truncated prior to the onset of instability and localization.

In the multilinear model, the elastic modulus of A992 steel is taken as 29,000 ksi with yield stress and tensile strength of 50 and 67 ksi, respectively. Data from five uniaxial tension test coupons performed by a producer of A913/A913M Gr. 80 hot-rolled, wide-flange shapes were provided for the current study. The stress-strain data is presented in Figure 3(b) with the fitted multilinear model used in the simulations as well as the elastic-perfectly plastic (EPP) model for comparison. It is observed that A913/A913M Gr. 80 material does not exhibit a yield plateau, and hence, the 0.2% offset method is used to calculate the yield stress of each coupon which, was found to be close to 80 ksi on average. The modulus of elasticity was comparable among the five tests performed, which is taken as 29,000 ksi in the multilinear model. The strain-hardening region is very small, demonstrating a lower ductility. Similar observations were made in the study performed by Stall et al. (2024) for ASTM A656/A656M (2018a) Gr. 80 steel.

Modeling of Initial Imperfection

Von Kármán (1907) identified out-of-straightness and out-of-plumbness as the most critical global imperfections affecting column buckling. Modern standards, including Eurocode 3, Part 1-1 (CEN, 2005a), and AISC 360-22, set limits on these imperfections, with Eurocode 3 being more conservative. The out-of-straightness imperfection amplitude of $L/1500$ was adopted for the AISC 360 standard (Tide, 2001) for developing the column buckling curves, which is close to the average value determined statistically by Bjorhovde (1972), whereas Eurocode 3 adopted $L/1000$ as the out-of-straightness imperfection value (Beer and Schulz, 1975; Strating and Vos, 1975). These standardized values were established based on research conducted between the 1960s and 1980s in the United States, Europe, and Japan. Experimental studies by Fukumoto and Itoh (1983) showed that the maximum out-of-straightness imperfection is usually exhibited by the IPE160 sections, which is in the range of $L/1000$, while hot-rolled tubular and welded wide-flange sections had smaller out-of-roundness imperfections, leading to better buckling performance. As a result, the assumption of $L/1000$ initial imperfection for all the available column sections is an overly conservative approach of including the out-of-straightness in the buckling strength calculation in Eurocode 3. Note that the unified column curve in AISC 360-22 is based on SSRC Column Curve, 2P, which assumes an initial out-of-straightness of $L/1500$ for analytical purposes. However, it is important to note that AISC 360 itself does not prescribe fabrication or erection tolerances. Actual tolerances for out-of-straightness and out-of-plumbness are governed by AISC 303, *Code of Standard Practice* (2022a), which references applicable ASTM standards in Section 11.2.2.1. For wide-flange rolled shapes, these standards typically specify a fabrication tolerance of approximately $L/1000$, indicating that the imperfections used in the design curve derivation are slightly more severe than typical fabrication practice.

Beyond global imperfections, local imperfections arise due to fabrication processes, with their shape and amplitude varying by manufacturing method. While these imperfections were not directly studied in buckling experiments, their effects on flexural buckling resistance were included in statistical analyses alongside factors like boundary conditions, out-of-plumbness, and material properties (Bjorhovde, 1972; Fukumoto and Itoh, 1983).

For nonlinear buckling analysis to be accurate using finite element simulation, it is necessary to set an initial imperfection in the column being modeled along with the residual stress distribution. The shape of the geometric imperfection is based on the buckling mode belonging to the lowest eigenvalue from a linear buckling analysis. This usually results in a sinusoidal bow imperfection. The amplitude defining the maximum deviation from the ideal geometry is taken as $L/1500$ as used in AISC 360 for buckling simulation of the columns. The imperfections of the finite element model are established by first performing a linear buckling analysis on the perfect prismatic column model with given boundary conditions, then the relevant (displacement) normalized global buckling mode is extracted. In the following nonlinear FE calculations, the imperfections are established by importing the normalized displacements of the lowest global buckling mode in the relevant plane of buckling as shown in Figure 4, multiplying this by the maximum imperfection magnitudes and updating the nodal coordinates of the model by adding the established nodal imperfections.

Modeling of Residual Stresses

Structural steel members develop residual stresses due to manufacturing and fabrication processes. Depending on size and welding procedure, the magnitude and distribution of these residual stresses can vary significantly in members. Hence, it is challenging to accurately predict the magnitude

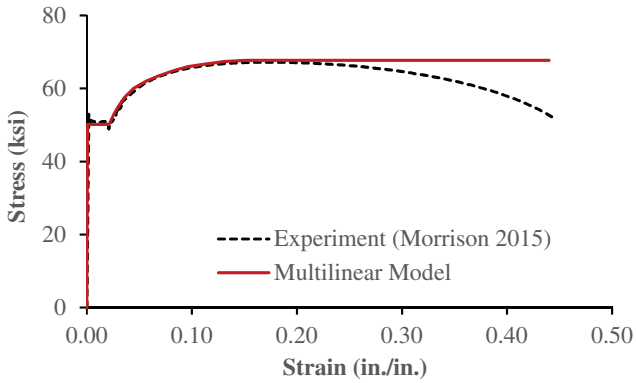

(a) ASTM A992 steel (data from Morrison, 2015).

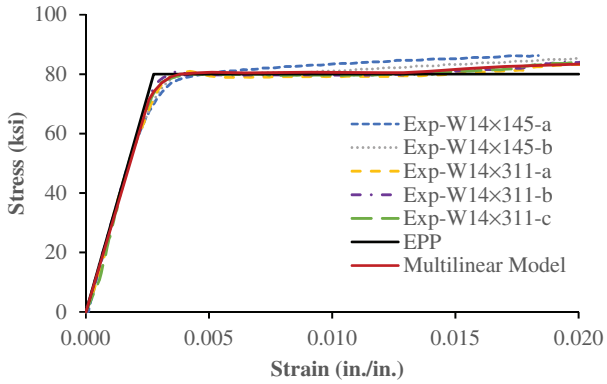

(b) A913/A913M Gr. 80 steel (producer supplied data).

Fig. 3. Uniaxial tension test data along with the fitted material models in engineering stress-strain format.

and distribution of residual stresses in steel structural members, which can substantially affect their structural performances, including global and local flange-buckling strengths, seismic performances, and low-cycle fatigue responses. Residual stresses are either ignored or a simplified distribution is assumed in the analysis and design of structural members. Literature suggests that the presence of residual stresses can influence the sensitivity of beam design curve (Rossi et al., 2021) in the intermediate length range and can be crucial for structural steel columns and welded connections (Huber, 1956; Lamarche and Tremblay, 2011; Mathur et al., 2012). The monotonic buckling strength and cyclic strength degradation of columns in a structural steel frame are substantially influenced by the initial residual stresses (IRSs) (Lamarche and Tremblay, 2011; Mathur et al., 2012).

Previous studies on the nonlinear buckling analysis of steel columns showed that the simplified linearized distribution of residual stresses yielded conservative results. However, most of the residual stress distribution for the rolled shapes available in the literature was developed in the 1970s based on ASTM A36 steel, and it is warranted that residual stresses be measured for high-strength steel rolled shapes. Jönsson and Stan (2017) pointed out that if the magnitude of residual stresses is wrongly assumed to be proportional to the yield stress, the column buckling capacity of steel columns found by finite element analysis will be underestimated for higher grades steel. A study by Boissonnade and Somja (2012) also demonstrated that placing different steel grades on the same buckling curve leads to an overly conservative design for high-strength steels. Hence, in this study, the multiaxial residual stress distribution in the rolled shapes considered in the analysis is developed by using a sequentially coupled thermomechanical analysis as presented in Quayyum and Hassan (2017). This computational scheme was validated against four W-sections using A36 steel (Quayyum and Hassan, 2017). In this study, the column buckling capacities are investigated for A992 and A913/A913M Gr. 80 steels. Hence, it is important to understand the accuracy of the computational scheme in predicting the magnitude and distribution of residual stresses in W-shapes using these steels.

The numerical scheme for residual stress simulation assumes that during the manufacturing of W-shapes, residual stress distribution observed in a W-shape primarily develops during the cooling process after hot rolling (Alpsten, 1968). Hence, this study simulated only the evolution of residual stresses during the cooling process. In cooling process simulation, the real-time temperature field in W-shapes during cooling after hot-rolling is calculated first by employing heat transfer analyses. The temperature field at each step of the heat transfer analysis is stored and used as an input in the residual stress analysis for calculating the evolution of stress and strain fields in the W-shapes during the cooling process—that is, the heat transfer analysis is sequentially coupled with thermomechanical residual stress analysis. The link between the heat transfer analysis and stress analysis is obtained through the temperature history, which is input as the thermal load in the residual stress analysis.

In the thermal analysis, the finite element models of the W shapes are discretized by 20-noded solid thermal elements (SOLID279). These elements have temperature as one degree of freedom at each node. The W-shapes are initially heated to a uniform temperature of 1300ºC, which is kept constant for 10 min before starting the air cooling. The

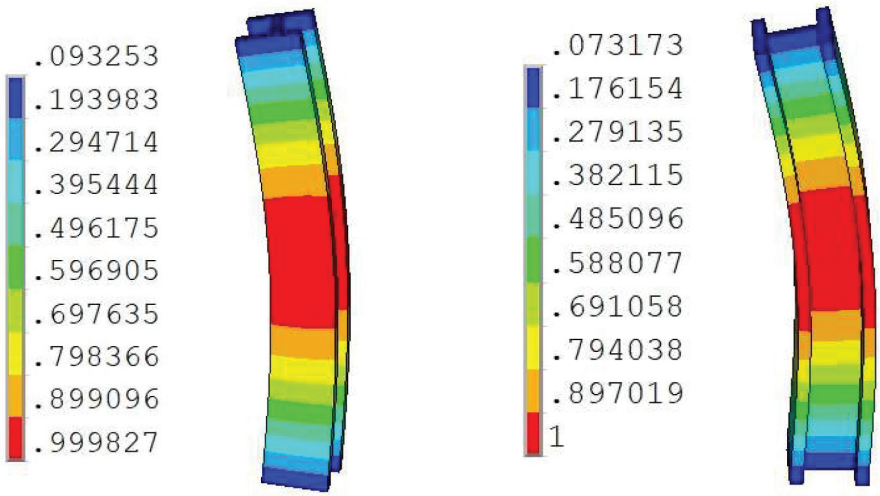

(a) Minor axis *(b) Major axis*

Fig. 4. Normalized displacements of the lowest global buckling mode from elastic buckling analysis.

air cooling is simulated in thermal analysis by using a heat transfer coefficient, which includes convection, conduction, and radiation into the air. The material is considered homogeneous and isotropic throughout the cross section, and the material coefficients such as specific heat, thermal conductivity, and heat transfer coefficient are defined as a function of temperature. The simulation of the heat transfer from the surface of the W-shapes largely depended on the heat transfer coefficient, which includes the effect of convection, conduction, and radiation. The density of the material is assumed constant. Enthalpy of the material is defined as a function of temperature in order to account for the phase transformation (Comini et al., 1974). In the thermal finite element analysis, a uniform temperature of 25°C is assigned to all nodes as the initial boundary condition and the reference temperature for thermal strain calculations. At each time step, heat transfer is applied to each node of the solid model surface, and then the solid model surface loads are transferred to finite element model. At each time step, the material properties are assigned as a function of nodal temperature. The temperature distribution of a W12×87 section is presented in Figure 5 at different stages of the cooling process.

This shows that the W-shapes are not uniformly cooled; the cooling is faster at the edges of the beam and at the mid-depth of the beam web compared to the flange-web junction area. The cooling rate is slightly reduced when the phase transformation temperature (650°–760°C) has been reached, owing to phase transformation heat. After the phase transformation region, the cooling rate increases almost to the rate at the inception of phase transformation and continued cooling with progressively reduced rates to reach the room temperature.

The residual stress analysis uses the temperature history from the thermal analyses as an input. The nodal temperature history at each of these steps shall be considered thermal load for the corresponding node from a structural model in this analysis. Therefore, it is necessary to match the number of meshes and nodes for stress analysis with those applied in a temperature analysis. This is accomplished by changing the element types from thermal solids (SOLID279) to structural solids (SOLID186) by using the ETCHG command available in ANSYS. For the constitutive model chosen, the temperature-dependent material properties for structural steel are required for the residual stress analysis. Note that material and geometrical nonlinearities are incorporated into the residual stress computation. The essential material properties required in the analysis are density, initial yield stress, elastic modulus, Poisson's ratio, and thermal expansion coefficient. It is assumed that the density remains constant while the other material properties are dependent on the temperature. The initial yield stress, the elastic modulus, and the multilinear kinematic hardening model parameters are determined from the monotonic stress-strain responses of ASTM A992 steel at various temperatures obtained from Hu et al. (2009) as shown in Figure 6. For details of the material properties and model parameters, the readers are referred to Quayyum and Hassan (2017).

In the thermomechanical analysis, 25ºC is considered as the reference temperature for thermal strain calculations, and the nodal temperatures at each time step from the thermal analysis are read to calculate the corresponding stresses and strains at the time step by using the temperature-dependent structural material properties of steel. The simulated residual stress contours for a W12×87

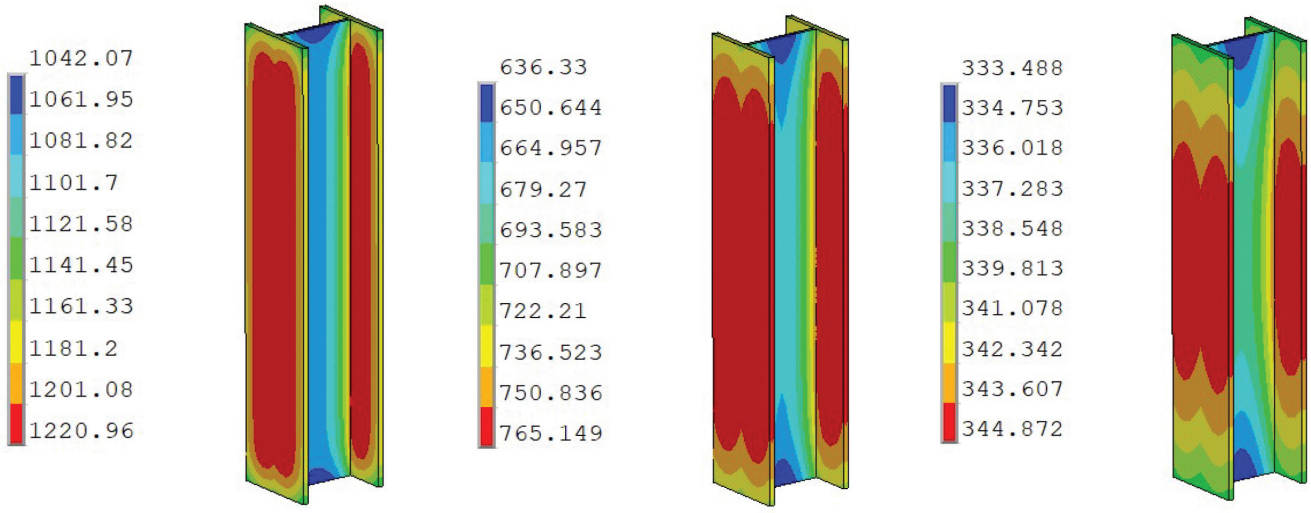

(a) 15 minutes *(b) 45 minutes* *(c) 105 minutes*

Fig. 5. Temperature distribution (in K) during cooling of W12×87 section from initial 1300°C reheat temperature.

section is plotted in Figure 7 at different stages of cooling. It is observed that the residual stresses are initially tensile in the web that turns compressive with the progression of cooling. On the other hand, the residual stresses are initially compressive in the flange-web junction but turn tensile with the progression of cooling. The residual stresses stabilized after 2 hr of cooling. The simulated residual stresses after cooling to ambient temperature at the beam mid-length are compared to the measured values from Lamarche and Tremblay (2011) in Figure 8. The simulation results show that the computation scheme is able to predict the residual stresses in the web and flanges of W12×87 section with good accuracy. This further validates that the computational scheme previously validated for A36 steel can also be applicable to determine the residual stresses in W-shapes with A992 steel. The residual stresses predicted by the model proposed by Galambos and Ketter (1959) are also plotted in Figure 8 for comparison purposes. It is observed that the flange and web stresses are underpredicted by the Galambos and Ketter model (1959). Note that the web stress is assumed tensile in the Galambos and Ketter (1959) model, whereas the measured stress in the web is both tensile and compressive. This is also true for many other shapes (Fujita, 1955; Huber, 1956; Alpsten, 1968). Based on this observation, this study considered residual stress distribution obtained from the finite element simulation as the initial stress state in the wide flange column shapes for buckling strength calculations.

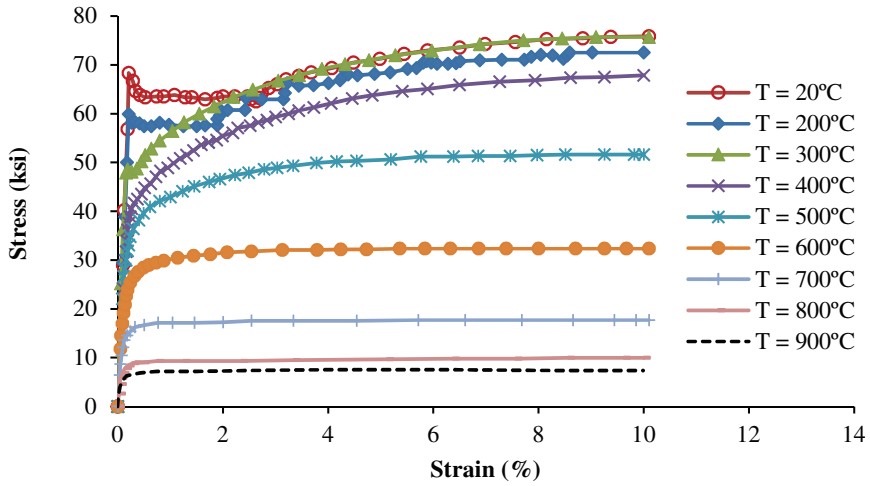

Fig. 6. Monotonic stress-strain response of ASTM A992 steel at various temperatures (Hu et al., 2009).

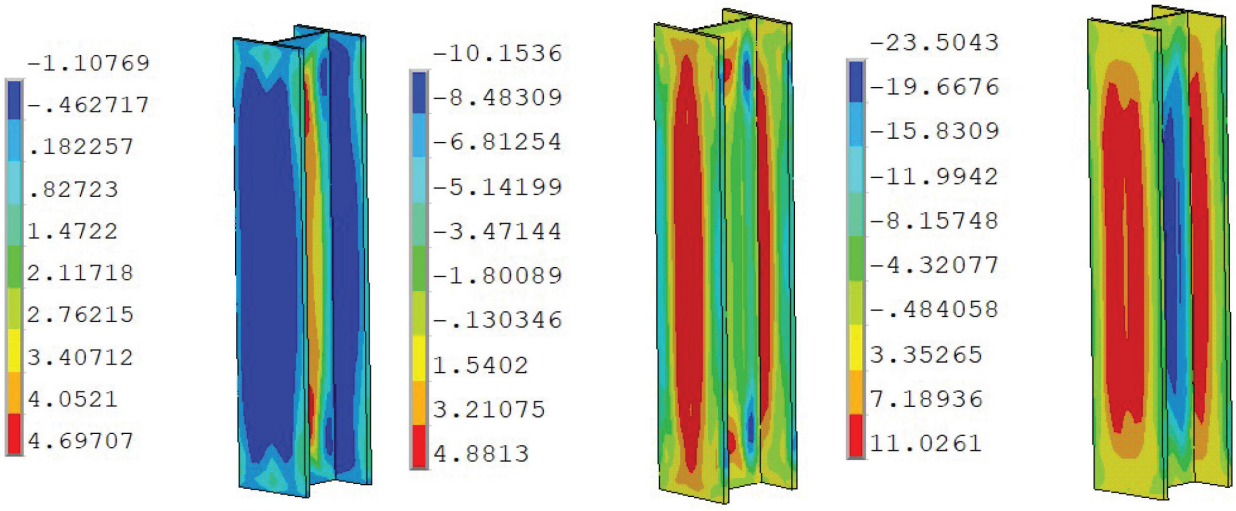

(a) 15 minutes *(b) 45 minutes* *(c) 2 hours*

Fig. 7. Longitudinal stress contour (in ksi) of hot-rolled W12×87 section at various instances after the start of cooling.

In order to investigate whether the computational scheme can predict the residual stresses in rolled wide-flange shapes made of A913/A913M Gr. 80 steel, the experimental data from Spoorenberg et al. (2013) is obtained for a W14×808 quenched and self-tempered (QST) section. This section is provided by ArcelorMittal (2020) with a yield stress around 80 ksi, and the residual stresses were measured by the sectioning method. The computational scheme as discussed earlier is used to simulate the residual stresses in a W14×808 section. However, material properties of A913/A913M Gr. 80 steel are not available for elevated temperatures. As a result, the thermal material properties, such as specific heat, thermal conductivity, enthalpy, and heat transfer coefficient, and some of the structural material properties, such as Poisson's ratio, density, and thermal expansion coefficient of A913/A913M Gr. 80 steel, are considered the same as used in the simulation of A992 steel. On the other hand, the elastic modulus and the stress-strain data for 80 ksi steel are obtained from the study performed by Huang et al. (2018) as shown in Figure 9, where they investigated the elevated temperature material properties of Chinese Q550 steel.

These stress-strain data were fitted with a multilinear model to incorporate the nonlinear material properties in the simulation at different temperatures. Similar to W12×87 consisting of A992 steel, it is observed that the residual stresses in W14×808 are initially tensile in the center of the web, which turns compressive with the progression of

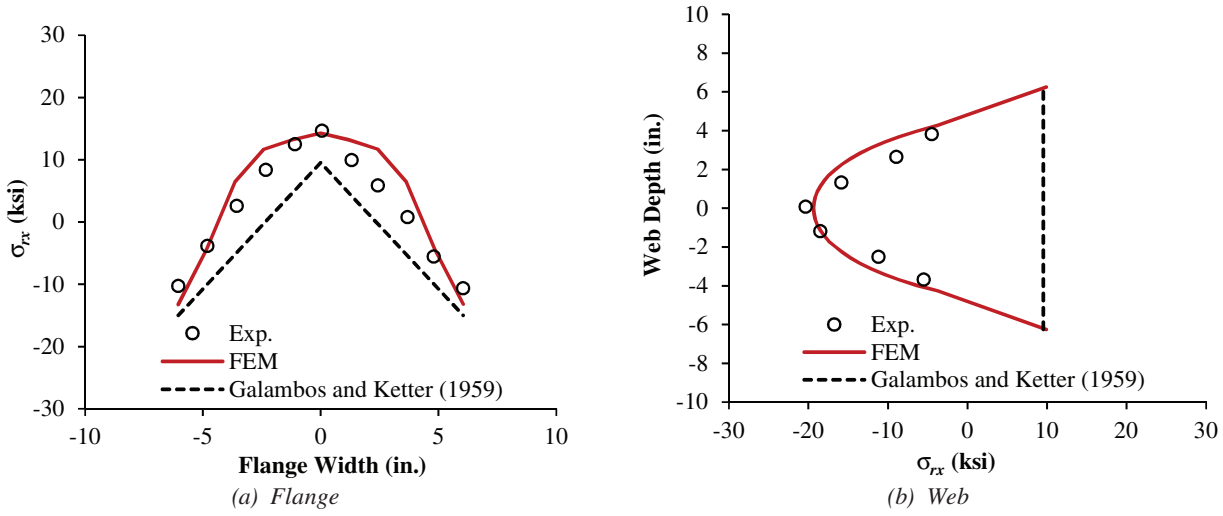

(a) Flange *(b) Web*

Fig. 8. Comparison of FEM and analytical simulations to measured IRSs in the flange and web of ASTM A992 W12×87 beam section (data from Lamarche and Tremblay, 2011).

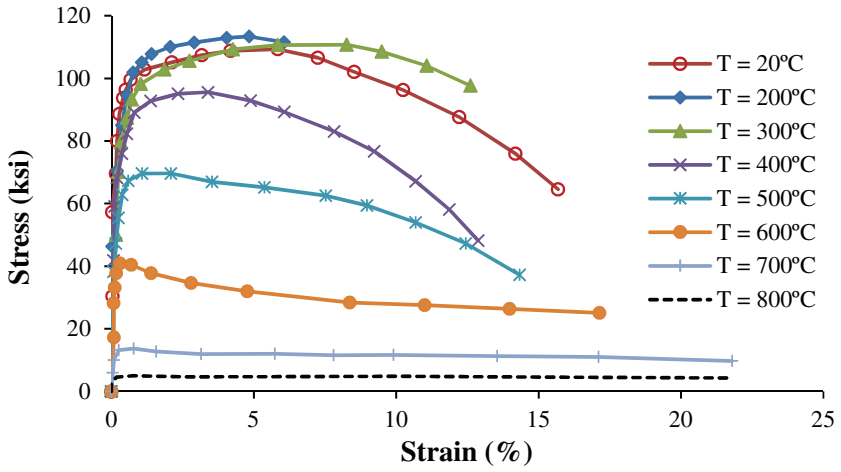

Fig. 9. Monotonic stress-strain response of Q550 steel at various temperatures (Huang et al., 2018).

cooling. On the other hand, the residual stresses are initially compressive in the flange-web junction, which turns tensile with the progression of cooling. Because of thicker flanges, the residual stresses stabilized almost after 12 hr of cooling. The simulated residual stresses after cooling to ambient temperature at the beam mid-length are compared to the measured values from Spoorenberg et al. (2013) in Figure 10 along with a comparison with the Galambos and Ketter (1959) model. The simulation results show good agreement with the measured values; hence, in the simulation of the buckling curves for rolled W-shapes using A913/A913M Gr. 80 material, the simulated residual stress distribution is considered for the rest of the analysis in this study. Note that the prediction of the residual stress in the flanges using the Galambos and Ketter (1959) model is also in good agreement with the measured values; however, the web stress is not predicted well by the Galambos and Ketter model. As mentioned before, the web stress is entirely considered as tensile stress in Galambos and Ketter (1959) model, whereas measured values show the presence of both tensile and compressive stresses in the web.

VALIDATION OF THE FINITE ELEMENT MODEL

The FEM simulated residual stress of W12×87 section shown in Figure 7 is used in the finite element buckling analysis of a column with a 12 ft 2 in. length under displacement-controlled monotonic axial compression. The initial residual stresses are considered as the initial stress state of the column, and the nodal coordinates of the model are updated by adding the established nodal imperfections from elastic buckling analysis. Figure 11(a) shows the global buckling of column about its minor axis from the analysis considering the presence of the simulated residual stresses. Note in Figure 11 that when residual stress is included in the analysis, the initiation of global buckling occurs similarly as in the experiment (Lamarche and Tremblay, 2011), whereas, without residual stress the column remains elastic until buckling initiates. Moreover, simulated responses show local buckling at the mid-height of the column which was also observed during the experiment as shown in Figure 12 (Lamarche and Tremblay, 2011).

Consequently, simulated responses of axial load versus axial displacement [Figure 13(a)] and axial load versus lateral deflection [Figure 13(b)] are compared well to the experimental responses (from Lamarche and Tremblay, 2011) when residual stress is included in the analysis. These results demonstrate the excellent simulation of the buckling strength if FEM simulated multiaxial residual stress is included in the analysis, and overprediction of about 10% is obtained if residual stress is not included in the analysis. Once the global buckling is initiated, the lateral deflection gradually increases, and the axial load decreases with the increase in axial displacement. The post-buckling responses with or without residual stress, however, are very similar to the experimental responses, especially when lateral deflection becomes large [Figures 13(a) and 13(b)]. The validation of the numerical scheme indicates that the finite element modeling techniques described earlier can be utilized further to develop column flexural buckling curves for rolled shapes using A992 and A913/A913M Gr. 80 steels. An important modeling simplification in this study

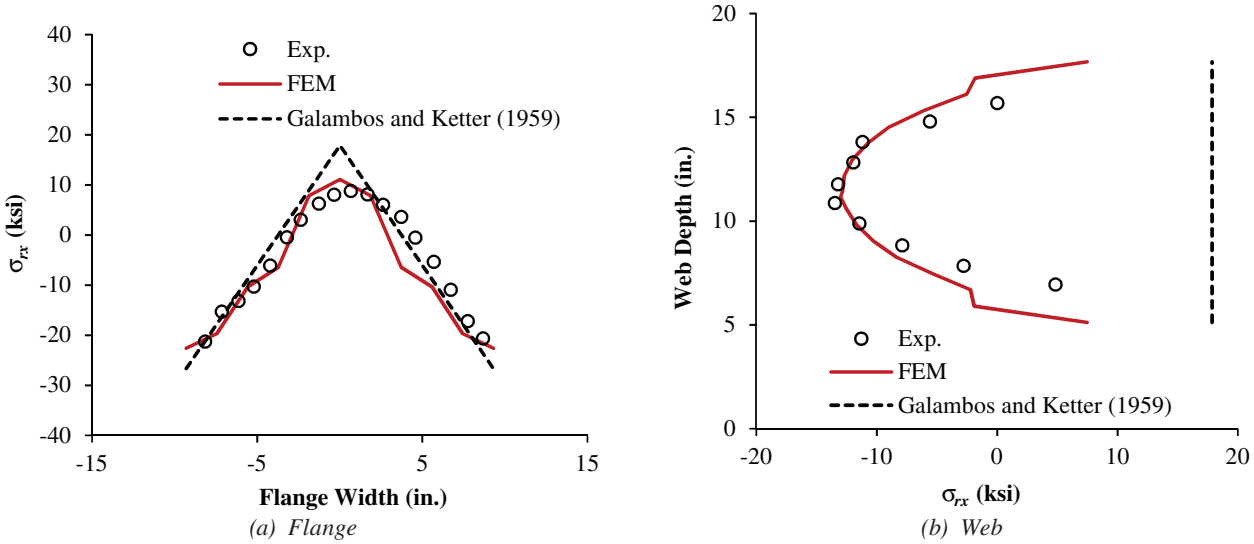

(a) Flange *(b) Web*

Fig. 10. Comparison of FEM and analytical simulations to measured IRSs in the flange and web of 80 ksi W14×808 beam section (data from Spoorenberg et al., 2013).

(a) Experimental response

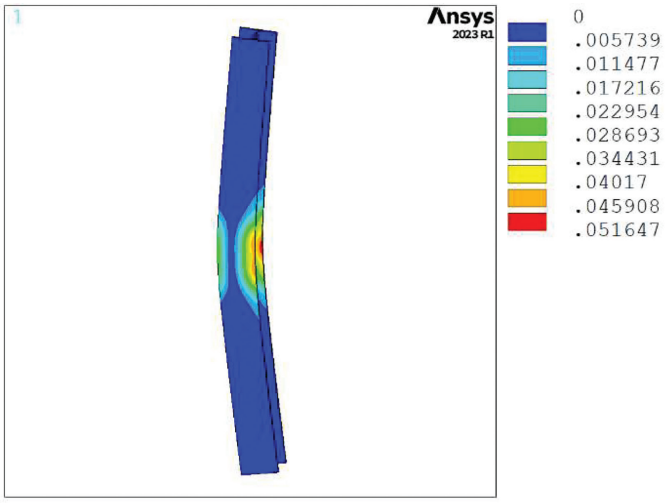

(b) Simulated von Mises plastic strain contour

Fig. 11. Experimental (from Lamarche and Tremblay, 2011) and simulated global buckling of W12×87 *shape about minor axis under monotonic axial compression.*

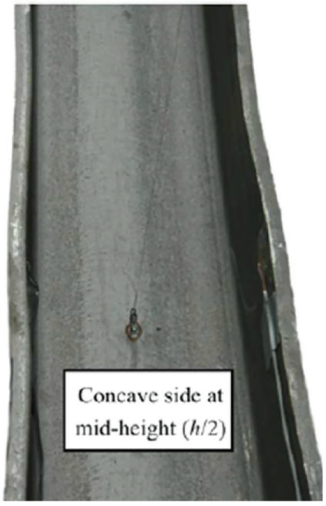

(a) Esperimental response

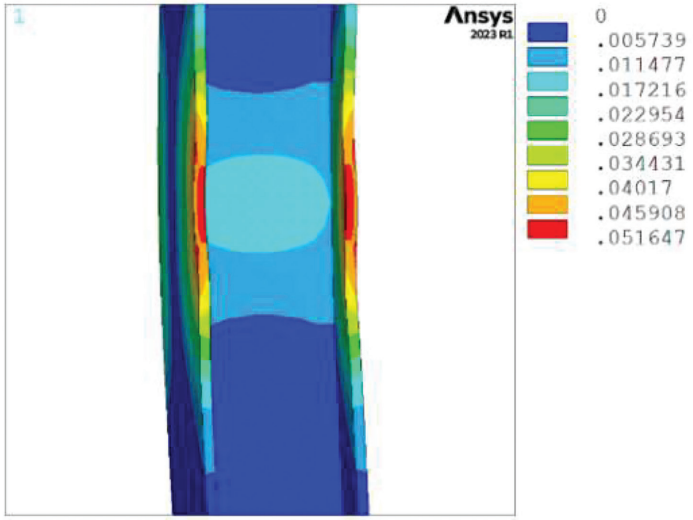

(b) Simulated von Mises plastic strain contour

Fig. 12. Experimental (from Lamarche and Tremblay, 2011) and simulated flange local buckling at the mid-height of W12×87 *shape under monotonic axial compression.*

Table 2. Cross-Sectional Properties of the W-Shapes Investigated for Column Flexural Buckling Using A992 Steel						
					Analysis Performed	
Column Designation	h/b	t_f (in.)	$b_f/2t_f$	h/t_w	Minor Axis	Major Axis
W14×808	1.23	5.12	1.82	3.04	x	
W14×605	1.20	4.16	2.09	4.39	x	
W12×336	1.25	2.96	2.26	5.47	x	x
W14×426	1.12	3.04	2.75	6.08	x	x
W14×257	1.03	1.89	4.23	9.71	x	
W14×193	0.99	1.44	5.45	12.8	x	x
W14×145	0.96	1.09	7.11	16.8	x	x
W12×87	1.03	0.81	7.48	18.9	x	x
W14×82	1.42	0.855	5.92	22.4	x	x
W14×53	1.71	0.66	6.11	30.9	x	

is the omission of the k-area (fillet region between flange and web) in the finite element geometry. While this simplification could influence the local residual stress distribution, especially in thick or heavy sections subjected to minor axis loading, its impact was evaluated by comparing simulation results to measured residual stress patterns and buckling behavior. Specifically, the residual stress distribution in the A992 W12×87 and A913 Grade 80 W14×808 sections was predicted accurately despite excluding the k-zone geometry.

Furthermore, the flexural buckling strength of the W12×87 section matched well with reference results supporting the validity of the modeling assumptions for global buckling behavior. While this simplification is justified for the scope of this study—focused on global flexural buckling response—it is indeed possible that inclusion of the k-zone could be important in future studies concerned with local instability, stress concentration effects, or failure initiation at the flange-web interface.

FLEXURAL BUCKLING CURVES FOR A992 STEEL COLUMNS

Initially, column flexural buckling curves are developed based on the simulation for selected W-shapes using A992 steel to recreate the past work on mild steel and characterize the expected uncertainty between known column behavior and the current AISC 360-22 column curve. The W-shapes chosen for the analysis are presented in Table 2 with their corresponding height-to-width ratio, h/b, flange thickness, t_f, width-to-thickness, $b_f/2t_f$, and web slenderness, h/t_w, ratios. The shapes are chosen for a wide range

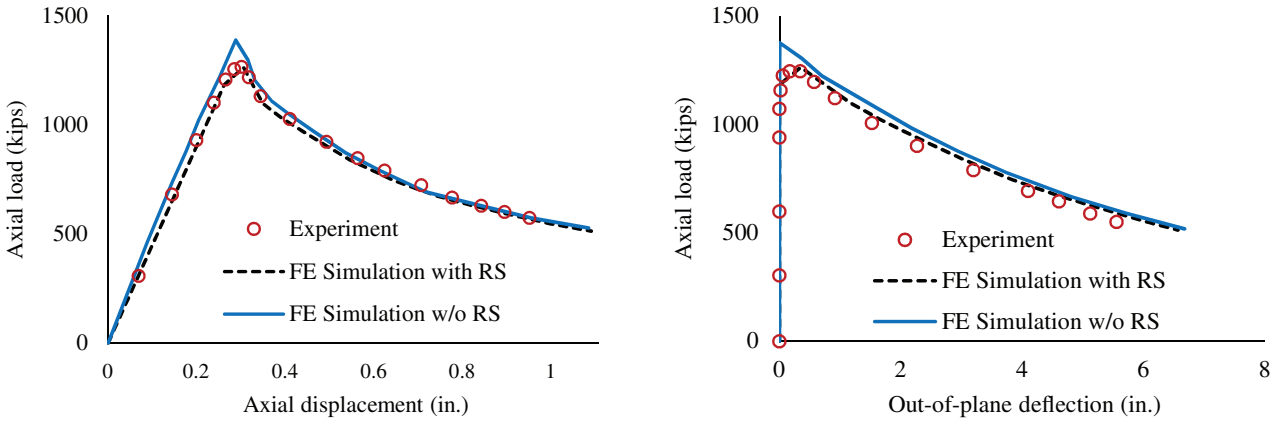

(a) Axial load displacement *(b) Axial load-lateral deflection*

Fig. 13. Buckling analysis vs. experimental (data from Lamarche and Tremblay, 2011) responses under monotonic axial loading for ASTM A992 W12×87 section.

of these ratios so that the analyses can capture their effect on the flexural buckling resistance of the columns. The columns are analyzed up to a slenderness ratio, KL/r, of 200. Finite element analyses are performed on these shapes by changing the slenderness ratio of the column using different column lengths, and the buckling strengths are determined for different slenderness ratios about both minor and major axes using A992 steel with a yield stress of 50 ksi. Because the column is considered pin-connected at both ends, the effective length factor K is taken as 1.0. To make the column curves comparable between different W-shapes having different radii of gyrations about the minor and major axes, and different yield strengths of steel, the critical buckling strength, F_{cr} is normalized by the yield stress, F_y, which is the same as the reduction factor χ in Eurocode 3, and it is plotted against the relative slenderness ratio λ as given by Equation 1. Note that the initial geometric imperfection is taken as $L/1500$ at the mid-height of the column to be comparable with the AISC 360 column curve, and for each of the shape, the simulated residual stresses are considered as the initial state of stress. Figure 14 shows column buckling curves about minor and major axes for six sections of Table 2 made of A992 steel along with their design curves as given by AISC 360 (2022) and Eurocode 3 (CEN, 2005a).

From these figures, it is observed that the simulated column flexural buckling curves for the sections presented in Table 2 about the major axis are close to the AISC 360 and EC3 column design curves. The simulated flexural buckling resistances are on the AISC 360 column curve for small ($\lambda < 0.5$) and large ($\lambda > 1.5$) slenderness ratios, indicating that for the local and elastic buckling range, the AISC 360 column buckling curve agrees well with the simulated responses. For inelastic buckling range with intermediate slenderness ratios ($0.5 \le \lambda \le 1.5$), both the AISC 360 and Eurocode 3 column design curves underestimate the simulated major axis buckling strengths of A992 sections. However, the degree of underestimation is more pronounced for Eurocode 3, which predicts lower strengths across the full slenderness range compared to AISC. For the sections studied, AISC 360 underestimates the simulated strength by approximately 5–10%, while EC3 underestimates by a larger margin, particularly in the intermediate slenderness range ($0.5 \le \lambda \le 1.5$).

Similar to major axis buckling, simulated minor axis buckling curves as shown in Figures 14 and 15 for the sections in Table 2 agree well with the AISC 360 and EC3 column design curves for small ($\lambda < 0.5$) and large ($\lambda > 1.5$) slenderness ratios, indicating that for the local and elastic buckling range, AISC 360 and EC3 column buckling curves agree well with the simulated responses. However, in the inelastic buckling range with intermediate slenderness ratio ($0.5 \le \lambda \le 1.5$), the AISC 360 column curve agrees well with the simulated column curve for nonheavy sections with $t_f \le 1.5$ in. with $b_f/2t_f \ge 5.45$, and $h/t_w \ge 12.8$ (e.g., W14×53, W14×82, W12×87, W14×145, and W14×193) and overestimates the buckling capacity for heavy sections with $t_f >$ 1.5 in. with $b_f/2t_f < 5.45$, and $h/t_w < 12.8$ (e.g., W14×257, W14×426, W12×336, W14×605, and W14×808). The residual stress distribution pattern in all these sections is more or less similar, with tensile residual stresses at the center of the flange and compressive residual stresses at the edges of the flange [see Figures 8(a) and 10(a)], and compressive residual stress in the middle of the web and tensile residual stresses the ends of the web [see Figures 8(b) and 10(b)]. Since inelastic flexural buckling of columns is preceded by flange local buckling, the magnitude and distribution of the compressive residual stress in the flange plays a substantial role in the flexural buckling strength of the columns. For lighter W-shape sections, the maximum compressive residual stress in the flange is relatively small compared to the higher residual stresses typically developed in heavier sections. For example, in the W14×82 column section, the maximum compressive stress on the flange is ~8.6 ksi [Figure 16(a)], whereas for a W14×426, the maximum compressive stress on the flange is ~23.3 ksi [Figure 16(b)].

Moreover, the maximum compressive stress develops at the center of the web for a W14×82 section, whereas the compressive stress is maximum at the edge of the flange and at the center of the web for a W14×426 section. As a result of high compressive residual stresses on the flange, the heavier shapes develop local instability earlier than the nonheavy shapes followed by global instability. The AISC 360 column curves were developed based on the Galambos and Ketter (1959) residual stress model considering a linear distribution of residual stresses with a magnitude of $0.3F_y$ tensile at the center of the flange and $-0.3F_y$ compressive at the edges of the flange and uniformly distributed tensile residual stress throughout the depth of the web. The simulated compressive residual stresses on the flange of heavy shapes are substantially higher than those considered in the Galambos and Ketter (1959) model. Additionally, both tensile and compressive residual stresses are observed on the web of the section from the simulation, which is not considered in the Galambos and Ketter (1959) model. As a result, the flexural buckling strengths of the heavier columns are less than the AISC 360 column curve for $0.5 \le \lambda \le 1.5$, which is typically the inelastic buckling range. For example, within the relative slenderness range between 0.5 and 1.5, the AISC 360 column curve overestimates the column buckling capacity of A992 steel columns by 12% for the W14×426 section. This is consistent with the findings of ECCS Technical Committee 8 (2008), where they confirmed that residual stresses in larger hot-rolled sections increase disproportionately due to slower cooling rates, lowering their buckling resistance. As noted from Figure 1, EC3 column buckling curves are overly conservative for all the sections in the intermediate slenderness ratios. Eurocode 3 Part 1-1 (CEN, 2005a), considers these

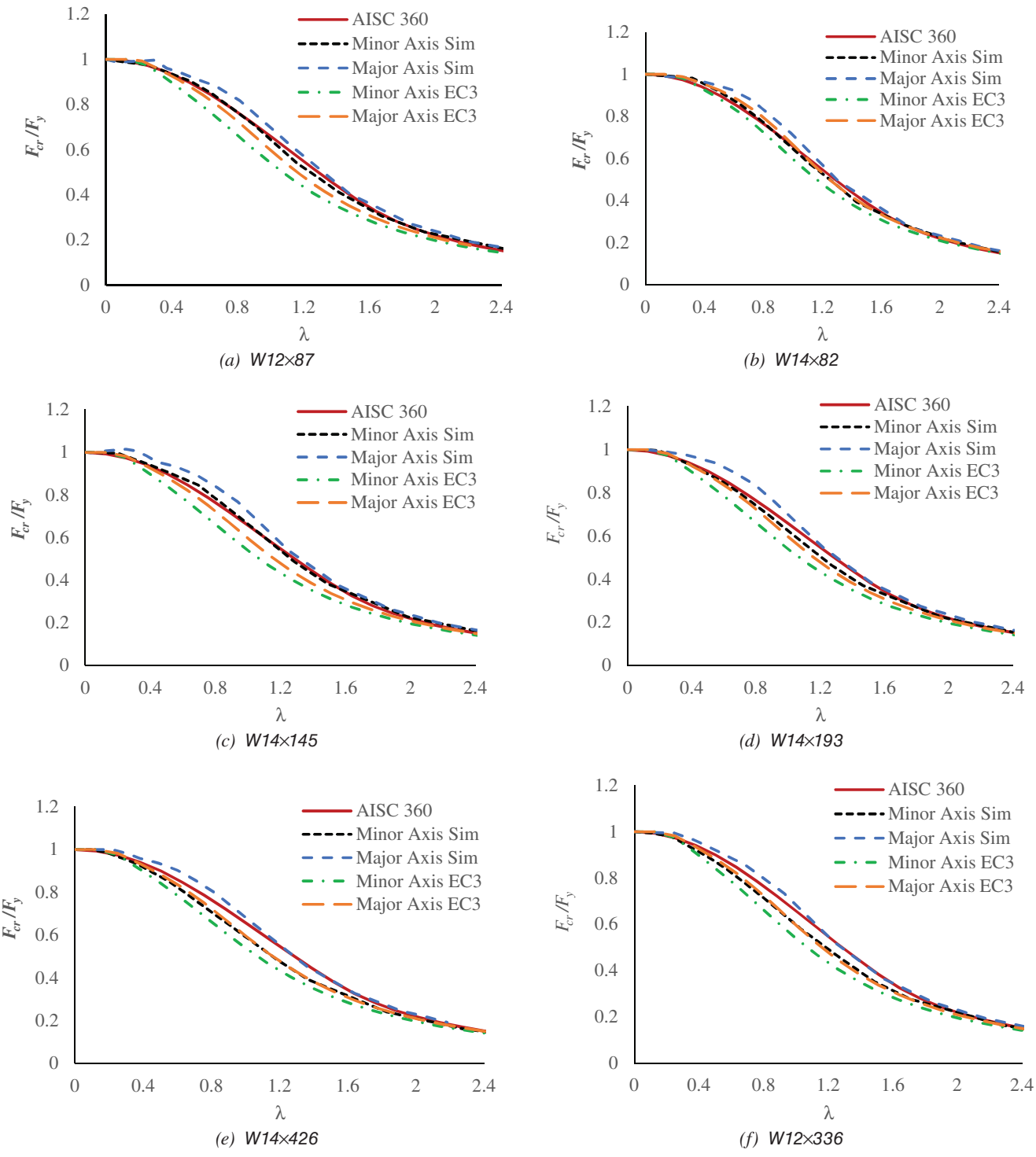

(a) W12×87 (b) W14×82

(c) W14×145 (d) W14×193

(e) W14×426 (f) W12×336

Fig. 14. Column flexural buckling curves for A992 steel sections.

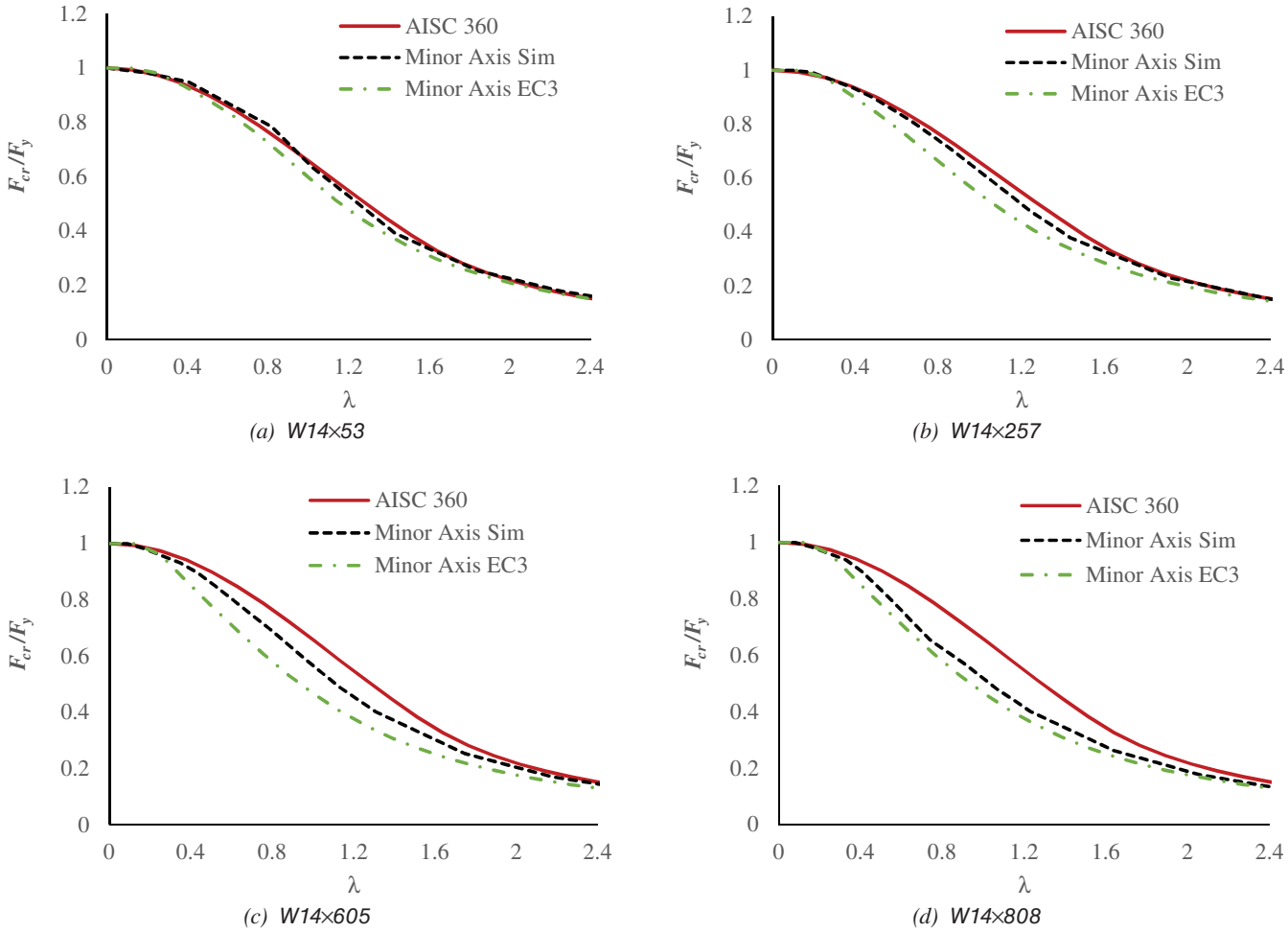

(a) W14×53 (b) W14×257

(c) W14×605 (d) W14×808

Fig. 15. Column flexural buckling curves about the minor axis for A992 steel sections.

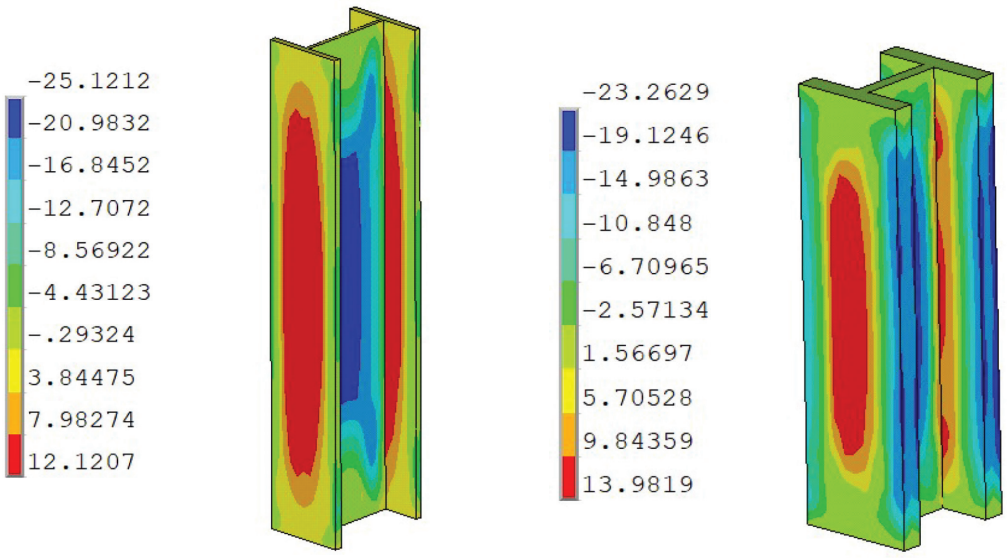

(a) W14×82 (b) W14×426

Fig. 16. Simulated longitudinal residual stress contour (in ksi) of A992 steel sections.

Table 3. Cross-Sectional Properties of W-Shapes Investigated for F_y = 80 ksi Steel Column Buckling Curves				
Column Designation	h/b	t_f (in.)	$b_f/2t_f$	h/t_w
W14×808	1.23	5.12	1.82	3.04
W14×605	1.20	4.16	2.09	4.39
W14×500	1.15	3.50	2.43	5.21
W14×426	1.12	3.04	2.75	6.08
W14×342	1.07	2.47	3.31	7.41
W14×257	1.03	1.89	4.23	9.71
W14×211	1.00	1.56	5.06	11.6
W14×193	0.99	1.44	5.45	12.8
W14×176	0.97	1.31	5.97	13.7
W14×145	0.96	1.09	7.11	16.8
W14×132	1.00	1.03	7.15	17.7
W14×120	0.99	0.94	7.80	19.3
W14×90	0.97	0.71	10.2	25.9
W14×82	1.41	0.855	5.92	22.4
W14×68	1.40	0.72	6.97	27.5
W14×53	1.94	0.66	6.11	30.9
W12×87	1.03	0.81	7.48	18.9
W12×336	1.25	2.96	2.26	5.47

variations in the residual stresses and geometric imperfections based on the geometry of the shapes by incorporating the imperfection factor. EC3's five different buckling curves, a_0, a, b, c, and d depend on the section's h/b ratio and flange thickness, t_f. As per EC3, the W14×426 section belongs to column curve b with an imperfection factor of 0.34. The corresponding column curve developed based on the EC3 is plotted in Figure 14(e) for section W14×426, where it is observed that the EC3 column curve accounted for this reduction in the buckling strength in the inelastic buckling range; however, the EC3 curves are overly conservative compared to the simulated responses and AISC 360 column curves. Based on the responses using A992 steel, it is demonstrated that the finite element models developed in this study provide reliable column buckling capacity prediction for rolled shapes; hence, the models are further utilized to investigate the column buckling capacity of rolled shapes using A913/A913M Gr. 80 steel.

FLEXURAL BUCKLING CURVES FOR A913/A913M GRADE 80 STEEL COLUMNS

In this section, comparisons are made between the simulated column buckling curves using A913/A913M Gr. 80 steel and AISC 360 (2022b) and EC3 (CEN, 2005a) column design curves to understand how effectively the AISC 360 column design curve predicts the flexural buckling capacity of high-strength steel rolled shape columns. Finite element analyses are performed on 17 W14 and 2 W12 sections as shown in Table 3, using the validated finite element model with multilinear kinematic hardening material model and $L/1500$ bow imperfection. Residual stresses are incorporated by using the sequentially coupled thermo-mechanical analysis as discussed in the "*Modeling of Residual Stresses*" section for all the shapes using A913/A913M Gr. 80 steel. The residual stress distribution for six of the shapes of Table 3 using A913/A913M Gr. 80 steel are presented in Figure 17. While all listed W-shape sections were modeled using A913 Grade 80 material properties, not all are currently produced in accordance with ASTM A913 due to QST process limitations, which require a minimum flange and web thickness to achieve proper self-tempering. In particular, lighter sections such as W14×82, W14×68, W14×53, and W12×87 may not meet this requirement and are not typically available from producers offering A913 Grade 80. These shapes were included in the numerical study for comparative and parametric analysis purposes only to explore the sensitivity of flexural buckling strength across a broader geometric spectrum.

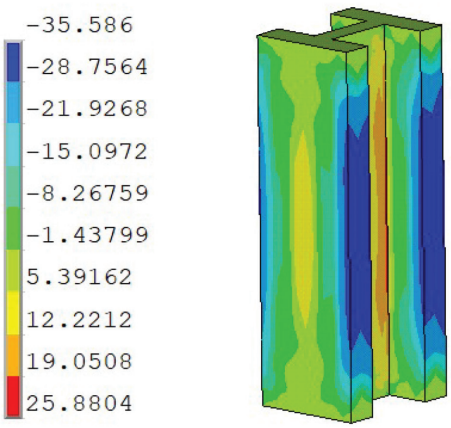

(a) W14×808

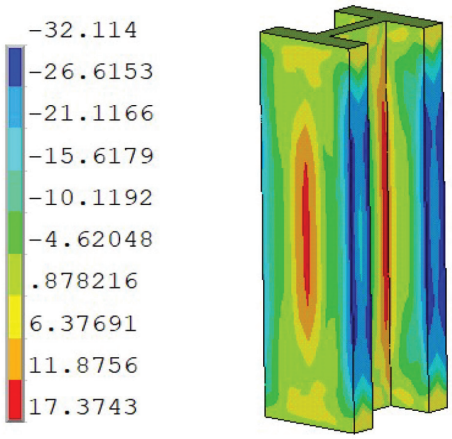

(b) W14×605

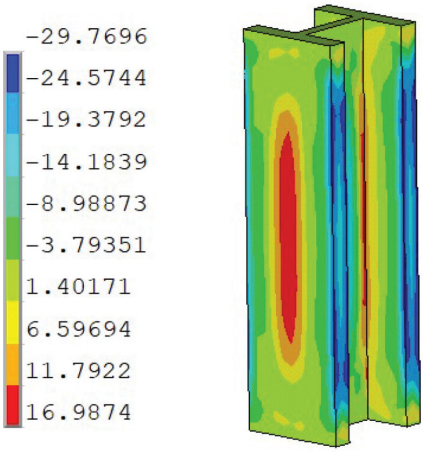

(c) W14×426

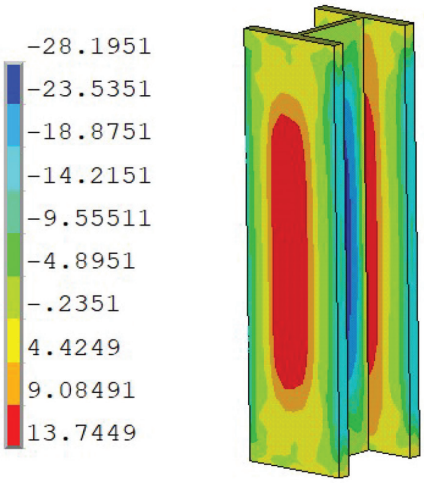

(d) W14×257

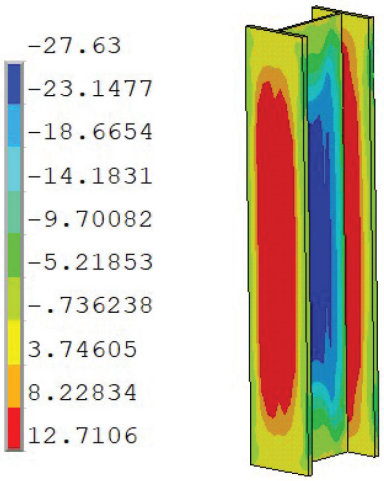

(e) W14×82

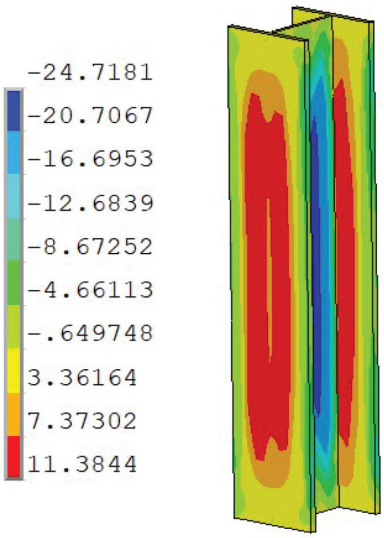

(f) W12×87

Fig. 17. Simulated longitudinal residual stress contour (in ksi) of A913 Gr. 80 steel sections.

Note that European research has suggested that high-strength steels, such as S460 (yield stress of 460 MPa or 65 ksi), have different residual stress distributions, strain-hardening behavior, and imperfections sensitivity compared to lower-grade steels. As a result, Eurocode 3 proposed separate curves for high-strength steel S460 based on the cross-section type (I-section, box, circular, etc.), the buckling mode (minor/major axis), and the fabrication method (rolled vs. welded). In addition, study by Snijder et al. (2014) demonstrated that the EC3 buckling curves for S460 high-strength steel columns can also be used to predict the buckling strength of S500 (yield stress of 72 ksi) high-strength steel columns. Figures 18, 19, and 20 present comparisons of the simulated column buckling curves with the AISC 360 and EC3 design column curves for the sections shown in Table 3 for buckling about both the minor and major axes.

Based on the observations of the simulated column buckling curves using A913/A913M Gr. 80 steel, it is noted that the simulated column curves show differences from the AISC 360 and EC3 column design curves within the relative slenderness values of 0.3–1.5 for buckling about the minor axis and within relative slenderness values 0.5–2 for buckling about the major axis, which is typically the inelastic buckling range for the columns. For smaller and larger relative slenderness ratios, the simulated column curves agree well with the AISC 360 and EC3 column curves, which are typically the compression yielding and elastic buckling range of the columns. From the simulated column curves, it is observed that both the AISC 360 and EC3 column design curves underestimate the major axis buckling capacity for all the sections analyzed. The percent increase in the simulated buckling strength compared to the AISC 360 column design curve varies between 3 and 14% depending on the λ values, h/b ratio, and the flange thickness of the sections as shown in Figures 21, 22, and 23.

Sections with $h/b \geq 1.12$ and flange thickness t_f more than 3 in. such as W14×808, W14×605, W14×500, and W14×426 sections show less of an increase in the buckling capacity, whereas sections with $h/b < 1.12$ and flange thickness t_f less than 3 in. such as W14×193, W14×145, W14×120, and W14×90 demonstrate a substantial increase in the buckling capacity compared to the AISC 360 column design curve. For example, at $\lambda = 0.5$, 0.75, and 1, the percent increase in the simulated major axis buckling capacity vary between 3 and 8% for sections with flange thickness more than 3 in., as shown in Figures 21–23. On the other hand, the percent increase in the simulated major axis buckling capacity vary between 8 and 14% for sections with flange thickness less than 3 in. at $\lambda = 0.5$, 0.75, and 1.0. For sections W14×53, W14×68, and W14×82, the simulated column buckling curves do not show a significant increase in the buckling capacity, even though the flange thickness is less than 1 in.

These sections have a higher h/b ratio, which is in the range of 1.4–1.94. The simulated column buckling curves about the minor axis are compared with the AISC 360 and EC3 column curves in Figures 18–20. It is observed that for heavy sections with $h/b \geq 1.12$ and $t_f \geq 3$ in. such as W14×808, W14×605, W14×500, and W14×426, the AISC 360 column curve overestimates the buckling capacity that depends on the λ values, h/b ratio, and the flange thickness of the sections. This is mostly observed in the inelastic buckling range with λ values between 0.4 and 1.5. These heavy shapes develop high compressive residual stresses in the flanges, and as a result, the thicker the flange, the higher the overestimation for heavy sections with $h/b \geq 1.12$ and $t_f \geq 3$ in. Nevertheless, the overestimation is in the range of 2–8% depending on the h/b ratio and the flange thickness of the sections as shown in Figures 21–23. For sections with $h/b < 1.12$ and $t_f < 3$ in, the AISC 360 column design curve underestimates the buckling strength of A913/A913M Gr. 80 columns between λ values of 0.3 and 1.5, and it is observed that as the h/b value and the flange thickness decrease, the difference between the simulated column buckling strength about the minor axis and the AISC 360 column design curve increases. It is noted from Figures 21–23 that the AISC 360 column curve underestimates the buckling capacity about minor axis by 4–11%, depending on the flange thickness and h/b ratio of the section for λ values between 0.3 and1.5.

For sections with $1.00 \leq h/b \leq 1.12$ and $1.56 \leq t_f \leq 3.00$ in., the simulated column buckling curves about the minor axis exhibit a 5% increase compared to the AISC 360 column curve, whereas for any sections with $h/b < 1.00$ and $t_f < 1.56$ in., the simulated column buckling curves about the minor axis are 5–11% stronger than the AISC 360 column curve. For sections W14×53, W14×68, and W14×82, the simulated column buckling curves do not show substantial increase in the buckling capacity even though the flange thickness is less than 1 in. These sections have a higher h/b ratio, which is in the range of 1.4~1.94. On the contrary, for λ values between 0.4 and 1.5, EC3 column buckling curves underestimate the buckling capacity for heavy sections with $h/b \geq 1.2$ and $t_f \geq 4$ in., such as for W14×873, W14×808, and W14×605 sections, even though EC3 has separate curves for 65 ksi high-strength steel. However, for sections with $h/b < 1.2$ and $t_f < 4$ in., the simulated column buckling curves about the minor axis agree well with the EC3 S460 high-strength column curves in the inelastic buckling range. For elastic buckling range and compression yielding, the simulated column buckling curves about the minor axis agree well with both the AISC 360 and EC3 column curves. Moreover, note that the major axis buckling curves for all the sections analyzed are always higher than the minor axis buckling curves. This indicates that using the same design curve for major and minor axis buckling may underestimate

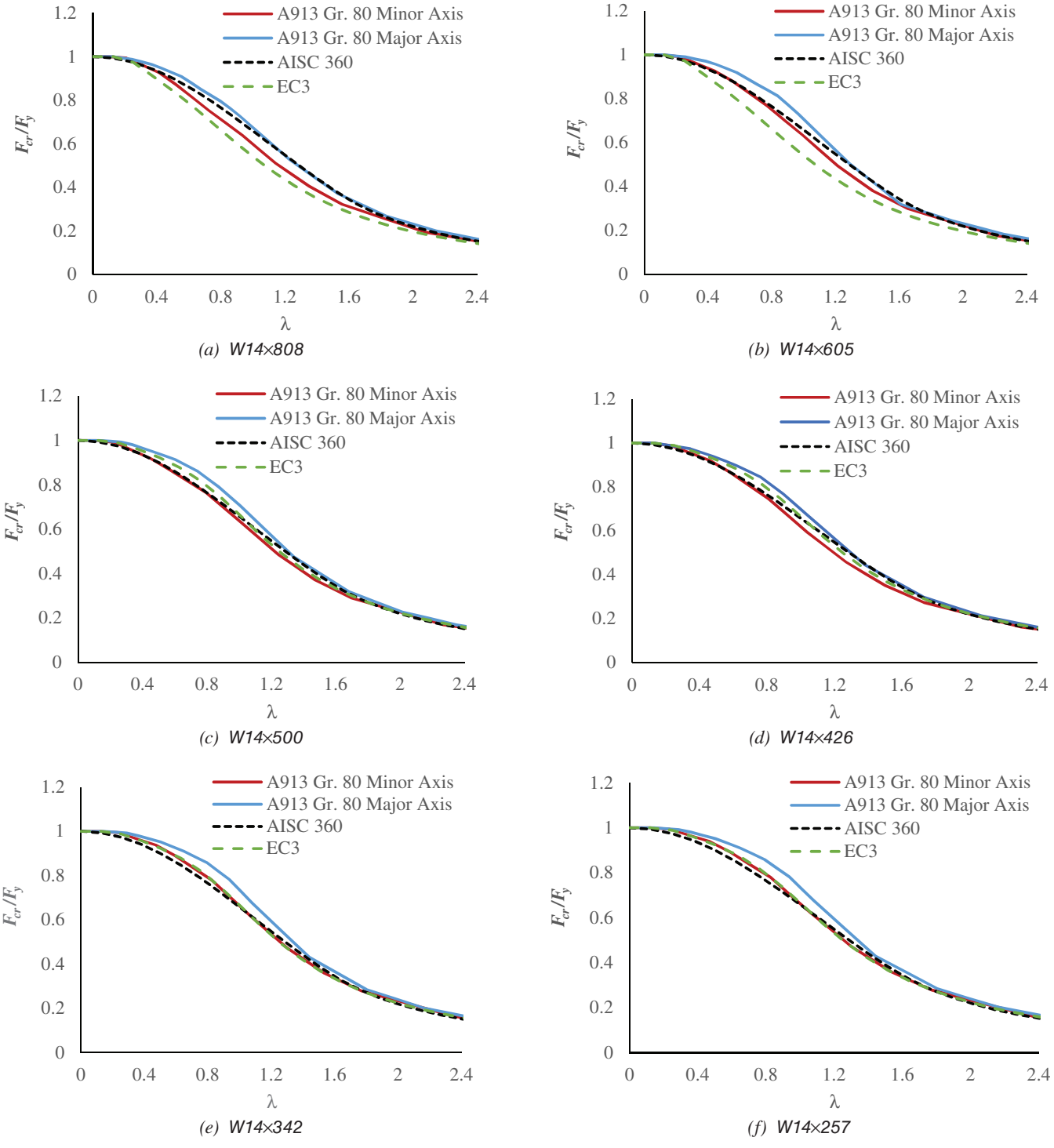

(a) W14×808 *(b) W14×605*

(c) W14×500 *(d) W14×426*

(e) W14×342 *(f) W14×257*

Fig. 18. Column flexural buckling curves for A913/A913M Gr. 80 steel sections.

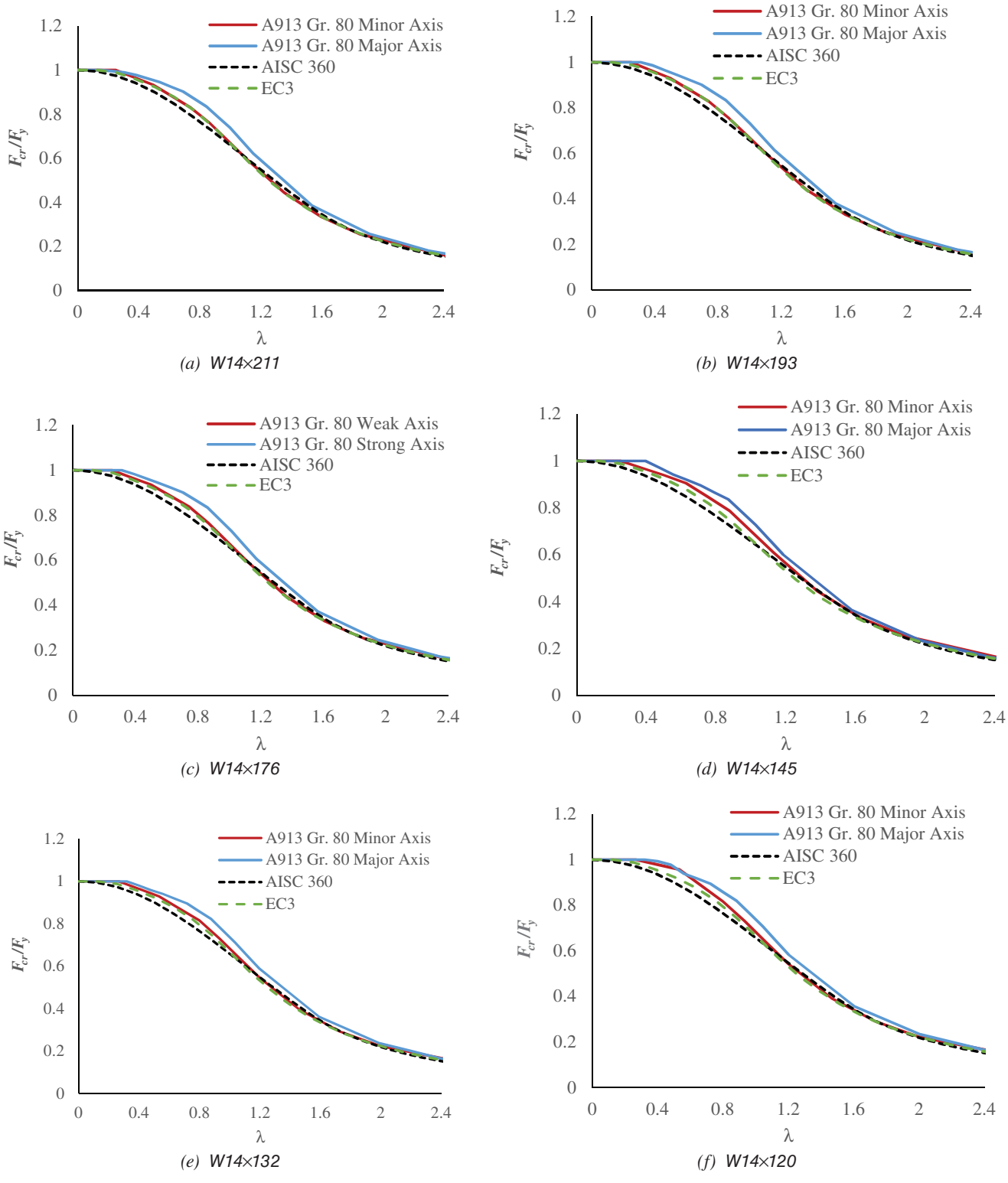

(a) W14×211 (b) W14×193

(c) W14×176 (d) W14×145

(e) W14×132 (f) W14×120

Fig. 19. Column flexural buckling curves for A913/A913M Gr. 80 steel sections.

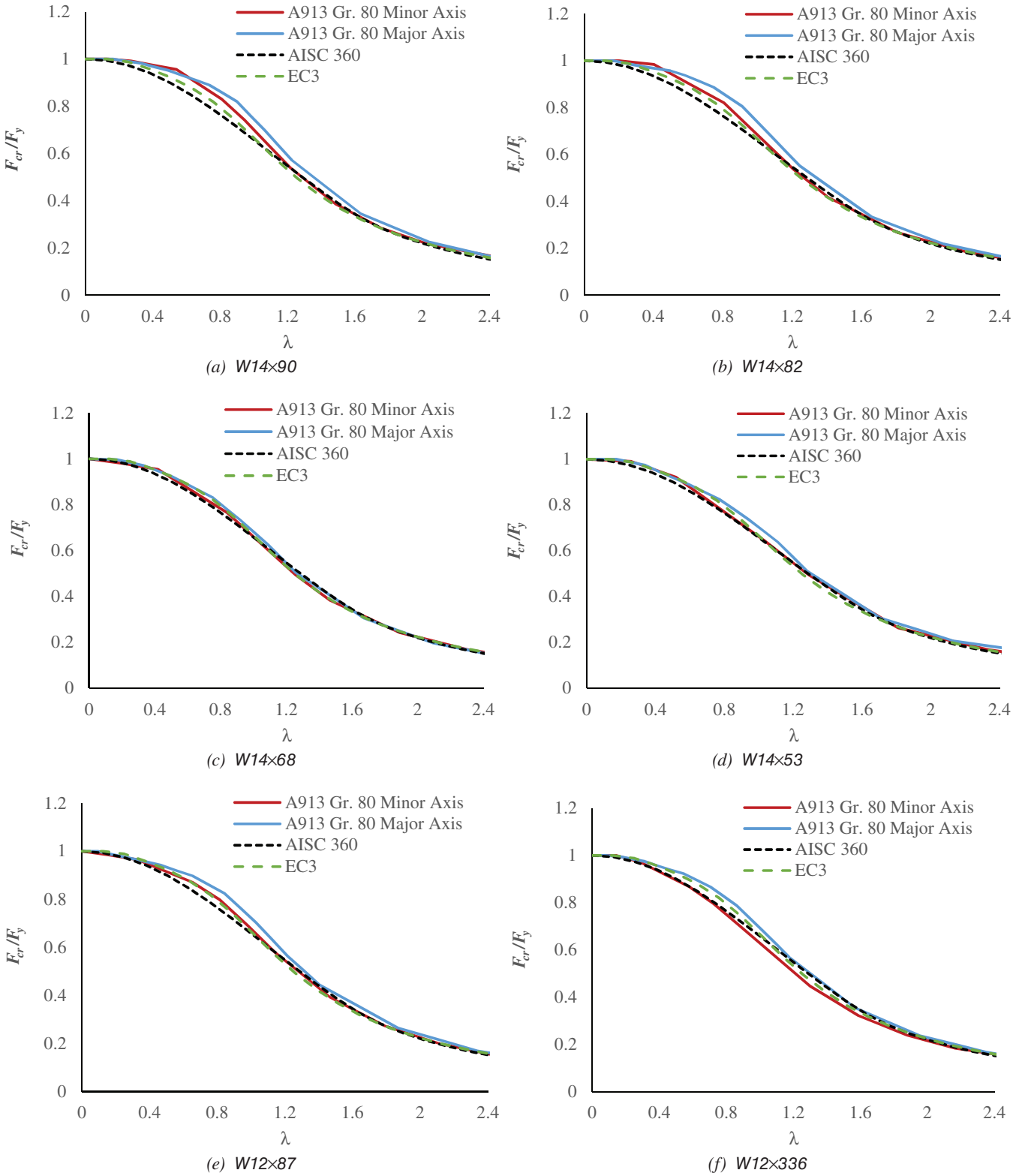

Fig. 20. Column flexural buckling curves for A913/A913M Gr. 80 steel sections.

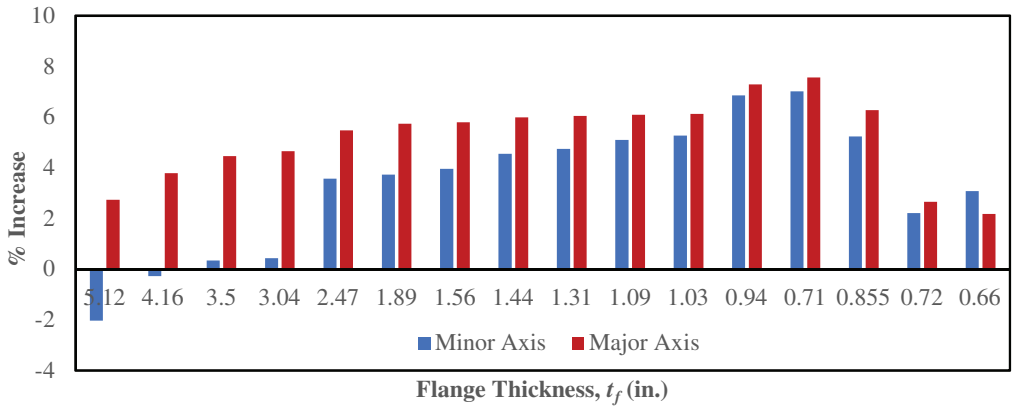

Fig. 21. Percent difference between the simulated and AISC 360 column buckling curves of ASTM A913 Gr. 80 W-shape sections for different flange thickness for λ = 0.5.

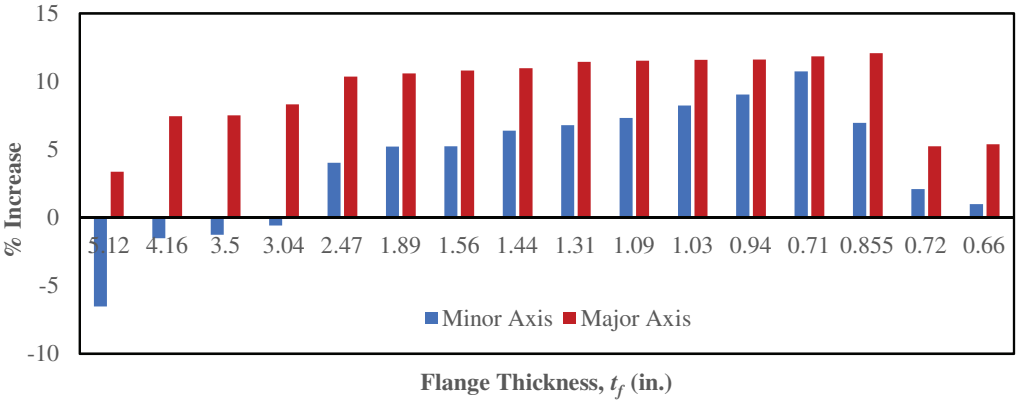

Fig. 22. Percent difference between the simulated and AISC 360 column buckling curves of ASTM A913 Gr. 80 W-shape sections for different flange thickness for λ = 0.75.

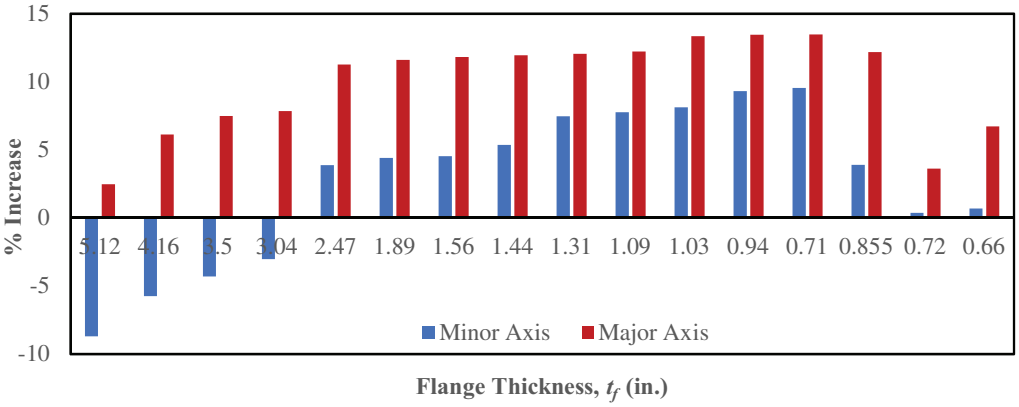

Fig. 23. Percent difference between the simulated and AISC 360 column buckling curves of ASTM A913 Gr. 80 W-shape sections for different flange thickness for λ = 1.0.

the buckling strength of the columns about the major axis significantly, especially for high-strength steels.

This was accounted for in the development of column design curves for stainless steel in AISC 370 (2021), where separate buckling curves for minor and major axis are proposed. In summary, A913/A913M Gr. 80 steel columns exhibit higher flexural buckling strength about both minor and major axes for intermediate slenderness values compared to the AISC 360 column curves. This increase in the flexural buckling strength is applicable for sections with $h/b < 1.2$ and $t_f < 3$ in. and can range from 5–11% for minor axis buckling and 5–14% for major axis buckling. For heavy shapes, the AISC 360 column curve overpredicts the flexural buckling capacity by 2–8% due to the presence of high compressive residual stresses on the flanges as discussed in the "Modeling of Residual Stresses" section. These results suggest that while the AISC 360 column design curve performs reasonably well for many cases, its direct application to high-strength steel columns such as A913/A913M Gr. 80 may lead to unconservative or overly conservative predictions depending on the section geometry. Therefore, potential modifications or refinements to the current design curve may be warranted to improve accuracy for high-strength applications.

A913/A913M GRADE 80 VS. A992 COLUMN FLEXURAL BUCKLING CURVES

Now let's compare the simulated column buckling curves of the A913/A913M Gr. 80 steel columns with those of the columns made of A992 steel and also, how they compare with the AISC 360 column design curve. Figure 24 presents a comparison of A992 and A913/A913M Gr. 80 steel column buckling curves about both the minor and major axes with the AISC 360 column curve for several sections with different h/b ratios and flange thicknesses, namely, W14×426, W12×336, W14×193, W14×145, W12×87, and W14×82. It is observed that for $\lambda = 0.5$~2, the major axis buckling curves for A992 steel columns are 3–12% stronger than the AISC 360 column curves, whereas the major axis buckling curves for A913/A913M Gr. 80 steel columns are 5–14% stronger than the AISC 360 column curves. The column buckling curves for A913/A913M Gr. 80 steel columns about the major axis is always 2–5% stronger than those of the A992 steel columns, regardless of the sectional dimensions and λ values between 0.5~2.0. On the contrary, the simulated buckling curves about the minor axis for A913/A913M Gr. 80 steel columns are always stronger than the relevant column buckling curves for A992 steel columns between $\lambda = 0.3$~1.5. For example, the minor axis buckling curves for W14×82 and W14×145 sections where the thickness of the flange is less than 1.56 in., AISC 360 column design curve underestimates the buckling strength of A913/A913M Gr. 80 columns by 5–11% between λ values of 0.3 and 1.5, whereas, the buckling strength of A992 columns are predicted correctly by the AISC 360 column curve [see Figures 24(d) and 24(f)]; that is—the column buckling curves for A913/A913M Gr. 80 steel columns are 5–11% stronger than the column curves for A992 steel columns.

As the flange thickness increases to 2.96~3.04 in. for W12×336 and W14×426 sections, the simulated column curves about the minor axis for A913/A913M Gr. 80 steel columns are 8–10% stronger than the corresponding column curve for A992 steel column between λ values of 0.5 and 1.5 [see Figures 24(a) and 24(b)]. When the thickness of the flange is further increased to around 4.16 and 5.12 in. for W14×605 and W14×808 sections, respectively, AISC 360 column design curve overestimates the buckling strength compared to both A913/A913M Gr. 80 and A992 steel columns; however, the buckling strengths of A913/A913M Gr. 80 steel columns are still 8–16% stronger than the corresponding column buckling strengths of A992 steel columns in the inelastic buckling range [see Figures 25(a) and 25(b)]. On average, for the sections considered in this study, the buckling strength of A913/A913M Gr. 80 steel columns about the minor axis is around 8–12% higher than that of A992 steel columns, and it depends on the h/b ratio and the flange thickness of the sections, which is consistent with the Eurocode 3, Part 1-1 (CEN, 2005a). In addition, Eurocode 3, Part 1-1, dictated that high-strength steel columns exhibit higher flexural buckling strengths than conventional grade steel columns regardless of the sectional dimensions, which is consistent with the findings of this study where it is observed that A913/A913M Gr. 80 steel column possesses 8–12% higher buckling strength about the minor axis and 2–5% higher buckling strength about the major axis than the corresponding A992 steel column in the inelastic buckling range for the sections considered in this study.

CONCLUSIONS

This study investigated the flexural buckling behavior of wide-flange rolled steel columns fabricated from both conventional structural steel (ASTM A992, $F_y = 50$ ksi) and high-strength steel (ASTM A913 Grade 80, $F_y = 80$ ksi). A suite of nonlinear finite element simulations was conducted incorporating measured material stress-strain behavior, realistic geometric imperfections, and residual

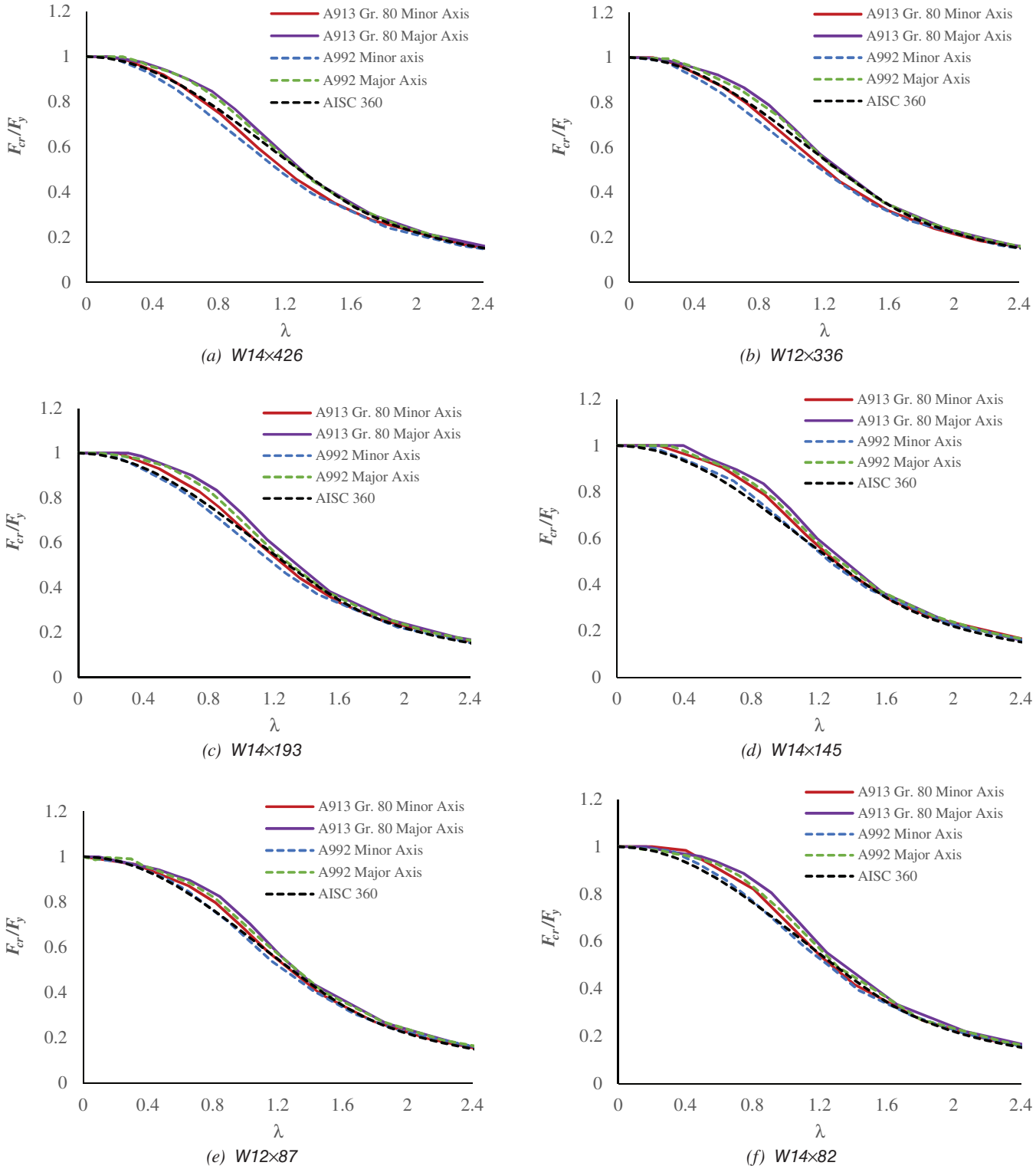

Fig. 24. Simulated column flexural buckling curves for sections using A913/913M Gr. 80 and A992 steels.

stress distributions obtained through sequentially coupled thermomechanical analysis. Simulated buckling responses were used to generate column curves over a broad range of slenderness ratios and section geometries, enabling direct comparison with the AISC 360-22 and Eurocode 3 (EC3) design curves.

Results for A992 columns show that the AISC 360-22 unified column curve generally captures flexural buckling strength with reasonable accuracy in major axis buckling, with underpredictions of 5–10% in the intermediate slenderness range ($\lambda = 0.5$~2.0). However, for minor axis buckling of nonheavy sections with $h/b \leq 1.0$ and $t_f \leq 1.5$ in., the AISC 360-22 column buckling curve agrees well with the simulated responses; however, for minor axis buckling of heavy sections with $h/b > 1.0$, $t_f > 1.5$ in., AISC 360 overestimates capacity by 10–15% in the inelastic buckling range due to elevated compressive residual stresses on the flanges. In contrast, EC3 column curves were uniformly more conservative, particularly in the inelastic range. These findings suggest that for heavier W-shapes, particularly in minor axis buckling, some modification to the AISC 360-22 design curve may be worthy of consideration to improve accuracy and prevent overestimation of capacity.

For A913 Gr. 80 columns, the AISC 360 curve remained acceptable overall, yet underpredictions of 5–12% about the minor axis and 5–14% about the major axis were observed depending on slenderness and section classification. In nonheavy sections ($h/b < 1.12$, $t_f < 3$ in.), the AISC 360 curve underpredicted buckling strength in the inelastic buckling range, while for heavier sections, it overpredicted capacity. Additionally, the flexural buckling strengths of A913 columns in the inelastic buckling range were consistently 5–12% higher than those of A992 counterparts, especially in the minor axis direction. These trends indicate that the current AISC 360 curve performs acceptably for $F_y = 80$ ksi steel; nevertheless, it highlights a potential for material and section-specific adjustments to the AISC 360 design curve in the inelastic buckling range when applied to high-strength rolled shapes and heavier sections. However, the moderate gains from developing a new curve specific to this grade may not justify the complexity, especially considering the results for $F_y = 50$ ksi already show a mix of under- and overpredictions. In that context, proposals for a new design curve for $F_y = 80$ ksi should carefully weigh the benefits of localized conservatism reduction against the risks of unconservative predictions in other regimes.

While the findings affirm the general applicability of the AISC 360-22 unified curve to both A992 and A913 rolled shapes, they also reveal nuances in performance that depend on cross-sectional proportions, loading direction, and residual stress profiles. A single unified curve may not fully capture these effects, particularly for heavy or high-strength shapes with $F_y \geq 80$ ksi buckling in the inelastic range. Although this study does not propose a new column curve, it highlights the potential limitations of the existing design provisions and lays the groundwork for further research. As such, future research should explore the viability of shape-dependent or strength-tiered column curves. Full-scale experimental validation will be essential to confirm these numerical trends and guide refinement of design provisions. Collaboration between academic researchers and industry partners—including ongoing discussions within the AISC technical committees—will be vital to advancing the adoption of high-strength steel in design practice and improve the safety-efficiency balance in modern high-strength steel design.

Ultimately, this study underscores that while the current design provisions are generally effective, their limitations should be acknowledged, especially when applied to rolled shapes fabricated from emerging high-strength steels.

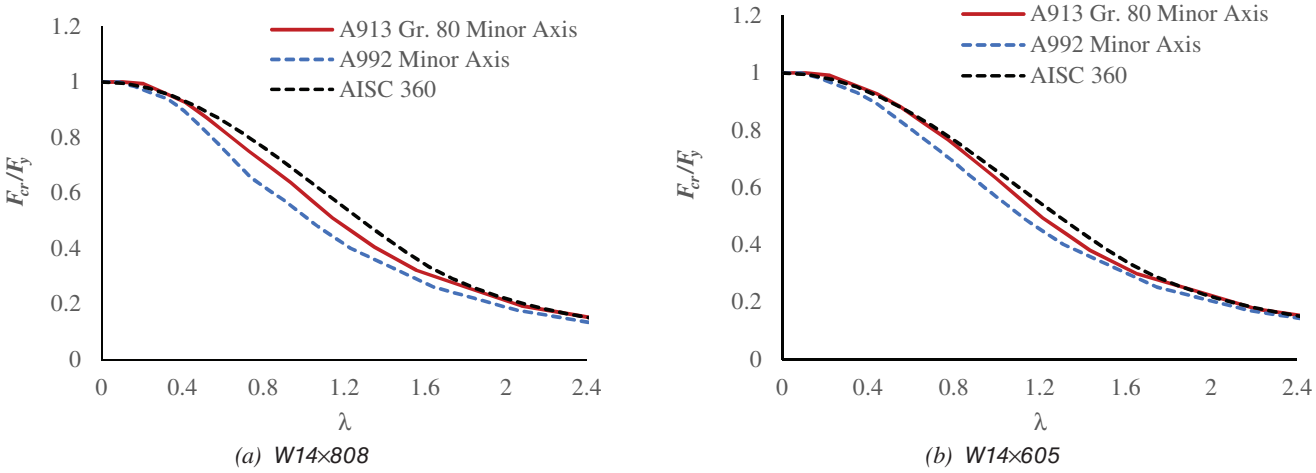

(a) W14×808 (b) W14×605

Fig. 25. Simulated column buckling curves about the minor axis for sections using A913/913A Gr. 80 and A992 steels.

Refinement—not replacement—of existing curves, with attention to shape, strength level, and directional sensitivity, appears to be a more realistic and impactful approach.

FUTURE TASKS

Future work may explore the development of column buckling curves for high-strength hollow structural sections (HSS), which differ substantially from rolled W-shapes in both manufacturing process and residual stress behavior. Unlike ASTM A913, which applies to hot-rolled W-shapes, high-strength HSS products are typically fabricated from cold-formed and welded plate or strip materials governed by ASTM A500 (2021a) or ASTM A1085 (2015) specifications. These differences affect geometric tolerances, residual stress distributions, and imperfection sensitivity. Accordingly, any extension of buckling curve calibration to high-strength HSS will require a tailored modeling approach that reflects these characteristics and production constraints.

While this study does not propose a new design equation, the validated numerical framework and consistent trends observed—particularly the underestimation of strength for A913 Gr. 80 rolled sections—form the basis for future reliability-based calibration. Future work will expand the simulation database to include additional W-shapes and HSS sections and will evaluate whether separate or modified buckling curves are warranted for A913 Gr. 80 or higher strength steels. The methodology will follow reliability provisions in AISC 360, Appendix 1, and incorporate statistical variability in material properties and geometric imperfections.

ACKNOWLEDGMENTS

The author is grateful to AISC for funding this research and for sharing all the relevant information for this project. However, any opinions presented in this paper are solely those of the author. The author also greatly acknowledges the A913 Gr. 80 high-strength steel material testing data provided by steel producers and coordinated through AISC. The guidance provided by Professor Ronald Ziemian from Bucknell University, Professor Benjamin Schafer from Johns Hopkins University, and Dr. Devin Huber from AISC throughout the completion of this project is greatly appreciated.

REFERENCES

AISC (2016), *Specification for Structural Steel Buildings*, ANSI/AISC 360-16, American Institute of Steel Construction, Chicago, Ill.

AISC (2019), "High Strength Steel," Task Group Report prepared by the AISC Committee on Specifications Ad Hoc Task Group on High Strength Steel, December 19, American Institute of Steel Construction, Chicago, Ill.

AISC (2021), *Specification for Structural Stainless-Steel Buildings*, ANSI/AISC 370–21, American Institute of Steel Construction, Chicago, Ill.

AISC (2022a), *Code of Standard Practice for Steel Buildings and Bridges*, ANSI/AISC 303-22, American Institute of Steel Construction, Chicago, Ill.

AISC (2022b), *Specification for Structural Steel Buildings*, ANSI/AISC 360-22, American Institute of Steel Construction, Chicago, Ill.

Alpsten, G.A. (1968), "Thermal Residual Stresses in Hot-Rolled Steel Members," Fritz Engineering Laboratory Report No. 337.3, Lehigh University, Bethlehem, Pa.

ANSYS (2023), ANSYS® Mechanical APDL, Release 2023 R1, Theory Reference, ANSYS, Inc.

ArcelorMittal (2019), "High-Rise Building Brochure," ArcelorMittal Europe-Long Products, Sections and Merchant Bars, Luxembourg.

ArcelorMittal (2020), *"High-Strength Structural Shapes: ASTM A913 Grade 65 and Grade 70,"* ArcelorMittal USA. Retrieved from: https://usa.arcelormittal.com.

AS (2020), *Steel Structures*, AS 4100:2020, Standards Australia, Sydney, Australia.

ASTM (2015), *Standard Specification for Cold-Formed Welded Carbon Steel Hollow Structural Sections (HSS)*, ASTM A1085/1085M, ASTM International, West Conshohocken, Pa.

ASTM (2018a), *Standard Specification for Hot-Rolled Structural Steel, High-Strength Low-Alloy Plate with Improved Formability*, ASTM A656/656M, ASTM International, West Conshohocken, Pa.

ASTM (2018b), *Standard Specification for Structural Steel for Bridges*, ASTM A709/709M, ASTM International, West Conshohocken, Pa.

ASTM (2019a), *Standard Specification for Carbon Structural Steel*, ASTM A36/36M, ASTM International, West Conshohocken, Pa.

ASTM (2019b), *Standard Specification for High-Strength Low-Alloy Steel Shapes of Structural Quality, Produced by Quenching and Self-Tempering Process (QST)*, ASTM A913/913M, ASTM International, West Conshohocken, Pa.

ASTM (2020), *Standard Specification for Structural Steel Shapes*, ASTM A992/992M, ASTM International, West Conshohocken, Pa.

ASTM (2021a), *Standard Specification for Cold-Formed Welded and Seamless Carbon Steel Structural Tubing in Rounds and Shapes*, ASTM A500/500M, ASTM International, West Conshohocken, Pa.

ASTM (2021b), *Standard Specification for High-Strength Low-Alloy Columbium-Vanadium Structural Steel*, ASTM A572/572M, ASTM International, West Conshohocken, Pa.

Ban, H., Shi, G., Shi, Y., and Bradford, M.A. (2013), "Experimental Investigation of the Overall Buckling Behaviour of 960 Mpa High Strength Steel Columns," *Journal of Constructional Steel Research*, Vol. 88, pp. 256–266.

Bauschinger, J. (1886), "On the Change of the Elastic Limit and the Strength of Iron and Steel, by Drawing Out, by Heating and Cooling, and By Repetition of Loading (Summary)," *Minutes of Proceedings of the Institution of Civil Engineers with Other Selected and Abstracted Papers, 87*, p. 463.

Beer, H. and Schulz, G. (1975), "The European Column Curves," in *Construction Métallique*, Vol. 3.23, pp. 385–398.

Bjorhovde, R. (1972), "Deterministic and Probabilistic Approaches to the Strength of Steel Columns," PhD Thesis, Lehigh University, Bethlehem, Pa.

Boissonnade, N. and Somja, H. (2012), "Influence of Imperfections in FEM Modeling of Lateral Torsional Buckling," *Proceedings of the Annual Stability Conference*, Structural Stability Research Council, Grapevine, Texas, pp. 18–21.

CEN (2005a), *Eurocode 3: Design of Steel Structures—Part 1-1: General Rules and Rules for Buildings*, EN 1993-1-1:2005, Comite Européen de Normalisation, Brussels, Belgium.

CEN (2005b), *Eurocode 3: Design of Steel Structures—Part 1-2: General Rules—Structural Fire Design,* EN 1993-1-2:2005, Comite Européen de Normalisation, Brussels, Belgium.

Comini, D.G., Del Guidice, S., Lewis, R.W., and Zienkiewicz, O. (1974), "Finite Element Solution of Non-Linear Heat Conduction Problems with Special Reference to Phase Change," *International Journal for Numerical Methods in Engineering*, Vol. 8, No. 3, pp. 613–624.

ECCS Technical Committee 8 (2008), *The Residual Stresses in Hot-Rolled Structural Sections and Their Effect on Column Strength*, European Convention for Constructional Steelwork.

Ferreira Filho, J.O., Tankova, T., Carvalho, H., Martins, C., and da Silva, L.S. (2022), "Experimental and Numerical Flexural Buckling Resistance of High Strength Steel Columns and Beam-Columns," *Engineering Structures*, Vol. 265, pp. 114414.

Fujita, Y. (1955), "The Magnitude and Distribution of Residual Stress," Fritz Engineering Laboratory Report No. 220A.20, Lehigh University, Bethlehem, Pa.

Fukumoto, Y. and Itoh, Y. (1983), "Evaluation of Multiple Column Curves Using the Experimental Data-Base Approach," *Journal of Constructional Steel Research*, Vol. 3, No. 3, pp. 2–19.

Galambos, T.V., ed. (1998), *Guide to Stability Design Criteria for Metal Structures*, 5th Ed., Structural Stability Research Council, Wiley, New York, N.Y.

Galambos, T.V. and Ketter, R.L. (1959), "Columns under Combined Bending and Thrust," *Journal of the Engineering Mechanics Division*, Vol. 85, No. 2, pp. 1–30.

Hu, G., Morovat, M.A., Lee, J., Schell, E., and Engelhardt, M. (2009), "Elevated Temperature Properties of ASTM A992 Steel," *Proceedings of the ASCE/SEI Structures Congress 2009: Don't Mess with Structural Engineers: Expanding Our Role*, pp. 1–10.

Huber, A.W. (1956), "The Influence of Residual Stress on The Instability of Columns," Doctoral Dissertation, University Microfilms, Inc., Ann Arbor, Mich.

Huang, L., Li, G.Q., Wang, X.X., Zhang, C., Choe, L., and Engelhardt, M. (2018), "High Temperature Mechanical Properties of High Strength Structural Steels Q550, Q690 And Q890," *Fire Technology*, Vol. 54, pp. 1,609–1,628.

Jönsson, J. and Stan, T.C. (2017), "European Column Buckling Curves and Finite Element Modelling Including High Strength Steels," *Journal of Constructional Steel Research*, Vol. 128, pp. 136–151.

Khan, Q.S., Uy, B., Tao, Z., and Mashiri, F. (2013), "Concentrically Loaded Short High Strength Steel Columns with Normal and High Strength Concrete Infill," *Engineering Structures*, Vol. 49, pp. 905–917.

Lamarche, C.P. and Tremblay, R. (2011), "Seismically Induced Cyclic Buckling of Steel Columns Including Residual-Stress and Strain-Rate Effects," *Journal of Constructional Steel Research*, Vol. 67, pp. 1,401–1,410.

Li, G.Q., Wang, Y.Q., and Chen, S.W. (2012), "Experimental Study on the Overall Buckling Behavior of High Strength Steel Columns," *Journal of Constructional Steel Research*, Vol. 74, pp. 145–150.

Li, T.J., Li, G.Q., Chan, S.L., and Wang, Y.B. (2016), "Behavior of Q690 High-Strength Steel Columns: Part 1: Experimental Investigation," *Journal of Constructional Steel Research*, Vol. 123, pp. 18–30.

Ma, Y., Gardner, L., and Yuan, H. (2015), "Buckling of Ferritic Stainless Steel Members under Combined Axial Compression and Bending," *Journal of Constructional Steel Research*, Vol. 110, pp. 190–198.

Mathur, K., Fahnestock, L.A., Okazaki, T., and Parkolap, M.J. (2012), "Impact of Residual Stresses and Initial Imperfections on the Seismic Response of Steel Moment Frames," *Journal of Structural Engineering*, Vol. 138, No. 7, pp. 942–951.

Moghadam, S.J. (2015), "Plastic Buckling of Columns and Plates," Doctoral Dissertation, Department of Civil and Environmental Engineering, Imperial College London, London, U.K.

Morrison, M. (2015), "Innovative Seismic Performance Enhancement Techniques for Steel Building Moment Resisting Connections," PhD Dissertation Research, North Carolina State University, Raleigh, N.C.

Quayyum, S. and Hassan, T. (2017), "Initial Residual Stresses in Hot-Rolled Wide-Flange Shapes: A Computational Technique and Influence on Structural Performances," *Journal of Structural Engineering*, Vol. 143, No. 5, pp. 04017013.

Rasmussen, K.J.R. and Hancock, G.J. (1995), "Tests of High Strength Steel Welded I-Section Columns," *Journal of Constructional Steel Research*, Vol. 32, No. 2, pp. 167–187.

Rossi, A., Saito, D.H., Martins, C.H., and de Souza, A.S.C. (2021), "The Influence of Structural Imperfections on the LTB Strength of I-Beams," *Structures*, Vol. 29, pp. 1173–1186.

Shi, G., Ban, H., and Bijlaard, F. S. (2012), "Tests and Numerical Study of Ultra-High Strength Steel Columns with End Restraints," *Journal of Constructional Steel Research*, *70*, 236–247.

Snijder, H.H., Cajot, L.G., Popa, N., and Spoorenberg, R. C. (2014), "Buckling Curves for Heavy Wide Flange Steel Columns," *Romanian Journal of Technical Science: Applied Mechanics*, Vol. 59, No. 1/2, pp. 178–204.

Somodi, B. and Kövesdi, B. (2016), "Flexural Buckling of Cold-Formed High-Strength Steel Rectangular Hollow Section Columns," *Journal of Constructional Steel Research*, Vol. 122, pp. 614–626.

Somodi, B. and Kövesdi, B. (2017), "Flexural Buckling of Welded Box Section Columns Made of High Strength Steels," *Journal of Constructional Steel Research*, Vol. 128, pp. 567–579.

Spoorenberg, R.C., Snijder, H.H., Cajot, L.-G., and May, M.S. (2013), "Experimental Investigation on Residual Stresses in Heavy Wide Flange QST Steel Sections," *Journal of Constructional Steel Research*, Vol. 89, pp. 63–74.

Stall, K., Culhane, A., Sun, L., Cross, R.C., and Steiner, M. (2024), "Tensile Coupon Testing and Residual Stress Measurements of High-Strength Steel Built-Up I-Shaped Sections," *Engineering Journal*, AISC, Vol. 61, No. 3, pp. 159–175.

Strating, J. and Vos, H. (1975), "Computer Simulation of the ECCS Buckling Curve—Using a Monte-Carlo Method," *Construction Métallique*, Vol. 3.23, pp. 334–358.

Stroetmann, R. and Penner, G. (2024), "Buckling Resistance and Residual Stresses of Welded Box Columns Made of High-Strength Steels," *10th International Conference on Steel and Aluminum Structures (ICSAS24)*, Rio de Janeiro, Brazil.

Sun, Y., Liang, Y., and Zhao, O. (2020), "Minor-Axis Flexural Buckling Behaviour and Resistances of Pin-Ended S690 High Strength Steel Welded I-Section Columns," *Thin-Walled Structures*, Vol. 156, pp. 106980.

Tide, R.H.R. (2001), "A Technical Note: Derivation of the LRFD Column Design Equations," *Engineering Journal*, AISC, Vol. 38, No. 4, pp. 137–139.

von Kármán, T. (1907), "Festigkeitsprobleme im Maschinenbau," F. Klein and C. Müller, Eds., Vol. 4. 4, B.G. Teubner, pp. 311–385.

Wang, J. and Gardner, L. (2013), "Testing and Numerical Simulation of High Strength Steel Hollow Sections under Bending," *Journal of Constructional Steel Research*, Vol. 80, pp. 100–108.

Yun, X., Zhu, Y., Meng, X., and Gardner, L. (2023), "Welded Steel I-Section Columns: Residual Stresses, Testing, Simulation and Design," *Engineering Structures*, Vol. 282, pp. 115631.

Evaluation of Seismic Design Parameters for Modular Metal Buildings in High Seismic Zones

MOHAMMAD T. NIKOUKALAM, SHAHABEDDIN TORABIAN, and BENJAMIN W. SCHAFER

ABSTRACT

The objective of this paper is to evaluate the seismic design parameters for modular metal building systems in high seismic zones in the United States using the FEMA P695 (ATC, 2009) methodology. Modular metal buildings, commonly used for large open spaces such as warehouses and data centers, combine traditional built-up tapered steel frames with intermediate gravity-only columns. A suite of archetype buildings with varying spans, heights, and number of modules was developed in collaboration with industry and analyzed using nonlinear static and dynamic procedures. High-fidelity shell finite element models, validated against component and shake table tests, capture key failure modes, including local and global buckling. Results from pushover and quasi-static cyclic analyses were used to calibrate nonlinear single-degree-of-freedom models for subsequent incremental dynamic analyses against the FEMA P695 earthquake suite. The study demonstrates that modular metal buildings designed with a response modification factor $R = 3.5$ meet the FEMA P695 collapse performance criteria, provided that lateral bracing systems are designed to meet both strength and stiffness requirements of AISC 360. Buildings using traditional strength-only bracing exhibited limited ductility due to premature column buckling, whereas AISC-compliant bracing achieved stable post-peak response and improved collapse margins. A collapse drift limit of 6% is proposed based on system flexibility and observed behavior. The findings confirm the adequacy and applicability of current ASCE 7 ordinary moment frame provisions for modular metal building systems, with important implications for design practice in high-seismic regions.

Keywords: metal buildings, seismic performance, nonlinear, incremental dynamic analysis, fragility.

INTRODUCTION

Metal building systems in the United States typically consist of I-shaped structural steel frames built up from plate and tapered (particularly in depth) to meet dominant demands, secondary cold-formed steel purlins and girts connecting from frame to frame, diagonal rod bracing to provide diaphragm and cross-frame stiffness, and finished with walls of either steel sheeting or tilt-up concrete panels with roofs of through-fastened or standing seam metal panels. For long-span metal buildings, it is common to support the main frame periodically with gravity columns—creating a "modular" metal building system—as opposed to shorter span systems without interior gravity columns known as "clear-span" metal buildings. It is common to utilize noncompact and slender sections within the tapered main frames to provide sufficient stiffness and necessary strength. For seismic design (in the frame direction), metal building systems are typically categorized as ordinary moment frames (OMFs) and thus are only required to meet the design provisions of AISC 360, *Specification for Structural Steel Buildings* (2016), hereafter referred to as AISC 360. Metal building systems have commonly performed well in earthquakes, but there has been keen interest over the last 20 years to better understand the seismic design of these systems (Uang et al., 2011; Smith, 2013; Hatch, 2014).

In particular, the experimental work led by Uang at the University of California–San Diego (UCSD) has provided important benchmarks for predicting the performance of metal building systems and components. Quasi-static cyclic tests on a 20 ft × 60 ft (6.1 m × 18.3 m) clear-span primary frame demonstrated elastic behavior up to approximately 2.5% drift, beyond which stiffness and strength degraded due to lateral-torsional buckling (LTB) in the column (Hong and Uang, 2006). Cyclic component testing of column-knee-rafter connections demonstrated that large drifts were accompanied by LTB in the rafter between brace points, along with flange local buckling (FLB), and the members could undergo multiple cycles and large drifts (beyond 6%) without fracture, but with strength loss. Comparisons of test results with AISC Design Guide 25, *Frame Design Using Web-Tapered Members* (Kaehler et al., 2011), demonstrated that accurate prediction of LTB capacity requires explicit consideration of bracing conditions.

Mohammad T. Nikoukalam, PhD, PE, Consulting Engineer, Simpson Gumpertz & Heger Inc., Washington D.C. Email: mtnikoukalam@sgh.com

Shahabeddin Torabian, PhD, PE, SE, Senior Project Manager, Simpson Gumpertz & Heger Inc., Washington D.C. Associate Scientist, Department of Civil and Systems Engineering, Johns Hopkins University, Baltimore, Md. Email: storabian@sgh.com (corresponding)

Benjamin W. Schafer, PhD, PE, Consulting Principal, Simpson Gumpertz & Heger Inc., Washington D.C., Willard and Lillian Hackerman Professor, Department of Civil and Systems Engineering, Johns Hopkins University, Baltimore, Md. Email: schafer@jhu.edu

Paper No. 2025–07

Finally, full-scale shake table testing of three clear-span metal buildings to evaluate seismic performance under varying configurations, including light and heavy wall cladding and mezzanines, was performed at UCSD (Figure 1) (Uang et al., 2011; Smith, 2013). The tests demonstrated significant system overstrength, with all specimens remaining stable up to 150% of the Imperial Valley ground motion scaled to ASCE 7-16, *Minimum Design Loads and Associated Criteria for Buildings and Other Structures* (2016), design earthquake (DE) levels, and one specimen tested up to 300% DE without collapse. [Note: Maximum considered earthquake levels, (MCE) are 150% DE.] Maximum drift ratios experienced across the specimens varied from 3.5% to 5.4% and LTB, FLB, and panel zone buckling and yielding were observed in the specimens. The buildings with heavy wall attachments exhibited limit states at earlier drifts than those with light walls. None of the buildings collapsed under the imposed excitations, and the tests stopped due to other experimental limitations on the shake table.

To complement the experimental findings, high-fidelity finite element modeling has become essential for evaluating seismic performance, particularly in utilizing the FEMA P695, *Quantification of Building Seismic Performance Factors* (ATC, 2009), procedure to validate seismic response modification coefficients (e.g., R). The second and third authors of this paper were part of a team that developed a peer-reviewed seismic modeling procedure for the seismic performance of clear-span metal buildings shaking in the direction of the main frames (Meimand et al., 2018; Moen et al., 2019). The overall approach utilized a high-fidelity, primarily shell, finite element model of the metal building system to characterize the nonlinear static hysteretic response of the frame and a nonlinear single degree of freedom model to perform the required incremental dynamic analyses (IDA) across a suite of earthquakes to assess the predicted collapse margin ratio. The high-fidelity model incorporated all typical metal building details, including flange braces, metal roof panels, and rod bracing, and was validated against component testing of the main frame and the shake table tests at UCSD (Moen et al., 2019). The peer-reviewed P695 study confirmed the applicability of the OMF seismic response modification coefficient $R = 3.5$ for both traditional light walls and tilt-up heavy walls for clear-span metal buildings (Meimand et al., 2018; Moen et al., 2019). Highlights of the overall findings from this work included (1) clear-span metal building systems are unique in that the gravity and lateral framing systems are combined and member depths and details are influenced prominently by both gravity and lateral demands in the same frame; (2) the period of metal buildings is typically longer than empirical expressions provided in ASCE 7 (ASCE, 2016), and therefore, story drifts (even within the elastic regime) are often greater than conventional steel-frame building systems; and (3) the bracing connected between the purlins or girts and the main frame is critical to achieving a stable large lateral deformation response even as global (e.g., lateral-torsional) buckling initiates.

Beyond the United States, similar modeling efforts have been undertaken to investigate the seismic performance of both clear-span and modular metal building systems in Canada (Bagatini Cachuço, 2021; Bagatini Cachuço and Yang, 2021) and provide guidance on appropriate seismic

Fig. 1. Assembled specimen on shaking table (Smith et al., 2013).

Table 1. Metal Building Archetypes Dimensions and Design Loads				
Archetype	***H*** ft (m)	**N × Span** N × ft (m)	**Bay** ft (m)	V_r kips (kN)
AM1	25 (7.6)	2 × 50 (15.2)	25 (7.6)	17.6 (78.3)
AM2	25 (7.6)	3 × 50 (15.2)	25 (7.6)	25.6 (113.9)
AM3	45 (13.7)	2 × 50 (15.2)	25 (7.6)	18.6 (82.7)
AM4	45 (13.7)	3 × 50 (15.2)	25 (7.6)	26.6 (118.3)
AM5	25 (7.6)	2 × 100 (30.4)	25 (7.6)	33.8 (150.2)
AM6	45 (13.7)	2 × 100 (30.4)	25 (7.6)	34.8 (154.8)

response modification coefficients for use in equivalent lateral force procedures in the National Building Code of Canada (NBCC). The analytical framework employed included shell finite element models of components (e.g., the column-knee-rafter segment) in ABAQUS (Simulia, 2014) then utilized to calibrate a beam finite element model of the main frame implemented in OpenSees (McKenna et al., 2004). IDA was conducted on the OpenSees model for a suite of earthquake motions relevant to western Canada. The researchers performed a series of trial designs considering different levels of assumed ductility-based seismic force reductions (in Canada overstrength and ductility seismic force reductions are separated into two parts) and concluded that the ductility-based force reductions should be approximately 1.3 for metal buildings in western Canada.

The research reported herein uses the framework of Moen et al. (2019) to evaluate the seismic response modification coefficients for modular metal building systems in high-seismic regions in the United States. A series of modular metal building system archetypes are designed in collaboration with industry. A high-fidelity shell finite element model of the archetypes is developed and exercised through modal analysis, geometric and material nonlinear static pushover analysis, and geometric and material nonlinear static cyclic analysis. A nonlinear single degree of freedom surrogate model is calibrated to the high-fidelity model and utilized for IDA across the FEMA P695 earthquake suite. Formal P695 evaluation is performed to assess the adequacy of the assumed seismic response modification coefficients. The scope is limited to modular metal buildings up to 45 ft (13.7 m) in eave height and with roof loads no greater than 20 psf (0.96 kN/m^2) in high-seismic zones.

DESIGN OF MODULAR METAL BUILDING ARCHETYPES

A critical step in the assessment of seismic performance modification factors per FEMA P695 is the development of system archetypes. Previously, for clear-span metal buildings, four archetypes covering light and heavy walls and ranges of height-to-span for the main frames consistent with known practice were developed (Moen et al., 2019). For modular metal buildings, six archetypes were developed, as summarized in Table 1 and depicted in Figure 2. The buildings cover heights of 25 ft (7.6 m) and 45 ft (13.7 m) and utilize either two or three modules with spans between the interior columns of 50 ft (15.2 m) and 100 ft (30.4 m). The archetype buildings were designed and detailed by engineers at Metal Building Manufacturers Association (MBMA) member companies using their own internal design, detailing, and optimization software with the parameters defined in Table 1 and Table 2.

To ensure more sections of the frames are controlled by seismic demand, snow load combinations were not included in developing the frame designs because this leads to lower-weight design [see Moen et al. (2019) for influence of snow loads on seismic designs]. To ensure realistic secondary member sizes and eliminate site specificity, roof purlins, roof decks, diaphragms, girts, and lateral braces were designed against the U.S. average wind load for components and cladding, which corresponds to a wind speed of 110 mph (177 kph), assuming wind exposure category B (ASCE, 2016); however, wind did not control design of the frame members (i.e., seismic controls the lateral demands). The modular archetype metal buildings are designed for the design earthquake (DE) per ASCE 7-16 (2016). The values taken for the spectral response acceleration parameter at short period, S_s, and for the spectral response acceleration parameter at a period of 1.0, S_1, are based on recommendations provided in FEMA P695 (ATC, 2009).

NUMERICAL MODELING

This section describes the high-fidelity (primarily shell) finite element model used to predict the nonlinear lateral response of a modular metal building frame. The frame columns and rafters as well as the purlins, girts, and sheeting are all modeled with shell finite elements (Figure 3). Therefore, the model is capable of capturing local and global buckling of the rafters and columns; local, distortional, and

global buckling (including stiffness loss) of the purlins and girts; as well as buckling and yielding of the panel zone. The model does not include consideration of fracture. The initial modeling protocols, as detailed further below in their current use, were developed for the study on clear-span metal building frames (Meimand et al., 2018; Moen et al., 2019) and subject to peer review (see the Acknowledgments for the peer review team details). The main frame (rafter) modeling was validated against quasi-static cyclic frame subassembly tests conducted using AISC 341-10, *Seismic Provisions for Structural Steel Buildings* (2010), protocol (Smith et al., 2013). The complete model was validated against three full-scale shake table tests conducted at UCSD (Uang et al., 2011; Smith et al., 2013).

All finite element modeling in this study is performed in ABAQUS (Simulia, 2014). Model generation was automated using MathWorks (2018) to get all geometrical and material properties of the archetypes and generate ABAQUS input files. The inputs include rafter and column sizes, tapering, purlin and girt shapes, roof and wall panel sizes, main frame lateral bracing, lateral rod bracing, horizontal roof truss diaphragm, and the material properties of all associated parts.

The main frame is modeled with four-node S4R finite strain shell elements in ABAQUS, following mesh density guidelines defined in Schafer et al. (2010), which set a minimum of four nodes per local buckling half-wavelength. The plate-to-plate connections at the web-to-flange juncture or stiffeners to other elements are provided by common nodes, or tie constraints, and the welds are not explicitly modeled herein.

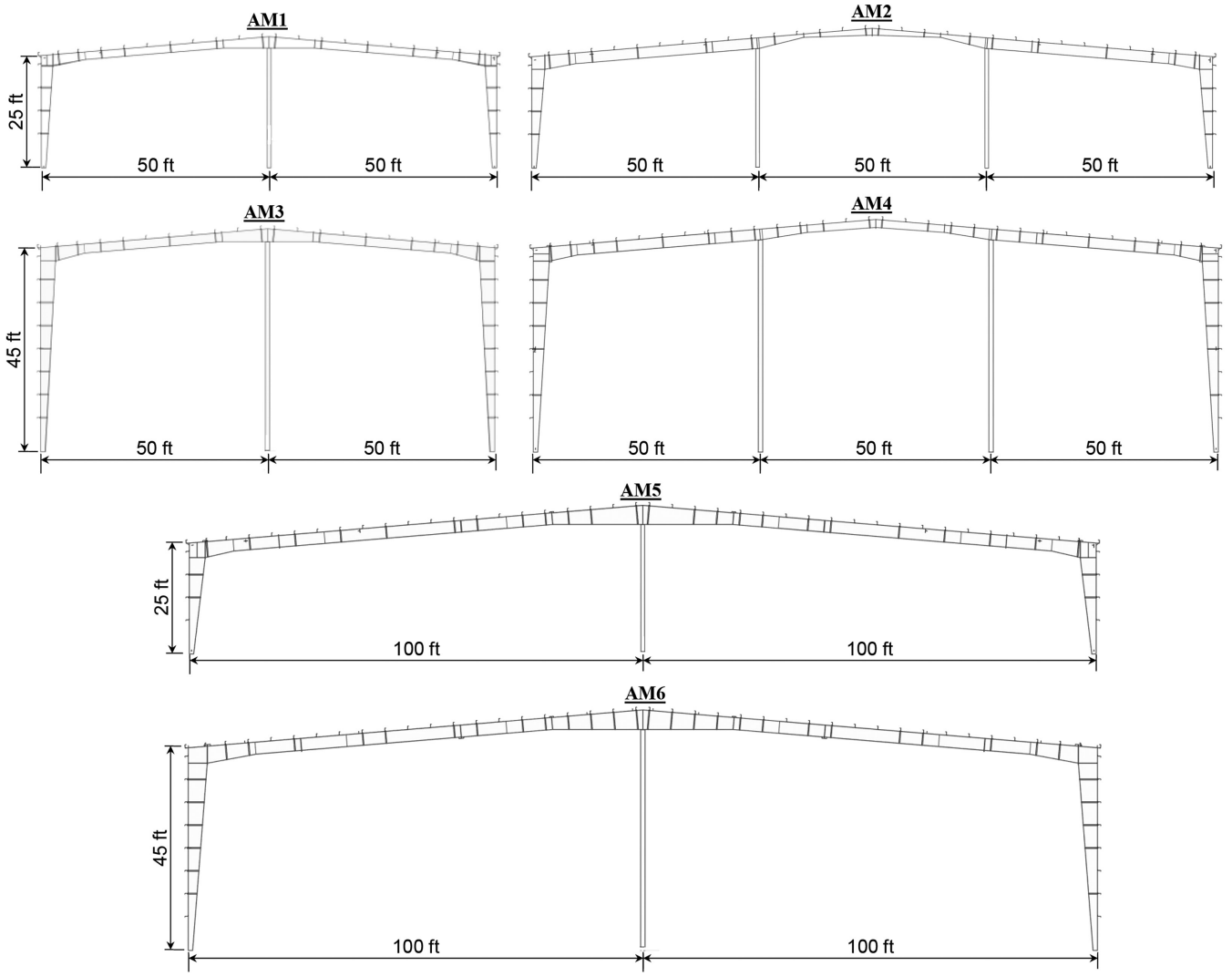

Fig. 2. Schematic elevation view of modular archetype buildings.

Table 2. Archetype Design Assumptions	
Summary of Demand Side (ASCE 7) Design Assumptions	
Building risk/occupancy category	II
Roof slope	1:12
Roof dead load [psf (Pa)]	2.2 (105.3)
Self-weight [psf (Pa)]	2.5 (119.7)
Collateral load [psf (Pa)]	7 (335.2)
Roof live [reducible) (psf (Pa)]	20 (957.6)
Snow load [psf (Pa)]	0 (0)
Rain load [psf (Pa)]	0 (0)
Wind speed [mph (kph)]	110 (177)
Wind exposure category	B
Seismic importance factor	1.0
Seismic design category	D
Site class	D
F_a, F_v	1, 1.7
S_s (g), S_1 (g)	1.5, 0.6
S_{DS}, S_{D1}	1, 0.68
R, Ω_o, C_d	3.5, 2.5, 3
Redundancy factor (ρ)	1.3
Design method	Allowable stress design
Seismic load	Equivalent lateral force procedure
Drift limit	No limit. Exterior walls accommodate frame drift (ASCE 7, Table 12.12-1, footnote c)
Summary of Capacity Side (AISC 360) Design Assumptions	
Metal building frame seismic detailing specifications	OMF
	Three-plate members; pinned base; no restriction on member compactness; no restriction on member splice locations; no restrictions on taper, pinch point, belly points; no special design of the panel zone
AISC 341 *Seismic Provisions*: overstrength conditions	AISC Design Guide 16 connection type, design knee connection with $R = 1.0$
	Use Ω_o forces only for column and base plate axial load, including anchor rods and welding.
Material	Specified $F_y = 55$ ksi (379 MPa), $F_u = 70$ ksi (482 MPa)
Welding	AWS D1.8 provisions, no protected zones
Anchor rods	ASTM F1554 A36

The pretensioned bolts of the end plate connections are not explicitly modeled, but the rafter (or column) end plate and the knee end plate are modeled to always stay in contact, assuming that the precompression is not overcome during the simulations.

The imperfections are considered as distortional buckling half-wavelength with the maximum web imperfection of $\delta = h/250$, where h is the depth of the web, as shown in Figure 4(a). A global out-of-plane sweep in the main frame span of $L/1000$ is also included based on measurements taken in the UCSD cyclic subassembly tests (Smith, 2013).

Thermal self-equilibrating residual stresses are modeled in the main frames with the stress distributions shown in Figure 4(b). The stress magnitudes are chosen based on the suggestions from Prawel and colleagues (1974) and Kim (2010) for built-up steel members.

Purlins and girts are also modeled using S4R shell elements, with a cross-section node pattern extruded along the length. The purlins are connected to the main frames with numerical constraints that link a group of nodes in the web and the bottom flange of the secondary member to a group of nodes on the main frame flange. These constraints approximate a typical clip connection. The girts and purlins are connected to the wall and roof panels by fasteners, where the fastener connection is modeled as a rigid constraint between coincident nodes using the MPC beam

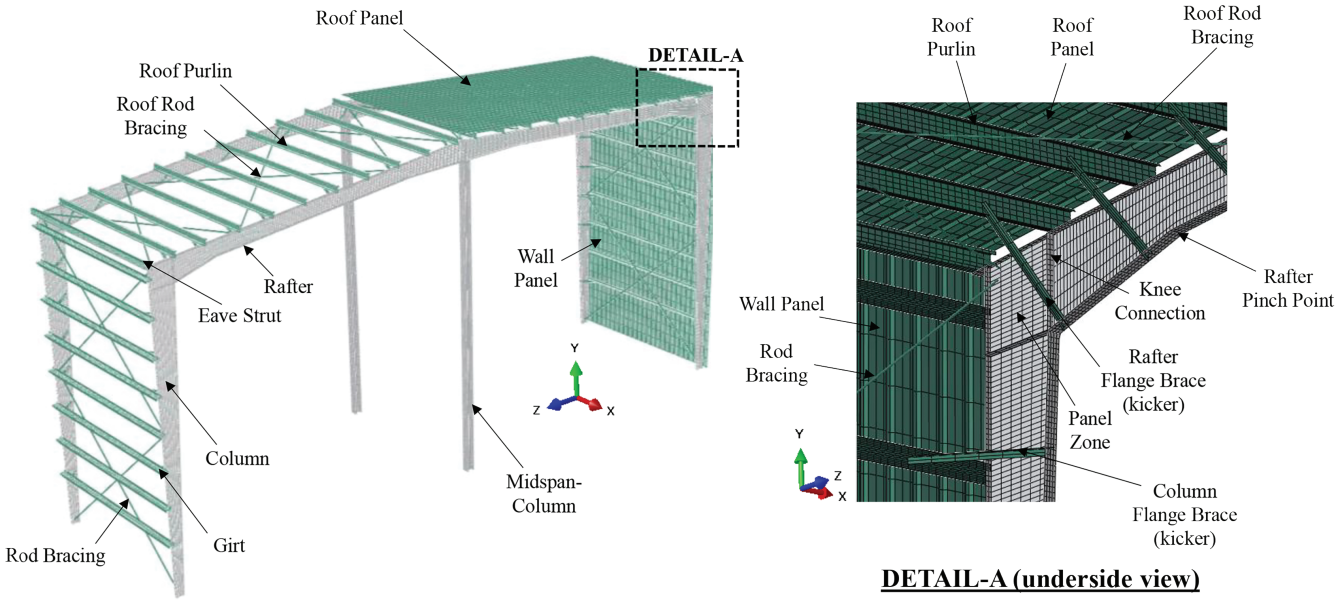

Fig. 3. High-fidelity finite element model.

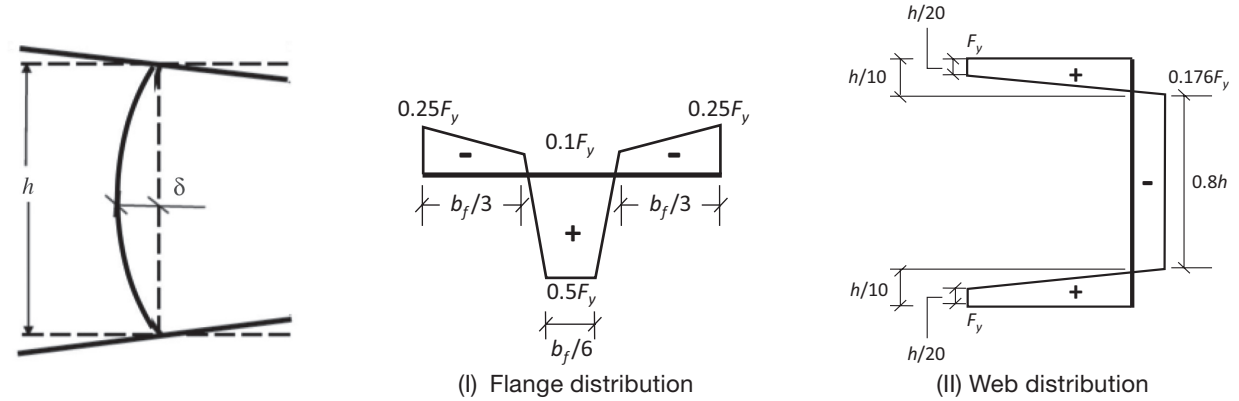

(a) Cross-sectional geometric imperfection pattern

(b) Thermal residual stress pattern (Kim, 2010)

Fig. 4. Mainframe cross-sectional geometric imperfection pattern and thermal residual stress pattern.

in ABAQUS. Initial geometric imperfections and residual stresses from manufacturing are not considered for any secondary members.

Rod braces are modeled with B33 beam elements in ABAQUS, and multi-point constraint (MPC) connections are used on the web near the top flange. The brace angle cross sections are modeled with S4R shell elements, and the brace ends are numerically constrained to node groups in the main frame flange and the purlin.

Wall and roof steel deck sheathing are modeled using shell elements, where sidelaps and endlaps are assumed to be continuous. Screw-fastened roofs are evaluated in this study, and each panel-to-purlin and panel-to-girt screw connection is modeled with a single-node rigid MPC.

Yield stress of 55 ksi (379 MPa) and ultimate stress of 70 ksi (482 MPa) are used for all steel structural elements. An isotropic-kinematic plasticity model, where the von Mises yield surface both expands and shifts to include residual stresses that remain after elastic unloading (i.e., the Bauschinger effect), is considered in both static and cyclic models. All secondary structural elements, including purlins, girts, and lateral braces, have a yield stress of 50 ksi (345 MPa) and an engineering strain hardening slope of 0.25% with isotropic hardening, where E is the elastic modulus of the steel material.

The base of the main frame columns was modeled as pinned, consistent with typical anchor rod and baseplate details in metal building systems. To check this assumption, the nonlinear spring model developed in Moen et al. (2019) was implemented for archetype AM2 with and without degradation, and the resulting ductility and overstrength values were found to be similar to those obtained using the pinned-base model.

ANALYSIS AND EVALUATION OF ARCHETYPE BUILDINGS

Pushover Analysis

Prior to performing nonlinear cyclic or dynamic analyses, a pushover analysis of the high-fidelity metal building model is performed. This analysis is utilized to determine the period-based ductility parameter (μ_T) and the system overstrength factor (Ω_o) for each archetype per FEMA P695. Additionally, the pushover analysis helps check the accuracy of the model and identify the expected failure modes. The pushover response also aids in defining a drift-based collapse limit, as detailed later in the Incremental Dynamic Analysis section. The model is fully geometric and material nonlinear and therefore includes all large deformation (P-Δ and P-δ) effects.

Figure 5 provides the static pushover response in terms of base shear versus roof displacement for all archetype buildings. "Tall buildings" AM3 and AM4 have insufficient ductility for successful seismic performance. Both suffer greater than 20% strength loss at peak load, although they have sufficient strength (i.e., the peak strength is well in excess of the design strength). The observed post-peak response for AM3 and AM4 are provided in Figures 5 and 6(a) and (c), respectively, and in both cases, one can observe that the girts are unable to brace the column rafter and that LTB in the column is occurring across multiple brace points. Consultation with the design engineers resulting in learning that the purlin and girt designs for AM3 and AM4 followed historical practice of using 2% of the compressive force (or flange force) in sizing the brace. AISC 360, Appendix 6, requires that both strength (often less than 2%) and stiffness be supplied by the bracing system. In this case, a redesign was required using heavier (thicker) girts to meet the stiffness requirement.

The performance of the redesigned AM3 and AM4 archetypes, designated as AM3R and AM4R, are provided in Figures 5 and 6(b) and (d). The overall response of the redesigned AM3R and AM4R results in adequate post-peak ductility and moves the limit state from LTB in the column to local buckling and yielding in the rafter. AM6 (the final tall building) was designed after AM3R and AM4R and also had the bracing provisions of AISC 360, Appendix 6 applied in its design. Note, AM1, AM2, and AM5 (the shorter buildings) did not have the AISC 360, Appendix 6 bracing provisions applied; however, they still performed well. Figure 5 provides the pushover response, and Figure 7 provides the deformed shape and stress contours for AM1, AM2, and AM5. The initial limit state is rafter yielding and local buckling at the haunch, and detrimental column LTB does not occur until larger drifts. It is anticipated that similar strength but improved post-peak performance is possible in these archetypes if they were to be redesigned to AISC 360, Appendix 6 bracing stiffness and strength provisions; however, given the performance was adequate as designed, the investigation of the overall performance proceeded without redesign and reanalysis on these archetypes.

Based on the nonlinear static pushover response, the resulting system overstrength (Ω_o), ductility (μ), and period-based ductility (μ_T) for each archetype are summarized in Table 3. The system overstrength is defined as:

$$\Omega_o = V_{max}/V_{design} \tag{1}$$

where V_{max} is the maximum base shear and V_{design} is the design base shear—that is, the lateral demand at the design earthquake (DE) level calculated using the ASCE 7-16 fundamental period, T_{ASCE7}. The ductility is defined as

$$\mu = \delta_u/\delta_y \tag{2}$$

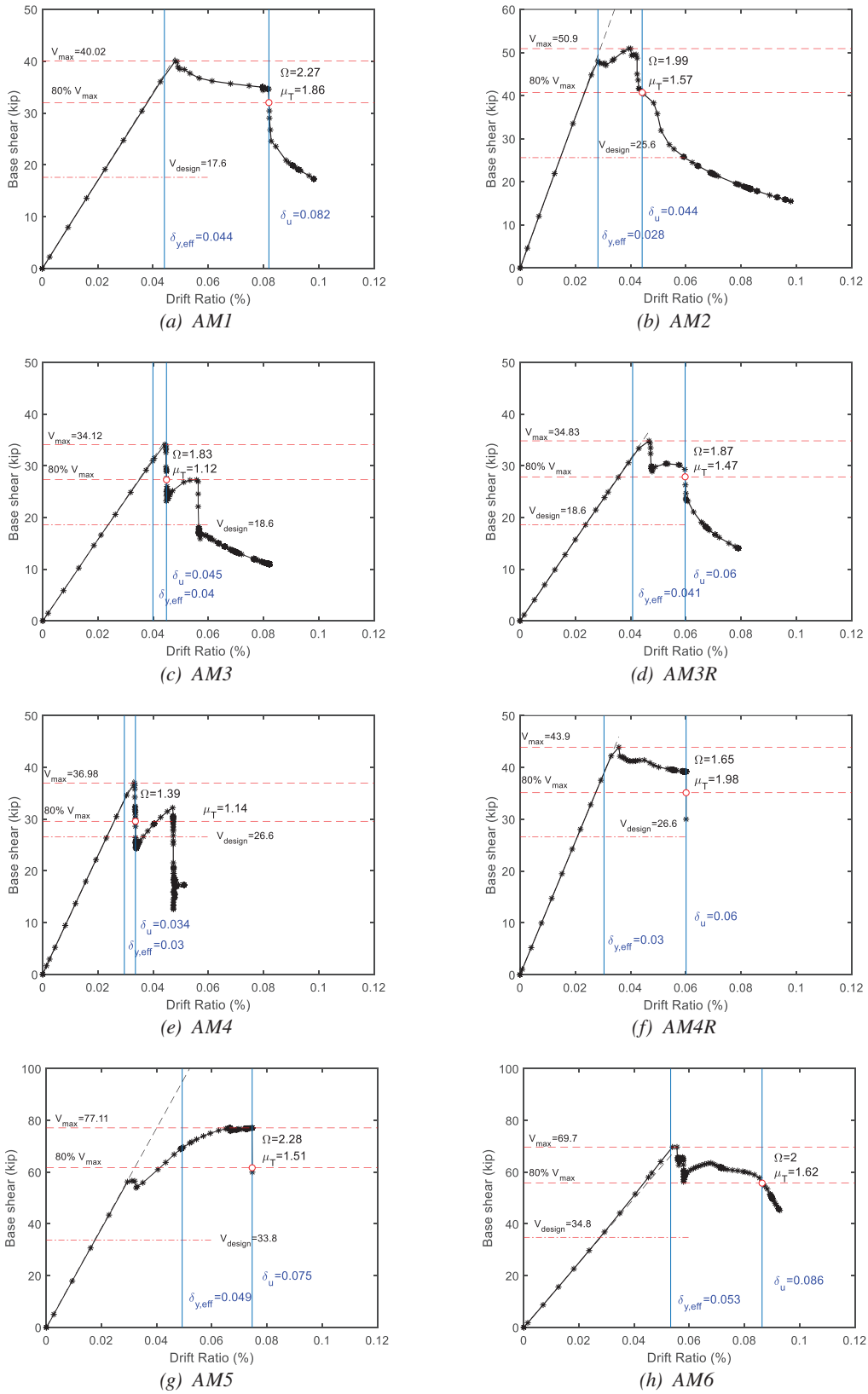

Fig. 5. Static pushover curve of archetypes (1 kip = 4.448 kN).

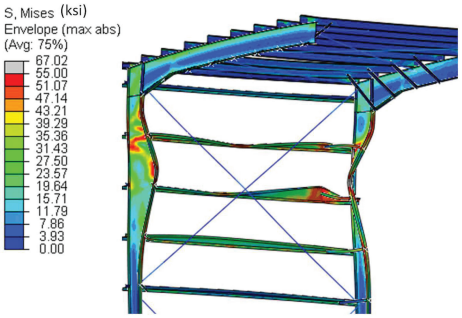

Column and girt LTB

(a) AM3: 4.5% drift ratio

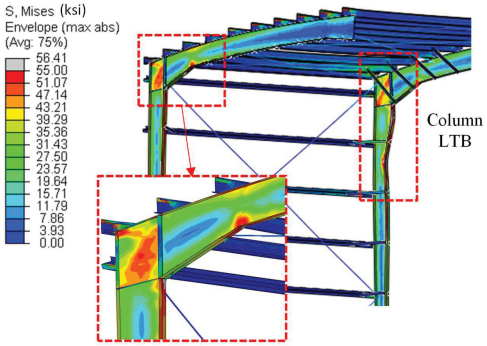

Rafter yielding and local buckling at haunch

(b) AM3R: 4.7% drift ratio

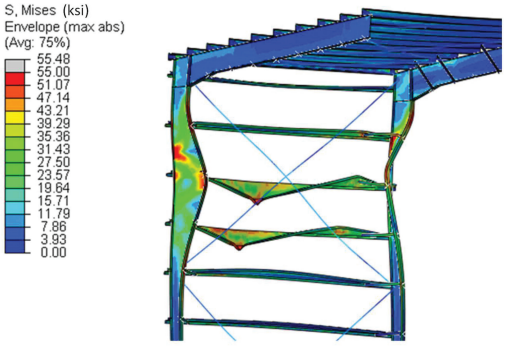

Column and girt LTB

(c) AM4: 3.4% drift ratio

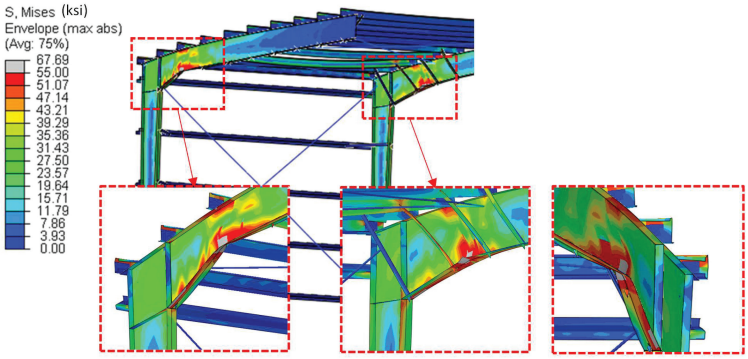

Rafter yielding and local buckling at haunch

(d) AM4R: 3.6% drift ratio

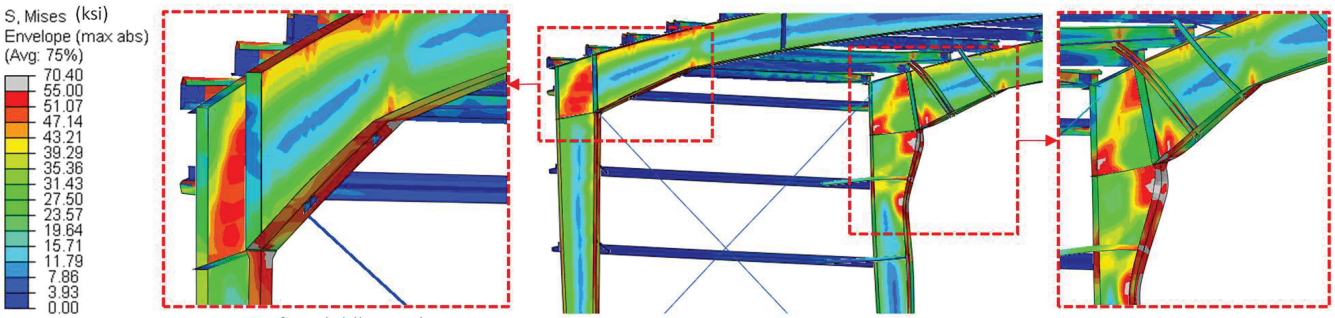

(e) AM6: 5.6% drift ratio

Fig. 6. First failure mode in tall buildings [45 ft (13.72 m)] (1 ksi = 6.895 MPa).

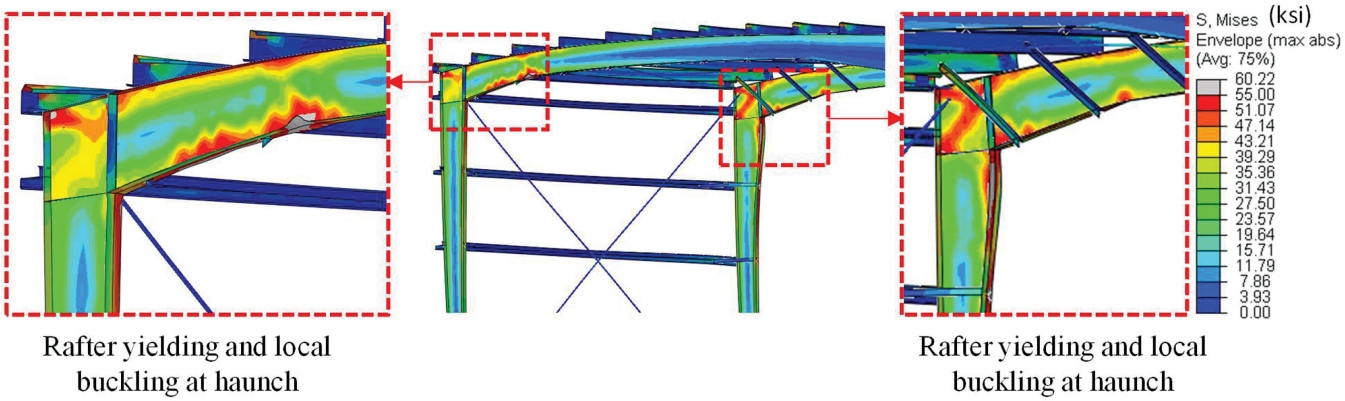

(a) AM1: 4.9% drift ratio

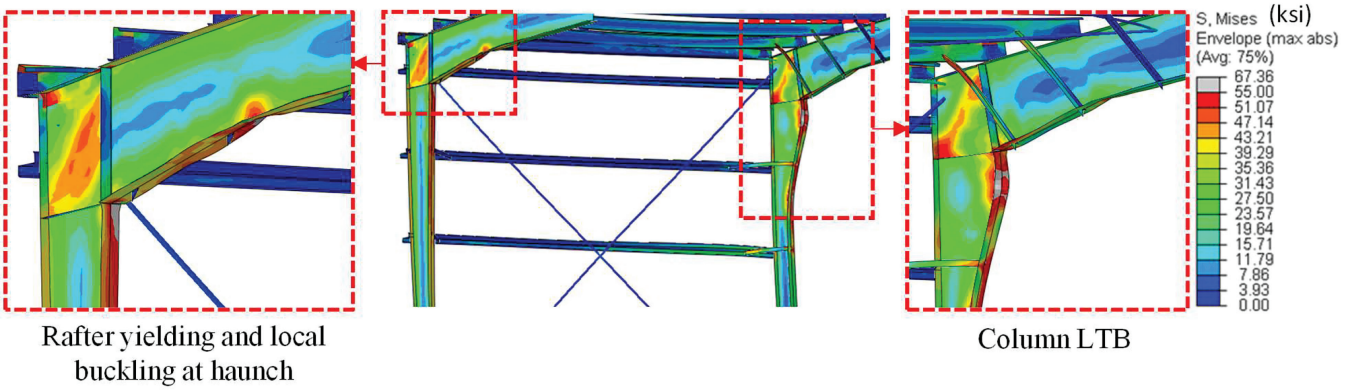

(b) AM2: 3.0% drift ratio

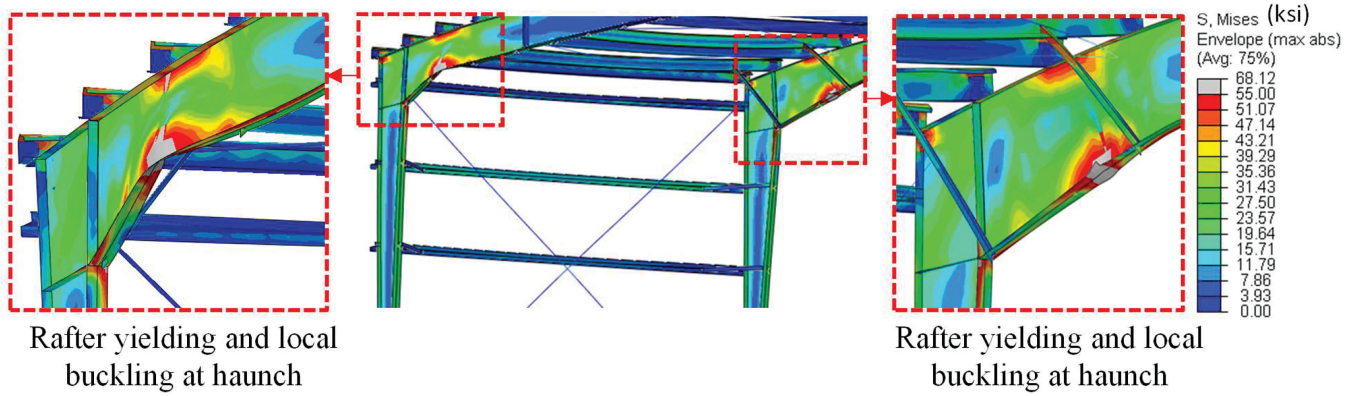

(c) AM5: 3.3% drift ratio

Fig. 7. First failure mode in short buildings [25 ft (7.62 m)] (1 ksi = 6.895 Mpa)

Table 3. Summary of System Overstrength (Ω_o), Ductility, and Period-Based Ductility (μ_T) Factors for Each Archetype.			
Archetype	**Overstrength**	**Ductility**	**Period-Based Ductility**
	Ω_o	μ	μ_T
AM1	2.27	1.67	1.86
AM2	1.99	1.49	1.57
AM3R	1.87	1.39	1.47
AM4R	1.65	>1.94*	>1.98*
AM5	2.28	>1.48*	>1.51*
AM6	2.00	1.47	1.62
Average	2.01	>1.57	>1.67
Archetypes Prior to Redesign of Bracing Stiffness per AISC 360			
AM3	1.83	1.07	1.12
AM4	1.39	1.09	1.14
* ">" indicates that the structure did not exhibit a 20% post-peak strength loss in the pushover analysis; the value is based on the last converged step and represents a conservative lower bound.			

Table 4. Sequence of Observed Behavior in Each Archetype						
	Observed Behavior					
Archetype	**Drift (%)**	**First Significant Behavior**	**Drift (%)**	**Second Significant Behavior**	**Drift (%)**	**Third Significant Behavior**
AM1	4.9	Rafter Y and LB	5.1	Rafter and column LTB	8.0	Rafter and PZ Y
AM2	3.0	Rafter Y and LB Column LTB	4.2	Rafter and PZ Y	4.3	Column LTB
AM3R	4.7	Rafter Y and LB Column LTB	4.7	Column LTB	5.8	Rafter and PZ Y
AM4R	3.6	Rafter Y, LB, and LTB	3.8	Rafter LTB and purlin LB	6.0	Rafter and PZ Y
AM5	3.3	Rafter Y, LB, and LTB	4.9	Rafter and PZ Y	6.7	Purlin LTB
AM6	5.6	Rafter Y and LB Column LTB	5.8	Rafter and purlin LTB	6.8	Rafter and PZ Y
Archetypes Prior to Redesign of Bracing Stiffness per AISC 360						
AM3	4.5	Column and girt LTB	5.6	Rafter and PZ Y	5.6	Column LTB
AM4	3.3	Column LTB	3.4	Girt LTB	4.7	Rafter Y Column LB and LTB
Note: Y: yielding, LB: local buckling, LTB: lateral-torsional buckling, PZ: panel zone						

Table 5. Summary of the Modal Analysis Results of the High-Fidelity Models and Period Evaluation of the Archetype Buildings per ASCE 7-16 Method

Archetype	Mass Participation Ratio	T_1 (s)	T_{ASCE7} (s)	T_{Design} (s)	$\frac{T_1}{T_{ASCE7}}$	$\frac{T_1}{T_{Design}}$
AM1	0.92	1.44	0.39	1.42	3.67	1.02
AM2	0.99	1.19	0.40	1.20	2.95	0.99
AM3R	0.96	2.02	0.61	1.98	3.31	1.02
AM4R	0.97	1.89	0.62	1.89	3.05	1.01
AM5	0.74	1.53	0.42	1.35	3.67	1.13
AM6	0.93	2.39	0.63	2.24	3.79	1.07

T_1: First period of high-fidelity shell finite element model
T_{ASCE7}: Estimate period based on ASCE 7-16, Equation 12.8-7 (ASCE, 2016)
T_{Design}: Period estimate by metal building designer based on beam element approximation

where δ_u is the ultimate roof drift displacement—that is, the roof displacement at $0.8V_{max}$—and δ_y is the yield roof drift displacement, defined as

$$\delta_y = V_{max}/k_e \tag{3}$$

where k_e is the initial (elastic) stiffness of the building. The period-based ductility is defined as

$$\mu_T = \delta_u/\delta_{y,eff} \tag{4}$$

where δ_u is the ultimate roof drift—that is, the roof displacement at $0.8V_{max}$—and $\delta_{y,eff}$ is the effective yield roof drift displacement, defined in FEMA P695 as:

$$\delta_{y,eff} = C_o\left(\frac{V_{max}}{W}\right)\left(\frac{g}{4\pi^2}\right)\left[max(T, T_1)\right]^2 \tag{5}$$

where T is the fundamental period per ASCE 7-16, T_1 is the fundamental period of the building models computed using eigenvalue analysis (see Frequency Analysis section), W is the seismic weight of the building, g is the acceleration of gravity, V_{max} is the maximum base shear of the building, and C_o is the modal coefficient (which is 1.0 for a single-story structure like a metal building).

According to Table 3, the calculated overstrength factors are in the range of 1.6 to 2.3. According to the FEMA P695 procedures, the system overstrength, Ω_o, is calculated as the maximum of the average from the different performance groups, but not to exceed a maximum value of Ω_o = 3.0. Accordingly, from the archetype analysis summarized in Table 3, the design value would be set to Ω_o = 2.0, governed by the average value of the performance group.

The nonlinear static pushover analysis provides a clear examination of the expected limit states. The sequence of failure modes observed in each archetype is presented in Table 4.

Major observations from the nonlinear static response include the following:

- In "short" archetypes [H = 25 ft (7.62 m)] AM1, AM2, and AM5, the post-peak response is primarily dominated by rafter yielding and local buckling at the haunch, followed by rafter span LTB at larger drift ratios in all three archetypes and minor column LTB in AM1 and AM2.
- In tall archetypes [45 ft (13.72 m)] with column lateral bracing designed per the strength-only (2%) method (i.e., AM3 and AM4), the post-peak strength degradation is dominated by severe column LTB [Figures 6(a) and (c)], followed by girt LTB due to the diagonal brace (kicker) force at the location of column lateral braces. The high sensitivity of AM3 and AM4 to column LTB results in significantly lower ductility than the other archetypes. These bracing designs do not meet the criteria of AISC 360.
- In tall archetypes with column lateral bracing designed per AISC 360 (AM3R, AM4R, and AM6), the post-peak strength degradation is primarily dominated by rafter yielding and local buckling at the haunch followed by rafter span or minor column LTB [Figures 6(b), (d), and (e)]. The lower sensitivity of AM3R, AM4R, and AM6 to column LTB results in a more stable post-peak response and higher ductility than AM3 and AM4.

With these findings, it was concluded that application of the OMF criteria in seismic design of metal buildings must adhere to all provisions of AISC 360, including the bracing provisions, and that the design of braces for 2% of the compressive force is not sufficient. Therefore, further analysis would only be conducted on AM3R and AM4R. As a result, in the analyses that follows AM3 and AM4 are replaced by AM3R and AM4R.

Frequency (Modal) Analysis

The natural periods and mass participation of the modular metal building archetypes are provided in Table 5. The natural period of the tall archetypes (AM3R, AM4R, and AM6) is between 2.02 and 2.39 s, while that of the shorter ones (AM1, AM2, and AM5) ranges from 1.19 to 1.89 s. The high-fidelity model and the beam element model used in the design agree strongly, while the empirical equations in ASCE 7-10 (ASCE, 2010) were found to assume far stiffer response than is typically realized in metal building frames.

Cyclic Analysis

The high-fidelity models are used to characterize the quasi-static cyclic response of the archetypes, including strength and stiffness degradation. Each archetype metal building is subjected to cyclic horizontal displacements per AISC 341 cyclic loading protocol at the knee level. The cyclic response is defined as the base shear versus drift ratio in Figure 8. The cyclic results generally follow the pushover backbone, but some minor cyclic degradation is observed in the archetypes. The quasi-static cyclic behavior is used to calibrate a nonlinear single-degree-of-freedom (SDOF) model utilized in incremental dynamic analysis and discussed in the following section.

Incremental Dynamic Analysis

The objective of the nonlinear incremental dynamic analysis (IDA) is to determine the ground motion intensity corresponding to the collapse of the structure, per the FEMA P695 procedure. A collapse limit (e.g., drift limit) is required in the IDA procedure to estimate the probability of collapse and determine the acceptability of the seismic response modification coefficients utilized in design. Selection of the collapse limit for the modular metal buildings requires some care. In the available full-scale (clear-span) metal building shake table tests (Uang et al., 2011; Smith, 2013), collapse was not observed up to 4% story drift, so a direct experimental collapse drift limit is unavailable. Moen et al. (2019) utilized a 4.5% collapse drift limit in their modeling, based on the observation that plastic strain accumulation in the rafter and panel zone would eventually lead to fracture (which was not included in the model). Modular metal building systems are flexible. Review of the pushover response of Figure 5 indicates that most of the archetypes are in the elastic or initial post-yield hardening response at 4.5% drift; therefore, such a limit for collapse would be inappropriate. An archetype-dependent collapse drift limit is possible; however, a simpler approach was selected here—the collapse drift limit was assumed to be 6% for modular metal buildings. In all archetypes, except for AM2, the ultimate drift ratio (drift ratio corresponding to 20% strength loss) is greater than 6%. Plastic strain accumulation does not initiate until the first significant nonlinear response is observed, which is generally greater than 4%; thus, the use of 6% recognizes the inherent flexibility of the modular metal building archetype but still limits the total plastic strain accumulation in the response.

A set of 22 pairs of ground motions (44 total) specified in Appendix A of FEMA P695 were used for the IDA. The IDA procedure starts by defining the median spectral intensity of the far-field record set, S_T, measured at the fundamental period of the structure, and then the far-field record set is scaled by $\alpha = S_{MT}/S_T$, where α is the intensity factor and S_{MT} is the spectral intensity corresponding to the maximum considered earthquake (MCE) at the fundamental period of the structure. The median collapse intensity corresponding to the spectral acceleration at the fundamental period of the building at which half of the ground motions cause collapse is referred to as $\hat{S}_{CT}$. IDAs are performed using the nonlinear SDOF modeling protocol introduced in the following section.

Computationally Efficient Nonlinear Dynamic Analysis Framework

The dynamic behavior of metal buildings, as a single-story moment frame with roof masses, can be represented by a single-degree-of-freedom (SDOF) dynamic system. The first mode mass participation ratio of previously studied clear-span metal buildings is between 76% and 83% (Moen et al., 2019). The first mode mass participation ratio of the modular metal building archetypes with 50 ft (15.2 m) modules (AM1–AM4R) are between 92% and 99% per Table 5. The longer span 100 ft (30.4 m) modules of AM5 and AM6 have lower mass participation ratios, 74% and 93%, respectively. The long rafter spans and short columns of AM5 are indicative of the potential for some higher mode response in this specific archetype; however, the nonlinear static response and observed failure mechanism is benign in this archetype as indicated by its high overstrength and ductility (see Figure 5 and Table 3), and the lower mass participation ratio for this archetype was deemed acceptable for the study.

A classical SDOF dynamic model can be represented by a lumped mass, m, spring stiffness, K_t, and damping, c, as shown in Figure 9. The dynamic properties—specifically, the period of vibration, T—can be selected so the SDOF model is consistent with what would be expected for the actual building. Strength and stiffness degradation and the period shift as the building experiences damage during an earthquake are approximated by the nonlinear spring stiffness, K_t. A SDOF hysteretic material model may be matched to the cyclic hysteretic response of the high-fidelity model. With this high-fidelity to SDOF mapping, the SDOF cyclic response includes local and system-level responses,

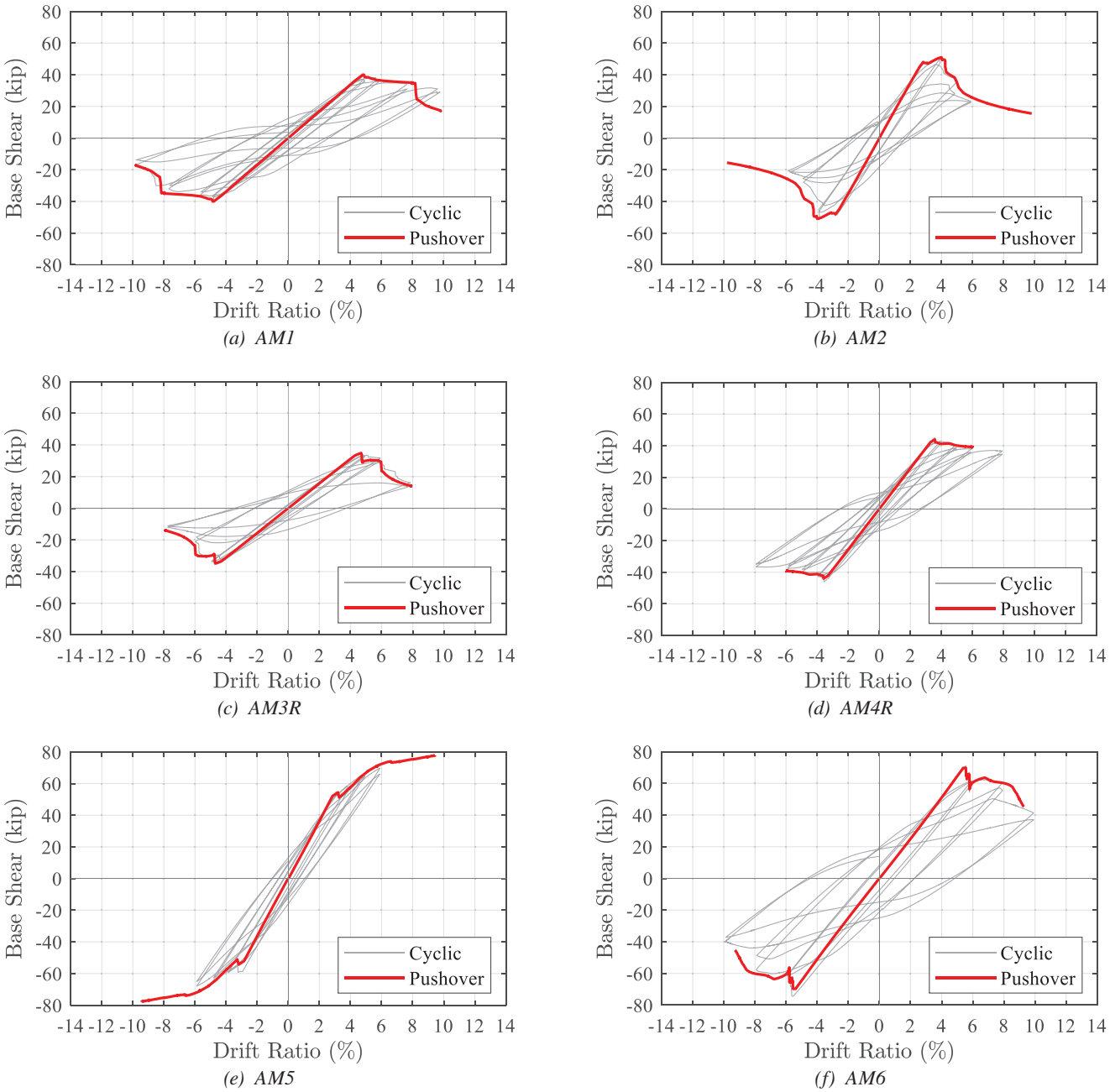

Fig. 8. Quasi-cyclic and pushover response of archetypes (1 kip = 4.448 kN).

including rafter lateral-torsional buckling and local buckling and bracing from the secondary structural system (purlins, girts, kickers, etc.).

The Pinching 04 material model in OpenSees is utilized for the nonlinear SDOF material hysteretic model. The Pinching 04 model includes the definition of four response points as illustrated in Figure 10 and additional parameters to handle loading/unloading (pinching) and cyclic degradation. Here, the backbone points and other parameters are established such that the per-cycle and accumulated error between the SDOF model and the high-fidelity model response are minimized, as illustrated for AM2 in Figure 11. This process is repeated for all studied archetypes. The Pinching 04 model fitting parameters for all archetypes are presented in Appendix Table A.

The seismic mass, m, is assumed to be equal to the mass used to calculate the design seismic weight in an equivalent lateral force procedure. Matching the fundamental building period to the SDOF model is desirable so that elastic behavior and the natural periods are consistent. The relationship among the mass, initial stiffness, and period of the building can be written as follows:

$$T_1 = 2\pi\sqrt{m/k_i} \tag{6}$$

where m is the seismic mass, k_i is the initial stiffness of the building in the SDOF model, and T_1 is the fundamental period of the SDOF model. Because the building period is determined by high-fidelity analysis, and the seismic mass

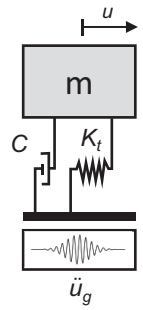

Fig. 9. Metal building nonlinear SDOF model definitions.

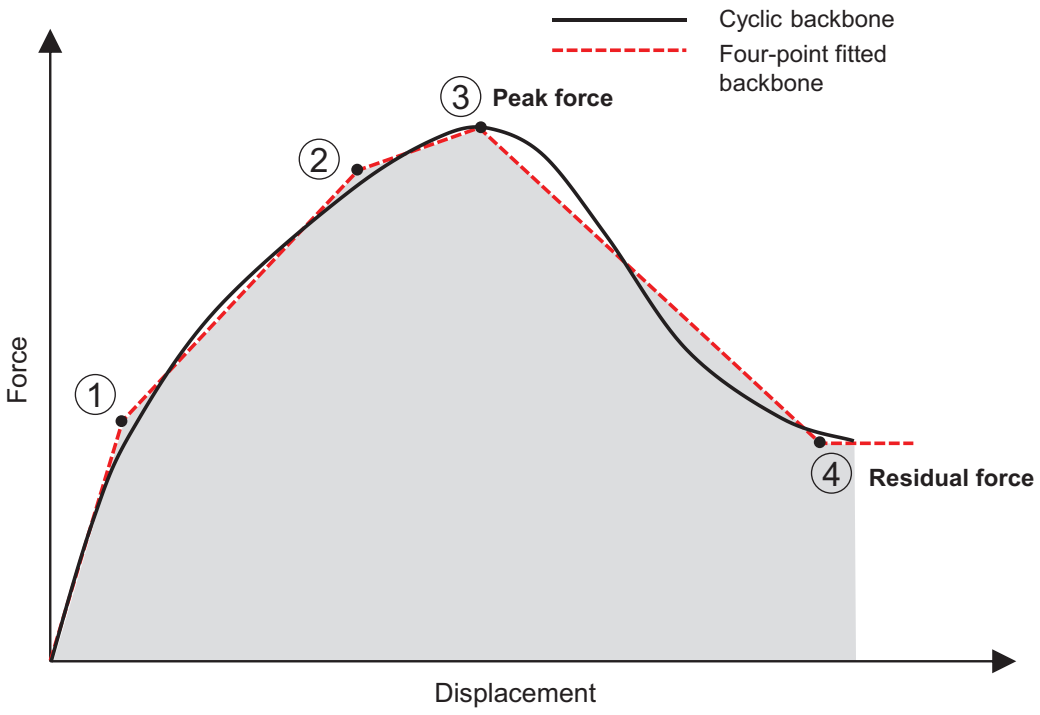

Fig. 10. A four-point backbone fitted to the cyclic backbone is shown in the first quadrant.

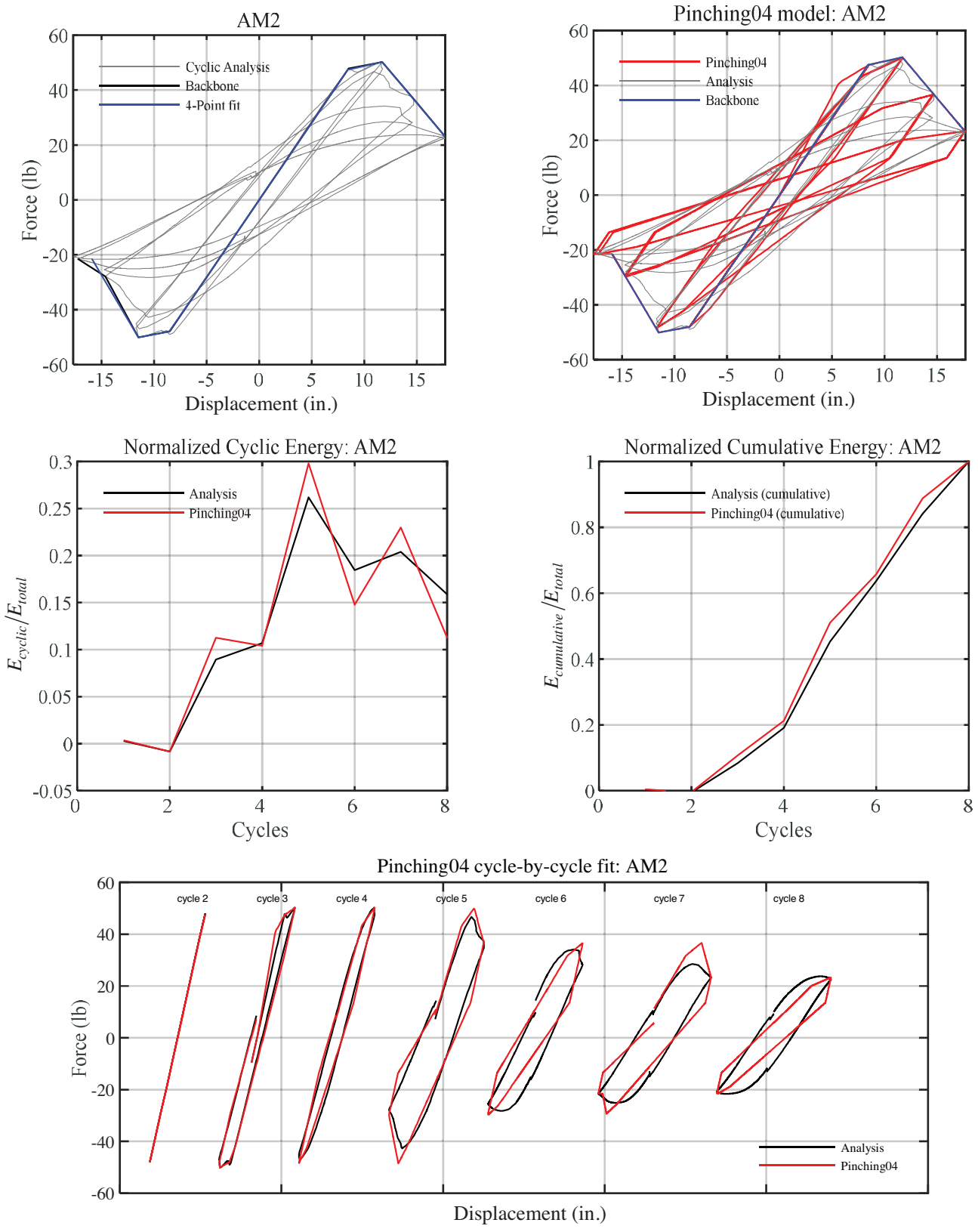

Fig. 11. Quasi-static cyclic response of AM2: High-fidelity simulation and fitted response using Pinching 04 hysteretic model in OpenSees (McKenna et al., 2004) (1 kip = 4.448 kN; 1 in. = 25.4 mm).

Table 6. Summary of Archetypes Analyses Results: Collapse Drift Limit of 6% ($R = 3.5$, $\Omega_o = 3$, $C_d = 3$)										
Archetype	Ω_o	μ_T	S_{CT} (g)	SMT (g)	*CMR*	*SSF*	*ACMR*	$ACMR_{10\%}$	$ACMR_{20\%}$	Check (Pass/Fail)
AM1	2.27	1.86	0.80	0.63	1.28	1.21	1.54	1.70	1.42	Pass
AM2	1.99	1.57	0.99	0.76	1.31	1.16	1.52	1.66	1.39	Pass
AM3R	1.87	1.47	0.79	0.45	1.78	1.16	2.07	1.65	1.39	Pass
AM4R	1.65	>1.98	0.85	0.48	1.79	1.23	2.20	1.72	1.43	Pass
AM5	2.28	>1.51	0.75	0.59	1.27	1.17	1.48	1.65	1.39	Pass
AM6	2.00	1.62	0.54	0.38	1.43	1.18	1.69	1.67	1.40	Pass
						Average	1.75	1.67	—	Pass

of the building is also defined in the seismic design of the building, an equivalent initial stiffness is required to match the actual building period to the SDOF model. Chapter 6 of FEMA P695 (ATC, 2009) addresses this challenge by defining an effective yield roof drift displacement, $\delta_{y,eff}$, as defined in Equation 5. For a single-story structure like a metal building, the modal coefficient C_o is 1.0, and by assuming that the actual period of the building is larger than the ASCE 7 (2010) prediction ($T_1 > T$), Equation 5 can be simplified to

$$V_{\max}/\delta_{y,eff} = 4\pi^2 m/T_1^2 \tag{7}$$

By further noting $k_{eq} = V_{max}/\delta_{y,eff}$, the equivalent initial stiffness for the SDOF model, k_{eq}, can be calculated as

$$k_{eq} = 4\pi^2 m/T_1^2 \tag{8}$$

This equivalent initial stiffness is used in the Pinching 04 models.

The last term to consider in the SDOF dynamic equation is energy dissipation treated with the viscous damping ratio, ξ. For all simulations in this study, $\xi = 2\%$ is selected, corresponding to a low-intensity elastic response, assuming that energy dissipation from yielding, buckling, and damage is accounted for in the hysteretic response.

IDA and Fragility Curves

Story-drift versus the earthquake spectral acceleration scale factor and the resulting fragility response for all archetypes are provided in Figures 12(I) and (II), respectively. As an example, for AM5, the median collapse capacity (from all 44 records) is $\hat{S}_{CT} = 0.75$ g [Figure 12(e) (II)], and the $CMR = \hat{S}_{CT}/S_{MT} = 0.75/0.59 = 1.27$. Collapse fragility curves are also used to express this information, where the cumulative collapse probability is related to the ground motion spectral intensity. The discrete points in Figure 12 are obtained directly from the collapse points of the IDA curve for each archetype. A lognormal distribution is fit to the data to get a smooth curve and obtain $\hat{S}_{CT}$.

Per FEMA P695, the fragility response should be modified with the spectral shape factor, *SSF*, to account for the spectral shape. The *SSF* is a function of the building fundamental period, *T*, and period-based ductility, μ_T, used to calculate the adjusted collapse margin ratio as $ACMR = SSF \times CMR$. For AM5, for example, $ACMR = 1.17 \times 1.27 = 1.48$. Similar results are provided for all studied archetypes in Table 6.

SEISMIC PERFORMANCE ASSESSMENT PER FEMA P695 METHODOLOGY

Per FEMA P695 (ATC, 2009), the performance of a system is judged by comparing the adjusted collapse margin ratios (ACMR) to the lower bound acceptable collapse margin ratios: $AMCR_{10}\%$ or $AMCR_{20}\%$ as specified in FEMA P695. The performance of a structural system is acceptable if, under the MCE ground motion, each archetype has a large enough collapse capacity such that the probability of collapse is less than 20% ($ACMR > ACMR_{20\%}$), and the performance group must, on average, have less than 10% probability of collapse ($\overline{ACMR} > ACMR_{10\%}$, where $\overline{ACMR}$ is the average ACMR of the performance group). The acceptable ACMRs are calculated by assuming the distribution of collapse level spectral intensities is lognormal, with a median equal to $\hat{S}_{CT}$, and a standard deviation of β_{TOT}, which represents the total uncertainty in the collapse behavior of the system calculated as

$$\beta_{TOT} = \sqrt{\beta_{RTR}^2 + \beta_{DR}^2 + \beta_{TD}^2 + \beta_{MDL}^2} \tag{9}$$

where β_{RTR} is the record-to-record collapse uncertainty defined as

$$\beta_{RTR} = 0.1 + 0.1\mu_T \le 0.4 \tag{10}$$

and β_{DR} reflects the uncertainty in the implementation of design and quality assurance requirements, β_{TD} demonstrates the uncertainty in the quality and completeness of

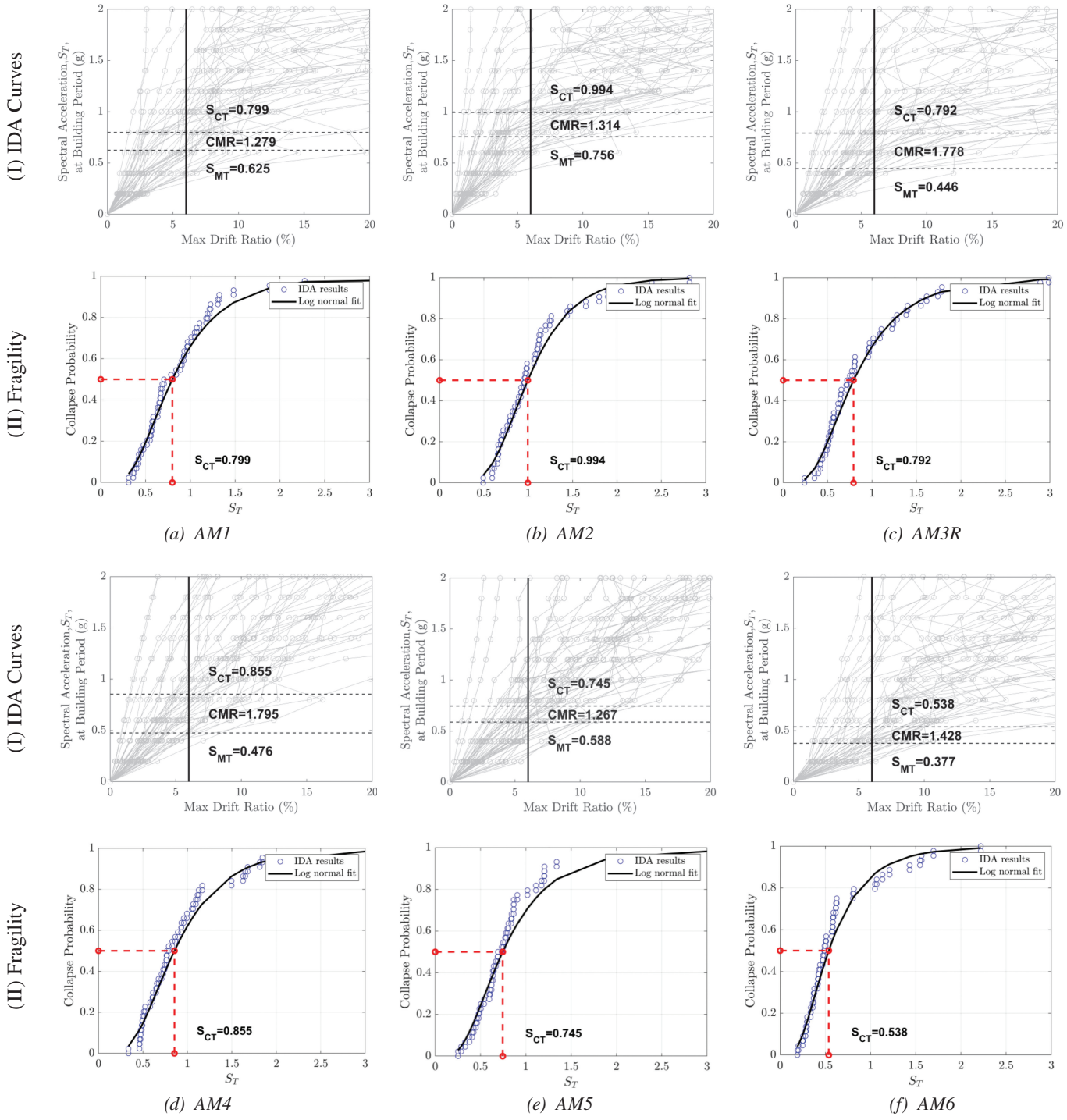

(a) AM1 *(b) AM2* *(c) AM3R*

(d) AM4 *(e) AM5* *(f) AM6*

Fig. 12. IDA and fragility curves for archetypes.

the test data to characterize the structural behavior, and β_{MDL} reflects the uncertainty in the accuracy and variability of the structural modeling (ATC, 2009).

For the present study, β_{TOT} was defined using Equation 9, and the assumed uncertainties were $\beta_{DR} = 0.20$, $\beta_{TD} = 0.20$, and $\beta_{MDL} = 0.10$. β_{DR} is low because the archetype buildings are designed professionally, and the designs are reviewed internally and by the MBMA seismic steering group. The test data-related uncertainty β_{TD} is low since shake table test data are available for the underlying modeling protocol development. The modeling-related uncertainty β_{MDL} is low because collapse characteristics, including local and global buckling, are represented well in high-fidelity and nonlinear SDOF models.

The seismic response parameters, specifically, the median collapse intensity, $\hat{S}_{CT}$, the collapse margin ratio, *CMR*, the adjusted collapse margin ratio, *ACMR*, and acceptable collapse margin ratios ($ACMR_{10\%}$ and $ACMR_{20\%}$) are summarized in Table 6. The index archetypes meet the individual and group acceptance criteria. Thus, the assumed design seismic response modification factor R = 3.5 (Table 2) is deemed to satisfy the minimum acceptance criteria of FEMA P695 for modular metal buildings with two and three spans with different heights and span widths.

DISCUSSION

High-fidelity simulations coupled with surrogate models can provide an effective means for evaluating metal building system seismic performance. Conventional design processes provide acceptable outcomes in past experimental work and current P695-based modeling efforts but may still behave differently than expected by engineers. Drift is driven largely by LTB between and across brace points, not yielding. Modifying R in the initial design does not typically result in significantly different frame performance given the limited range in which lateral loads control the moment envelope and given that frames are fully optimized to that moment envelope. Lateral performance of the frames in modular metal buildings is not markedly different from clear-span buildings; however, they can be much more flexible. Innovative seismic systems and the necessity of the limits of current ASCE 7 code provisions (height, weight, etc.) could all now be efficiently explored using the developed models and protocols.

SUMMARY AND CONCLUSION

This study evaluated the seismic performance of modular metal buildings in high seismic zones using the FEMA P695 methodology. A representative set of archetype buildings, reflecting current industry design practices and incorporating ordinary moment frame (OMF) behavior with a response modification factor of R = 3.5, was developed and analyzed through modal analysis, nonlinear static pushover, quasi-static cyclic simulations, and incremental dynamic analyses (IDAs). High-fidelity finite element models, calibrated to experimental data from prior shake table and subassembly tests, were used to capture the nonlinear behavior of the archetypes and to provide an accurate assessment of collapse performance, with fracture not explicitly modeled. For the FEMA P695 evaluation, these high-fidelity models were further idealized into calibrated nonlinear single-degree-of-freedom (SDOF) systems, which formed the basis of the collapse assessment.

The results of this study confirm that modular metal buildings designed with R = 3.5 can meet the FEMA P695 acceptance criteria, provided that lateral bracing systems for both columns and rafters are designed to satisfy the strength and stiffness requirements of AISC 360, Appendix 6. In contrast, buildings designed with traditional strength-only (2%) bracing methods exhibited reduced ductility and early onset of lateral-torsional buckling (LTB) in columns, which significantly compromised ductility. Redesign of the lateral bracing to include adequate stiffness, in accordance with AISC provisions, resulted in improved post-peak behavior and increased system ductility.

The nonlinear static and dynamic analyses also showed that modular metal buildings remain largely elastic up to approximately 4% story drift and that ultimate drift ratios generally exceed 6%. Based on this observed performance, a collapse drift limit of 6% is proposed as more appropriate for modular metal buildings than the 4.5% previously adopted in studies of clear-span metal buildings for use within the FEMA P695 evaluation framework only, and not as a prescriptive limit for design practice. The calibrated SDOF models used in this study were able to effectively reproduce the cyclic and collapse behavior of the archetypes, enabling efficient implementation of the FEMA P695 framework.

Overall, the results confirm the applicability and adequacy of the ASCE 7 seismic design provisions where modular metal buildings are categorized as ordinary moment frames when modern bracing design practices are employed. The study highlights the importance of meeting both strength and stiffness criteria in lateral bracing systems and provides a technical foundation for the continued use of R = 3.5 in the seismic design of modular metal buildings, within the scope of modular metal buildings up to 45 ft (13.7 m) in eave height and with roof loads not exceeding 20 psf (0.96 kN/m²).

ACKNOWLEDGMENTS

The authors would like to thank the Metal Building Manufacturers Association (MBMA) Seismic Research Steering Group who provided thoughtful advice, input, effort, and

feedback throughout this project. In addition, several engineers in this group provided the complete designs for the metal building system archetypes. The authors would also like to thank the peer review panel, comprised of Dr. Greg Deierlein, Dr. Michael Engelhardt, and Dr. Tom Sabol, who reviewed the modeling protocols and conclusions in detail for the clear-span seismic study that preceded this work. In addition, Dr. Chia-Ming Uang was gracious with his time and data during the validation phase of the modeling. Finally, Dr. Lee Shoemaker and Mr. Vincent Sagan of MBMA were instrumental in shepherding this project to a meaningful end. The team would also like to recognize the financial support of MBMA in conducting the work.

REFERENCES

AISC (2010), *Seismic Provisions for Structural Steel Buildings*, AISC 341-10, American Institute of Steel Construction, Chicago, Ill.

AISC (2016), *Specification for Structural Steel Buildings*, ANSI/AISC 360-16, American Institute of Steel Construction, Chicago, Ill.

ASCE (2010), *Minimum Design Loads and Associated Criteria for Buildings and Other Structures*, ASCE/SEI 7-10, Reston, Va.

ASCE (2016), *Minimum Design Loads and Associated Criteria for Buildings and Other Structures*, ASCE/SEI 7-16, Reston, Va.

ATC (2009), *Quantification of Building Seismic Performance Factors*, FEMA P695, Federal Emergency Management Agency, Washington, D.C.

Bagatini Cachuço, F. (2021), "Seismic Performance Evaluation of Steel Building Systems in Canada," Master's Thesis, University of British Columbia, Vancouver, Canada.

Bagatini Cachuço, F. and Yang, T.Y. (2021), "Seismic Performance Assessment of Pre-Engineered Steel Buildings on the West Coast of Canada," *Steel and Composite Structures: An International Journal*, Vol. 41, No. 3, pp. 461–474, https://doi.org/10.12989/scs.2021.41.3.461.

Hong, J.K. and Uang, C.M. (2006), "Cyclic Performance Evaluation of a Metal Building System with Web-Tapered Members," Report No. SSRP-06, Department of Structural Engineering, University of California–San Diego, La Jolla, Calif.

Hatch, J. (2014, August), "New Advances in Design and Testing for Seismic Demands," *STRUCTURE Magazine*, https://www.structuremag.org/.

Kaehler, R.C., White, D.W., and Kim, Y.D. (2011), *Frame Design Using Web-Tapered Members*, Design Guide 25, AISC, Chicago, Ill.

Kim, Y.D. (2010), "Behavior and Design of Metal Building Frames with General Prismatic and Web-Tapered Steel I-Section Members," Doctoral Dissertation, Georgia Institute of Technology, Atlanta, Ga.

MathWorks (2018), The MathWorks, Inc., Natick, Mass., www.mathworks.com.

McKenna, F., Fenves, G.L., and Scott, M.H. (2004), "Open System for Earthquake Engineering Simulation," Pacific Earthquake Engineering Research Center, University of California–Berkeley, Berkeley, Calif.

Meimand, V., Moen, C., and Schafer, B. (2018), "Examination of Seismic Response Modification Coefficients for Metal Building Systems with FEMA P695 Process," in *Proceedings of the 11th National Conference on Earthquake Engineering (NCEE)*, Earthquake Engineering Research Institute, Los Angeles, Calif.

Moen, C.D., Torabian, S., and Schafer, B.W. (2019), "Evaluation of Metal Building System Seismic Response Modification Coefficients," Johns Hopkins University, https://jscholarship.library.jhu.edu/items/3fb18f3a-c7e9-4696-b32a-188fd336af76.

Prawel, S.P., Morrell, M.L., and Lee, G.C. (1974), "Bending and Buckling Strength of Tapered Structural Members," *Welding Research Supplement*, Vol. 53, No. 2, pp. 75–84.

Schafer, B.W., Li, Z., and Moen, C.D. (2010), "Computational Modeling of Cold-Formed Steel," *Thin-Walled Structures*, Vol. 48, No. 10–11, pp. 752–762, https://doi.org/10.1016/j.tws.2010.05.004.

Simulia (2014), ABAQUS (Version 6.14), Dassault Systèmes.

Smith, M.D. (2013), "Seismic Testing and Analytical Studies for the Development of New Seismic Force Resisting Systems for Metal Buildings," Doctoral Dissertation, University of California–San Diego, La Jolla, Calif.

Smith, M.D., Turner, K.T., and Uang, C.M. (2013), "Experimental Investigation of Cyclic Lateral Buckling of Web-Tapered I-Beams," Report No. SSRP-12, Department of Structural Engineering, University of California–San Diego, La Jolla, Calif.

Uang, C.M., Smith, M.D., and Shoemaker, W.L. (2011), "Earthquake Simulator Testing of Metal Building Systems," in *Structures Congress 2011*, pp. 693–704, American Society of Civil Engineers, Las Vegas, Nev., https://doi.org/10.1061/41171(401)62.

APPENDIX

Table A. Pinching 04 Model Parameters for All Archetypes							
		Archetype					
Parameter	**Unit**	**AM1**	**AM2**	**AM3R**	**AM4R**	**AM5**	**AM6**
ePf1	kips	23.6	29.4	17.4	27.1	41.8	43.2
ePd1	in.	8.6	5.2	12.2	11.4	6.9	18.4
ePf2	kips	31.6	47.4	30.6	36.1	58.5	56.5
ePd2	in.	11.6	8.4	21.6	15.2	10.9	24.0
ePf3	kips	39.4	50.2	35.1	45.1	69.7	71.1
ePd3	in.	14.6	11.7	25.5	19.3	17.7	30.0
ePf4	kips	31.2	23.3	16.0	36.7	50.0	41.4
ePd4	in.	26.7	17.6	43.6	35.3	20.0	54.7
eNf1	kips	–24.1	–26.3	–21.5	–29.4	–29.9	–44.7
eNd1	in.	–8.8	–4.7	–15.0	–12.3	–4.9	–18.9
eNf2	kips	–28.8	–48.0	–28.4	–35.6	–60.6	–56.0
eNd2	in.	–10.5	–8.6	–19.8	–15.0	–10.0	–23.7
eNf3	kips	–39.6	–50.1	–35.6	–46.0	–67.9	–74.4
eNd3	in.	–14.2	–11.5	–25.6	–19.2	–17.7	–30.4
eNf4	kips	–16.7	–21.5	–12.1	–36.6	–50.0	–39.9
eNd4	in.	–30.7	–15.9	–38.4	–32.6	–20.0	–53.8
rDispP	–	0.705	0.667	0.648	0.751	0.656	0.533
rForceP	–	0.917	0.863	0.857	0.834	0.757	0.979
uForceP	–	–0.615	–0.581	–0.564	–0.585	–0.617	–0.514
rDispN	–	0.603	0.789	0.810	0.797	0.625	0.799
rForceN	–	0.934	0.877	0.877	0.835	0.763	0.982
uForceN	–	–0.638	–0.631	–0.629	–0.609	–0.608	–0.631
dmgType	–	Energy	Energy	Energy	Energy	Energy	Energy

Steel Structures Research Update

The Novel SnapLocX Column Splice

JUDY LIU

INTRODUCTION

Research on an innovative, rapid-assembly column splice is highlighted. The research is led by Dr. Jeffrey Berman and Dr. Dawn Lehman, professors in civil and environmental engineering at the University of Washington, and by Reid Zimmerman, Technical Director at KPFF in Portland, Oregon. Dr. Berman and Dr. Lehman share interests in seismic performance and design of steel structures, performance-based seismic design, and innovative structural systems. Both are recognized for their expertise in large-scale experimental testing, analytical investigations, and synthesis of experimental-analytical research to advance the state of the art and of the practice. Their honors include distinguished teaching and outstanding paper awards from multiple organizations, including the American Society of Civil Engineers (ASCE). Mr. Zimmerman is active in code development for ASCE 7 and ASCE 41, including helping to lead efforts in resilient seismic design and functional recovery. An AISC grant supports this column splice research. The SnaplocX connection is introduced, and highlights from work to date are presented.

MOTIVATION AND RESEARCH OBJECTIVES

This project arose from AISC's Need for Speed initiative. AISC has supported research that aligns with the Need for Speed goal to "increase the speed of designing, fabricating, and erecting steel buildings and bridges by 50%" (AISC, n.d.). In 2022, AISC hosted a SpeedConnection competition and selected a few projects, including the SnapLocX research (Huber and Colsia, 2025).

The basic concept of the proposed column splice is to save construction time and labor with a "snap-and-lock" operation. The SnapLocX connection provides an alternative to the conventional bolted column-to-column splice (Figure 1). Columns arrive on site with snap-and-lock components attached and do not require any field welding or field bolting. Locking plates are shop welded to the upper columns, and snapping plates are shop bolted to the lower columns (Figure 2). Shear keys in the snapping plates align with corresponding slots in the locking plates. With this initial condition, the upper column is lowered toward the lower column. In the intermediate condition, the snapping plates bend outward as the upper column is placed into position. In the final condition, the connection snaps into place, the snapping plates and shear keys then engage with the locking plates and shear key slots (Figure 3). The connection idea was conceived by Reid Zimmerman, who serves as a co-investigator and industry advisor to the project.

The primary objectives of this first phase of the multi-phase project were to demonstrate the feasibility of the SnapLocX splice and to provide a design methodology for an industry-ready connection. The research team fully developed the snap-and-lock connection using selected wide-flange sections. Considering the appropriate demands for column splices in gravity framing, including AISC *Seismic Provisions for Structural Steel Buildings* (2022a) requirements for gravity frame columns, they created design procedures utilizing mechanics principles, structural steel specifications (AISC, 2022b), OSHA's Safety Standards for Steel Erection (OSHA, 2001), and ASCE/SEI 7-22 design loads (2022). The team considered a range of column sizes, outlined the relative geometric requirements of the components, and demonstrated the procedure with an example design. They took the SpeedConnection concept a step further with sets of standardized designs and tabular design aids facilitating quick selection of SnapLocX components for different pairings of column sections. In this manner, the research team has reduced design time as well as construction time.

THE SNAPLOCX CONNECTION

The SnapLocX connection's snapping and locking plate assemblies and shear keys transfer shear and moment while compression is transferred through bearing of the column ends. Each assembly consists of multiple plates. The shear key, plates, bolts, and welds are sized to enable the snap-and-lock action of the connection and to resist the design loading, the latter being often controlled by the shear strength requirements from the AISC *Seismic Provisions* (2022a) for column splices that are not part of the seismic force-resisting system. By satisfying those shear strength requirements, the connection can be used in gravity framing in any part of the country.

Judy Liu, PhD, Research Editor of the AISC *Engineering Journal*, Professor, Oregon State University, School of Civil and Construction Engineering, Corvallis, Ore. Email: judy.liu@oregonstate.edu

Fig. 1. Bolted column splice example.

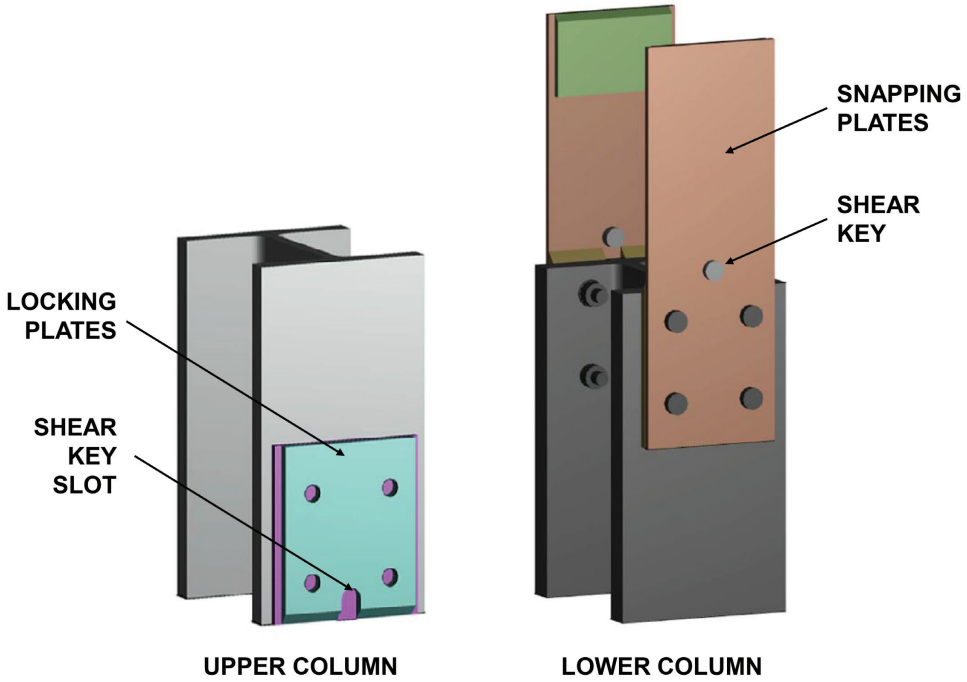

Fig. 2. Upper and lower columns with shop-attached connection plates.

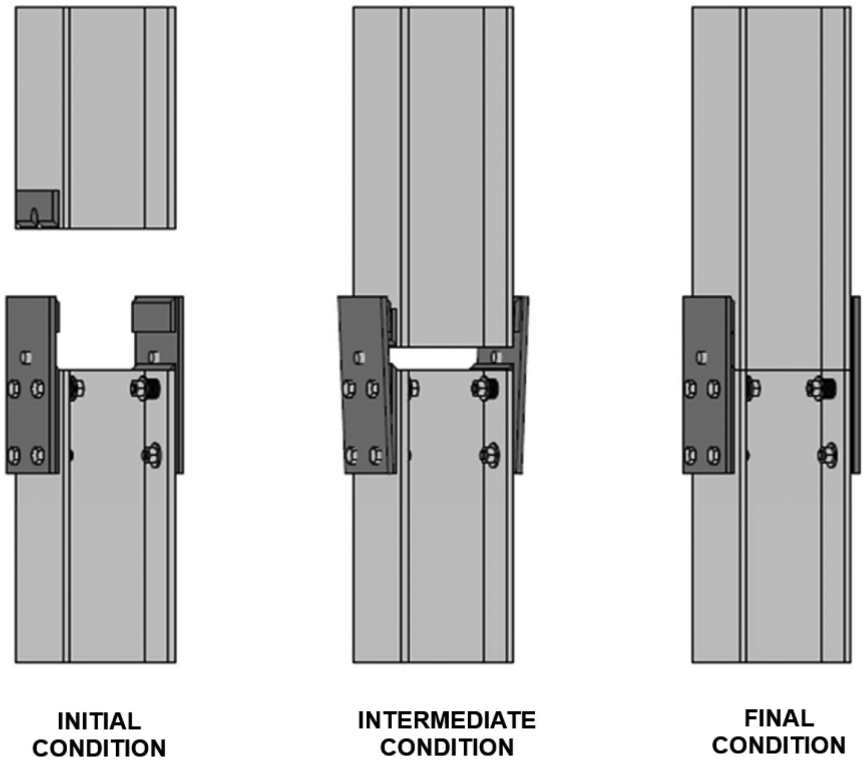

Fig. 3. Initial, intermediate, and final conditions for the snap-and-lock assembly.

The snapping plate assembly consists of an outer plate (OP), upper lock plate (ULP), inner plate (IP), bolts with disc springs, and a shear key (SK) (Figure 4). The ULP and shear key (SK) are welded to the OP (Figure 2). The top of the ULP is beveled at a 45° angle to help align the upper and lower columns and then push the OP outward for the snapping mechanism. An IP is welded to the lower column and sandwiched between the OP and lower column flange in a four-bolt connection. The upper pair of bolts utilizes disc springs—that is, Belleville washers—and are installed with a specified pretension. The disc springs work with the OP for the "snapping" mechanism. Additional details of the washers and other components are provided in Hinaus (2024).

The locking plate assembly consists of a lower lock plate (LLP) and a shim plate (SP) (Figure 4). The LLP is welded to the SP, which is directly welded to the upper column (Figure 2). The LLP has a slot for the shear key and a 45° angle bevel that bears on the matching bevel on the lower column IP.

COMPONENT DESIGN

SnapLocX connection design may be considered in two stages: (1) column splice component design and detailing and (2) snapping assembly design. A brief overview of the component design and detailing is followed by highlights of the snapping assembly design. Additional details and an example design can be found in Hinaus (2024) and Berman et al. (2025).

Component design and detailing includes sizing of plates, bolts, and welds for demands and geometry. The shim plate thickness is determined by the difference in column depths. A minimum upper column depth is recommended to ensure sufficient contact area with the lower column for bearing capacity (Berman et al., 2025). The SnapLocX is currently

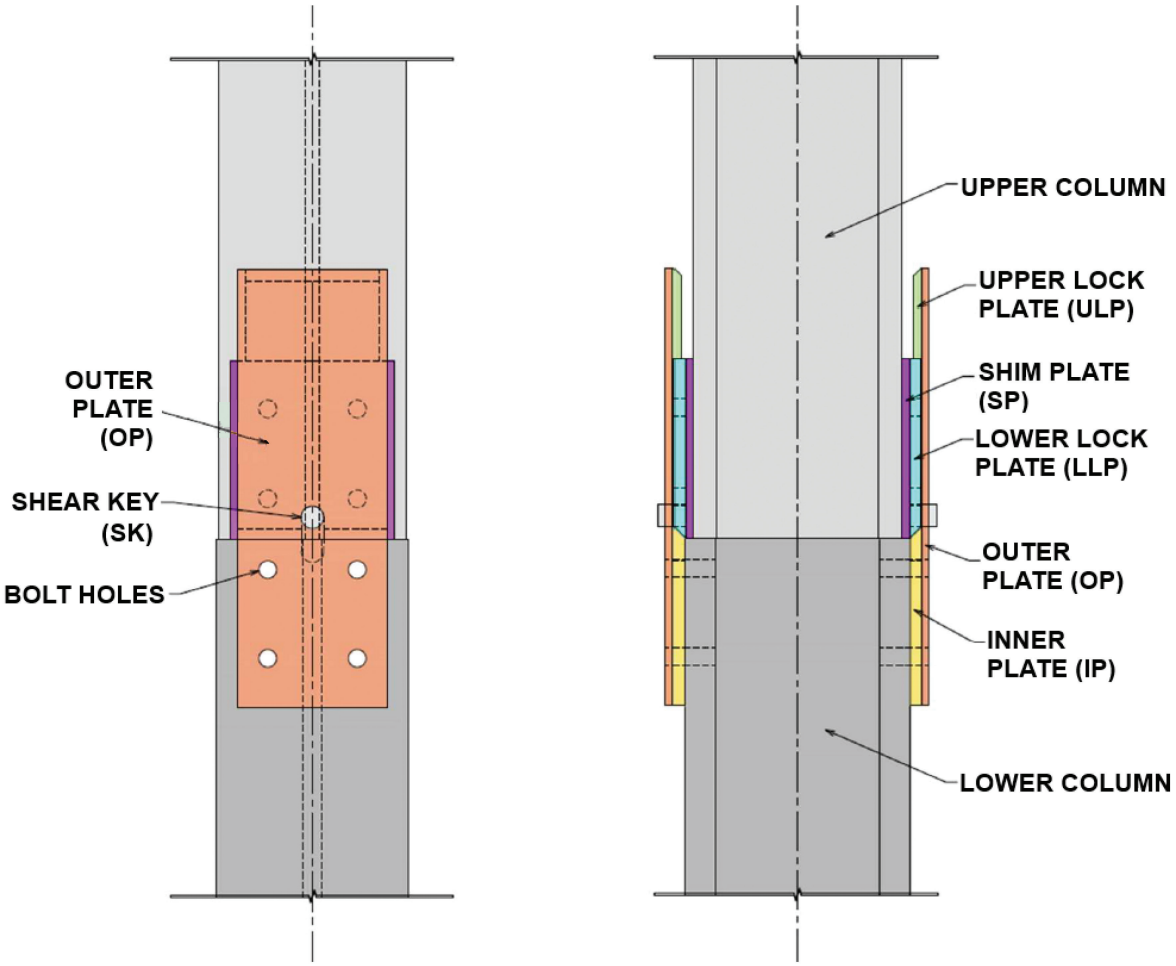

(a) At one flange *(b) Viewed from the side*

Fig. 4. SnapLocX column splice components.

to be used for splicing columns of the same rolled series (e.g., W14× to a W14×). The inner plates (IPs) transfer the major axis column shear forces. The 45° angle bevel and bearing prevent relative movement of the IP and upper lock plate (ULP); the IP therefore resists the shear through its thickness. The minor axis shear is transferred from the upper column to the lower column through the shear key (SK), bearing on the shear key slot in the lower lock plate (LLP) and the bolts connecting the outer plate (OP) to the lower column. Bolts and welds are designed for the resulting demands. For example, the shear key force imposes an eccentric loading on the lower column bolt group. Meanwhile, major-axis flexural demands are resisted by a combination of column flange bearing in compression and transfer of tensile forces through the upper and lower column plates, welds, and bolts. Details of the load path and limit states are provided in Hinaus (2024).

The OPs are designed to accommodate the deformations during assembly. As the upper column is lowered into place, the outer plate bends and must be checked for yielding. The curvature in the outer plate is the largest when the upper lock plate (ULP) is at the leading edge of the lower lock plate (LLP) (Figure 5). The nonlinear elastic load-deformation behavior of the disc springs must also be considered. The research team developed a MatLab script to calculate the resulting moment, shear, and deformation demands along the outer plate (Hinaus, 2024).

Another unique consideration for the SnapLocX connection is the snapping friction. During assembly, the normal force between the ULP and LLP creates a frictional

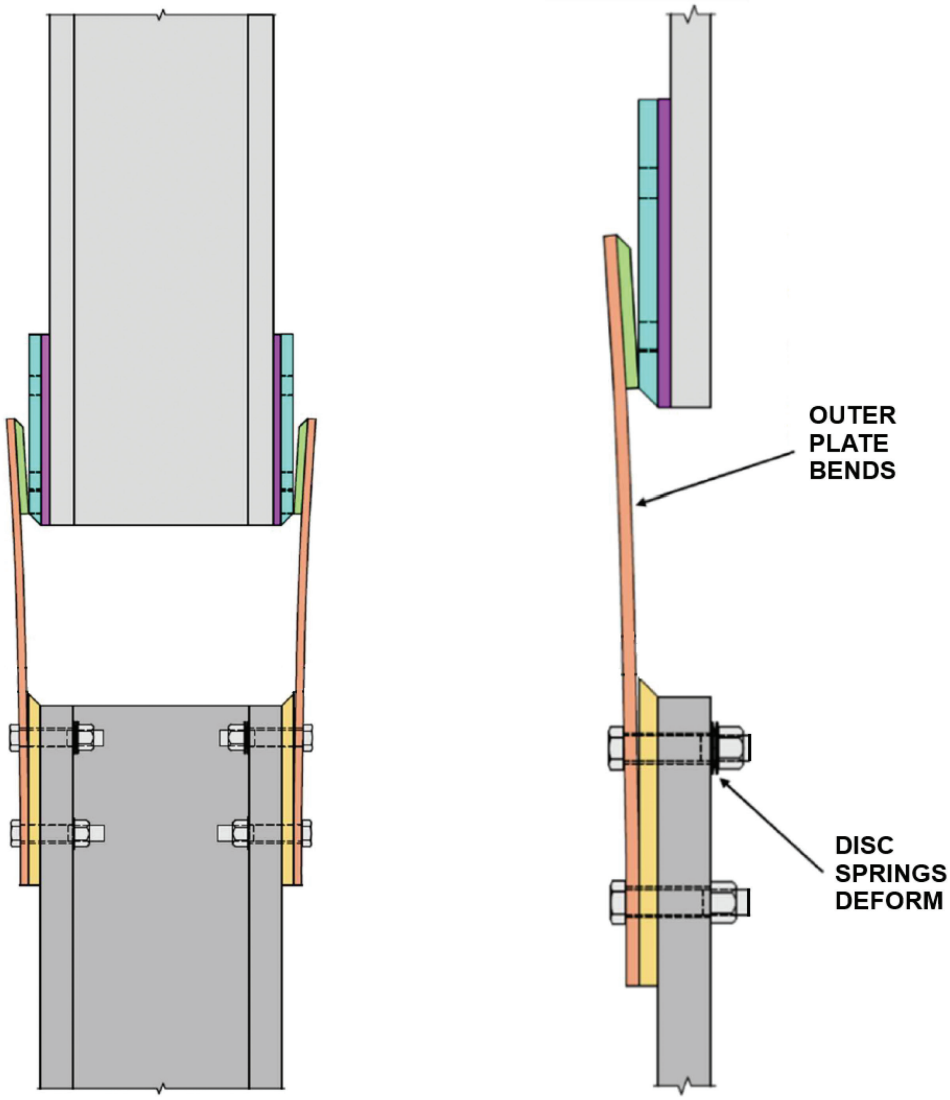

Fig. 5. Intermediate condition of column assembly with bending of the outer plates and deformation of the disc springs.

resistance. The weight of the upper column should be large enough to overcome the friction so that it can drop and snap into place. The research team assumed a friction coefficient of 0.3 in their designs (Berman et al., 2025).

STANDARDIZED DESIGNS

The team has created a tabular process to facilitate design and fabrication of the SnapLocX column splices. The tables are based on sets of standardized splices for a range of potential W10, W12, and W14 sections. The column sizes were partitioned into groups corresponding to specific plate designs. Further refinement produced a selected number of plate designs that satisfy requirements for most potential column splices. This approach limits the number of unique plate designs needed for a building project, aiding in design and fabrication. The approach also allows for potential mass production of certain components that could reduce costs.

This tabular design process provides quick determination of plate combinations and properties for given column sections. First, the upper and lower column sizes are used to determine the plate combination and shim plate (SP) thickness. In Figure 6, the column pairing points to a cell with the SP thickness and a color corresponding to the plate combination (color key at the upper right). For example, a W14×132 upper column with a W14×211 lower column requires plate combination D-5–5 and a ½-in.-thick shim plate. Figure 7 then provides plate design information, including SP width. If the shim plate thickness from Figure 6 is marked with an *, the (*) SP width is used. There is no * in this case, and the SP width is 11 in. Plate D is to be used for the outer plate (OP), and Plate 5 will be used for the inner plate (IP) and lower lock plate (LLP). Additional tables (not shown here) provide the dimensions, as shown in Figure 8 for the LLP, for each plate letter or number (Hinaus, 2024; Berman et al., 2025).

SUMMARY AND FUTURE WORK

Phase 1 of the research has demonstrated feasibility and produced a design methodology for the rapid-assembly SnapLocX column splice. The "snap-and-lock" procedure saves construction time and labor at the acknowledged expense of additional fabrication cost. The designs satisfy requirements for gravity frame column splices. Standardized designs limit the number of unique assemblies needed and reduce design time as well. With this first phase complete, AISC notes that "this connection shows great promise in increasing the speed of steel construction" (Huber and Colsia, 2025).

Phase 2 research plans include SnapLocX mockups, experimental testing, and finite element modeling. The team will design and practice assembly of the column splices. Tests of full-scale specimens will be evaluated for strong- and weak-axis shear and flexural strengths. The experimental results, together with finite element analyses, will be used to support the proposed design methodology and identify any gaps in the procedure.

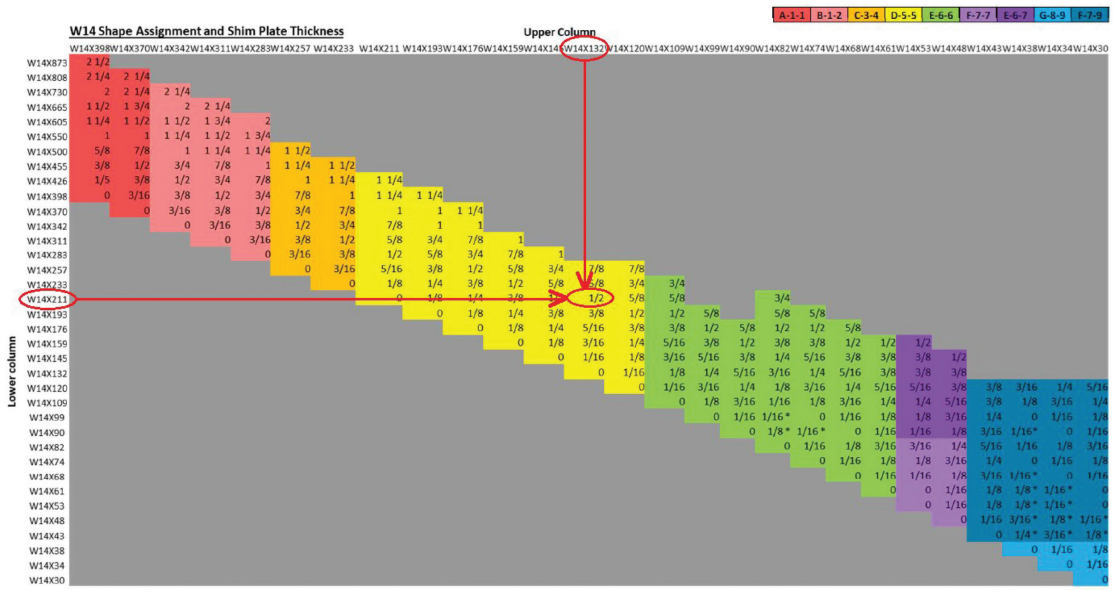

Fig. 6. Sample SnapLocX design and shim plate assignment for W14 column combination.

Phase 2 work may address questions about costs, tolerances, and alternative details. The savings in construction time might be offset by fabrication costs. The proposed mockups and collaborations with steel fabricators and erectors may help to answer questions about the tradeoff between fabrication cost and erection time saved. The mockups for assembly and structural testing could also be used to investigate the impact of tolerances (e.g., for flange thickness and tilt) on construction and structural performance. Meanwhile, alternatives for the shear key could also be explored with consideration for fabrication costs and erection speed.

ACKNOWLEDGMENTS

Thank you to Jeff Berman and Dawn Lehman for their many contributions to this article. The work of graduate researcher Megan Hinaus is also acknowledged. The research is funded by the American Institute of Steel Construction (AISC). The research team would also like to thank industry advisor Reid Zimmerman and the AISC oversight committee: Devin Huber, Jordan Jarrett, Tom Kuznik, Amit Kanvinde, Josh Mouras, Pat Hassett, and JP Martinez. Any findings or recommendations are those of the researchers and do not necessarily reflect the views of the sponsor.

Outer Plate	Inner Plate	Lower Lock Plate	SP Width	(*) SP Width
A	1	1	15 in.	-
B	1	2	13 in.	-
C	3	4	11 in.	-
D	5	5	11 in.	-
E	6	6	9 in.	9 in.
F	7	7	7 in.	-
E	6	7	7 in.	-
G	8	9	5 in.	6 in.
F	7	9	5 in.	7 in.

Fig. 7. Sample plate combination and shim plate width.

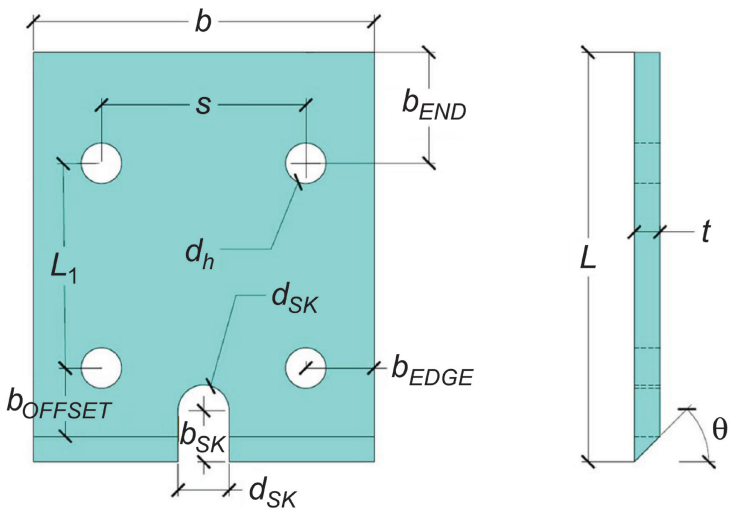

Fig. 8. Design dimensions for the lower lock plate.

REFERENCES

AISC (2022a), *Seismic Provisions for Structural Steel Buildings*, AISC/ANSI 341-22, American Institute of Steel Construction, Chicago, Ill.

AISC (2022b), *Specification for Structural Steel Buildings*, AISC/ANSI 360–22, American Institute of Steel Construction, Chicago, Ill.

AISC (n.d.), *Need for Speed*, American Institute of Steel Construction (aisc.org), https://www.aisc.org/technical-resources/need-for-speed/.

ASCE (2022), *Minimum Design Loads and Associated Criteria for Buildings and Other Structures,* ASCE/SEI 7-22. American Society of Civil Engineers, Reston, Va.

Berman, J., Hinaus, M., and Lehman, D. (2025), *Investigation of a Novel Column Splice Connection: The SnapLocX*, Final Project Report to the American Institute of Steel Construction, University of Washington, Seattle, Wash.

Hinaus, M (2024), *The SnapLocX Connection: A Novel Approach to Interlocking Steel W-Shape Column Splices*, MS Thesis, University of Washington, Seattle, Wash.

Huber, D. and Colsia, C. (2025), "Speed Studies," *Modern Steel Construction,* Vol. 65, No. 1, pp. 50–55, https://lsc-pagepro.mydigitalpublication.com/article/Speed+Studies/4901210/837158/article.html.

OSHA (2001), *Safety Standards for Steel Erection*, 29 CFR 1926 Subpart R, Occupational Safety and Health Administration, U.S. Department of Labor, Washington, D.C.

Guide for Authors

Scope *Engineering Journal* is dedicated to the improvement and advancement of steel construction. Its pages are open to all who wish to report on new developments or techniques in steel design, research, the design and/or construction of new projects, steel fabrication methods, or new products of significance to the uses of steel in construction. Only original papers should be submitted.

General Go to **aisc.org/ej** for complete submittal instructions.

All papers within the scope outlined above will be reviewed by engineers selected from among AISC, industry, design firms, and universities. The standard review process includes outside review by an average of three reviewers, who are experts in their respective technical area, and volunteers in the program. Published papers become the property of the American Institute of Steel Construction and are protected by appropriate copyrights. No typesetting proofs will be provided to authors.

Manuscripts Manuscripts must be provided in Microsoft Word format. Include a PDF with your submittal so we may verify fonts, equations, and figures. View our complete author guidelines at **aisc.org/ej**.

Archives Search at **aisc.org/ej**. Article downloads are free.

Smarter. Stronger. Steel.

American Institute of Steel Construction
130 E Randolph St, Ste 2000, Chicago, IL 60601
312.670.2400 | aisc.org/ej